INSTITUTE OF LOW TEMPERATURE AND STRUCTURE RESEARCH
POLISH ACADEMY OF SCIENCES

Division of Nanomaterials Chemistry and Catalysis.

Doctoral Thesis

Piotr Woźniak

The role of the architecture of $Ce_{1-x}REE_xO_{2-x/2}$ and $Au/Ce_{1-x}REE_xO_{2-x/2}$ (REE- rare-earth element) hierarchical materials in catalytic oxidation of C, CO and C_3H_8.

Supervisor: Dr hab. Eng. Małgorzata Małecka

Wrocław, 2022

Składam serdeczne podziękowania
Pani dr hab. inż. Małgorzacie Małeckiej
za wskazanie mi obszaru badawczego pracy doktorskiej
oraz wszechstronną i życzliwą opiekę
w trakcie jej wykonywania

Table of contents

Summary

This Dissertation describes the role of the architecture of the hierarchical ceria-based gold catalytic systems in the catalytic combustion processes, aiming to provide knowledge to ground the quest of searching new catalysts for environmental applications on an informed basis. In particular, it presents the results of the catalytic activity, selectivity, and stability of the materials in the reactions of carbon monoxide, propane, and soot oxidation, while the structural hierarchy is an examined property of the special interest.

Three goals were set in this work: (i) elaboration of the synthetic procedure for obtaining hierarchical ceria-based $Ce_{1-x}(REE)_xO_{2-x/2}$ (REE- rare-earth element) catalytic supports along with investigation of their properties and catalytic performance, (ii) elaboration of the knowledgeable strategy of decoration of hierarchical supports by gold nanoparticles having desired size, (iii) examining the catalytic properties of gold-decorated ceria-based hierarchical catalysts and determining the role of the materials architecture in catalytic performance.

The synoptic description of the structural hierarchy, surface properties and catalytic performance has been obtained by the following techniques: TEM, HRTEM, SAED, ET, STEM-XED, SEM, XEDS, PXRD, SI-EELS, ATR-FTIR, Raman, H_2-TPR, CO-TPR, TPD-MS, N_2 physisorption, TGA, NAP-XPS, along with CO, C_3H_8 and soot catalytic oxidation tests. Moreover, statistical analysis of the TEM-derived particles size data for assessment of stability of the metal active phase as well as new approach for TOF calculation has been presented.

The proposed hydrothermal and wet chemical methods allow to obtain mixed-cerium oxide hierarchical particles having star-shaped and tube-like morphology and differing in texture. Particles are characterized by three levels of hierarchical organization, and each level of the hierarchical structure has its own functionality and is vulnerable to further modifications.

As synthesized hierarchical catalyst supports show the improved catalytic performance in CO, propane and soot oxidation when compared to non-hierarchical powdered nanoparticles. This effect has been explained by the phenomenon of the facilitated mass transfer and the increased active sites availability due to the introduced hierarchical architecture. The analysis of the temperature-dependent and dopant-dependent PXRD profiles had allowed to assess structural stability of the supports. Rietveld refinement of PXRD had allowed to get insight into microstructure of the materials. Also, the microscopic analysis and developing the temperature-dependent profiles of specific surface area based on N_2 physisorption study had allowed to characterize morphological stability of the systems. Two dopant-dependent architecture transformation patterns induced by temperature has been observed, and the fine architecture of the ceria-based hierarchical particles is preserved up to 600°C that is particularly important in the low-temperature catalytic oxidation processes.

The knowledgeable control of the gold deposition onto hierarchical materials is reached by adjustment of the value of the surface coverage parameter in the urea deposition-precipitation method. Its calculation is based on the knowledge of the total surface area of the hierarchical catalyst support. Among three studied variables, i.e., the surface NO_3^- contamination, the curvature of the surface, and the ratio of the total support surface area to the molar content of gold precursor, the last one is decisive factor in growth of desired-size gold

nanoparticles on ceria systems. The proposed gold decoration approach allows to produce variety of gold-decorated hierarchical catalysts.

The gold-decorated ceria hierarchical catalysts outperform non-hierarchical gold-decorated ceria nanocubes in propane and CO oxidation. Also, the process of doping the materials by Gd^{3+} further increase propane oxidation activity showing two-fold TOF increase. Moreover, such Gd^{3+}-doped catalyst shows four-fold TOF increase over the undoped non-hierarchical one, proving the synergistic effect of doping and structural hierarchy in propane oxidation. The increased activity in CO oxidation has been ascribed to the maximization of Au/ceria interface contact in hierarchical systems and the confinement of Au nanoparticles within pores of hierarchical support.

The texture differences between studied systems plays important role in catalytic performance for non-decorated catalytic supports. This effect is not observed for decorated systems; however, the presence of gold nanoparticles significantly improves selectivity of the propane oxidation. The stability of Au nanoparticles is increased by their confinement in the porous hierarchical structure when compared to the gold-decorated ceria nanocubes in which Au nanoparticles are present only at the surface.

To sum up, the introduction of hierarchy into ceria systems enhances catalytic activity in the studied combustion processes. The fine architecture of catalyst support is retained in low temperature regimes and the metallic active phase is stabilized due to confinement. However, pore geometry and size may restrict the growth of optimally sized Au NPs leading to activity decline, as demonstrated in CO oxidation reaction. Also, doping modifies particles architecture that influences the process of growth of Au nanoparticles. Thus, the knowledge of the material architecture and its temperature-dependent stability is necessary for the precise design of active multifunctional hierarchical catalysts.

Streszczenie

W niniejszej rozprawie opisana została tematyka wpływu architektury hierarchicznych katalizatorów cerowo-złotowych na procesy katalitycznego utleniania, celem dostarczenia ugruntowanego w danych empirycznych rezerwuaru wiedzy dla usprawnienia procesu poszukiwania nowych katalizatorów do zastosowań w ochronie środowiska. W pracy tej zbadano aktywność katalityczną, selektywność oraz stabilność zsyntezowanych materiałów w reakcjach utleniania tlenku węgla(II), propanu oraz sadzy, a hierarchia strukturalna jest wyodrębnioną i intencjonalnie wprowadzoną do materiałów cerowych właściwością, której funkcjonalna rola jest badaną cechą o szczególnej istotności.

W pracy zostały postawione i zrealizowane trzy cele: (i) opracowanie metody syntezy nośników katalitycznych typu $Ce_{1-x}(REE)_xO_{2-x/2}$ (REE- pierwiastek ziem rzadkich) o budowie hierarchicznej wraz z dokonaniem fizykochemicznej charakteryzacji materiałów i zbadaniem ich właściwości katalitycznych, (ii) opracowanie metody dekorowania nośników hierarchicznych nanocząstkami złota o pożądanej wielkości, (iii) zbadanie właściwości fizykochemicznych i katalitycznych układów cerowo-złotowych o budowie hierarchicznej i określenie roli architektury materiałów w wydajności katalitycznej.

Synoptyczny opis architektury układów, charakterystyki powierzchni i właściwości katalitycznych cząstek uzyskano za pomocą następujących technik: TEM, HRTEM, SAED, ET, STEM-XED, SEM, XEDS, PXRD, SI-EELS, ATR-FTIR, Raman, H_2-TPR, CO-TPR, TPD-MS, fizysorpcja N_2, TGA, NAP-XPS wraz z testami katalitycznego utleniania CO, C_3H_8 oraz sadzy. Ponadto przeprowadzona została analiza statystyczna danych pozyskanych metodą mikroskopową celem oceny stabilności metalicznej fazy aktywnej oraz przedstawione zostało nowe podejście do obliczania parametru liczby cykli katalitycznych (TOF).

Zaproponowane metody syntezy umożliwiają wytworzenie cząstek tlenku ceru o budowie hierarchicznej, charakteryzujących się gwiaździstą i rurkową morfologią oraz różniących się teksturą. Cząsteczki charakteryzują się trzema poziomami budowy hierarchicznej, a każdy poziom struktury hierarchicznej ma swoiste własności funkcjonalne i jest podatny na intencjonalne modyfikacje, celem dalszej optymalizacji właściwości materiałów.

Nośniki katalityczne o budowie hierarchicznej wykazują wzmożoną aktywność katalityczną w utlenianiu CO, C_3H_8 oraz sadzy w porównaniu z niehierarchicznymi sproszkowanymi nanocząstkami CeO_2. Efekt ten został wyjaśniony zjawiskiem ułatwionego transportu masy oraz zwiększonej dostępności miejsc aktywnych w materiałach hierarchicznych. Analiza temperaturowo-zależnych profili PXRD próbek, których skład był modulowany dodatkowo obecnością domieszki, pozwoliła na ocenę stabilności strukturalnej nośników katalitycznych. Udokładnienie profili PXRD metodą Rietvelda pozwoliło uzyskać wgląd w mikrostrukturę badanych materiałów. Dodatkowe wykreślenie temperaturowo-zależnych profili powierzchni właściwej materiałów w oparciu o badania fizysorpcyjne wraz z analizą mikroskopową materiałów pozwoliło scharakteryzować stabilność morfologiczną układów. Zaobserwowano występowanie dwóch trybów zmian architektury pod wpływem temperatury, których przebieg był zależny od obecności domieszki. Architektura badanych nośników katalitycznych o budowie hierarchicznej jest zachowana dla temperatur poniżej 600°C, co jest cechą szczególnie istotną w zastosowaniach w niskotemperaturowych procesach utleniania katalitycznego.

Kontrolę nad procesem osadzania nanocząstek złota na nośnikach katalitycznych o budowie hierarchicznej uzyskuje się dzięki dostosowaniu wartości parametru pokrycia

powierzchni, gdy do osadzania użyta jest metoda osadzania-wytrącania z użyciem mocznika. Jego obliczenie jest oparte na znajomości całkowitego pola powierzchni nośnika katalitycznego. Spośród trzech badanych zmiennych, tj. zanieczyszczenia powierzchni przez grupy NO_3^-, krzywizny powierzchni, a także stosunku całkowitej powierzchni podłoża do zawartości molowej prekursora złota, ta ostatnia zmienna jest decydującym czynnikiem wpływającym na proces wzrostu nanocząstek złota o pożądanych rozmiarach w układach cerowych. Proponowane podejście do osadzania złota pozwala na wytwarzanie układów charakteryzujących się zróżnicowaną architekturą.

Dekorowane złotem katalizatory cerowe o budowie hierarchicznej są bardziej aktywne katalitycznie w procesach utleniania CO i propanu w porównaniu do dekorowanych złotem nanokostek CeO_2. Ponadto domieszkowanie materiałów jonami Gd^{3+} dodatkowo zwiększa aktywność katalityczną układów w reakcji utleniania propanu, wykazując dwukrotny wzrost wartości parametru TOF w porównaniu do układu niedomieszkowanego. Katalizator cerowo-złotowy o budowie hierarchicznej domieszkowany jonami Gd^{3+} wykazuje ponad czterokrotny wzrost wartości parametru TOF w stosunku do niedomieszkowanego katalizatora niehierarchicznego, co dowodzi synergicznego efektu domieszkowania i hierarchii strukturalnej w procesie utleniania propanu. Zwiększenie aktywności materiałów w procesie utleniania CO przypisuje się maksymalizacji kontaktu Au/CeO_2 w układach hierarchicznych oraz efektowi zamknięcia nanocząstek Au w ograniczonej przestrzeni porów hierarchicznego nośnika.

Różnice tekstury układów cerowych o budowie hierarchicznej odgrywają istotną rolę we wzmożeniu wydajności katalitycznej dla układów niedekorowanych zlotem. Dla układów dekorowanych efekt te nie został zaobserwowany, jednak obecność nanocząstek złota znacznie poprawia selektywność procesu utleniania propanu. Stabilność nanocząstek złota jest zwiększona dzięki efektowi ich przestrzennego zamknięcia w ograniczonej przestrzeni porowatej hierarchicznej struktury materiałów w porównaniu z dekorowanymi nanocząstkami złota nanokostkami CeO_2, w których są one obecne tylko na powierzchni nośnika.

Podsumowując, wprowadzenie hierarchii do materiałów cerowych poprawia aktywność katalityczną układów w badanych w tej pracy procesach katalitycznego utleniania. Stabilność architektury nośnika katalitycznego o budowie hierarchicznej zachowywana jest dla reżimu temperatur do 600°C, a metaliczna faza aktywna jest stabilizowana dzięki efektowi zamknięcia nanocząstek złota w ograniczonej przestrzeni porów. Jednak geometria i rozmiar porów mogą ograniczać wzrost nanocząstek Au o optymalnej wielkości, prowadząc do spadku aktywności, co wykazane zostało w reakcji utleniania CO. Ponadto domieszkowanie modyfikuje architekturę nośników katalitycznych, co wpływa na proces wzrostu nanocząstek Au. Zatem znajomość architektury materiałów oraz jej stabilności jest niezbędna do intencjonalnego projektowania aktywnych, wielofunkcyjnych katalizatorów hierarchicznych.

1. Scope and research goals

The aim of this Dissertation is to determine structure-reactivity dependencies of hierarchical ceria-based gold catalytic systems in catalytic combustion processes. This subject fits within a research activity of searching new active catalysts for environmental applications and focuses particularly on examining the role of material architecture in catalytic oxidation performance. The research project is parted into three main objectives, and each one is subdivided into specific research goals.

The first objective includes elaboration of synthetic procedure for obtaining hierarchical $Ce_{1-x}(REE)_xO_{2-x/2}$ (REE- rare-earth element) catalytic supports along with a thorough description of their architecture as well as physicochemical and catalytic properties. Specific research goals involve investigation of temperature- and dopant-dependent architecture stability of synthesized supports, comparison of their reactivity with non-hierarchical ceria material, examining the influence of dopant on the particle's stability under oxidation process conditions, and determining selectivity in total oxidation reactions. Also, the influence of the differences in architecture in terms of texture of hierarchical macroparticles on the catalytic performance has been studied.

The second objective involves elaborating method of knowledgeable decoration of ceria-based supports by gold nanoparticles having desired size falling within the range with the highest expected catalytic activity (2-4 nm). This size range was chosen based on literature premises such as high activity [1], stability due to interfacial anchoring [2], and efficiency of metal-support interaction tuning [3] Specific research goals included the determination of critical factor influencing the size of gold nanoparticles in the process of its deposition on ceria-based supports as well as developing the method of intentional decoration of hierarchical systems by gold nanoparticles.

The third objective involves determination of the role of architecture of gold-decorated $Au/Ce_{1-x}(REE)_xO_{2-x/2}$ hierarchical systems in catalytic oxidation performance. In particular, several merits of materials architecture such as (1) surface area and porosity, (2) mutual arrangement of support crystallites, (3) nanoparticles confinement, (4) optimal size of nano-gold, (5) metal-support contact has been identified and discussed to explain the effect of enhanced catalytic activity. Selectivity and stability of catalysts have also been investigated.

This thesis is a collection of articles that has been published in the refereed international scientific journals. It also includes the brief recapitulation of research and literature review that has been contained in the following chapters: Theoretical background, Experimental Techniques, Results, Conclusions, and Additional Materials.

2. List of publications with graphical abstracts

D1. Woźniak, P., Miśta, W., Małecka, M.A., Function of various levels of hierarchical organization of porous $Ce_{0.9}REE_{0.1}O_{1.95}$ mixed oxides in catalytic activity, CrystEngComm, 2020, 22, 5914-5930.

D2. Woźniak, P., Małecka, M.A., Chinchilla, L., Trasobares, S., 3D hierarchically structured $Ce_{1-x}Gd_xO_{2-x/2}$ mixed oxide particles: the role of microstructure, porosity and multi-level architecture stability in soot and propane oxidation, Mater. Res. Bull., 2022, 151, 111816.

D3. Małecka, M.A. Woźniak, P., Hierarchical macroparticles of ceria with tube-like shape – synthesis and properties, CrystEngComm, 2021, 23, 6743-6754.

D4. Małecka, M.A., Matus, K., Woźniak, P., Decoration of Cube-Like Ceria Crystals by Well- Dispersed Au Nanoparticles: Surface Influence, ChemistrySelect 2020, 5, 2871-2877.

D5. Woźniak, P., Małecka, M.A., Kraszkiewicz, P., Miśta, W., Bezkrovnyi, O., Chinchilla, L., Trasobares, S., Confinement of nano-gold in 3D hierarchically structured gadolinium- doped ceria mesocrystal: synergistic effect of chemical composition and structural hierarchy in CO and propane oxidation. Catal. Sci. Technol., 2022, 12, 7082-7113.

D6. Woźniak, P., Kraszkiewicz, P., Małecka, M.A., Hierarchical Au/CeO2 systems – influence of Ln^{3+} dopants on the catalytic activity in the propane oxidation process, CrystEngComm, 2022, 24, 6408–6420.

Graphical abstracts

[D1]

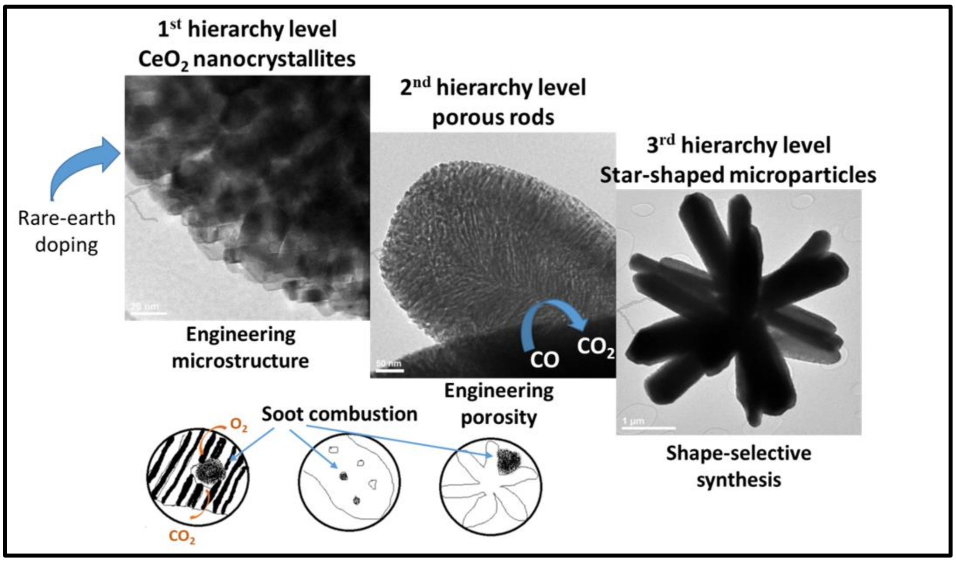

[D2]

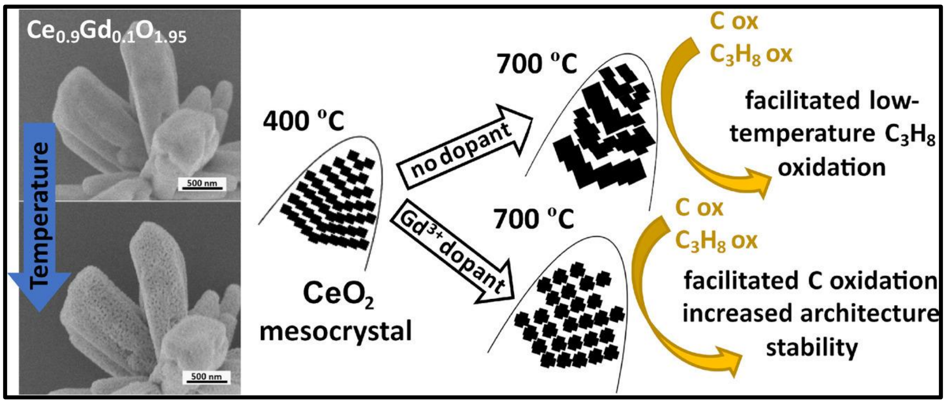
$Ce_{0.9}Gd_{0.1}O_{1.95}$
Temperature
500 nm
500 nm
400 °C
CeO_2 mesocrystal
no dopant
Gd^{3+} dopant
700 °C
700 °C
C ox
C_3H_8 ox
facilitated low-temperature C_3H_8 oxidation
C ox
C_3H_8 ox
facilitated C oxidation
increased architecture stability

[D3]

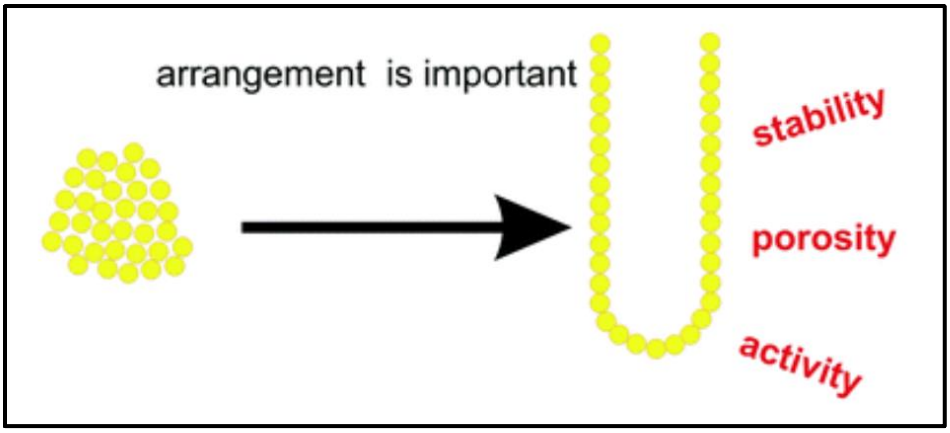
arrangement is important
stability
porosity
activity

[D4]

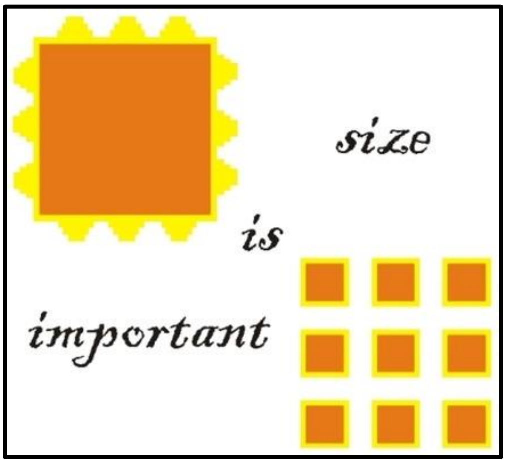
size
is
important

[D5]

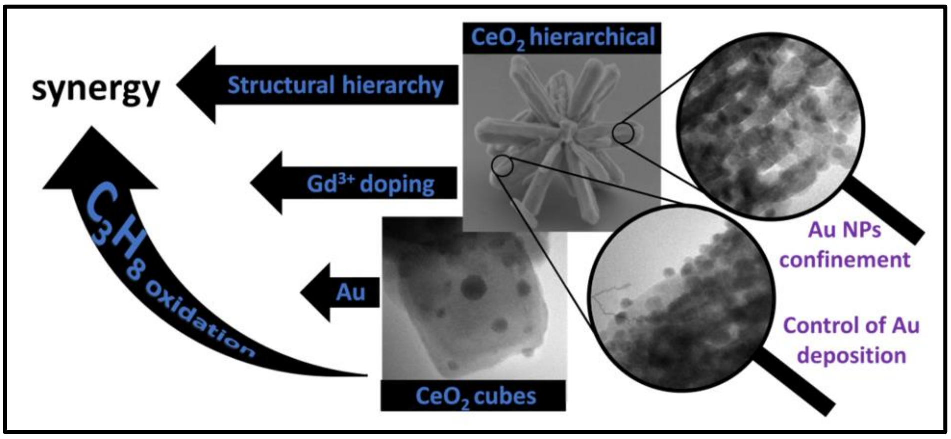
synergy
Structural hierarchy
Gd3+ doping
Au
CeO2 hierarchical
CeO2 cubes
C3H8 oxidation
Au NPs confinement
Control of Au deposition

[D6]

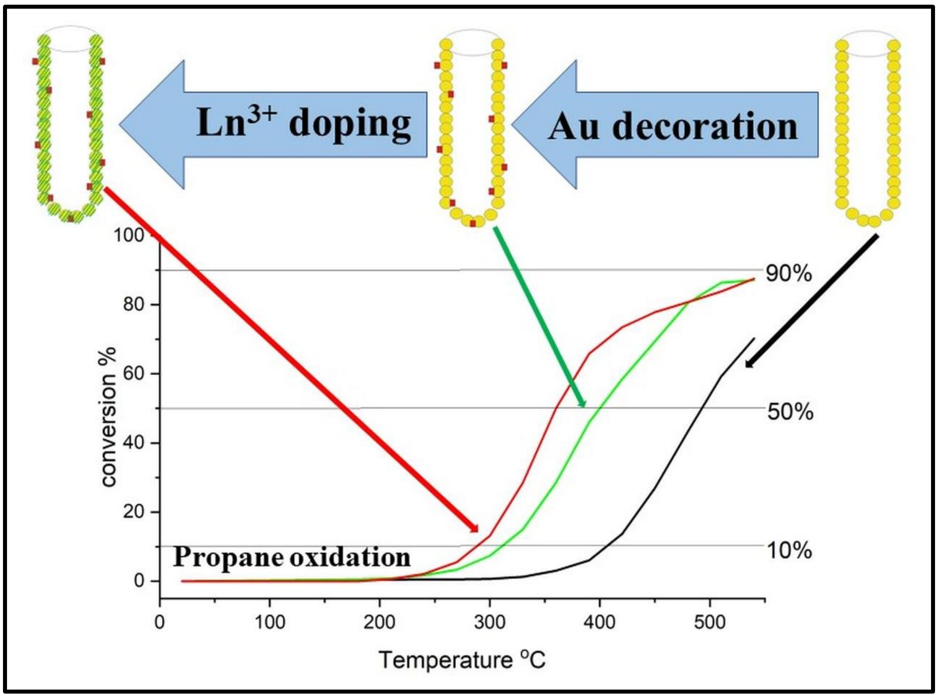
Ln3+ doping
Au decoration
Propane oxidation
conversion %
Temperature °C
0
20
40
60
80
100
0
100
200
300
400
500
90%
50%
10%

3. Theoretical background

Environmental catalysis refers to emission control of hazardous, environmentally unacceptable compounds. This includes developing technologies and processes for atmospheric pollutants abatement, solid and liquid waste treatment, greenhouse gas emission decrease, reduction of indoor pollution [4]. Automotive exhaust gasses in the form carbon monoxide (CO), hydrocarbons (HCs), nitrogen oxides (NOx) as well as particulate matter (PM) constitute the main environmentally harmful pollutants due to ever increasing human mobility [5,6]. Because of the undesirable formation of by-products caused by not complete combustion of fuel in automotive engines [7], the search for pollutants abatement from mobile sources is a current issue of the research activity. The elimination of toxic CO, short-chain alkanes such as propane, and particulate matter as soot emitted from Diesel engines is important for the protection of human health and achieving environmental sustainability [8,9].

Cerium oxide has been an object of structural and catalytic examination for a long time due to its unique redox capabilities, namely the ability to store or release oxygen depending on environmental gaseous conditions that is known in the literature as oxygen storage capacity (OSC) [10]. Due to that feature, it has been widely utilized in the motor industry as a three-way catalyst [11], among other applications in solid oxide fuel cells [12], water-gas shift reaction materials [13] and volatile organic compound catalytic conversions [14]. The high activity of ceria-based catalysts is due to their ability to reversibly change the oxidation state of cerium $Ce^{4+} \leftrightarrow Ce^{3+}$ ($Ce^{IV}O_2 \leftrightarrow Ce^{IV}_{1-x}Ce^{III}_{x}O_{2-x/2}$) [15]. This reduction–oxidation reaction is fully reversible and may be performed cyclically. Also, each low-index crystallographic face of CeO_2 exposes a different number of vacancies and has a specific O-vacancy formation energy, and hence the oxidation activity is highly dependent on the surface chemistry of ceria, following the order of {110} > {100} > {111} [16].

Moreover, due to the dependence of the oxygen vacancy concentration on size of the ceria particles, the oxygen uptake/release may be enhanced by knowledgeable nanometer-level design of the shape and size of the particles [17–19]. The ‘nanosize effect’ is linked to the increase of defect concentration in nanomaterials [20,21], but also relates to a modification of such physicochemical characteristics of the particles as lattice parameter [22], surface area [23], microstrain [24], surface complexation patterns [25] and electronic band structure [26]. Hence, cerium oxide is a promising material as the active support for metal catalysts, making it suitable for rational morphology design.

However, the agglomeration and sintering of the powdered samples may limit ceria nanoparticles commercial utilization. Also, there are safety concerns related to usage of nano-sized materials that may affect environment and biological organisms in an unpredictable way [25]. One of the possible solutions to this problem is designing hierarchically structured porous materials composed of ceria crystallites that preserve nanosize-arised properties while keeping the large size of nanoparticles assemblage unit.

Various types of material hierarchies have been highlighted in the literature, such as morphological, structural, compositional, and porous hierarchy [27]. Morphological hierarchy describes materials having units with defined morphology spanning different numbers of structure levels (e.g., multi-shell hollow spheres) [28]. Structural hierarchy relates to the repetitive combination of units, forming superstructures composed of mutually ordered nanoparticles (mesocrystals) [29] or materials with distinguished levels of structural units, forming complex structures (e.g., hollow nano-cone-constructed ceria [30], ceria nanobundles [31] and 3D flowerlike ceria [32]). Compositional hierarchy refers to the spatial distribution of various building units differing in composition (e.g., core–shell mesoporous nanospheres [33] and hollow@mesoporous yolk–shell structure [34] and the porous hierarchy involves the distribution of multimodal pores in a material (e.g., micro–macroporous zeolites [35]). The ensemble of nanoparticles that form a higher-order hierarchical structure may possess unique properties that differ from those of individual nanoparticles and corresponding bulk samples, which may contribute to its catalytic performance [36]. Engineering 3-dimensionally hierarchically structured materials composed of ceria nanoparticles for HCs oxidation may add value to the present automotive exhaust gas treatment.

In addition to designing material on a meso-to-macro scale, dopants may be introduced into nanoparticles which modify their properties at the micro-scale level. Presence of dopant in the cerium oxide structure is inevitably linked to creation of oxygen vacancies by substitution of Ce^{4+} ions by their low-valent counterparts and subsequent removal of oxygen atoms for charge balance [37]. Such defect engineering in ceria has been studied extensively in the past with different rare earth and transition elements [38]. Such introduction of trivalent lanthanide dopants enhances the OSC by facilitating oxygen mobility (creation of extrinsic oxygen vacancies in the lattice), which enhances the redox properties of the mixed oxide [39,40]. Also, the presence of rare earths in the cerium matrix improves its stability through the hindrance of grain growth under high temperature reducing and oxidizing conditions of operation [41]. Thus, rare-earth-doped hierarchically structured ceria is a promising improved candidate material for catalytic applications. Nonetheless, little attention has been put on a modification of nano-sized building units within hierarchical architectures, listing just a few examples in the literature [42,43].

Another way to modify hierarchical material is to embed metal particles. Supported gold nanoparticles have been the object of intensive research due to their exceptional catalytic activity in technologically and environmentally important reactions [44]. The properties of heterogeneous gold catalysts have been summarized in many excellent reviews involving their structure and surface chemistry [45], the role of supports [46], and the type of catalyzed reaction [47]. Also, many suggestions on the optimization of supported gold catalysts to enhance their activity, selectivity, and stability in established reactions, such as adjusting the Au nanoparticle size [48–50], engineering metal– support interaction [3,51], shape modification of nanostructured support [18], and doping [52] have been provided.

Thus, gold-decorated hierarchical materials may show further beneficial properties due to the additional interfaces between the metal and oxide, inducing multiple interactions [53], or increased sintering resistance due to the confinement of the metal nanoparticles [54]. However, limited systematic research has been devoted to this topic, especially controlling the catalytic properties as a function of multi-level catalyst architecture and surface chemical properties of these advanced systems [53].

In this Dissertation, the role of the hierarchical architecture of ceria-based catalytic supports and gold-decorated ceria-based hierarchical catalysts on catalytic oxidation performance has been studied. Although the majority of recent research focused on metal-decorated 0D and 1D nanostructures, this research concentrates on knowledge-driven 3D hierarchical mesocrystal catalyst design and studying the influence of architectural attributes including (i) size, morphology and composition of the catalyst support nanoparticles, (ii) mutual arrangement of support crystallites, (iii) porosity, (iv) size and distribution of catalyst metal nanoparticles in hierarchical materials, and (v) surface properties, on the catalytic activity. Also, selectivity and stability of materials have been examined. The knowledgeable combination of these structural merits can enable to design real working catalysts for environmental protection.

4. Experimental techniques

4.1. Synthesis

Hierarchical star-shaped ceria-based catalytic support (HSNPs) was synthesized by solvothermal method coupled with oxidation thermolysis. Details are presented in [D1, D2, D5].

Hierarchical tube-like ceria-based catalytic support (tubes) was synthesized by multi-step wet-chemical approach. Details are presented in [D3, D6].

Cube-like ceria-based nanoparticles (cubes) were synthesized by hydrothermal method. Details are presented in [D4, D5].

Non-hierarchical ceria-based nanoparticles (NPs) were synthesized by microemulsion (water-in-oil) technique. Details are presented in [D1-D3, D5-D6].

The deposition-precipitation method was used to embed gold nanoparticles on catalytic supports. Details are presented in [D4, D5, D6].

4.2. Physicochemical characterization

To get insight into the structure and microstructure of materials, to confirm phase purity as well as to estimate crystalline grain size powder X-ray diffractograms (PXRD) were recorded on a PANalytical X'Pert Pro X-ray diffractometer. Scherrer formula was applied to estimate crystallite sizes. Strain and size contributions to PXRD patterns were resolved by Rietveld refinement. Instrumental broadening was included by refinement of standard silicon sample followed by refinement of PXRD profiles with the use of TCH Pseudo-Voigt function.

For particle architecture examination Transmission Electron Microscope (TEM) imaging and High-Resolution Transmission Electron Microscope (HRTEM) imaging in bright-filed (BF) and dark-field (DF) modes were collected via the use of Philips CM-20 SuperTwin as well as double aberration corrected FEI Titan^3 Themis 60-300 microscopes at the accelerating voltage of 160 kV and 200 kV, respectively. Nanoparticles size and shape, crystal structure, size dispersity, agglomeration degree, and materials porosity were determined.

To get insight into textural characteristics of hierarchical samples Selected Area Diffraction (SAED) patterns were collected.

To obtain 3D visualization of the architecture of hierarchical catalyst Electron Tomography (ET) was performed.

For visualization of the surface and overall shape of hierarchical macroparticles Scanning Electron Microscope (SEM) images were collected on FEI Nova NanoSEM 230 equipped with ETD and TLD detectors.

Elemental analysis was performed using X-ray Energy Dispersive Spectroscopy (XEDS) (EDAX PegasusXM4). Global concentration measurements were performed on samples placed in carbon resin. Also, individual macroparticles were analyzed via selected area mode.

Local composition of the samples at a nanometer scale was studied by Scanning Transmission Electron Microscope- X-ray Energy Dispersion Spectroscopy (STEM-EDX) technique using the C_s-corrected S/TEM Titan 80-300 FEI microscope equipped with EDAX EDX

The acquisition of XEDS maps was carried out using an electron probe less than 0.5 nm. The elemental distribution maps of cerium and gadolinium were generated.

Cerium oxidation state analysis was performed by Spectrum Imaging- Electron Energy Loss Spectroscopy (SI-EELS) technique employing a source at 200 kV.

The surface chemical profile was checked by Fourier Transform Infrared (FTIR) spectroscopy on a Nicolet Is 50 spectrometer.

Raman spectra were collected on Renishaw InVia Raman microscope equipped with confocal DM 2500 Leica optical microscope, a thermoelectrically cooled CCD as a detector and an argon laser operating at 488 nm.

To get insight into mass loss ratio in thermolysis process during synthesis of hierarchical ceria Thermogravimetric Analysis (TGA) was performed.

N_2 physisorption study was performed on a Fisons Sorptomatic 1900 instrument on ASAP 2020 Micromertics to get insight into materials porosity and stability of architecture. The specific surface area (S_{BET}) of the nanomaterials was assessed by applying the Brunauer–Emmett–Teller equation to the as collected isotherms.

To get insight into chemical surface characteristics of studied materials Temperature Programmed Reduction tests (H_2-TPR and CO-TPR) were performed on Autochem II 2920 (Micromeritics, USA) equipped with TCD detector. Also, Temperature-Programmed Desorption (TPD-MS) measurement on the bare CeO_2 hierarchical sample was performed.

For in situ surface characterization of catalysts and determination of oxidation state of gold Near-Ambient Pressure X-Ray Photoelectron Spectroscopy (NAP-XPS) measurements were performed using a laboratory NAP-XPS system.

4.3. Catalytic tests

Catalytic tests were performed in CO, propane, and soot oxidation reactions. Briefly, for CO oxidation 50 mg of the catalyst (fine, unfractionated powder) was placed in a quartz U-type microreactor and installed in a commercial apparatus (Autochem II 2920, Micromeritics). The feed gas consisted of 1% CO, 5% O_2 and 94% He with a total flow rate of 50 ml min^{-1} with 3°C min^{-1} temperature increases between 25 - 400°C. The composition of gases was measured with an OmniStar QMS-200 Pfeiffer Vacuum mass spectrometer. The stepwise propane conversion measurements (50 mg of the sample) were performed in the temperature range of 20–540°C in a gas flow (mixture 2500 ppm C_3H_8 in air (10% O_2 in N_2), 100 cm^3 min^{-1}) followed by gas chromatography analysis. Soot combustion tests were performed in "tight contact" mode by placing a ground mixture of 40 mg of ceria and 20 mg soot in a corundum crucible into a TG analyzer Derivatograph MOM Q-1500D with a programmed temperature increase of 5°C min^{-1} in the range 25 – 700°C.

Details related to research techniques used may be find directly in publications [D1-D6].

5. Results

The first objective involved development of the procedure for synthesizing hierarchical $Ce_{1-x}(REE)_xO_{2-x/2}$ catalytic supports along with a survey of their structural and chemical properties. Two types of such supports differing by the architecture and texture are described in [D1] (star-like particles) and [D3] (tube-like particles). The detailed description of the support multi-level architecture and the role of each level of the material hierarchical organization in catalytic performance has been presented in [D1] and advanced in [D2].

The second objective was to develop the method of knowledgeable decoration of ceria-based supports by gold nanoparticles. The elaboration of decoration procedure tested on a nonhierarchical model system, i.e., CeO_2 nanocubes, is presented in [D4]. The refined method that enables to decorate hierarchical supports has been advanced and described in [D5].

The third objective was to determine the role of the architecture of gold-decorated $Au/Ce_{1-x}(REE)_xO_{2-x/2}$ hierarchical systems in catalytic oxidation performance. Catalytic performance in terms of reactivity, selectivity and stability of studied systems has been presented in [D5] and [D6].

Table 1 summarizes types of oxidation processes and catalytic performance parameters studied in publications D1-D3 and D5-D6. Reactivity is described in terms of half-oxidation temperature (T_{50}) [D1-D3, D5-D6], specific reaction rate (r) or turnover frequency (TOF) [D5]. Selectivity is described in terms of chromatography profile results analysis [D2, D6]. Stability is characterized in terms of a) temperature-dependent shape stability of support macroparticle [D1, D2, D3], b) temperature- and dopant-dependent stability of the support F-type crystal structure [D2, D6], c) dopant-dependent stability of macroparticle architecture [D2, D6], d) support stability under process conditions, e) temperature-dependent stability of size of Au nanoparticles [D5-D6)]

Table 1. Summary of the reaction types and properties studied in publications D1-D6.

Publication	**D1**	**D2**	**D3**	**D5**	**D6**
Hierarchical $Ce_{1-x}(REE)_xO_{2-x/2}$ system	star	star	tube	Au/star	Au/tube
CO oxidation	v	-	-	v	-
C_3H_8 oxidation	-	v	v	v	v
soot oxidation	v	v	v	-**	-**
reactivity	v	v	v	v	v
selectivity	-	v	- *	- **	v
stability	v	v	v	v	v

* described in D6; ** presented in Additional Materials

The main research results are briefly summarized in the following parts of this Dissertation. The discussion of many minor research results, which provide additional insight into the nature of the materials studied but constitute a digression to the main research goals of this Dissertation, have been omitted and can be found directly in publications or supplementary information files attached to each publication.

5.1. Hierarchical supports

5.1.1. Synthesis

Several synthetic protocols have been developed to produce ceria nanostructures, and typical examples involves hydrolysis [55], precipitation/coprecipitation [56], surfactant-templated synthesis [57], sol-gel [58], combustion [59], microemulsion [60], hydrothermal/solvothermal [61,62]. Hierarchically organized macrostructures composed of nanoparticles are produced with the use of combined templating strategies [63], self-assembly [64], post-synthetic modification [65], 3D printing [66]. A variety of CeO_2 systems showing hierarchical architecture have been described in the literature and this is summarized in Table 1 in ESI [D1]. The most catalytically active architectures in CO oxidation involve globin-like spheres [67], nanobundles [31] and hollow cone particles [30]. However, somewhat limited systematic research has been devoted to study the influence of materials architecture on its catalytic behavior, especially controlling catalytic properties as a function of multi-level catalyst architecture [53].

The novel combined hydrothermal synthesis of mixed rare-earth-doped cerium formates followed by post-synthetic oxidative thermolysis of the material yielding star-shaped oxide hierarchical particles has been presented in [D1]. The morphology of the particles (see Fig. 1.A) is dissimilar to the flower-, coral- and urchinlike hierarchical ceria reported in the literature differing in diameter of the arms, mean particle size and porosity [D1, D2]. Such morphological differences influence the physical properties of the hierarchical material affecting stability and catalytic performance. The preservation of star-shape morphology after thermolysis has been confirmed by microscope imaging, and this proves the effectiveness of this synthetic strategy in production of hierarchical ceria particles co-doped with all rare earth elements [D1].

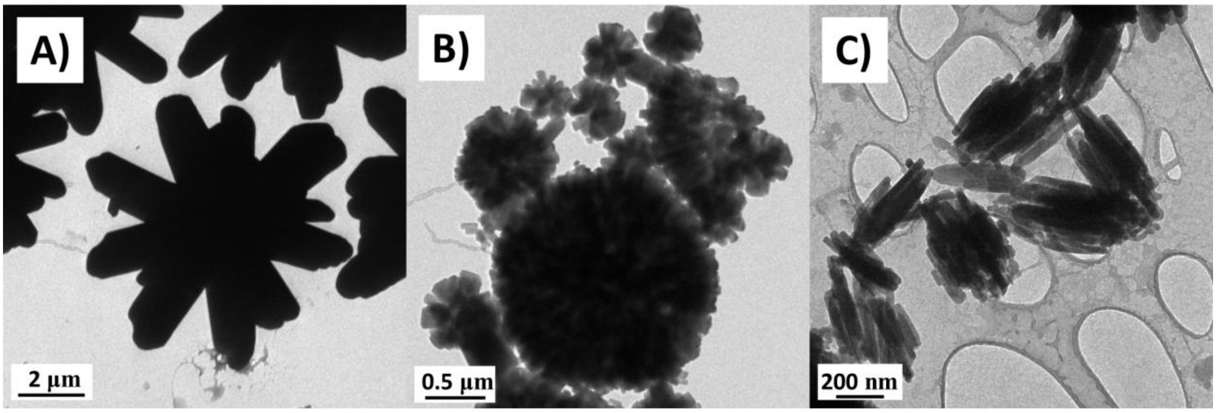

Fig. 1. TEM images of $Ce(HCOO)_3$ particles synthesized in different conditions: A) Star-shaped morphology (DMF and formic acid), B) Sphere-shaped morphology (formic acid), C) Clumped rod-shaped morphology (DMF and formic acid neutralized by ammonia) (adapted from Fig. 1 in D2).

The advancement on the nature of the morphology formation of star-shaped cerium formate particles has been presented in [D2]. The morphology of cerium formate crystals depends on two factors recognized in the literature, i.e., temperature and type of ceria precursor, leading to the formation of needle-shaped or rod-shaped crystals [68]. In addition to the recognized factors, the composition of the solvothermal reaction mixture also influences the particles morphology, as has been shown in [D2]. Synthetic protocol modification leads to formation of sphere-like $Ce(HCOO)_3$ particles under strongly acidic conditions without the use of dimethylformamide (Fig. 1.B) or clumped rod-shaped $Ce(HCOO)_3$ particles after neutralization of the reaction mixture by NH_3 (Fig. 1.C). This experimental observations have been discussed in the light of possible non-classical crystal growing processes involving (1) assembly of fully developed crystals, (2) aggregation of formate nanoparticles/nanocluster at early crystallization stage followed by star-shaped-like multidirectional crystal elongation or (3) site-selective adsorption of additives/the DMF decomposition products inducing preferential growth [D2]. To confirm either of the presented hypothesis further research on the early stages of cerium formate crystal formation using in situ microscopy techniques like fluid cell HRTEM imaging or, alternatively, cryo-TEM shock-frozen samples is needed.

The novel wet chemical synthesis of hierarchical Yb-doped ceria macroparticles with tube-like morphology has been presented in [D3]. The multi-step synthesis involved microemulsion-based preparation of CeO_2 nanoparticles, subsequent chemical transformation of nanoparticles into $Ce(HCOO)_3$ followed by surfactant-assisted precipitation method. This strategy produced hollow inside and closed on one side tube-like hierarchical macroparticles composed of ceria nanocrystallites (Fig. 2).

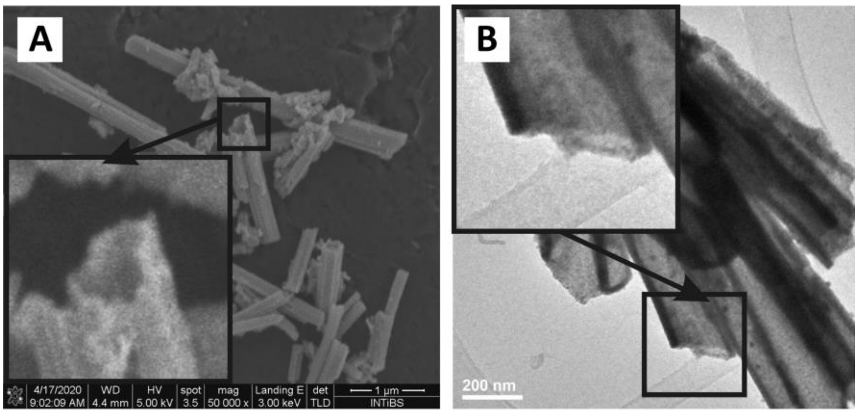

Fig. 2. (A) SEM and (B) TEM image of CeO_2 tube-like hollow inside hierarchical macroparticle (adapted from Fig. S2 in D3).

Optimization of this synthetic procedure involving modification of surfactant and base ratios in the reaction mixture has been presented in Supplementary materials in [D3]. Presence of CTAB and proper amount of NH_4OH is necessary for the correct run of the synthesis. The complete transformation of $Ce_{1-x}Yb_xO_{2-x/2}$ into $Ce_{1-x}Yb_x(HCOO)_3$ at an early stage of material preparation is confirmed by PXRD (Fig. A1 in Additional Materials). The mechanism of final CeO_2 morphology formation probably includes template-assisted assembly of nanoparticles, but its exact form has not been identified.

5.1.2. Architecture

The distinctive feature of rare-earth-doped ceria particles with star-shaped morphology is their three-level hierarchical architecture (Fig. 3.A-C), and preferential orientation of ceria crystallites within hierarchical macroparticle that has been confirmed by SAED pattern collected from the large area of the particle (Fig. 3.B). The first level is composed of nano-sized ceria crystallites. In the second hierarchy level, the nanocrystallites are arranged into porous rod-shaped arms. Then, these mesocrystalline units are arranged into star-shaped particles on the third organizational tier. The preservation of star-shape morphology of doped-ceria material after thermolysis process has been confirmed by TEM, HRTEM and SEM imaging and thoroughly described in [D1], proving the effectiveness of the applied synthetic strategy in production of hierarchical material.

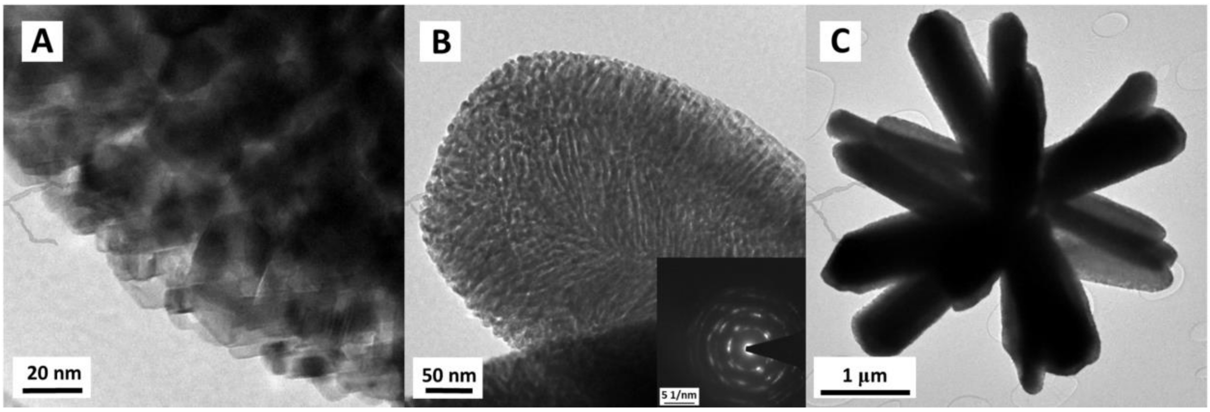

Fig. 3. TEM images showing the three-level hierarchical architecture of $Ce_{0.9}REE_{0.1}O_{1.95}$ oxide material. (A) 1st level: CeO_2 nanocrystallites; (B) 2nd level: porous arm; the inset presents a SAED pattern collected from the whole area visible in the image; (C) 3rd level: star-shaped microparticle (adapted from Fig. 2 in D1).

Each level of the hierarchical architecture of the star-like mixed oxides has its own functionality and it is vulnerable to modifications. Briefly, the introduction of a rare-earth dopant modifies physicochemical properties of nanocrystalline building blocks at the first hierarchy level affecting nanoparticle size [D1, D2], microstrain [D2], oxygen vacancy concentration [D1], H_2 reducibility [D1, D2], while the overall hierarchical architecture of the macroparticle is preserved. The properties may be further modified by varying the dopant concentration. Also, the introduction of dopant modifies properties at the second hierarchy level, i.e., affecting the type of porosity [D2] and specific surface area [D1, D2]. The presence of varied-sized pores may facilitate mass transfer and thus enhance combustion performance when compared to the non-hierarchical material. Vulnerability for modification of the architecture at the second hierarchy level is related to control of the physical conditions of the thermolysis process that may affect porosity and texture [65]. The third level of organization permits easy anchoring of soot particles between the arms of the star-shaped particle increasing the contact of soot with active ceria surface in the catalytic process (Fig. 4.B-C). Also, large external surface provides larger area for deposition of metal active phase. Morphology change by synthetic conditions manipulation is a potential area for further modification of third-level architecture of the particle.

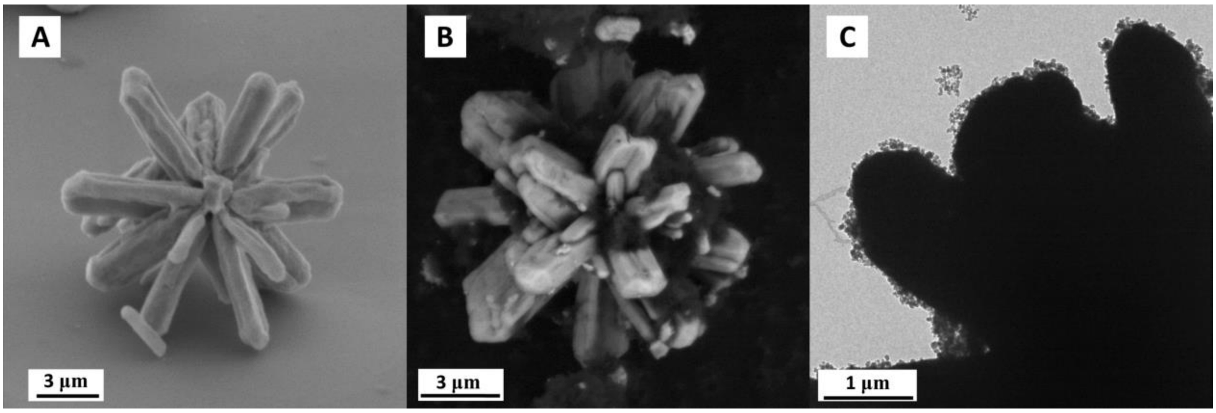

Fig 4. Anchoring of soot in hierarchical particle; SEM images of CeO_2 star-shaped particle (A) before addition of soot and (B) after addition of soot. (C) TEM image of arms of CeO_2 star-shaped particle after mixing with soot (adapted from Fig. S10 in D1).

The properties of hierarchical star-shaped particles as a function of concentration of dopant and temperature treatment have been investigated in [D2]. Gd ions have been chosen based on literature premises, since Gd-doped ceria possess the highest conductivity values which is ascribed to optimized ionic radii mismatch and subsequent structural distortions [38]. The particle architecture, in terms of star-shaped morphology and porosity, is preserved up to 70% of the dopant concentration level, and the highest surface area has been observed for 40% Gd-doped sample (180 m^2/g). The porosity is characterized by occurrence of slits and cavities creating confined spaces and overall S_{BET} area may be increased by changing dopant concentration. The samples preserve high surface area (> 115 m^2 /g) after heat treatment in 550°C [D2]. Also, preferential orientation of ceria nanoparticles is preserved in 550°C, and some loss of organization is observed when particles are heated in 900°C [D1]. Temperature-dependent study of the F-type structure stability of ceria nanocrystallites revealed preservation of ceria fluorite structure up to 700°C, however, this effect depends on dopant concentration (see Fig. 4 in [D2]).

The three-level architecture of the star-shaped particles is affected mutually by dopant concentration and temperature. For the first hierarchical organization level, two temperature-dependent nanoparticles growing modes have been observed. When the material is heated at temperatures up to 600°C, the NPs size increase is rather slow on behalf of a fast reduction of NPs microstrain [D2]. This contributes to maintaining the stability of macroparticle architecture, which is especially important in low-temperature catalytic oxidation. Increasing dopant concentration induces enhancement of microstrain. The second mode above 600°C is linked to the fast growth of nanoparticles, which modifies the particle architecture (Fig. 5.A). Moreover, the temperature-induced architecture changes depend also on the presence of dopant. While undoped CeO_2 HSNPs form system of grown-together cube-octahedral particles of different sizes in which well-defined architecture is preserved to lesser extent (Fig. 5.B), Gd-doped ceria evolve into fused small crystallite agglomerates forming the porous arm with the well-preserved mesoscale organization (Fig. 5.C) Such collective intergrowth of NPs in mesocrystal creates additional porosity, as was inspected by SEM imaging (Fig. 5.D-E). This thermally induced functional adaptation of the material is linked to greater stability of such architecture in violent soot combustion reaction.

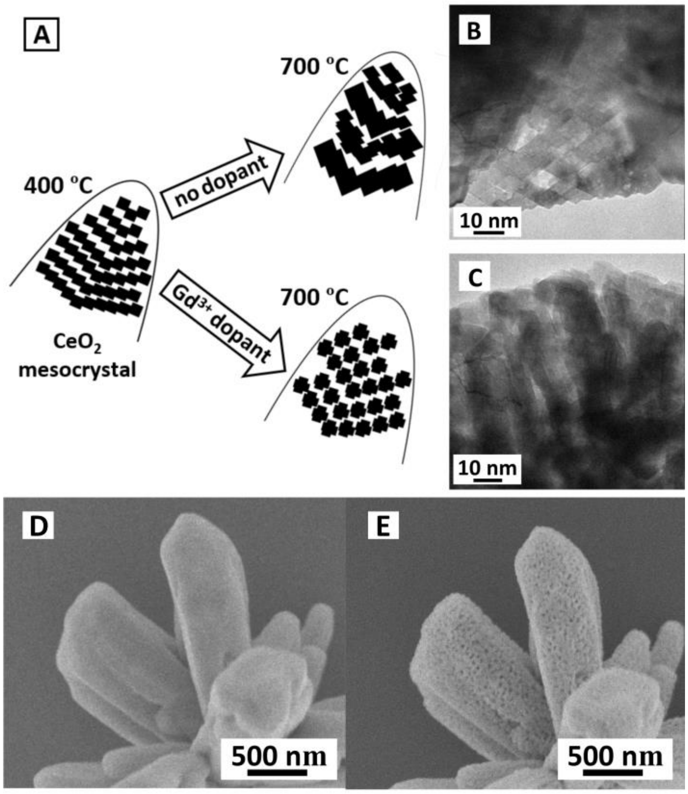

Fig. 5. (A) Scheme showing dopant-dependent changes of mesocrystal architecture induced by temperature; (B) TEM image of the arm of CeO_2 HSNPs heated in 700°C; (C) TEM image of the arm of $Ce_{0.9}Gd_{0.1}O_{1.95}$ HSNP heated in 700°C; (D) SEM image of $Ce_{0.9}Gd_{0.1}O_{1.95}$ HSNPs heated in 400°C; (E) SEM image of $Ce_{0.9}Gd_{0.1}O_{1.95}$ HSNPs heated in 900°C. (A-C adapted from Fig. 15 in D2, and D-E from Fig. 10 in D2).

The tube-like particles show hierarchical architecture composed of three levels. The average size of ceria nanocrystallites at the first level of hierarchical organization is around 10 nm, and this value is similar to the size of CeO_2 crystallites that build star-shaped particles [D3]. Ceria crystallites are non-rigidly aggregated at the second organization tier forming porous walls of tube-like macroparticles. CeO_2 NPs do not adhere closely to each other creating small slit-like pores, and the crystallites are not organized preferentially (Fig. 6.A) as opposed to star-shaped particles (Fig. 6.B). This difference in texture makes a significant distinction between the two hierarchical materials. The third hierarchy level forms tube-like macroparticles hollow inside and closed on one side.

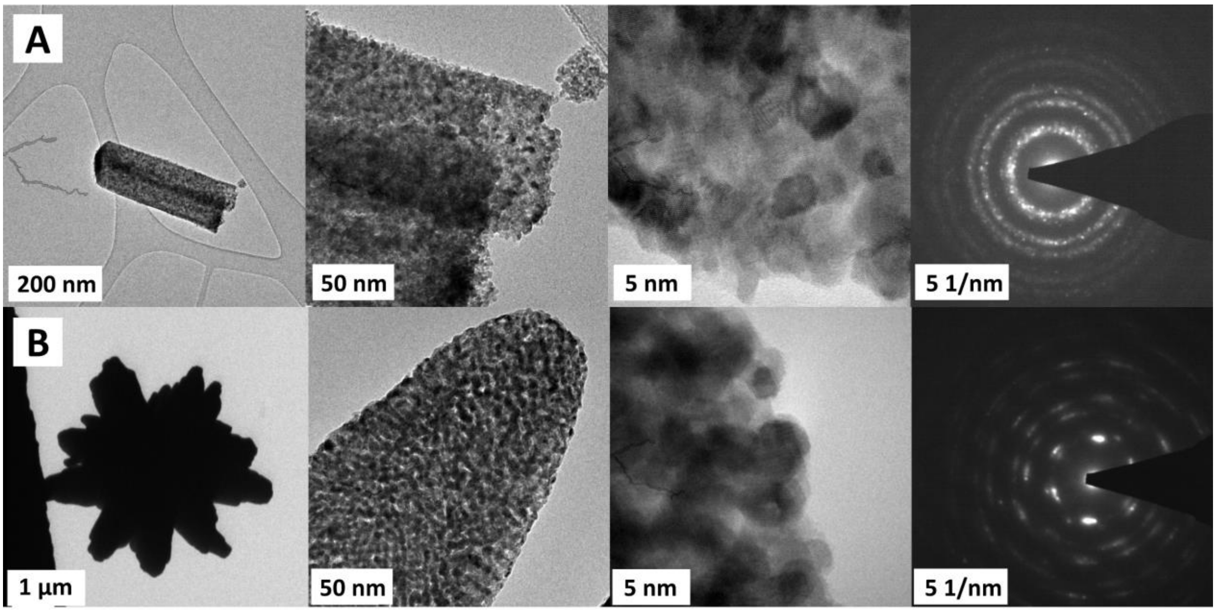

Fig. 6. (A) TEM images of tube-like hierarchical support and (B) star-shaped hierarchical support. SAED patters shown on the right. (A presented as Fig. A2 in Additional Materials and B adapted from Fig. S8 in D1).

The tube-like morphology of hierarchical particles is preserved up to 20% of Yb^{3+}concentration level, and rather shapeless agglomerates form above this doping level value. This may be related to either phase separation [69] or formation of defective F-type (F#) and C-type (C#) structures of crystallites [70] that hinders the formation of hierarchical macroparticle during synthesis [D3]. The overall shape of the macroparticle is maintained even after annealing at 900°C, despite the rapid growth of CeO_2 NPs building units (see Fig. 1 in [D3]).

For comparison purposes non-hierarchical powdered ceria samples composed of shapeless nanoparticles (average size 6.8 nm) and nanocubes with well-defined morphology (average size 17.8 nm) were produced by microemulsion wet chemical synthesis and hydrothermal method, respectively. Such crystallites do not organize into the higher order structure and form loose agglomerates of nanoparticles (see Fig. 6 in [D5]). The detailed description of the temperature-dependent growth of microemulsion-derived NPs is presented in [D1] and [D5]. The physicochemical characterization of nanocubes is presented in [D5].

5.1.3. Catalytic performance

Sectorial emissions of air pollutants from road and non-road transport indicates that non-methane volatile organic compounds and particulate matter constitute considerable input into total environmental pollution [71]. Utilization of noble metal-free CeO_2-based mixed oxides show potential in low-to-middle temperature oxidation of CO and soot particles [37]. Utilization of nanocrystalline ceria in C_3H_8 oxidation has been somewhat limited [72]. The soot combustion process is sensitive to nanoparticle morphology [73,74]. Also, CO oxidation is structure-sensitive when catalyzed by ceria-based materials differing in morphology and porosity [75]. In this Dissertation the influence of the organization of nanoparticles into hierarchical macrostructures on catalytic oxidation performance has been studied. The results of catalytic reactivity testes in CO oxidation, soot combustion, and C_3H_3 oxidation have been presented in publications [D1, D2, D3], and are summarized in Table 1.

Table 1. Catalytic performance of active catalytic supports differing in morphology (non-hierarchical nanoparticles (NPs) or hierarchically structured nanoparticles (HSNPs)) and presence of dopant (undoped CeO_2 or Gd-doped ceria (GDC-10%)). All samples within reaction groups were tested in similar reaction conditions.

	Catalyst support	T_{50} [°C]		Catalyst support	T_{50} [°C]	$r_{330°C}$ / $r_{390°C}$ x 10^6 [mol $m^{-2} h^{-1}$] [#]
CO oxidation	CeO_2 NPs	>400 [D1] *	C_3H_8 oxidation	CeO_2 NPs	508 [D2], 550 [D3] *	5.6 [D2], 1.4 [D3] * / 15.5 [D2], 5.7 [D3] *
	CeO_2 HSNPs (star)	334 [D1] *		CeO_2 HSNPs (star)	450 [D2]	15.1 [D2] / 18.2 [D2]
	GDC-10% HSNPs (star)	323 [D1] *		CeO_2 HSNPs (tube)	495 [D3]	2.4 [D3] / 11.4 [D3]
C oxidation	CeO_2 NPs	539 [D2] *		GDC-10% NPs	470 [D2] *	1.2 [D2] * / 7.3 [D2] *
	CeO_2 HSNPs (star)	443 [D1] *		GDC-10% (star)	425 [D2]	3.8 [D2] / 18.3 [D2]
	CeO_2 HSNPs (tube)	468 [D3]		YDC-10% HSNPs (tube)	455 [D3]	1.3 [D3] / 10.9 [D3]

* sample pre-heated in 550°C; items without asterisk designate smaples pre-heated in 400°C

[#] calculated from data presented in [D2] and [D3]

CO oxidation performance in terms of temperature of half-oxidation (T_{50}) is enhanced for hierarchical star-shaped particles when compared to powdered non-hierarchical ceria NPs. This effect has been ascribed to the facilitated mass transfer and the increased surface active sites availability in a hierarchical system [D1]. Since all tested samples were pre-heated in 550°C to clean the surface from carbonate or nitrate residues [76], the effect of catalytic enhancement has been ascribed to materials architecture rather that surface chemistry effects. Introduction of Gd^{3+} ions into ceria crystallites slightly improves CO oxidation performance shifting T_{50} into lower values. This effect has been ascribed to modification of ceria crystallites microstructure. PXRD data post-processing have revealed that the nanoparticles strain is increased after doping (cf. Fig 7 and Table in [D2]), and simultaneous enhancement of relative surface H_2 consumption is observed that indicates increased surface reducibility of doped hierarchical material (cf. Table 2 in [D1]).

Also, T_{50} values for soot combustion indicate superior reactivity of both hierarchical systems, star-shaped and tube-like, over non-hierarchical ceria nanoparticles. Key-lock catalysis concept has been used to explain this effect [77]. A schematic representation of this concept adopted for star-shaped hierarchical particles studied here is presented in Fig. 7. Thanks to the possibility of fitting the shape of soot agglomerates and soot nanoparticles to diversified porosity and morphology of hierarchical particles soot combustion is enhanced due to maximized soot-ceria interphase contact [D1]. Such soot-ceria contact is limited in case of non-hierarchically structured bulk ceria (Fig.7). Interestingly, CeO_2 HSNPs show slightly better soot oxidation performance when pre-heated in 550°C (T_{50} = 443°C) than pre-heated in 400°C (T_{50} = 463°C). This may be related to the temperature-induced change of ceria crystallites morphology without loss of preferential orientation of crystallites [D1]. Even that specific surface area is reduced for sample pre-heated in 550°C, large external surface area of star-shaped macroparticles enables easy anchoring of soot.

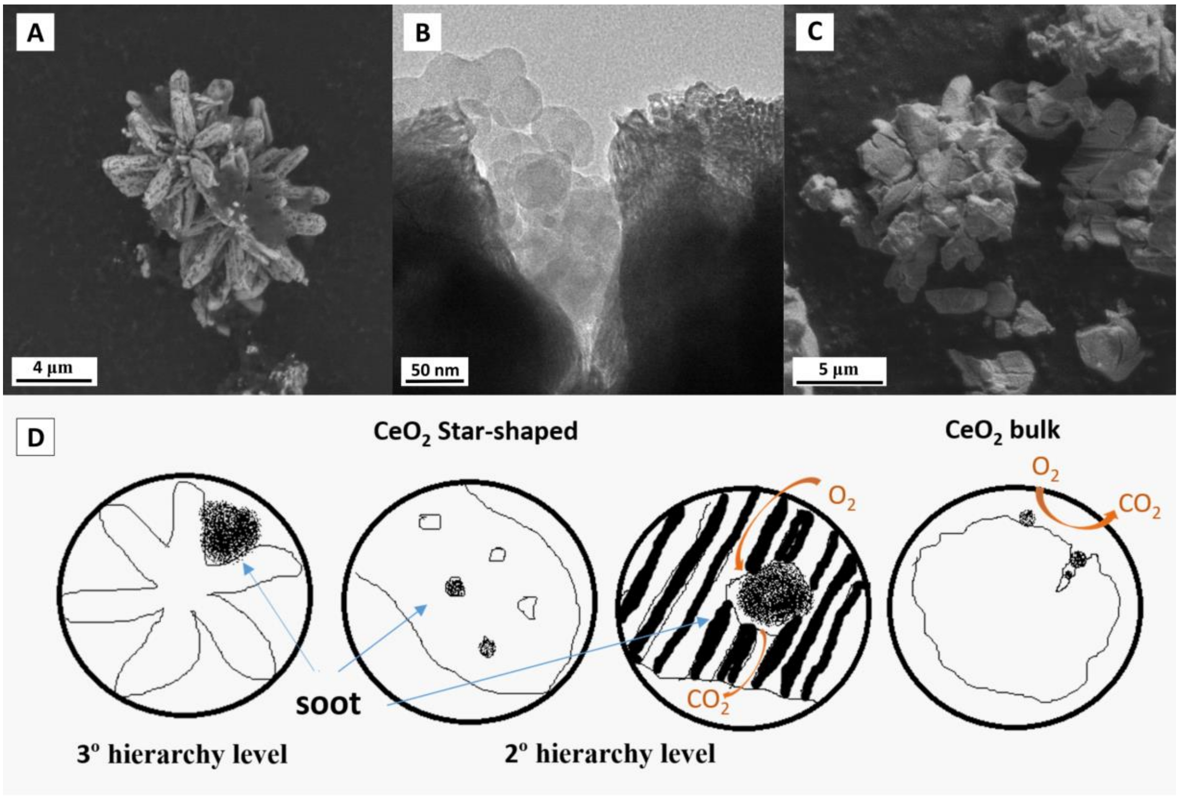

Fig. 7. Image of (A) soot embedded within the porous star-shaped CeO_2 macroparticle (SEM), (B) soot particles within macropore of the arm of CeO_2 HSNPs (TEM), (C) bulk CeO_2 particle (SEM) and (D) model of soot combustion by hierarchical HSNPs (key-lock concept) (adapted from Fig. 12 in D1).

Propane oxidation performance shows superiority of both, undoped and doped, hierarchical materials of either star-shape or tube-like morphology over non-hierarchical ceria particles (see T_{50} in Table. 1). Moreover, the preferential orientation of ceria crystallites within star-shaped particles facilitates oxidation since the shift of T_{50} to lower vales is observed when compared to tube-like particles. To weigh up activity of catalyst supports the reaction rates at 330°C and 390°C normalized by catalyst BET specific surface area were calculated based on data presented in publications [D2] and [D3], and the results are shown in Table 1. The data show emergent phenomenon in catalytic propane oxidation, i.e., the substantial increase of reaction rate in low temperature regimes for CeO_2 star-shaped HSNPs (see $r_{330°C}$ in Table 1). This effect relates to ceria nanocrystallites mesoscale organization into hierarchical architecture, since no such effect occurs for non-hierarchical nanoparticles [D2] and nanocubes [D5]. The presence of Gd-dopant kills the occurrence of as observed low-temperature mechanism of propane oxidation, however, dopant induces shift of T_{50} into lower values as compared to CeO_2 HSNPs. The effect of dopant in facilitating oxidation rate is not visible at 390°C. This can be caused by blockage of active sites for propane oxidation by dopant at the surface of ceria.

Selectivity of catalytic oxidation by star-shaped and tube-like hierarchical materials was examined in propane oxidation reaction and analyzed via inspection of gas chromatography profiles [D2, D6]. Two oxidation modes have been observed. Total propane oxidation proceeds for both materials at temperatures up to 390°C. At temperatures above 400°C the gradual increase of trace amount of conversion by-product is detected. Its relative quantity reaches 0.3%-1.4% at 540°C for hierarchical samples and it is treated as minor impurity in the oxidation process. The retention time close to the propane peak one suggests that this decomposition product possesses relatively high molecular weight. Its occurrence may be link to the shift from the surface heterogeneous pathway of propane oxidation (<400°C) into mixed hetero-homogeneous mechanism (>400°C) for which gas phase reactions start to dominate [78]. Comparison of this by-product formation in hierarchical samples with non-hierarchical ceria-based supports (cubes and NPs) shows similarity in magnitude, but the formation extent is stabilized at lower conversion temperatures for low-doped hierarchical samples (cf. Fig. S9 in [D2] and Fig. A3 in Additional Materials).

Stability of the star-shaped hierarchical catalytic support under process conditions was examined in CO, propane, and soot oxidation reactions. The temperature of 900°C is known for being sufficient for ceria sintering that is confirmed by TEM imaging of microemulsion-derived ceria NPs sample (cf. Fig S8 in [D1]). CeO_2 star-shaped particles proved to be more resistant to high-temperature treatment during catalytic CO oxidation over non-hierarchical NPs in terms of preserved conversion level and specific surface area [D1]. While CO conversion reaches ~45% in 400°C for star-shaped particles heated in 900°C, the conversion falls to <10% in 400°C for ceria NPs heated in 900°C. Star-shaped particles show the presence of a residual inner surface that is over twofold higher than for nonhierarchical NPs [D1]. Microscopic inspection of particles after propane oxidation tests shows preservation of star-shaped morphology (third level of the material hierarchical organization) and mesoscale nanocrystal arrangement (second level of the material hierarchical organization [D2]. The similar effect of preservation of hierarchy has been observed in the violent soot oxidation for Gd-doped star-shaped catalytic support. The effect of doping on the support stability enhancement is presented in Fig. 8 [D2]. Shape-stability of tube-like catalytic support has been confirmed by microscopic imaging of high temperature-treated sample (900°C) [D3].

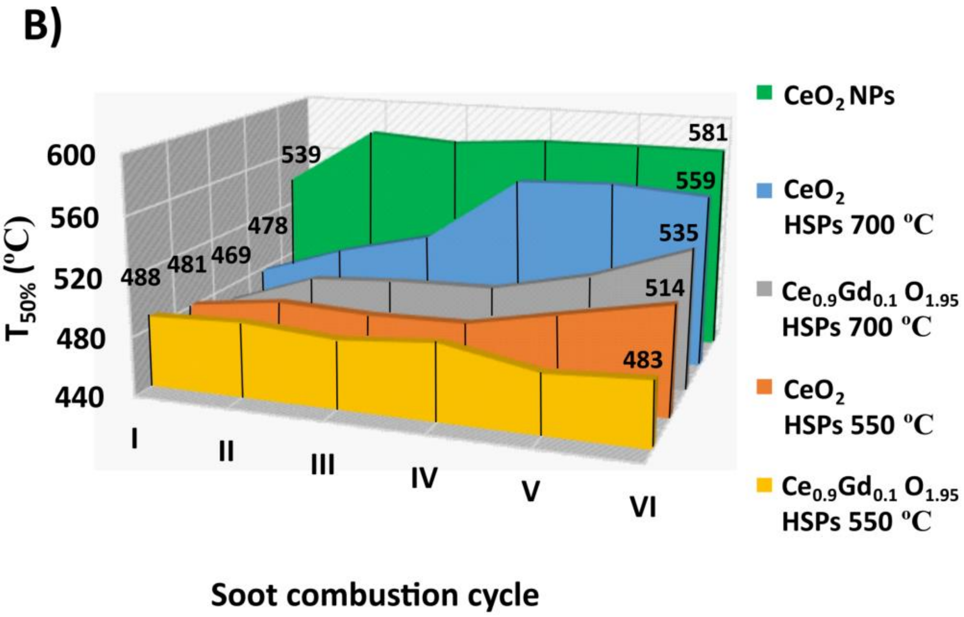

Fig. 8 . Functional stability of undoped or Gd-doped hierarchical star-shaped support tested in six cycles of soot oxidation. Final temperature for each cycle was 550°C or 700°C. (adapted from Fig. 12 in D2).

5.2. Gold decoration

5.2.1. Model nanocubes

Several methods of deposition of gold on active and inactive catalytic supports have been presented in the literature [79–82]. These methods include impregnation [83], co-precipitation [84], deposition-precipitation with the use of NaOH (DP NaOH) [85] or urea (DP urea) as precipitating agent [79], anion/cation adsorption [79,86], chemical vapor deposition [87]. The principle of deposition-precipitation method is that the surface acts as nucleating agent for metal hydroxide formation, and the use of urea provides the gradual and homogeneous addition of hydroxide ions throughout the reaction mixture. Thus, this prevents precipitation of gold particles away from the support surface producing systems with high metal loading and small Au particle sizes [79]. Due to that formation of metal agglomerates or large Au particles is avoided, as this is the case for simpler and industrially attractive impregnation method. The capability of the DP urea method for controlling the form of nano-gold species deposited on model ceria cubes and hierarchical materials has been investigated in publication [D4] and [D5], respectively.

The gold decoration process with the use of the DP urea approach proceeds easily for large CeO_2 cube-like nanocrystals (d_{av} = 67 nm) resulting in the presence of uniformly distributed Au NPs with average size of 3 nm [D4]. Contrarily, application of the same deposition procedure with one change, i.e., the use of small CeO_2 cube-like nanocrystals (d_{av} = 14 nm) instead of large ones, gives systems with no visible Au NPs while presence of gold is detected spectroscopically in SEM-EDX measurements (Fig. 9.A). Moreover, temperature treatment of the sample in a reducing atmosphere (H_2 flow) induces formation of Au NPs on the surface of small ceria nanocubes. In publication [D4] three hypotheses have been tested to explain the effect of no Au NPs presence on the surface of small ceria nanocubes.

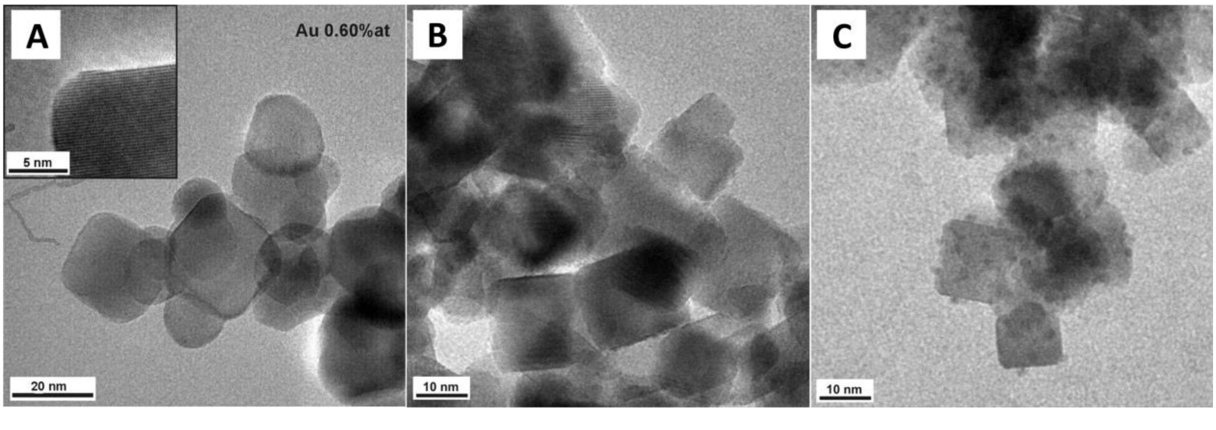

Fig. 9. Gold-decorated CeO_2 nanocubes (d_{av} = 14 nm): (A) no Au NPs visible o the ceria surface; low value of M_{Au}/S_{CeO2} (B) Au NPs visible on the ceria surface (d_{av} = 1 nm); intermediate value of M_{Au}/S_{CeO2} ; (C) Au NPs visible on ceria surface (d_{av} = 3 nm); high value of M_{Au}/S_{CeO2} (adapted from Fig. 3 and Fig. 8 in D4).

Firstly, the effect of post-synthetic surface contamination by NO_3^- groups was examined [76]. Heating samples at 550°C to remove nitrates followed by deposition of gold with the use of the same synthetic protocol have shown no presence of Au NPs. Thus, the NO_3^- surface groups do not prevent the formation of Au NPs.

Secondly, the influence of curvature of the surface of ceria nanocubes on growth of Au nanoparticles has been investigated [88]. In particular, the hypothesis that the curved surface of small ceria nanocubes prevents formation of gold nanoparticles has been tested. Deposition process was conducted on the specially designed sample composed of variously sized ceria nanocubes having both, flat and curved surface. It turns out that Au NPs form on small, curved ceria nanocrystals, thus the curvature of the surface is not the critical factor preventing formation of Au NPs.

Thirdly, the ratio of the total support surface area to the molar content of the chloroauric acid in the reaction mixture (M_{Au}/S_{CeO2}) has been tested to explain the lack of Au NPs visibility on small ceria nanocubes. The determination of the surface area of the support has been made basing on empirical distributions of the nanocube particles size that was obtained from TEM images [D4]. This approach takes into account the contribution of all lognormally distributed particle sizes, and it is a better approximation of the total surface area than arithmetic mean-based approach. Increasing the as defined ratio proved to be successful in controlling the form of gold species formed, since larger Au NPs (d_{av} = 3 nm) are visible for high values of the ratio (Fig. 9.C) and small Au NPs (d_{av} = 1 nm) form on the surface when intermediate ratio values of chloroauric acid to the total surface area is used in deposition procedure (Fig. 9.B). Moreover, for small ratio values the thin film of gold/the ultra-small gold clusters are formed. Their presence has been confirmed by a combination of HRTEM and TEM-EDX techniques [D4]. This explains spectroscopic detection of gold in the sample for which no Au NPs is observed during microscopic investigation (Fig. 9.A). In summary, exceeding some threshold value of M_{Au}/S_{CeO2} ratio leads to the growth of nanoparticles according to the Stranski-Krastanov (SK) model, as the most likely scenario [89].

5.2.2. Hierarchical systems

The modification of the gold deposition procedure has been developed in [D5] in order to better estimate the values of the M_{Au}/S_{CeO2} ratio for variously gold loaded samples, and to test the applicability of as taken approach for decoration of hierarchical systems by gold nanoparticles. In the new approach, the surface area of the support was determined from N_2 physisorption (S_{BET} specific surface area), and M_{Au}/S_{CeO2} ratio was remodified into surface coverage parameter (SC) [D5]. Due to the structural complexity of star-shaped and tube-like particles, this approach allows to precisely calculate the needed amount of the gold precursor ($HAuCl_4$).

For low value of the surface coverage parameter (SC = 0.5) no gold particles have been observed in TEM inspection of the gold decorated star-shaped particles (Fig. 10.A), however, the gold presence inside the support was confirmed by SEM-EDS selected-region elemental analysis that indicates 2.7 Au-wt% in CeO_2 sample. Due to lack of electron transparency in the thicker areas of the support particles the exact morphological form of gold has not been identified. The use of larger value of SC = 2 leads to the formation of Au NPs that deposit along the pores inside the hierarchical support that is confirmed by TEM imaging (Fig. 10.B). However, for this SC value no Au particles were observed on the support exterior surface. Accelerated diffusion of metal precursor into the crystal mesopores may be responsible for the formation of nano-gold particles in the interior of hierarchical support at first when relatively low SC values are used [90]. Increasing gold loading (SC = 5) induces additional formation of gold nanoparticles on the exterior surface of the hierarchical catalyst support (Fig. 10.C). Presence of Au NPs inside the hierarchical support has been confirmed by Electron Tomography (see animation in CS&T repository[1]). A large value of the surface coverage parameter (SC = 8) causes formation of metal agglomerates on the particles exterior surface (Fig. 10.D). Such gold overloading decreases metal-support contact. Due to the large capacity for metal loading hierarchical systems have promising use in electrocatalysis [91].

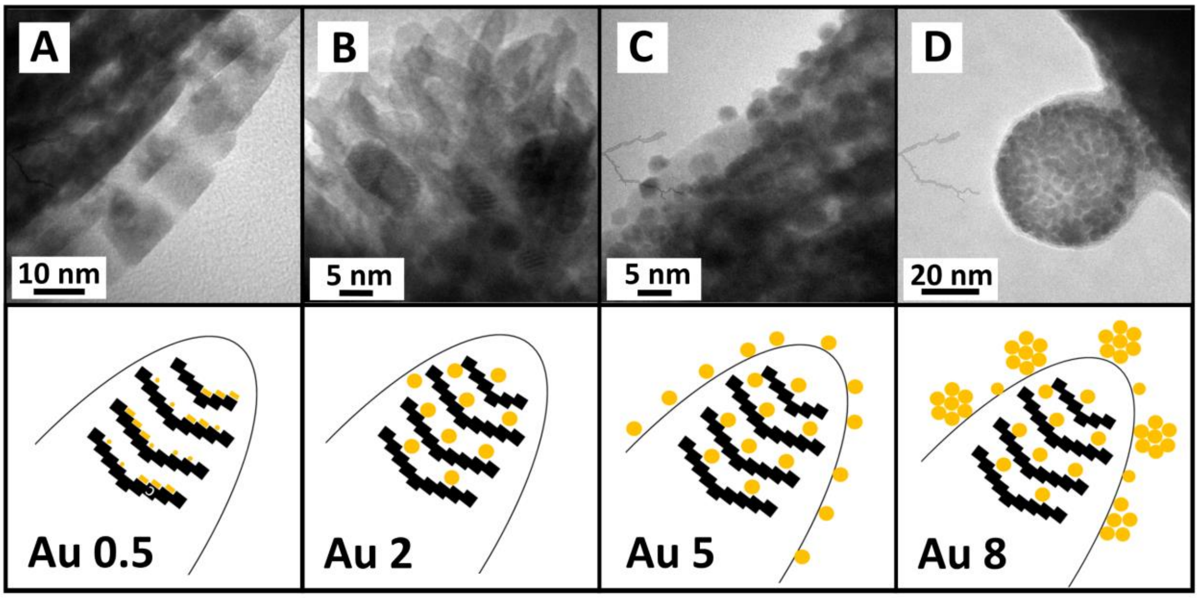

Fig. 10. TEM images of Au/CeO_2 catalyst showing the influence of the surface coverage parameter (SC) value on the 4th level of the particle's architecture (gold-decorated hierarchical material): A) SC = 0.5, B) SC = 2, C) SC = 5 and D) SC = 8 (adapted from Fig. 3 in D5).

The course of N_2 adsorption–desorption isotherms of the gold-decorated materials is similar to non-decorated samples preserving the same hysteresis loop type, which proves the stability of the architecture after the gold deposition process. Also, the small loss of specific surface area from S_{BET}=144 m^2/g to S_{BET}=117 m^2/g after gold decoration is observed for CeO_2 hierarchical star-shaped system, which proves preservation of porosity of hierarchical materials after the process of urea-assisted gold deposition [D5].

At the same time, this gold deposition approach is not effective for precise gold decoration of the non-hierarchically structured ceria NPs, leading to the formation of large gold crystals (5-30 nm) next to the ceria nano-sized particles. This indicates that the organization of the ceria nanoparticles into a hierarchical structure allows for easier manipulation of the material in terms of its further processing in metal deposition while retaining nanosized properties of the support at the same time [92].

---

[1] Supplementary movie reposited at https://pubs.rsc.org/en/Content/ArticleLanding/2022/CY/D2CY01214F#!

5.3. Hierarchical catalysts

5.3.1. Activity

Catalytic activity of gold decorated materials has been tested in propane and CO oxidation for star-shaped hierarchical systems and propane oxidation for tube-like systems [D5,D6]. Also, for comparison purposes soot oxidation test results have been presented in Additional Materials (see Fig. A4 in Additional Materials).

To evaluate propane oxidation TOF was determined at low conversions of a given process (<15%). In [D5], the TOF, defined as the rate of propane consumption per number of active sites, was calculated in two ways depending on the assumptions about the nature of the catalyst active sites. Firstly, the specific reaction rate was normalized to the mole number of Au contained in the mass of the active catalyst phase ($Au/Ce_{1-x}O_{2-y}$) [93]. As this approach assumes that each gold atom is an active site, it is suitable for systems in which the particles are highly dispersed and have a narrow size distribution. Since hierarchical systems are characterized by a high degree of complexity (gold deposited on the active support, high gold loading, relatively broad Au NPs size distribution, and varied localization of Au NPs within hierarchical system) a different approach has been taken to describe hierarchical gold catalysts.

In the new approach presented in [D5] the gold atoms at the Au/ceria interface have been taken as active sites and the number of Au atoms in the ring around gold nanoparticles (modeled as a half-sphere) has been quantified based on histograms generated from TEM data. This approach is rationalized by DFT-confirmed experimental observation that the oxidation of Au-bounded CO occurs at the Au/CeO2 interface [94]. Also, chemisorption study revealed that despite the lower accessibility of the metal surface in embedded $Au@CeO_2$ systems, the increased activity may be ascribed to the larger extent to metal-support interaction [95]. Such approach allows to determine the number of active sites more accurately than just taking the average particle size, especially for the polydisperse or the non-uniformly distributed wide particles size range systems.

Propane oxidation activity in terms of as defined TOF was compared between catalysts differed by three attributes, i.e., morphology, dopant presence, and gold loading (Table 2). Firstly, activity of gold-decorated nanocubes was compared with gold-decorated hierarchically structured star-shaped system ($Au5/CeO_2$ cubes vs $Au5/CeO_2$ HSNPs). Secondly, hierarchical ceria catalysts have been compared with Gd-doped hierarchical ceria catalysts ($Au5/CeO_2$ HSNPs vs Au5/GDC-10% HSNPs). Thirdly, variously gold loaded catalysts, in terms of surface coverage parameter values, has been compared ($Au2/CeO_2$ HSNPs vs $Au5/CeO_2$ HSNPs).

As a result, hierarchically structured gold catalysts, both, undoped and Gd-doped, outperform non-hierarchical nanocubic gold ones (see TOF in Table 2). This effect has been ascribed to the maximization of Au/ceria interface contact in hierarchical systems. Both systems, cubic and hierarchical, are characterized by similar Au NPs size. However, twofold difference in gold loading in terms of weight percentages between hierarchical catalyst ($Au2/CeO_2$ HSNPs) and non-hierarchical ($Au5/CeO_2$ cubes) sample may be responsible for the observed result. Nevertheless, two-fold increase of gold loading in ceria hierarchical systems ($Au2/CeO_2$ HSNPs vs $Au5/CeO_2$ HSNPs) shows insubstantial changes in TOF values. Thus, gold loading plays smaller role in activity enhancement on behalf of metal-support contact maximization. Due to the confinement of Au NPs within hierarchical supports this contact is increased, which is discussed in the literature as a crucial factor facilitating catalytic activity [95,96]. The influence of surface properties of catalysts has been discussed in [D5].

Table 2. Activity of catlaysts in propane oxidation (adapted from Table 2 in [D5]).

Catalyst	**$r_{300°C}$ × 10^2 (mol_{CO} g_{Au}^{-1} h^{-1})**	**$TOF_{300°C}$ × 10^2 (s^{-1})**
Au2/CeO_2 HSNPs (star)	0.77	0.49
Au5/CeO_2 HSNPs (star)	0.61	0.43
Au5/CeO_2 cubes	0.76	0.26
Au5/CeO_2 HSNPs (tube)	1.10	-
Au2/GDC-10% HSNPs (star)	1.85	1.18
Au5/GDC-10% HSNPs (star)	0.72	1.11
Au5/GDC-10% cubes	0.96	0.61
Au5/GDC-10% HSNPs (tube)	0.89	-

On the other hand, Gd doping facilitates propane oxidation for both nonhierarchical and hierarchical gold catalysts, showing a two-fold TOF increase. Also, the Gd-doped hierarchical gold catalyst shows over four-fold TOF increase as compared to the undoped non-hierarchical one, proving the synergistic effect of doping and structural hierarchy in propane oxidation [D5].

Comparison of propane oxidation activity between star-shaped and tube-like hierarchical catalysts has been also presented in Table 2. Due to small contrast differences between Au and Ce in TEM imagining as well as specificity of the examined tube-like hierarchical system such as (a) the lack of clearly defined ceria planes at the surface of hierarchical macroparticles, (b) similarity of size of Au and CeO_2 nanoparticles, (c) lack of porosity, and thus reduced electron transparency on the sample edges, the construction of reliable histograms was infeasible. Due to that, catalysts were compared in terms of reaction rates at 300°C. Contrary to the undecorated catalyst supports, where the preferential orientation of the ceria crystallites at the second hierarchy level improved the activity of the system (cf. star-shaped and tube-like HSNPs in Table 1), this effect is not observed for gold-decorated systems (Table 2) in terms of reaction rate values. Further research to determine the TOF would provide more insight.

Comparison of the influence of the type of admixture (10%-Gd or 5%-La-5%-Yb) indicates that double doped ceria significantly lowers T_{50} in propane oxidation over Gd-doped ceria having values T_{50} = 361°C and T_{50} = 391°C, respectively. Since this two samples have similar mean radius of doped entities (see Table 1 in [D6]), but are differed in the type of lattice deformation, it is inferred that it is not the mere presence of deformations (defects) in the support crystal lattice that matters, but its type also plays significant role in altering catalytic behavior of studied catalysts [D6].

The CO oxidation activity of the star-shaped hierarchical catalysts differed by the gold loading and the Gd doping has been summarized in Fig. 11.A. Hierarchical gold catalysts (Au5/CeO_2) reduces CO oxidation to ambient temperature (T_{50}=18°C) as compared to non-hierarchical gold-decorated Au5/CeO_2 nanocubes (T_{50} = 85°C). This effect is caused by the confinement of Au NPs within pores of hierarchical support. TOF values calculated based on Au/ceria interface contact extent correlate well with the percentage values of the contribution of optimally sized

Au NPs (2-4 nm) to the whole distribution of Au NPs sizes (Fig. 11.B). This also correlates with the order of T_{50} in CO oxidation (Fig. 11.A). Analysis of interdependence between catalyst architecture, Au NPs size, and gold loading indicates that the presence of optimally sized Au NPs leads to enhancement of CO oxidation. Trade-off between gold size and maximization of Au/interface contact within hierarchical support is crucial in catalytic performance facilitation [D5]. Moreover, increasing gold loading does not necessary lead to catalytic oxidation enhancement. Pore geometry and size may restrict the growth of optimally sized Au NPs leading to activity decline. Thus, the knowledge of the materials porosity is necessary for optimal catalyst design [D5].

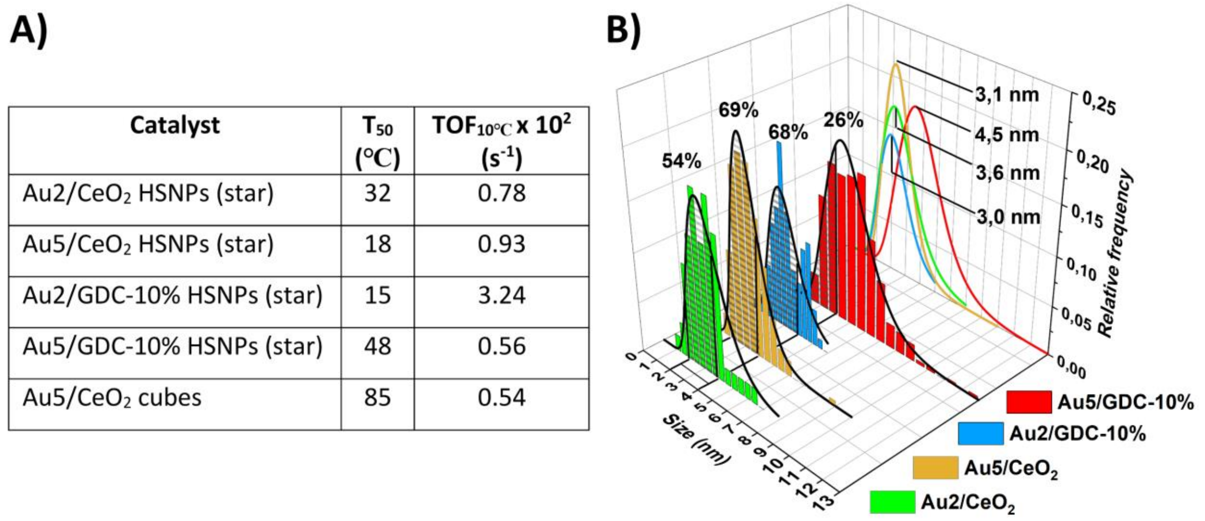

Catalyst	T_{50} (°C)	$TOF_{10°C} \times 10^2$ (s^{-1})
Au2/CeO_2 HSNPs (star)	32	0.78
Au5/CeO_2 HSNPs (star)	18	0.93
Au2/GDC-10% HSNPs (star)	15	3.24
Au5/GDC-10% HSNPs (star)	48	0.56
Au5/CeO_2 cubes	85	0.54

Fig. 11. (A) Activity of catalysts in CO oxidation; (B) Size distribution plots of Au NPs detected in the surface/sub-surface region of hierarchically structured catalysts (adapted from data in D5 and Fig. 13 in D5).

Catalytic oxidation of soot by gold-decorated hierarchical systems depends on the architecture of the catalyst support. Whereas for star-shaped gold-decorated catalyst slight enhancement of catalytic performance is observed, the opposite effect is visible for tube-like systems (Fig. A4 in Additional Materials). This effect may be linked to greater stability of gold nanoparticles within pores of hierarchical star-shaped support (discussed in Section 5.3.3). The influence of ceria-supported gold nanoparticles on soot oxidation performance has been observed in the literature [97].

5.3.2. Selectivity

Combustion process, especially in the automotive gas emission, results in formation of primary products of carbon dioxide and water as well as pollutants such as CO, hydrocarbons, nitrous oxides, sulfur oxides, Diesel soot [98]. Selectivity of catalytic processes in emission control is of major importance to deal with environmental atmospheric contamination. In this research, selectivity of gold-decorated star-shaped and tube-like hierarchical catalysts was evaluated in propane oxidation reaction. According to Maillet et al. there are two possible ways for partial oxidation of propane [99]. The first takes place at temperatures below 400 °C, and the reaction products are CO_2 and H_2O (complete oxidation). On the other hand, at temperatures above 400 °C, the reaction of incomplete propane oxidation takes place, which results in the presence of CO in the final gas mixture.

For no gold-decorated hierarchical particles the formation of additional co-product is observed, and this is probably hydrocarbon due to similar retention time to propane [D2, D6]. However, decorating the hierarchical ceria-based macroparticles with nanosized gold results in an improvement in the selectivity of propane oxidation up to 100% (no apparent co-products) [D6]. During the analysis of the catalytic results, it was noticed that the signal related to the presence of the unwanted co-product does not appear at all even at high temperatures [D6]. This may indicate a different mechanism of the propane oxidation taking place on the gold decorated and non-decorated samples. Probably, for non-decorated oxides, the dominant mechanism is associated with the use of lattice oxygen [100], while for the decorated systems, the process most likely goes according to the Langmuir-Hinshelwood mechanism with adsorption of propane and oxygen on different sites [101].

5.3.3. Stability

A typical lifetime of industrial catalysts for low temperature water gas shift reaction reaches 2-4 years [102]. Several factors contribute to catalyst stability such as resistance to poisoning and fouling, lack of thermal degradation and sintering, resistance to vapor formation or solid-solid reactions. Loss of stability of Au/ceria systems has been reported in the literature and possible factors that influence activity decline has been identified as: Au NPs growth, over-reduction of ceria, poisoning by carbon-related species [103]. Au/ceria system is generally of not heightened stability, and Au/zeolite is a promising more stable candidate for CO and VOC oxidation [104]. However, here the influence of hierarchical architecture on stability of gold nanoparticles has been closely examined [D5, D6].

As a result, it was shown that confinement of gold nanoparticles within star-shaped hierarchical support allows to preserve a significant fraction of small gold nanoparticles that play an important role in low-temperature CO oxidation [D5]. Au NPs size distribution from the collected TEM images of hierarchical catalysts examined before and after CO and propane oxidation is presented in Fig. 12.A-F. For both, undoped and Gd-doped hierarchical systems there is a systematic reduction in the proportion of particles with optimal size of 2-4 nm, however, this reduction is larger for Au5/GDC-10% HSNPs catalyst. This is due to the shift of the whole size distribution into larger values. Examination of Au NPs growth on model gold-decorated cubic samples shows the similar growing behavior, namely the shift of the whole size distribution into larger values (Fig. 12.G-J). This relates to the non-restricted growth of metal particles on the surface of this systems. Unique in this respect is the Au5/CeO_2 HSNPs catalyst, for which the shift of the entire size distribution is not observed, but the distribution in anchored in low size values (< 2 nm) (Fig. 12.B-C). TEM inspection shows that for this sample Au NPs are visible inside the pores of the hierarchical support [D5]. Thus, confinement of Au NPs within pores of hierarchical support enhances stability of catalyst active phase in terms of size of metal particles.

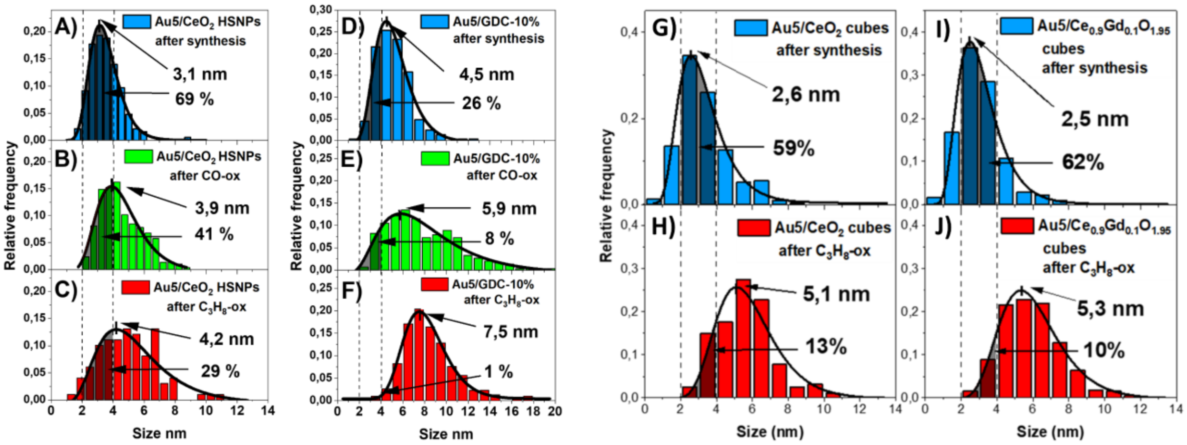

Fig. 12. Histograms showing size of Au NPs deposited on hierarchical supports (HSNPs) and nanocubes (cubes) before and after propane and CO oxidation. (adapted from Fig. 14 and S21 in D5).

The initial differences in the Au NPs mode size values within Au5/CeO_2 HSNPs and Au5/GDC-10% HSNPs systems are caused by differences in the support architecture. Namely, small pores in Gd-doped hierarchical support forces Au NPs out of the interior of the hierarchical material and leads to the growth of the Au NPs on the exterior surface of star-shaped particles [D5]. Also, collective intergrowth of GDC-10% crystallites may be linked to process of facilitated gold migration [D2, D5].

To confirm this observations, two-way ANOVA has been conducted on Au NPs size data. Two levels of the dopant presence (undoped Au5/CeO_2 and doped Au5/GDC-10%) and two levels of morphology (cubes and HSNPs) have been tested. Because of the lognormal nature of Au NPs size distribution all data were logarithmically transformed and met normality requirements (see details in Fig. S23 in ESI). The interaction between the dopant presence and morphology was significant, F(1.1307)=272.89, $p < .001$. Tukey HSD post-hoc analysis has shown that there is no significant difference between the size of Au NPs embedded in Au5/CeO_2 cubes and Au5/GDC-10% cubes ($p > .001$). Oppositely, there is significant difference in Au NPs size embedded in Au5/CeO_2 HSNPs and Au5/GDC-10% HSNPs ($p < .001$). Comparison of mode size values proves the rapid growth of particles within doped system, 4.2 nm for Au5/CeO_2 HSNPs and 7.5 nm for Au5/GDC-10% HSNPs. Interestingly, there is a significant difference in the Au NPs mode size between Au5/CeO_2 cubes and Au5/CeO_2 hierarchically structured particles ($p < .001$) with values of 4.2 nm and 5.1 nm, respectively. This proves confinement of nano-gold within CeO_2 hierarchically structured support having pore sizes sufficient for unrestricted growth of metal particles. Significant difference between GDC-10% cubes and GDC-10% hierarchically structured particles ($p < .001$) proves, again, the rapid growth of particles that may be caused by support intergrowth Thus, the knowledge of materials architecture is necessary for the precise design of optimal hierarchical catalyst [D5].

For tube-like hierarchical catalysts the significant growth of Au NPs is observed, and this is reflected in the loss of catalytic activity in propane oxidation [D6]. To further increase active phase stability alloying of Au nanoparticles is a possible strategy [102]. Also, addition of catalytic promoters may suppress gold migration within pores of hierarchical support. From the other hand doping ceria is a promising strategy to increase stability of hierarchical catalyst support [D2].

6. Conclusions

The realization of the first goal of this Dissertation is summarized in the following conclusions:

1. The synthetic protocols presented in this Dissertation are suitable for production of hierarchical materials having various architectures. Namely, the composition of the reaction mixture in the hydrothermal synthesis influences the morphology of rare-earth doped cerium formate particles leading to formation of the star-shaped, sphere-shaped, or rod-shaped particles. Further thermolysis leads to the formation of hierarchical ceria-based materials with a specific texture due to the preferential orientation of nano-ceria building units. Also, the multistep wet chemical synthesis allows to produce tube-like hierarchical ceria. The adjustment of synthetic protocols may lead to fabrication of hierarchical materials differing in characteristics on each of the three levels of hierarchical organization.

2. The ceria-based hierarchical catalyst supports show the improved catalytic performance in CO, propane and soot oxidation when compared to non-hierarchical powdered particles, either nanocubes (average size <18 nm) or nano-sized NPs (average size < 7 nm). This effect has been ascribed to the facilitated mass transfer and the increased surface active sites availability in hierarchical systems. Key-lock catalysis concept has been used to explain the effect of superior reactivity of both hierarchical catalytic supports, star-shaped and tube-like, in soot oxidation.

3. Stability of the architecture of ceria-based hierarchical catalytic supports was assessed in several experiments. Preferential orientation of crystallites and the high S_{BET} surface area is preserved up to at least 550°C, and morphology of particles up to 900°C. Temperature-dependent study of the F-type structure stability of ceria nanocrystallites reveals preservation of ceria fluorite structure up to 700°C. Introduction of dopant into ceria crystallites (demonstrated by Gd doping) increases preservation of architecture at the second and third level of hierarchical organization in the violent soot oxidation process.

4. The temperature-induced changes of the star-shaped particles architecture proceeds in two temperature regimes. For temperatures below 600°C, growth of NPs is rather slow on behalf of fast reduction of NPs microstrain. This contributes to maintaining the stability of particle architecture, which is especially important in low-temperature catalytic oxidation processes. The second mode above 600°C is linked to the fast growth of ceria nanoparticles but the architecture changes are dopant-dependent, and additional porosity is formed in the Gd-doped sample.

5. Two propane oxidation modes have been observed. The total propane oxidation proceeds for both materials in temperatures up to 390°C. At temperatures above 400°C the gradual increase of trace amount of conversion by-product is detected. Its occurrence may be link to the shift from the surface heterogeneous pathway of propane oxidation (<400°C) into mixed hetero-homogeneous mechanism (>400°C) for which gas phase reactions start to dominate.

The realization of the second goal of this Dissertation is summarized in the following conclusions:

1. The deposition-precipitation method is appropriate for the decoration of ceria surface by gold nanoparticles regardless of the morphology of nanocubes, either flat or curved. The run of the decoration process and the size of gold nanoparticles is very sensitive to the ratio of the total support surface area to the molar content of the chloroauric acid in the reaction mixture.

2. Knowledgeable control of the gold deposition onto hierarchical materials is attained by adjustment of the value of the surface coverage parameter. The calculation of this parameter is based on the knowledge of S_{BET} surface area of the catalyst support. Such control allows to produce variety of gold-decorated catalysts (layers/ clusters of gold, gold nanoparticles localized in different parts of the hierarchical support, and gold particle agglomerates).

3. The presented gold deposition approach that utilizes the concept of surface coverage parameter is not effective for precise gold decoration of the non-hierarchically structured ceria NPs having average size < 7 nm. Oppositely, the organization of ceria nanoparticles into a hierarchical structure allows for deposition of nanogold (< 4nm) on material composed of ceria nanoparticles (< 7 nm). Due to that nanosized-arised properties of both, gold and ceria, are retained at the same time.

The realization of the third goal of this Dissertation is summarized in the following conclusions:

1. Hierarchically structured ceria-based gold catalysts, both, undoped and Gd-doped, outperform non-hierarchical gold-decorated nanocubic ones in propane oxidation. Also, hierarchical gold catalysts (Au5/CeO_2) reduce CO oxidation to ambient temperatures (T_{50}=18°C) as compared to non-hierarchical gold-decorated Au5/CeO_2 nanocubes (T_{50} = 85°C). Those effects have been ascribed to the maximization of Au/ceria interface contact in hierarchical systems and the confinement of Au NPs within pores of hierarchical support.

2. New method for calculating TOF parameter has been presented. According to the proposed approach the gold atoms at the Au/ceria interface has been taken as an active sites, and the number of Au atoms in the ring around gold nanoparticles (modeled as a half-sphere) has been quantified based on histograms generated from TEM data. As demonstrated in propane oxidation reaction, Gd doping facilitates propane oxidation for both nonhierarchical and hierarchical gold catalysts, showing two-fold TOF increase. Also, the Gd-doped hierarchical gold catalyst shows four-fold TOF increase over the undoped non-hierarchical one, proving the synergistic effect of doping and structural hierarchy in propane oxidation.

3. The texture differences of non-decorated ceria-based hierarchical samples influences the catalytic performance in propane oxidation. Preferential orientation of ceria crystallites within star-shaped particles improves oxidation performance over tube-like

ceria that do not show this characteristic. However, gold-decorated hierarchical catalyst does not show preservation of this effect, indicating that the preferential orientation of crystallites does not modify the nature and the number of Au-Ce-O active sites in a substantial way. Instead, Gd-doping highly increases catalytic activity of the studied systems.

4. Decorating ceria-based macroparticles with gold nanoparticles significantly improves the selectivity of the propane oxidation process. The stability of Au NPs is increased by their confinement in the porous hierarchical structure when compared to the gold-decorated ceria nanocubes in which Au NPs are present only at the surface.

5. Increasing gold loading does not necessary lead to catalytic oxidation enhancement. Pore geometry and size may restrict the growth of optimally sized Au NPs leading to activity decline. This has been shown in CO oxidation reaction. Thus, the knowledge of the materials porosity is necessary for optimal catalyst design.

7. Literature

[1] M. Valden, X. Lai, D.W. Goodman, Onset of Catalytic Activity of Gold Clusters on Titania with the Appearance of Nonmetallic Properties, Science 281 (1998) 1647–1650. https://doi.org/10.1126/science.281.5383.1647.

[2] N. Ta, J. Liu, S. Chenna, P.A. Crozier, Y. Li, A. Chen, W. Shen, Stabilized gold nanoparticles on ceria nanorods by strong interfacial anchoring, J Am Chem Soc. 134 (2012) 20585–20588. https://doi.org/10.1021/ja310341j.

[3] T.W. van Deelen, C. Hernández Mejía, K.P. de Jong, Control of metal-support interactions in heterogeneous catalysts to enhance activity and selectivity, Nat Catal. 2 (2019) 955–970. https://doi.org/10.1038/s41929-019-0364-x.

[4] G. Centi, P. Ciambelli, S., Perathoner, P. Russo, Environmental catalysis: trends and outlook, Catal Today. 1-4 (2002) 3-15. https://doi.org/10.1016/S0920-5861(02)00037-8.

[5] A. Bueno-López, K. Krishna, M. Makkee, J.A. Moulijn, Enhanced soot oxidation by lattice oxygen via La^{3+}-doped CeO_2, J Catal. 230 (2005) 237–248. https://doi.org/10.1016/j.jcat.2004.11.027.

[6] J. Liu, Z. Zhao, J. Xu, C. Xu, A. Duan, G. Jiang, H. He, The highly active catalysts of nanocomposite K-Co-CeO_2 for soot combustion, ChemComm. 47 (2011) 11119–11121. https://doi.org/10.1039/c1cc14338g.

[7] W.O. Siegl, R.H. Hammerle, H.M. Herrmann, B.W. Wenclawiak, B. Luers-Jongen, Organic emissions profile for a light-duty diesel vehicle, Atmos Environ. 33 (1999) 797-805. https://doi.org/10.1016/S1352-2310(98)00209-X.

[8] A. Sydbom, A. Blomberg, S. Parnia #,}, N. Stenfors, T. Sandstro, S.-E. Dahle, Health effects of diesel exhaust emissions, Eur Respir. 17 (2001) 733-746. DOI: 10.1183/09031936.01.17407330

[9] A.C. Lloyd, T.A. Cackette, Diesel Engines: Environmental Impact and Control, J Air Waste Manage Assoc. 51 (2001) 809–847. https://doi.org/10.1080/10473289.2001.10464315.

[10] C. Sun, H. Li, L. Chen, Nanostructured ceria-based materials: Synthesis, properties, and applications, Energy Environ Sci. 5 (2012) 8475–8505. https://doi.org/10.1039/c2ee22310d.

[11] A. Trovarelli, P. Fornasiero, Catalysis by Ceria and Related Materials, 2nd ed., Imperical College Press, London, 2013.

[12] R. Chockalingam, V.R.W. Amarakoon, H. Giesche, Alumina/cerium oxide nano-composite electrolyte for solid oxide fuel cell applications, J Eur Ceram Soc. 28 (2008) 959–963. https://doi.org/10.1016/j.jeurceramsoc.2007.09.031.

[13] R.J. Gorte, S. Zhao, Studies of the water-gas-shift reaction with ceria-supported precious metals, Catal Today. 104 (2005) 18–24. https://doi.org/10.1016/j.cattod.2005.03.034.

[14] S. Scirè, S. Minicò, C. Crisafulli, C. Satriano, A. Pistone, Catalytic combustion of volatile organic compounds on gold/cerium oxide catalysts, Appl Catal B. 40 (2003) 43–49. https://doi.org/10.1016/S0926-3373(02)00127-3.

[15] S. Rossignol, F. Gérard, D. Mesnard, C. Kappenstein, D. Duprez, Structural changes of Ce-Pr-O oxides in hydrogen: A study by in situ X-ray diffraction and Raman spectroscopy, J Mater Chem. 13 (2003) 3017–3020. https://doi.org/10.1039/b306726b.

[16] J. Paier, C. Penschke, J. Sauer, Oxygen defects and surface chemistry of ceria: Quantum chemical studies compared to experiment, Chem Rev. 113 (2013) 3949–3985. https://doi.org/10.1021/cr3004949.

[17] N.J. Lawrence, J.R. Brewer, L. Wang, T.S. Wu, J. Wells-Kingsbury, M.M. Ihrig, G. Wang, Y.L. Soo, W.N. Mei, C.L. Cheung, Defect engineering in cubic cerium oxide nanostructures for catalytic oxidation, Nano Lett. 11 (2011) 2666–2671. https://doi.org/10.1021/nl200722z.

[18] A. Trovarelli, J. Llorca, Ceria Catalysts at Nanoscale: How Do Crystal Shapes Shape Catalysis?, ACS Catal. 7 (2017) 4716–4735. https://doi.org/10.1021/acscatal.7b01246.

[19] Y. Xu, S.S. Mofarah, R. Mehmood, C. Cazorla, P. Koshy, C.C. Sorrell, Design strategies for ceria nanomaterials: Untangling key mechanistic concepts, Mater Horiz. 8 (2021) 102–123. https://doi.org/10.1039/d0mh00654h.

[20] A. Filtschew, K. Hofmann, C. Hess, Ceria and Its Defect Structure: New Insights from a Combined Spectroscopic Approach, J Phys Chem C. 120 (2016) 6694–6703. https://doi.org/10.1021/acs.jpcc.6b00959.

[21] C. Sun, D. Xue, Size-dependent oxygen storage ability of nano-sized ceria, Phys Chem Chem Phys. 15 (2013) 14414–14419. https://doi.org/10.1039/c3cp51959g.

[22] S. Deshpande, S. Patil, S.V. Kuchibhatla, S. Seal, Size dependency variation in lattice parameter and valency states in nanocrystalline cerium oxide, Appl Phys Lett. 87 (2005) 1–3. https://doi.org/10.1063/1.2061873.

[23] S. Kurajica, I. Minga, M. Guliš, V. Mandić, I. Simčić, High Surface Area Ceria Nanoparticles via Hydrothermal Synthesis Experiment Design, J Nanomater. 2016(3) (2016) 1-8. https://doi.org/10.1155/2016/7274949.

[24] V.F. Solovyov, M. Gibert, T. Puig, X. Obradors, Size-dependent strain in epitaxial (001) gadolinium-doped ceria nanoislands, Appl Phys Lett. 97 (2010) 20–23. https://doi.org/10.1063/1.3527079.

[25] D. Andreescu, G. Bulbul, R.E. Özel, A. Hayat, N. Sardesai, S. Andreescu, Applications and implications of nanoceria reactivity: Measurement tools and environmental impact, Environ Sci Nano. 1 (2014) 445–458. https://doi.org/10.1039/c4en00075g.

[26] J.D. Cafun, K.O. Kvashnina, E. Casals, V.F. Puntes, P. Glatzel, Absence of Ce^{3+} sites in chemically active colloidal ceria nanoparticles, ACS Nano. 7 (2013) 10726–10732. https://doi.org/10.1021/nn403542p.

[27] L.-H. Chen, Y. Li, B.-L. Su, Hierarchy in materials for maximized efficiency, Natl Sci Rev. 7(11) (2020) 1626-1630. https://doi.org/10.1093/nsr/nwaa251.

[28] P. Xu, R. Yu, H. Ren, L. Zong, J. Chen, X. Xing, Hierarchical nanoscale multi-shell Au/CeO_2 hollow spheres, Chem Sci. 5 (2014) 4221–4226. https://doi.org/10.1039/c4sc01882f.

[29] L. Zhou, P. Obrien, Mesocrystals - Properties and applications, J Phys Chem Lett. 3 (2012) 620–628. https://doi.org/10.1021/jz2015742.

[30] J. Zhang, H. Yang, S. Wang, W. Liu, X. Liu, J. Guo, Y. Yang, Mesoporous CeO_2 nanoparticles assembled by hollow nanostructures: Formation mechanism and enhanced catalytic properties, CrystEngComm. 16 (2014) 8777–8785. https://doi.org/10.1039/c4ce01219d.

[31] R. Rao, M. Yang, C. Li, H. Dong, S. Fang, A. Zhang, A facile synthesis for hierarchical porous CeO_2 nanobundles and their superior catalytic performance for CO oxidation, J Mater Chem A Mater. 3 (2015) 782–788. https://doi.org/10.1039/c4ta03875d.

[32] W. Liu, L. Feng, C. Zhang, H. Yang, J. Guo, X. Liu, X. Zhang, Y. Yang, A facile hydrothermal synthesis of 3D flowerlike CeO_2 via a cerium oxalate precursor, J Mater Chem A Mater. 1 (2013) 6942–6948. https://doi.org/10.1039/c3ta10487g.

[33] G. Zhang, Y. Ma, F. Liu, Z. Tong, J. Sha, W. Zhao, M. Liu, Y. Zheng, Seeded Growth of Au@Cu_xO Core–Shell Mesoporous Nanospheres and Their Photocatalytic Properties, Front Chem. 9 (2021), 671220. https://doi.org/10.3389/fchem.2021.671220.

[34] L. Liu, W. He, Z. Fang, Z. Yang, K. Guo, Z. Wang, From Core-Shell to Yolk-Shell: Improved Catalytic Performance toward $CoFe_2O_4$ Hollow Mesoporous TiO_2 toward Selective Oxidation of Styrene, Ind Eng Chem Res. 59 (2020) 19938–19951. https://doi.org/10.1021/acs.iecr.0c03884.

[35] A.G. Machoke, A.M. Beltrán, A. Inayat, B. Winter, T. Weissenberger, N. Kruse, R. Güttel, E. Spiecker, W. Schwieger, Micro/macroporous system: MFI-type zeolite crystals with embedded macropores, Adv Mater. 27 (2015) 1066–1070. https://doi.org/10.1002/adma.201404493.

[36] Z. Nie, A. Petukhova, E. Kumacheva, Properties and emerging applications of self-assembled structures made from inorganic nanoparticles, Nat Nanotechnol. 5 (2010) 15–25. https://doi.org/10.1038/nnano.2009.453.

[37] D. Mukherjee, B.M. Reddy, Noble metal-free CeO_2-based mixed oxides for CO and soot oxidation, Catal Today. 309 (2018) 227–235. https://doi.org/10.1016/j.cattod.2017.06.017.

[38] M. Coduri, S. Checchia, M. Longhi, D. Ceresoli, M. Scavini, Rare earth doped ceria: The complex connection between structure and properties, Front Chem. 6 (2018) 1–23. https://doi.org/10.3389/fchem.2018.00526.

[39] S. Bernal, G. Blanco, G. Cifredo, J.A. Pérez-Omil, J.M. Pintado, J.M. Rodríguez-Izquierdo, Reducibility of ceria-lanthana mixed oxides under temperature programmed hydrogen and inert gas flow conditions, J Alloys Compd. 250 (1997) 449–454. https://doi.org/10.1016/S0925-8388(96)02825-3.

[40] G. Vlaic, P. Fornasiero, S. Geremia, J. Kašpar, M. Graziani, Relationship between the zirconia-promoted reduction in the Rh-loaded $Ce_{0.5}Zr_{0.5}O_2$ mixed oxide and the Zr-O local structure, J Catal. 168 (1997) 386–392. https://doi.org/10.1006/jcat.1997.1644.

[41] S. Liu, X. Wu, D. Weng, R. Ran, Ceria-based catalysts for soot oxidation: A review, J Rare Earths. 33 (2015) 567–590. https://doi.org/10.1016/S1002-0721(14)60457-9.

[42] F.F. Muñoz, L.M. Acuña, C.A. Albornoz, A.G. Leyva, R.T. Baker, R.O. Fuentes, Redox properties of nanostructured lanthanide-doped ceria spheres prepared by microwave assisted hydrothermal homogeneous co-precipitation, Nanoscale. 7 (2015) 271–281. https://doi.org/10.1039/c4nr05630b.

[43] G. Xiao, S. Li, H. Li, L. Chen, Synthesis of doped ceria with mesoporous flowerlike morphology and its catalytic performance for CO oxidation, Microporous and Mesoporous Mater. 120 (2009) 426–431. https://doi.org/10.1016/j.micromeso.2008.12.015.

[44] G.C. Bond, C. Louis, D.T. Thompson, Catalysis by Gold, Catal Sci Ser. 6 (2006). https://doi.org/10.1142/p450.

[45] R. Meyer, C. Lemire, S.K. Shaikhutdinov, H.-J. Freund, Surface Chemistry of Catalysis by Gold, Gold Bull. 37 (2004) 72-124. https://doi.org/10.1007/BF03215519.

[46] M. Sankar, Q. He, R. v. Engel, M.A. Sainna, A.J. Logsdail, A. Roldan, D.J. Willock, N. Agarwal, C.J. Kiely, G.J. Hutchings, Role of the Support in Gold-Containing Nanoparticles as Heterogeneous Catalysts, Chem Rev. 120 (2020) 3890–3938. https://doi.org/10.1021/acs.chemrev.9b00662.

[47] T. Takei, T. Akita, I. Nakamura, T. Fujitani, M. Okumura, K. Okazaki, J. Huang, T. Ishida, M. Haruta, Heterogeneous Catalysis by Gold, in: Advances in Catalysis, Academic Press Inc., 2012: pp. 1–126. https://doi.org/10.1016/B978-0-12-385516-9.00001-6.

[48] J.T. Miller, A.J. Kropf, Y. Zha, J.R. Regalbuto, L. Delannoy, C. Louis, E. Bus, J.A. van Bokhoven, The effect of gold particle size on Au-Au bond length and reactivity toward oxygen in supported catalysts, J Catal. 240 (2006) 222–234. https://doi.org/10.1016/j.jcat.2006.04.004.

[49] Z. Kónya, V.F. Puntes, I. Kiricsi, J. Zhu, J.W. Ager, M.K. Ko, H. Frei, P. Alivisatos, G.A. Somorjai, Synthetic insertion of gold nanoparticles into mesoporous silica, Chem Mater. 15 (2003) 1242–1248. https://doi.org/10.1021/cm020824a.

[50] S. Cao, F.F. Tao, Y. Tang, Y. Li, J. Yu, Size- and shape-dependent catalytic performances of oxidation and reduction reactions on nanocatalysts, Chem Soc Rev. 45 (2016) 4747–4765. https://doi.org/10.1039/c6cs00094k.

[51] E.S. Lokteva, E. v. Golubina, Metal-support interactions in the design of heterogeneous catalysts for redox processes, Pure Appl Chem. 91 (2019) 609–631. https://doi.org/10.1515/pac-2018-0715.

[52] T. Tabakova, D. Dimitrov, M. Manzoli, F. Vindigni, P. Petrova, L. Ilieva, R. Zanella, K. Ivanov, Impact of metal doping on the activity of Au/CeO_2 catalysts for catalytic abatement of VOCs and CO in waste gases, Catal Commun. 35 (2013) 51–58. https://doi.org/10.1016/j.catcom.2013.01.021.

[53] Z. Ma, S. Dai, Design of novel structured gold nanocatalysts, ACS Catal. 1 (2011) 805–818. https://doi.org/10.1021/cs200100w.

[54] K. Ariga, M. Nishikawa, T. Mori, J. Takeya, L.K. Shrestha, J.P. Hill, Self-assembly as a key player for materials nanoarchitectonics, Sci Technol Adv Mater. 20 (2019) 51–95. https://doi.org/10.1080/14686996.2018.1553108.

[55] M. Hirano, M. Inagaki, Preparation of monodispersed cerium(IV) oxide particles by thermal hydrolysis: Influence of the presence of urea and Gd doping on their morphology and growth, J Mater. 10(2) (2000) 473-477. DOI:10.1039/a907510k.

[56] F. Zhang, S.W. Chan, J.E. Spanier, E. Apak, Q. Jin, R.D. Robinson, I.P. Herman, Cerium oxide nanoparticles: Size-selective formation and structure analysis, Appl Phys Lett. 80 (2002) 127–129. https://doi.org/10.1063/1.1430502.

[57] M. Ramachandran, R. Subadevi, M. Sivakumar, Role of pH on synthesis and characterization of cerium oxide (CeO_2) nano particles by modified co-precipitation method, Vacuum. 161 (2019) 220–224. https://doi.org/10.1016/j.vacuum.2018.12.002.

[58] C. Laberty-Robert, J.W. Long, E.M. Lucas, K.A. Pettigrew, R.M. Stroud, M.S. Doescher, D.R. Rolison, Sol-gel-derived ceria nanoarchitectures: Synthesis, characterization, and electrical properties, Chem Mater. 18 (2006) 50–58. https://doi.org/10.1021/cm051385t.

[59] R.D. Purohit, B.P. Sharma, K.T. Pillai, A.K. Tyagi, Ultrafine ceria powders via glycine-nitrate combustion, 36(15) (2001) 2711-2721. https://doi.org/10.1016/S0025-5408(01)00762-0.

[60] Y. He, B. Yang, G. Cheng, Controlled synthesis of CeO_2 nanoparticles from the coupling route of homogenous precipitation with microemulsion, Mater Lett. 57 (2003) 1880–1884. https://doi.org/10.1016/S0167-577X(02)01093-5.

[61] Z. Wu, M. Li, J. Howe, H.M. Meyer, S.H. Overbury, Probing defect sites on CeO_2 nanocrystals with well-defined surface planes by Raman spectroscopy and O_2 adsorption, Langmuir. 26 (2010) 16595–16606. https://doi.org/10.1021/la101723w.

[62] C. Sun, L. Chen, Controllable synthesis of shuttle-shaped ceria and its catalytic properties for co oxidation, Eur J Inorg Chem. (2009) 3883–3887. https://doi.org/10.1002/ejic.200900362.

[63] I.Y. Kaplin, E.S. Lokteva, E. v. Golubina, V. v. Lunin, Template synthesis of porous ceria-based catalysts for environmental application, Molecules. 25 (2020) 4242. https://doi.org/10.3390/molecules25184242.

[64] S.C. Kuiry, S.D. Patil, S. Deshpande, S. Seal, Spontaneous self-assembly of cerium oxide nanoparticles to nanorods through supraaggregate formation, J Phys Chem B. 109 (2005) 6936–6939. https://doi.org/10.1021/jp050675u.

[65] B.B. Bokhonov, A.A. Matvienko, K.B. Gerasimov, D. v. Dudina, Formation of ordered nanocrystalline CeO_2 structures during thermal decomposition of cerium formate $Ce(HCOO)_3$, Ceram Int. 45 (2019) 19684–19688. https://doi.org/10.1016/j.ceramint.2019.06.219.

[66] I. Lucentini, I. Serrano, L. Soler, N.J. Divins, J. Llorca, Ammonia decomposition over 3D-printed CeO_2 structures loaded with Ni, Appl Catal A Gen. 591 (2020) 117382. https://doi.org/10.1016/j.apcata.2019.117382.

[67] Y. He, X. Liang, B. Chen, Globin-like mesoporous CeO_2: A CO-assisted synthesis based on carbonate hydroxide precursors and its applications in low temperature CO oxidation, Nano Res. 8 (2015) 1269–1278. https://doi.org/10.1007/s12274-014-0614-9.

[68] Y.B. Go, A.J. Jacobson, Solid solution precursors to gadolinia-doped ceria prepared via a low-temperature solution route, Chem Mater. 19 (2007) 4702–4709. https://doi.org/10.1021/cm071310k.

[69] B.P. Mandal, V. Grover, M. Roy, A.K. Tyagi, X-ray diffraction and Raman spectroscopic investigation on the phase relations in Yb_2O_3- and Tm_2O_3-substituted CeO_2, J Am Ceram. 90 (2007) 2961–2965. https://doi.org/10.1111/j.1551-2916.2007.01826.x.

[70] M.A. Małecka, J.J. Delgado, L. Kepiński, J.J. Calvino, S. Bernal, G. Blanco, X. Chen, Structure transformations and reducibility of nanocrystalline $Ce_{1-x}Yb_xO_{2-(x/2)}$ mixed oxides, Catal Today. 187 (2012) 56–64. https://doi.org/10.1016/j.cattod.2012.01.004.

[71] European Environment Agency, National emissions reported to the Convention on Long-range Transboundary Air Pollution (LRTAP Convention), (2022). https://www.eea.europa.eu/data-and-maps/data/national-emissions-reported-to-the-convention-on-long-range-transboundary-air-pollution-lrtap-convention-16 (accessed October 28, 2022).

[72] Q. Song, R. Ran, J. Ding, X. Wu, Z. Si, D. Weng, The controlled preparation and performance of Fe, Co-modified porous ceria nanorods for the total oxidation of propane, Mol Catal. 480 (2020) 110663. https://doi.org/10.1016/j.mcat.2019.110663.

[73] E. Aneggi, D. Wiater, C. de Leitenburg, J. Llorca, A. Trovarelli, Shape-dependent activity of ceria in soot combustion, ACS Catal. 4 (2014) 172–181. https://doi.org/10.1021/cs400850r.

[74] P. Miceli, S. Bensaid, N. Russo, D. Fino, CeO_2-based catalysts with engineered morphologies for soot oxidation to enhance soot-catalyst contact, Nanoscale Res Lett. 9 (2014) 1–10. https://doi.org/10.1186/1556-276X-9-254.

[75] M. Piumetti, T. Andana, S. Bensaid, N. Russo, D. Fino, R. Pirone, Study on the CO Oxidation over Ceria-Based Nanocatalysts, Nanoscale Res Lett. 11 (2016) 165. https://doi.org/10.1186/s11671-016-1375-z.

[76] M.A. Małecka, L. Kepiński, W. Miśta, Structure evolution of nanocrystalline CeO_2 and $CeLnO_x$ mixed oxides (Ln = Pr, Tb, Lu) in O_2 and H_2 atmosphere and their catalytic activity in soot combustion, Appl Catal B. 74 (2007) 290–298. https://doi.org/10.1016/j.apcatb.2007.02.021.

[77] D. Sorolla-Rosario, A. Davó-Quiñonero, E. Bailón-García, D. Lozano-Castelló, A. Bueno-López, Key-lock Ceria Catalysts for the Control of Diesel Engine Soot Particulate Emissions, ChemCatChem. 12 (2020) 1772–1781. https://doi.org/10.1002/cctc.201902177.

[78] C. Hognon, Y. Simon, P.M. Marquaire, C. Courson, A. Kiennemann, Hydrogen production by catalytic partial oxidation of propane over CeO_2, Chem Eng Sci. 181 (2018) 46–57. https://doi.org/10.1016/j.ces.2018.01.038.

[79] R. Zanella, S. Giorgio, C.R. Henry, C. Louis, Alternative methods for the preparation of gold nanoparticles supported on TiO_2, J Phys Chem B. 106 (2002) 7634–7642. https://doi.org/10.1021/jp0144810.

[80] R. Zanella, A. Sandoval, P. Santiago, V.A. Basiuk, J.M. Saniger, New preparation method of gold nanoparticles on SiO_2, J Phys Chem B. 110 (2006) 8559–8565. https://doi.org/10.1021/jp060601y.

[81] L. Prati, A. Villa, The art of manufacturing gold catalysts, Catalysts. 2 (2011) 24–37. https://doi.org/10.3390/catal2010024.

[82] A. Hugon, N. el Kolli, C. Louis, Advances in the preparation of supported gold catalysts: Mechanism of deposition, simplification of the procedures and relevance of the elimination of chlorine, J Catal. 274 (2010) 239–250. https://doi.org/10.1016/j.jcat.2010.07.008.

[83] A. Aboukaïs, S. Aouad, H. El-Ayadi, M. Skaf, M. Labaki, R. Cousin, E. Abi-Aad, Physicochemical characterization of Au/CeO_2 solids. Part 2: The impregnation preparation method, Mater Chem Phys. 137 (2012) 42–47. https://doi.org/10.1016/j.matchemphys.2012.08.074.

[84] L. Wolski, G. Nowaczyk, S. Jurga, M. Ziolek, Influence of co-precipitation agent on the structure, texture and catalytic activity of Au-CeO_2 catalysts in low-temperature oxidation of benzyl alcohol, Catalysts. 11 (2021) 641. https://doi.org/10.3390/catal11050641.

[85] S. Tsubota, D.A.H. Cunningham, Y. Bando, M. Haruta, Preparation of nanometer gold strongly interacted with TiO_2 and the structure sensitivity in low-temperature oxidation of CO, Stud Surf Sci Catal. 91 (1995) 227-235. https://doi.org/10.1016/S0167-2991(06)81759-3.

[86] D. Guillemot, M. Polisset-Thfoin, J. Fraissard, Preparation of nanometeric gold particles on NaHY, Catal Letters. 41 (1996) 143-148. https://doi.org/10.1007/BF00811481.

[87] M. Okumura, S. Nakamura, S. Tsubota, T. Nakamura, M. Azuma, M. Haruta, Chemical vapor deposition of gold on Al_2O_3 , SiO_2 , and TiO_2 for the oxidation of CO and of H_2, Catal Lett. 51 (1998) 53-58. https://doi.org/10.1023/A:1019020614336.

[88] P. Tabib Zadeh Adibi, T. Pingel, E. Olsson, H. Grönbeck, C. Langhammer, Pt nanoparticle sintering and redispersion on a heterogeneous nanostructured support, J Phys Chem C. 120 (2016) 14918–14925. https://doi.org/10.1021/acs.jpcc.6b03874.

[89] S. L. Brantley, J. D. Kubicki, A. F. White, Kinetics of Water-Rock Interaction, Springer, New York, 2008, p. 259.

[90] D. Xu, H. Lv, B. Liu, Encapsulation of metal nanoparticle catalysts within mesoporous zeolites and their enhanced catalytic performances: A review, Front Chem. 6 (2018) 550. https://doi.org/10.3389/fchem.2018.00550.

[91] Q. Li, L. Song, Z. Liang, M. Sun, T. Wu, B. Huang, F. Luo, Y. Du, C.-H. Yan, A Review on CeO_2 -Based Electrocatalyst and Photocatalyst in Energy Conversion , Advanced Energy and Sustainability Research. 2 (2021) 2000063. https://doi.org/10.1002/aesr.202000063.

[92] R.J. Macfarlane, From Nano to Macro: Thinking Bigger in Nanoparticle Assembly, Nano Lett. 21 (2021) 7432–7434. https://doi.org/10.1021/acs.nanolett.1c02724.

[93] K.A. Ledwa, L. Kępiński, M. Ptak, R. Szukiewicz, $Ru_{0.05}Ce_{0.95}O_{2-y}$ deposited on functionalized alumina as a smart catalyst for propane oxidation, Appl Catal B. 274 (2020) 119090. https://doi.org/10.1016/j.apcatb.2020.119090.

[94] H. Ha, S. Yoon, K. An, H.Y. Kim, Catalytic CO Oxidation over Au Nanoparticles Supported on CeO_2 Nanocrystals: Effect of the Au-CeO_2 Interface, ACS Catal. 8 (2018) 11491–11501. https://doi.org/10.1021/acscatal.8b03539.

[95] M. Cargnello, C. Gentilini, T. Montini, E. Fonda, S. Mehraeen, M. Chi, M. Herrera-Collado, N.D. Browning, S. Polizzi, L. Pasquato, P. Fornasiero, Active and stable embedded Au@CeO_2 catalysts for preferential oxidation of CO, Chem Mater. 22 (2010) 4335–4345. https://doi.org/10.1021/cm101499x.

[96] M. Haruta, Spiers Memorial Lecture: Role of perimeter interfaces in catalysis by gold nanoparticles, Faraday Discuss. 152 (2011) 11–32. https://doi.org/10.1039/c1fd00107h.

[97] Y. Wei, Y. Zhang, P. Zhang, J. Xiong, X. Mei, Q. Yu, Z. Zhao, J. Liu, Boosting the Removal of Diesel Soot Particles by the Optimal Exposed Crystal Facet of CeO_2 in Au/CeO_2 Catalysts, Environ Sci Technol. 54 (2020) 2002–2011. https://doi.org/10.1021/acs.est.9b07013.

[98] F. Garin, Environmental catalysis, Catal Today. 89 (2004) 255–268. https://doi.org/10.1016/j.cattod.2003.12.002.

[99] T. Maillet, J. Barbier, D. Duprez, Reactivity of steam in exhaust gas catalysis III. Steam and oxygen/steam conversions of propane on a Pd/Al_2O_3 catalyst, Appl Catal B. 9 (1996) 251–266.

[100] M.D. Krcha, M.J. Janik, Catalytic propane reforming mechanism over Mn-Doped CeO_2 (111), Surf Sci. 640 (2015) 119–126. https://doi.org/10.1016/j.susc.2015.02.012.

[101] R. Velinova, S. Todorova, G. Ivanov, D. Kovacheva, H. Kolev, A. Naydenov, Catalytic combustion of propane on Pd-modified Al–La–Ce catalyst – from reaction kinetics and mechanism to monolithic reactor tests and scale-up, Int J Chem React Eng. 18 (2020) 20200017. https://doi.org/10.1515/ijcre-2020-0017.

[102] M.D. Argyle, C.H. Bartholomew, Heterogeneous catalyst deactivation and regeneration: A review, Catalysts. 5 (2015) 145–269. https://doi.org/10.3390/catal5010145.

[103] A.M. Abdel-Mageed, S. Chen, C. Fauth, T. Häring, J. Bansmann, Fundamental Aspects of Ceria Supported Au Catalysts Probed by In Situ/Operando Spectroscopy and TAP Reactor Studies, ChemPhysChem. 22 (2021) 1302–1315. https://doi.org/10.1002/cphc.202100027.

[104] P.H. Ho, D. Yao, D. Creaser, L. Olsson, Advantages of High-Siliceous Zeolites in the Reactivity and Stability of Diesel Oxidation Catalysts, ACS Engineering Au. 2 (2022) 219–235. https://doi.org/10.1021/acsengineeringau.1c00035.

8. Additional Materials

The following list of figures presents the unpublished experimental results that have been used to support research presented in this Dissertation.

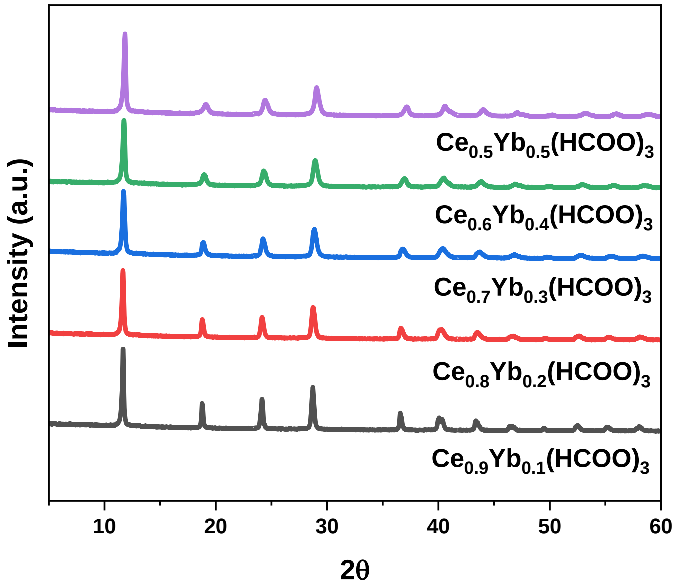

Fig. A1. PXRD of $Ce_{1-x}Yb_x(HCOO)_3$ (x = 0-0.5) as an intermediate product in wet chemical synthesis of tube-like $Ce_{1-x}Yb_xO_{2-x/2}$ hierarchical catalyst support.

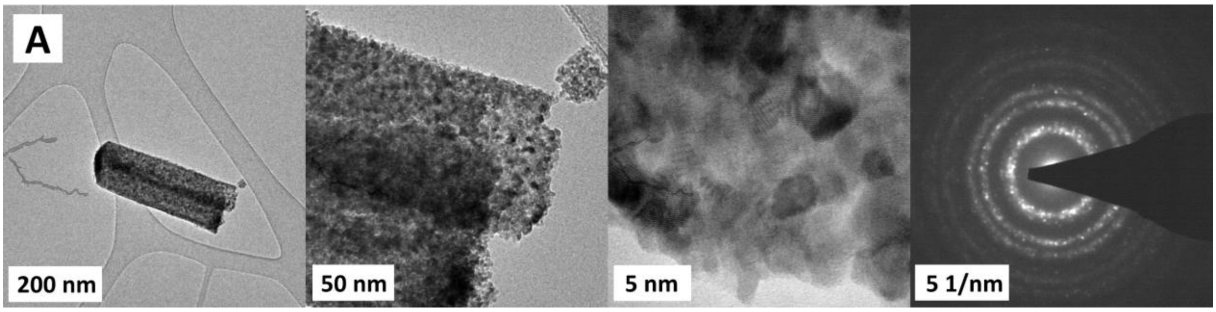

Fig. A2. TEM images of tube-like hierarchical support at different magnification levels. SAED pattern (rightmost image) show no preferential orientation of ceria crystallites.

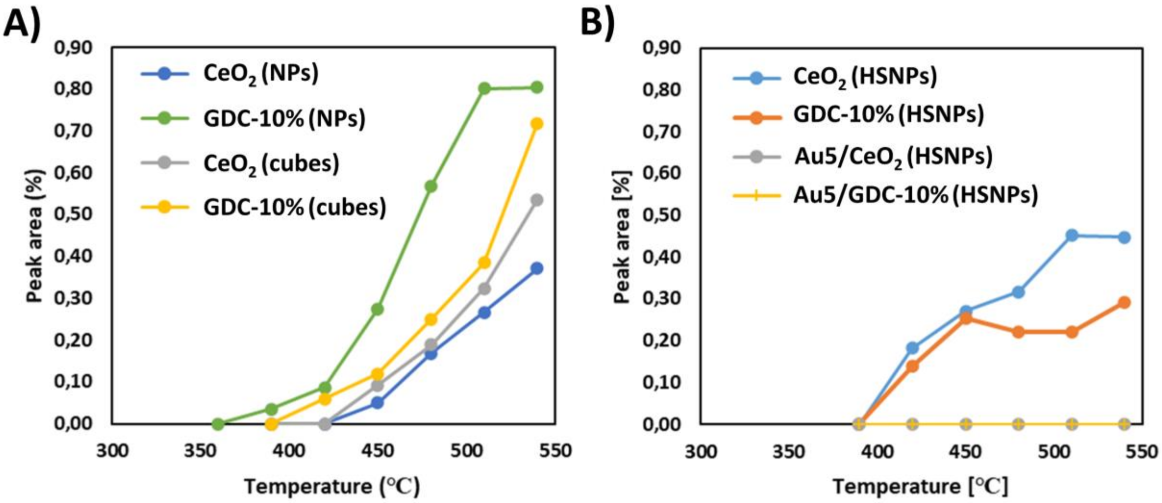

Fig. A3. By-product formation in propane oxidation by ceria-based supports differing in architecture (A) and presence of gold (B); HSNPs refers to star-shaped hierarchically structured nanoparticles, NPs refers to non-hierarchical powdered ceria nanoparticles.

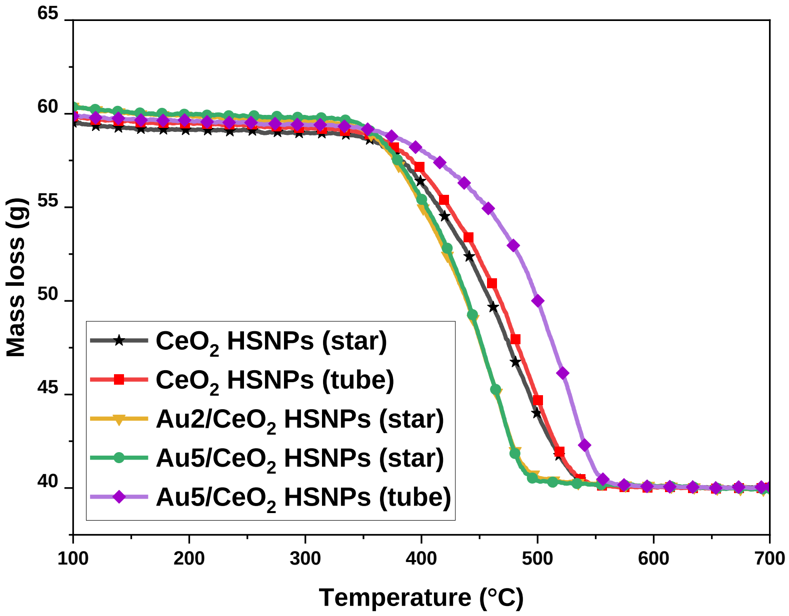

Fig. A4. TG curves of soot oxidation for hierarchical samples differed by the architecture (star-shaped or tube-like) and the presence of gold (Au x, x refers to the value of surface coverage parameter).

9. Academic Achievements

Scientific articles

1. Woźniak P., Kraszkiewicz P., Małecka M.A., Divergent influence of {1 1 1} vs. {1 0 0} crystal planes and Yb^{3+} dopant on CO oxidation paths in mixed nano-sized oxide Au/$Ce_{1-x}Yb_xO_{2-x/2}$ (x = 0 or 0.1) systems, CrystEngComm, 2020, 22, 5828–5840.
2. Woźniak P., Miśta W., Małecka M.A., Function of various levels of hierarchical organization of porous $Ce_{0.9}REE_{0.1}O_{1.95}$ mixed oxides in catalytic activity, CrystEngComm, 2020, 22, 5914–5930.
3. Małecka M.A., Matus K., Woźniak P., Decoration of Cube-Like Ceria Crystals by Well-Dispersed Au Nanoparticles: Surface Influence, ChemistrySelect, 2020, *5*, 2871 - 2877.
4. Małecka, M.A. Woźniak, P., Hierarchical macroparticles of ceria with tube-like shape – synthesis and properties, CrystEngComm, 2021, 23, 6743-6754
5. Woźniak, P., Małecka, M.A., Chinchilla, L., Trasobares, S., 3D hierarchically structured $Ce_{1-x}Gd_xO_{2-x/2}$ mixed oxide particles: the role of microstructure, porosity and multi-level architecture stability in soot and propane oxidation, Mater. Res. Bull. 2022, 151, 111816.
6. Woźniak, P., Kraszkiewicz, P., Małecka, M.A., Hierarchical Au/CeO2 systems – influence of Ln3+ dopants on the catalytic activity in the propane oxidation process, CrystEngComm, 2022, 24, 6408.
7. Woźniak, P. , Małecka, M.A., , Kraszkiewicz, P. , Miśta, W. , Bezkrovnyi, O. , Chinchilla, L. , Trasobares, S., Confinement of nano-gold in 3D hierarchically structured gadolinium-doped ceria mesocrystal: synergistic effect of chemical composition and structural hierarchy in CO and propane oxidation. Catal. Sci. Technol, 2022, 12, 7082-7113.
8. Dudek, M., Szalkowski, M., Misiak, M., Ćwierzona, M., Skripka, A., Korczak, Z., Piątkowski, D., Woźniak, P., Lisiecki, R., Goldner, P, Maćkowski, S., Chan, E.M., Schuck, P.J., Bednarkiewicz, A., Size-Dependent Photon Avalanching in Tm3+ Doped LiYF4 Nano, Micro, and Bulk Crystals, Adv. Optical Mater., 2022, 2201052.

Scientific conferences

1. XLV Ogólnopolska Szkoła Chemii "Chemia na fali", Rozewie, 2016.
   Poster: *Kiedy fluorowiec jest elektrofilem, czyli rzecz o wiązaniu halogenowym*
2. 60 Konwersatorium Krystalograficzne, Wrocław, 2018.
   Poster: *Orientacja nanocząstek złota na nośnikach* $Ce_{1-x}Yb_xO_{2-x/2}$ *(x = 0; 0.1) o zadanej morfologii*
3. LI Ogólnopolskie Kolokwium Katalityczne, Kraków 2019.
   Oral presentation: *Divergent influence of {111} vs {100} crystal planes and* Yb^{3+} *dopant on CO oxidation reaction paths in mixed oxide nano-sized* Au/$Ce_{1-x}Yb_xO_{2-y}$ *composites*

4. Joint Polish-German Crystallographic Meeting, Wrocław 2020.
   Poster and Oral presentation within the framework of *Lightning talks of young crystallogrpahers: Preferential orientation of* $Ce_{1-x}Ln_xO_{2-y}$ *nano-sized crystallites in star-shaped hierarchical porous particles.*
5. 62 Konwersatorium Krystalograficzne, Wrocław 2021.
   Poster: *3D architecture of cerium formate-derived* CeO_2 *hierarchically structured star-shaped particles*

Grants

1. European Union Horizon 2020 research and innovation programme, grant agreement No. 823717-ESTEEM3*, Hierarchically structured star-shaped porous micro-particles composed of Ce1-xLnxO2-y nano-sized crystallites as superior active catalytic media.*

Participation in projects

1. Undergraduate Research Opportunities Program, co-investigator in project *Synthesis and Photophysical Characterization of Highly Luminescent* $Ge_{1-x}Sn_x$*/ZnSe Core-Shell Nanocrystals,* VCU, Richmond VA, 2017.
2. Co-investigator in project 2016/21/D/ST5/01640, *Badanie wpływu stopnia zdefektowania powierzchni mieszanego tlenku* $Ce_{1-x}Ln_xO_{2-y}$ *na kształt i rozmiar osadzonych na nim nanocząstek metalu szlachetnego oraz ich orientacje względem nośnika*, INTIBS PAN, Wrocław 2019/2020.

Scholarships

1. KNOW scholarship, University of Wrocław, 2016/17.
2. Erasmus Student Exchange Programme, Chemistry, Charles University, Prague 2014/15.
3. International Students Exchange Programme (ISEP), Chemistry, Virginia Commonwealth University, Richmond VA, 2017.
4. POWR.03.02.00-00-I030/17.00 “Multidyscyplinarne studia doktoranckie - nanotechnologia w biomedycynie”, Wrocław 2018/22.

10. Appendix 1. Publications D1-D6, Supplementary Materials, Contribution Statements

The publications included in this Dissertation are presented in the following order:

D1. Woźniak, P., Miśta, W., Małecka, M.A., Function of various levels of hierarchical organization of porous $Ce_{0.9}REE_{0.1}O_{1.95}$ mixed oxides in catalytic activity, CrystEngComm, 2020, 22, 5914-5930.

D2. Woźniak, P., Małecka, M.A., Chinchilla, L., Trasobares, S., 3D hierarchically structured $Ce_{1-x}Gd_xO_{2-x/2}$ mixed oxide particles: the role of microstructure, porosity and multi-level architecture stability in soot and propane oxidation, Mater. Res. Bull., 2022, 151, 111816.

D3. Małecka, M.A., Woźniak, P., Hierarchical macroparticles of ceria with tube-like shape – synthesis and properties, CrystEngComm, 2021, 23, 6743-6754.

D4. Małecka, M.A., Matus, K., Woźniak, P., Decoration of Cube-Like Ceria Crystals by Well- Dispersed Au Nanoparticles: Surface Influence, ChemistrySelect, 2020, 5, 2871-2877.

D5. Woźniak, P., Małecka, M.A., Kraszkiewicz, P., Miśta, W., Bezkrovnyi, O., Chinchilla, L., Trasobares, S., Confinement of nano-gold in 3D hierarchically structured gadolinium- doped ceria mesocrystal: synergistic effect of chemical composition and structural hierarchy in CO and propane oxidation. Catal. Sci. Technol., 2022, 12, 7082-7113.

D6. Woźniak, P., Kraszkiewicz, P., Małecka, M.A., Hierarchical Au/CeO2 systems – influence of Ln^{3+} dopants on the catalytic activity in the propane oxidation process, CrystEngComm, 2022, 24, 6408–6420.

Supplementary Materials relating to the relevant publication were placed immediately after it. Contribution statements can be found at the end of Appendix 1.

The contents of this appendix are author accepted manuscripts (AAM) of publications D1-D6. The relevant publications have the following identifiers:

D1: doi.org/10.1039/D0CE00883D

D2: doi.org/10.1016/j.materresbull.2022.111816

D3: doi.org/10.1039/D1CE00755F

D4: doi.org/10.1002/slct.202000098

D5: doi.org/10.1039/D2CY01214F

D6: doi.org/10.1039/D2CE00827K

Function of various levels of hierarchical organization of the porous $Ce_{0.9}REE_{0.1}O_{1.95}$ mixed oxides in the catalytic activity.

Received 00th January 20xx,
Accepted 00th January 20xx

DOI: doi.org/10.1039/D0CE00883D

Piotr Woźniak,*[a] Włodzimierz Miśta[a] and Małgorzata A. Małecka[a]

In this paper, the effect of the nanocrystallites hierarchical arrangement on CO oxidation and soot combustion activity has been investigated. Hierarchically structured star-shaped particles (HS stars) were compared with microemulsion-derived, loosely arranged nanoparticles (NPs). The star-like $Ce_{0.9}REE_{0.1}O_{1.95}$ mixed oxides were synthesized by the oxidative thermolysis of the $Ce_{0.9}REE_{0.1}(HCOO)_3$ mixed formates. The study of the synthesis, structure and catalytic activity of the porous, star-like ceria based mixed oxides was presented for the first time. It was shown that each level of the hierarchical structure of the star-like mixed oxides has its own functionality and it is vulnerable for modifications. In-depth characterization of as synthesized ceria allowed to determine relationship between hierarchically-structured nature of material with its catalytic activity in CO oxidation and soot combustion. It was concluded that the presence of the 3D structure composed of ceria nanocrystals significantly improves the stability and catalytic activity of star-like material in comparison to nano-powdered one. Moreover, introduction of the trivalent RE-ion into the ceria structure lead to further improvement the CO oxidation performance. Finally, key-lock catalysis concept was applied to explain the enhanced activity of the hierarchically structured star-shaped ceria particles as a catalyst in the soot combustion process in comparison to nanocrystalline CeO_2.

I. Introduction

Cerium oxide has been an object of structural and catalytic studies for a long time due to its unique redox capabilities, namely the ability to store or release oxygen depending on environmental gaseous conditions that is known in the literature as oxygen storage capacity (OSC)[1]. Due to that feature it has been widely utilized in the motor industry as a three-way catalyst[2], among other applications in solid oxide fuel cells[3], water-gas shift reaction materials[4] and volatile organic compounds catalytic conversions[5]. High activity of ceria based catalysts in various applications (like oxidation of harmful organic compounds) is due to their ability to reversibly change oxidation state of cerium $Ce^{4+} \leftrightarrow Ce^{3+}$ ($Ce^{IV}O_2 \leftrightarrow Ce^{IV}_{1-x}Ce^{III}_xO_{2-x/2}$)[6]. This reduction-oxidation reaction is fully reversible and may be performed cyclically.

In recent times, the research efforts were directed to the characterization of cerium oxide nano-sized materials with specified morphology such as cubes, octahedrons, rods, nanosheets, putting specific attention to the influence of surface type on its chemical performance[1,7,8]. Among others of as so far obtained morphologies are nano- and microspheres, hollow spheres and nanowire arrays[9]. Nevertheless, three-dimensional materials that are hierarchically structured attract more and more researcher's attention.

In spite of the familiarity of the hierarchical organization concept in materials science and biosciences, fabrication of hierarchically 3D-structured devices composed of nano-sized building blocks was introduced in nanomaterials synthesis science relatively recently[10,11,12]. The property of 'hierarchy' refers to certain ordering of singled out units, and various types of hierarchy has been signalized in the literature depending on unit type. Structural hierarchy constitutes a tactical repetitive combination of structural units[13] that group into higher description-level classes in which building elements are denser within groups than between them[14]. Compositional hierarchy refers to the specific varied spatial arrangement of parts of a material (atoms, molecules, larger entities) whereas transport hierarchy describes distribution of flow through open pathways in fluid systems (pore systems). Hierarchical porosity may be described by the multimodal and multiscale pore distribution inside the material[15], however, the interplay between the pore systems that facilitates the flow distribution allows to name the system 'hierarchical'[13]. Functional adaptation at each level of organization is believed to be responsible for hierarchical materials exceptional properties[15]. Moreover, tunable porous structure, controllable macroscopic morphologies, variety of synthesis approaches and adjustable functions, make these materials useful in many applications such as gas monitoring, water treatment, catalytic conversion[12,15].

In the field of heterogeneous catalyst synthesis, one of the widespread foregoing scientific pursuits so far has been material pore engineering as well as reduction of the size of its

---

[a] *Institute of Low Temperature and Structure Research, Polish Academy of Sciences P.O. Box 1410, 50-950 Wrocław 2, Poland*

Electronic Supplementary Information (ESI) available: [Fig. S1-S12 and Table S1]. See DOI: 10.1039/x0xx00000x

building units to the nano-regime in order to obtain larger surface area. However, from an engineering point of view, nano-sized materials in the form of powders are difficult to handle. Creating hierarchical micro-sized structures that are built of nanoparticles seems to solve this obstacle. Unique properties of nanocrystalline particles, the concentration of edges and corners as well as significant surface to volume ratio, are retained. At the same time, the existence of a hierarchy creates pores that further increase the surface area of the material. Due to that reaction kinetics is favored via mass transfer melioration. This is confirmed by the previous studies in CO oxidation performance of hierarchically structured ceria such as nanobundles[16], globin-like spheres[17], coral-like[18], urchin-like[18,19], flower-like[20,21,22,23] and spindle-like[24] particles. Also, the soot combustion process is sensitive to nanoparticles morphology[25,26]. Five types of cerium oxide catalysts for soot oxidation has been differentiated so far[27]. While nanometric materials, fiber catalysts and three dimensional ordered mesoporous (3DOM) materials' architecture increases the contact area between ceria and soot particles, in the case of core-shell particles and exposed lattice plane-controlled catalysts the number of active sites is increased, as reviewed by Liu et al.[27].

Nonetheless, in all of the above mentioned studies concerning ceria hierarchical structures, little attention has been put into a modification of nano-sized building units via oxygen vacancy formation through doping, listing just a few examples in the literature[28,29]. Introduction of dopant into the cerium oxide modifies its structure, namely oxygen vacancy defect concentration, by the substitution of Ce^{4+} ions by their trivalent counterparts and subsequent removal of oxygen atoms; due to that the balance of charge in the material is retained[30]. In contrast to the well-known structures of pure oxides, the intermediate (defective) structures of the ceria based mixed oxides are much less known, and some ideas about a model of their structure has been presented in previous works[31,32,33,34,35,36]. As DFT study has shown, the energy of 4.55 eV is needed to remove oxygen atom from the surface of cerium oxide, while only 0.26 eV is needed when the Ce^{3+} ions are present on the surface in close proximity of oxygen vacancy already formed[37]. Hence, the introduction of trivalent lanthanide dopants enhances OSC by facilitating oxygen mobility (creation of extrinsic oxygen vacancies in the lattice), which enhances the redox properties of mixed oxide[38,39]. Also, the presence of rare earths in cerium matrix improves its stability through the hindrance of grain growth in high temperature reducing and oxidizing conditions of operation[27,29]. Thus, rare-earth doped hierarchically structured ceria is a promising improved candidate material for catalytic applications.

In this study, 3D hierarchical ceria material with three distinct structural hierarchy levels was synthesized, and the material demonstrated functionality at each organizational tier by combining three characteristics: (1) enhancement of OSC through rare earth doping at nano-sized level (2) well defined porosity at materials intermediate organizational tier, (3) shape-selectivity at micron-sized level of structural hierarchy. The following objectives were set for this work. Firstly, the presentation of facile and reproducible synthesis of star-shaped hierarchically structured material composed of mixed rare-earth cerium oxide nanoparticles as the building blocks. Secondly, proving the concept that all of the hierarchical organization levels are vulnerable to modification and serve a particular function in catalytic performance. Especially, the CO oxidation reaction has been chosen as an example. Thirdly, postulating the reasonable explanation for decreased temperature of soot combustion taking into account the role of material's hierarchical structure.

II. Methods and Characterization

II.A Materials and Synthesis

Mixed $Ce_{0.9}REE_{0.1}(HCOO)_3$ formate (REE refers to rare-earth element: La, Pr, Nd, Sm, Eu, Gd, Tb, Dy, Ho, Er, Tm, Yb, Lu, Sc, Y) star-shaped crystal agglomerates were obtained by solvothermal method. Proper amounts of $Ce(NO_3)_3*6H_2O$ and $REE(NO_3)_3*6H_2O$ were dissolved in 15 ml DMF under continuous stirring. At the same time benzenetricarboxylic acid was dissolved in 20 ml of dimethylformamide followed by the addition of 15 ml of formic acid. The two solutions were mixed with 1 min of stirring and subjected to heating at 130°C for 3 hours under autogenic pressure in the solvothermal reactor. To remove postsynthetic residues the obtained product was centrifuged and washed with DMF and acetone for several times and dried at 65ºC. Then the material was put into the furnace and subjected to oxidative thermolysis (in static air) for 3 h at 400°C to trigger the formation of $Ce_{0.9}REE_{0.1}O_{1.95}$ porous hierarchically structured crystalline material. For further catalytic studies samples were pre-heated at 550°C for 3 hours in static air to remove possible surface nitrate deposits as described in[40].

Nanocrystalline CeO_{2-y} oxide was synthesized by precipitation in microemulsion (water-in-oil) technique. Details of this technique is described in our previous paper[41]. The powder sample was dried and then preheated in static air at 550ºC for 3 h.

II.B Characterization methods

The as-prepared materials were subjected to detailed microscopic studies in order to investigate morphology, structure and microstructure. High resolution transmission electron microscopy images (HRTEM) and selected area electron diffraction patterns (SAED) were acquired by means of a Philips CM-20 SuperTwin microscope. Scanning electron microscope images were collected on FEI Nova NanoSEM 230 equipped with ETD and TLD detectors. For better Z-contrast, ESBD was applied while the pole tip protection mode was used to image detailed microstructure of materials. The elemental analysis was carried out with the use of the EDS spectrometer (EDAX PegasusXM4). Global concentration measurements were performed on samples placed in carbon resin and pressed at 180ºC in 250 bar in order to obtain a flat surface. Signals from three randomly selected areas of ca. 4500 μm^2 were collected to assure satisfactory statistical averaging.

Structure of materials was confirmed by the X-ray powder diffractograms (XRPD) recorded on a PANalytical X'Pert Pro X-ray diffractometer equipped with Ni-filtered Cu $K\alpha_1$ radiation ($K\alpha_1$ = 1.54060 Å, V = 40 kV, I = 30 mA). Application of Scherrer formula to (111), (200), (220) and (311) peaks of cerium oxide PXRD patterns was used to estimate crystallite mean sizes. The surface chemical profile was checked by FTIR spectroscopy on Nicolet Is 50 spectrometer. Raman spectra in the 50-1500 cm^{-1} range were measured using a Renishaw InVia Raman microscope equipped with confocal DM 2500 Leica optical microscope, a thermoelectrically cooled CCD as a detector and an argon laser operating at 488 nm.

Sorption properties of microemulsion-derived cerium nanoparticles and selected star-shaped mixed cerium oxide samples were tested on Sorptomatic 1900 Fisions. Temperature programmed reduction tests (H_2-TPR) were performed on Autochem II 2920 (Micromeritics, USA) equipped with TCD detector. 50 mg of sample was placed in quartz reactor and flushed with helium for 15 minutes followed by reduction measurements in the 30 cm^3/min flow of 5% H_2/Ar_2 in the temperature range of 25°C - 900°C and 10°C/min temperature increase.

II.C Catalytic tests

The catalytic activity of the samples was tested in CO oxidation reaction. Typically, 50 mg of the catalyst (fine, unfractionated powder) was placed in a quartz microreactor (U-type microreactor, H = 18 cm, D = 9 mm, D(active zone) ≈ 6 mm) and installed in a commercial apparatus (Autochem II 2920, Micromeritics). The feed gas consisted of 1% CO, 5% O_2 and 94% He with a total flow rate of 50 ml/min with 3°C/min temperature increase between 25°C - 400°C. The composition of gases was measured by OmniStar QMS-200 Pfeiffer Vacuum mass spectrometer that was calibrated by gas mixtures of known composition and purity (CO 4.7; H_2 5.0; He 5.0). Soot combustion tests were performed in "tight contact" mode by placing grinded mixture of 40 mg of ceria and 20 mg soot in corundum crucible into TG analyzer Derivatograph MOM Q-1500D with a programed temperature increase of 5ºC/min in range 25°C - 700°C. The model soot used in this work was a carbon black Printex-U from Degussa S.A.

III. Results and discussion

III A. Materials characterization

Solvothermal method employed in this study has led to the formation of mixed $Ce_{0.9}REE_{0.1}(HCOO)_3$ formate crystal agglomerates self-organized into the star-shaped micro-particles (see Figure 1A.). Only one type of morphology was observed in all of the investigated samples, as inspected by SEM and TEM microscopy. Self-organization phenomenon occurs frequently in nature and one of its most well-known illustration is process of snowflakes formation[42]. In the literature, many reports on the particle / crystallite organization of various types such as liquid crystals[43], nanoparticles[44] and biomaterials[45] might be found.

Heating formate particles at 400ºC induced oxidative thermolysis and formation of cerium oxide material with preserved star-shaped morphology and porous texture that is visible in the SEM image (Figure 1B). Thermogravimetric measurement presented in Figure 1C indicates that this temperature is optimal for material's synthesis, since complete combustion ends at 380ºC. As shown in Bokhonov et al.[46], the $Ce(HCOO)_3$ thermal decomposition process is strongly dependent on the heating atmosphere, since the decomposition temperature of the cerium formate changes from 300 to 400 °C for processes conducted at oxidative and inert atmosphere, respectively. Additionally, they postulated that the presence of oxygen in the gaseous atmosphere is crucial for obtaining ordered nanocrystalline CeO_2 from the $Ce(HCOO)_3$ precursor[46]. The mass difference (see Figure 1C)

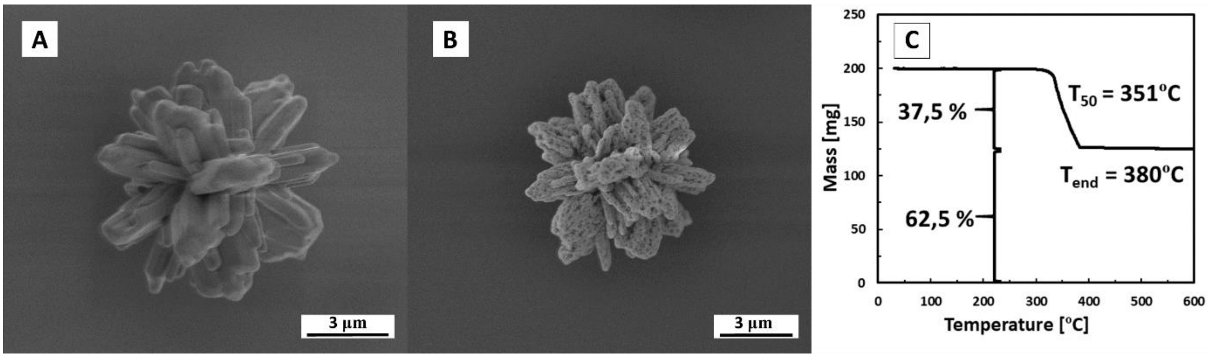

Fig 1. SEM images of star-shaped $Ce(HCOO)_3$ particles: A) before thermal treatment; B) after thermal treatment (CeO_2); C) Thermogravimetric curve of $Ce(HCOO)_3$ sample presenting mass loss ratio.

corresponds to the stoichiometric ratio between cerium formate and cerium oxide that confirms complete chemical change after thermal treatment.

Morphology of particles obtained in this study is significantly different from flower-, coral- and urchin- like ceria reported in the literature so far, inasmuch as the diameter of the arms[18,20,21,22,46] and mean particle size[22,23] are both larger in star-shaped particles (see Section III.B and III.D). It may be due to the use of different synthesis methods used in our and other works[18,22,46,47]. Such morphological differences may potentially be a source of differences in the physical properties of the above materials, such as mechanical strength. The correlation between morphology and physical properties of polymeric materials was discussed in the literature[48]. As has been concluded by Wei et al.[18] ceria hierarchical structures with thin arms suffer more damage during the decomposition process, hence larger arm thickness may increase durability of the material at higher temperatures of operation. Also, porosity of particles investigated here (see description of macroporosity in Section III.D) differs from previously reported star-shaped particles[26].

The distinctive feature of as synthesized ceria material is its three-level hierarchical organization that is presented in Figure 2. The first level is constituted by nano-sized oxide crystallites (Figure 2A) that are organized into a second-order structure of rods which are visible in TEM images as the arms of star-shaped particles (Figure 2B). The image shows the porous texture of the material while the inserted SAED pattern collected from the entire area of the image presented in Figure 2.B suggests preferential ordering of crystallites, as diffraction maxima are visible in the form of distinctive points instead of Laue circles. Third level comprises micro-particles with star-shaped morphology (figure 2C). The synthesis methods and some characteristic of the star-shaped porous particles build with the ceria nanoparticles has been presented previously in the literature[18,22,26,46]. However, the number of reports available is small and they are limited to the description of pure CeO_2 materials. Functionality and modification amenability of each of the as distinguished levels of hierarchy are presented in the following parts.

III.B. First level of structural hierarchy

The 1st level of hierarchical organization is comprised of nano-sized cerium oxide crystallites. This level was subjected to modification by incorporation of 10 mol% dopant into ceria matrix, leading to formation of series of $Ce_{0.9}REE_{0.1}O_{1.95}$ samples containing different rare earth metals (REE: Sc, Y, La, Pr, Nd, Sm, Eu, Gd, Tb, Dy, Ho, Er, Tm, Yb, Lu). In the literature, a lot of reports about the ceria based $Ce_{1-x}REE_xO_{2-x/2}$ mixed oxides (where REE: La[49,50], Nd[51,52], Sm[51,53], Eu[53,54], Gd[55,56], Tm[57], Yb[57,58] and Lu[58]) may be found. However, the most of the existing data are obtained for samples prepared by solid-state reaction between polycrystalline oxides at high temperatures in an oxidizing atmosphere. The phase composition of mixed oxides strongly depends on heating temperature and composition of the oxide (e.g. $Ce_{1-x}Yb_xO_{2-x/2}$)[51,53,55,59,60]. Different authors do not agree on the limits of RE-ions solubility in the ceria matrix[57,58,61,62]. However, various authors consent that for low levels of ceria matrix doping (as in our case ~10 mol%), the solid solutions $Ce_{1-x}RE_xO_{2-x/2}$ could be formed[51,53,55,58,59,60]. In this work, the gadolinium doped sample is used as a representative example to discuss as obtained results.

As shown in Figure 3.A., PXRD patterns confirm the formation of phase pure formate precursors, both in undoped and gadolinium doped materials, which proves well miscibility of dopant ions in the $Ce(HCOO)_3$ matrix. A literature review indicates that, in contrast to the mixed oxides, the data about mixed formates ($Ce_{1-x}RE_x(HCOO)_3$) has not been available before and it is a new and interesting topic. Diffraction maxima positions and their relative intensities correspond well with

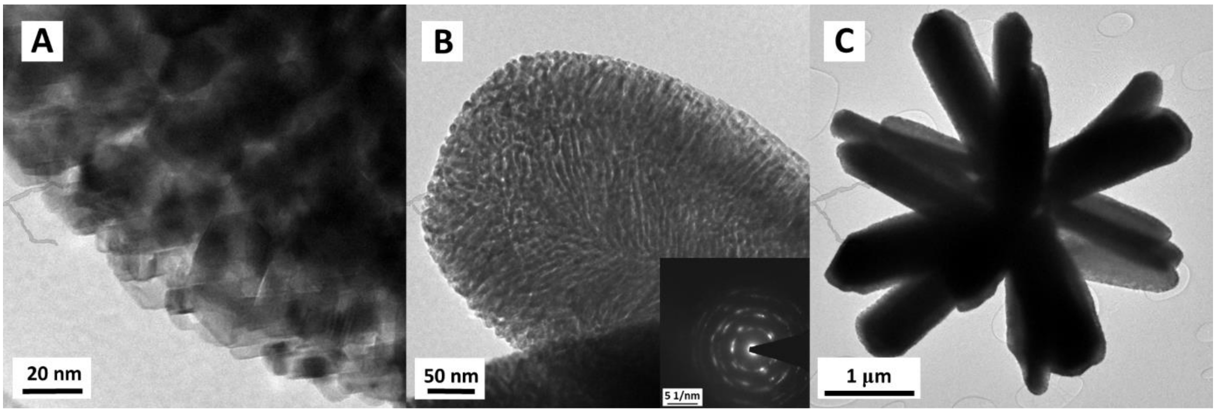

Fig 2. TEM images illustrating three-level hierarchical organization of $Ce_{0.9}REE_{0.1}O_{1.95}$ oxide material. A) 1st level: CeO_2 nanocrystallites; B) 2nd level: porous arm; an inlet presents SAED pattern collected from the whole area visible in the image; C) 3rd level: star-shaped micro-particle.

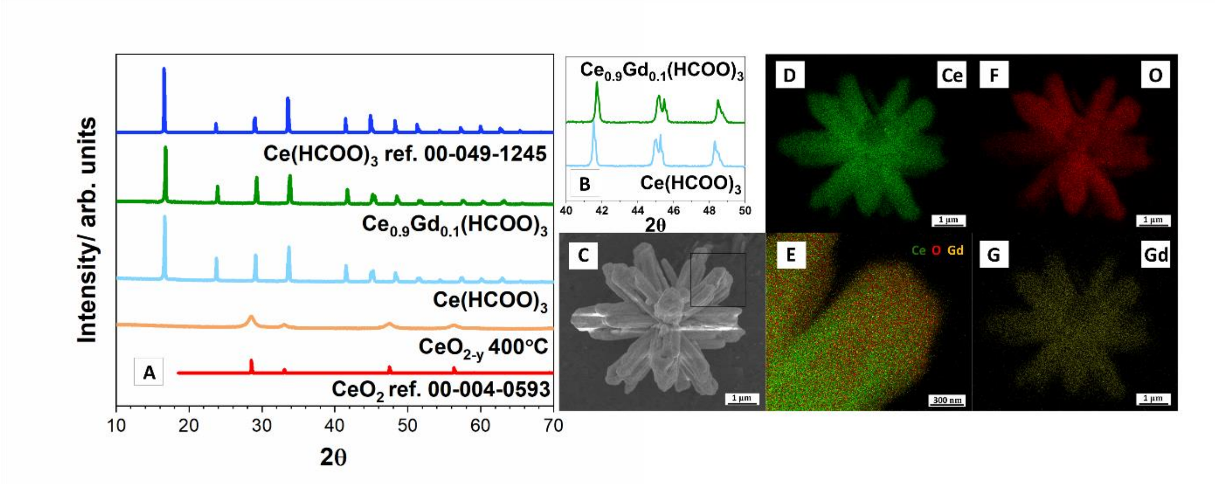

Fig. 3 A)-B) PXRD patterns of selected $Ce_{1-x}REE_x(HCOO)_3$ (x=0; 0.1) before and after thermal treatment; C) SEM image of porous $Ce_{0.9}Gd_{0.1}O_{1.95}$ micro-particle; D)-G) EDS mapping of $Ce_{0.9}Gd_{0.1}O_{1.95}$ star-shaped particle: D) cerium, E) elemental distribution on the particle arm (fragment marked on figure 3.C), F) oxygen, G) gadolinium.

cerium formate reference data (ICSD, ref. 00-049-1245). As Figure 3.B indicates, the presence of 10 mol% gadolinium dopant causes a shift of diffraction maxima into higher 2θ positions, which is in accordance with Vegard's law[63]. Since the incorporation of species with smaller ionic radius causes lattice constant decrease (R_{Ce3+}^{IX} = 0.1196 nm; R_{Gd3+}^{IX} = 0.1107 nm)[64], the proper trend reflecting Vegard's law is observed for all other rare earth doped samples with some divergence from linearity (see figure S1 in Supplementary Information). Also, PXRD data for temperature treated $Ce(HCOO)_3$ sample confirms the formation of pure CeO_2 oxide (ICSD, ref. 00-004-0593), what is in good agreement with the literature data[18,22,46].

PXRD patterns of all the rare-earth-doped formates as well as oxide samples confirm the full integration of dopants into formate crystal structure and fluorite lattice, respectively (Figure 4). Composition for almost all examined samples is close to the presumed theoretical value of 10 mol%, as EDS spectroscopy measurements indicate (see Table 1). The PXRD peaks shift is not observed only for Sc^{3+} ions that suggest its impaired incorporation into crystal lattice, which was confirmed by the SEM-EDX measurement. Out of all tested RE^{3+} dopants only this ion does not adopt coordination number IX that may explain miscibility decline, since this coordination is characteristic for Ce^{3+} in the formate structure (see $Ce(HCOO)_3$ structure visualization in Figure S2 in Supplementary Information). Additionally, as presented in Figure 3C-3F, the dopant ions are distributed evenly across all the volume of star-shaped micro-particle. For better illustration purposes the sample containing 50 mol% of gadolinium dopant was measured by the SEM-EDX-mapping.

As visible in Figure 4, location of 2θ diffraction maxima and their relative intensities follow the order of cerium formate reference data indicating homogenous growth of mixed rare-earth formate crystals in all the samples. Also, peak broadening observed in all $Ce_{0.9}REE_{0.1}O_{1.95}$ oxide samples indicates formation of small oxide crystals[65]. The mean size of $CeO_{2-\delta}$ nanocrystallites determined from PXRD data is 11.8 nm, and the size decrease for doped $Ce_{0.9}REE_{0.1}O_{1.95}$ nanocrystallites is observed that fall within the range from the lowest value of 6,3 nm for $Ce_{0.9}Lu_{0.1}O_{1.95}$ to highest value of 9.1 nm for $Ce_{0.9}Gd_{0.1}O_{1.95}$ (see Figure 5.A). Additives such as lanthanide RE^{3+} ions are

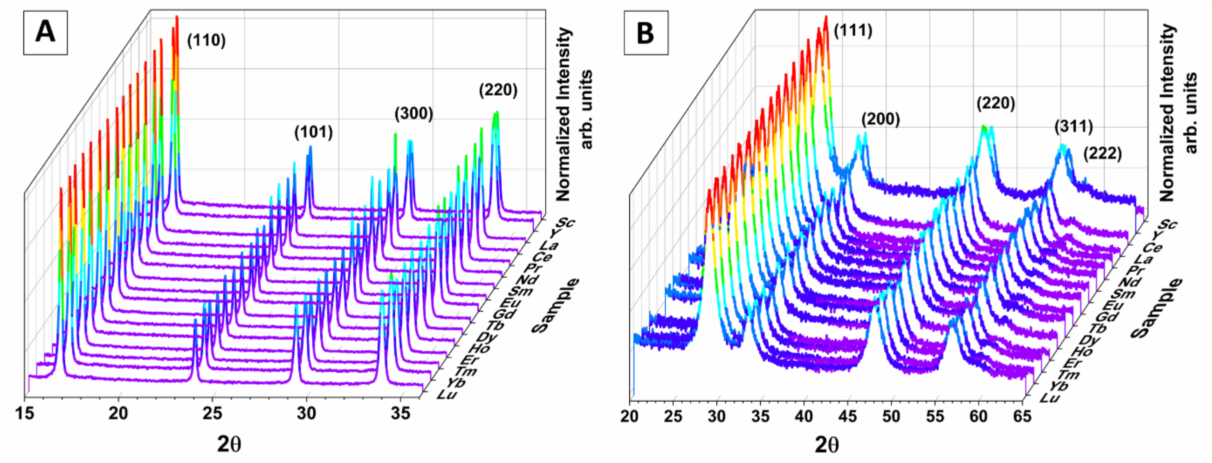

Fig 4. PXRD patterns of $Ce_{0.9}REE_{0.1}$ series : A) $Ce_{0.9}REE_{0.1}(HCOO)_3$ (formates); B) $Ce_{0.9}REE_{0.1}O_{0.95}$ (oxides).

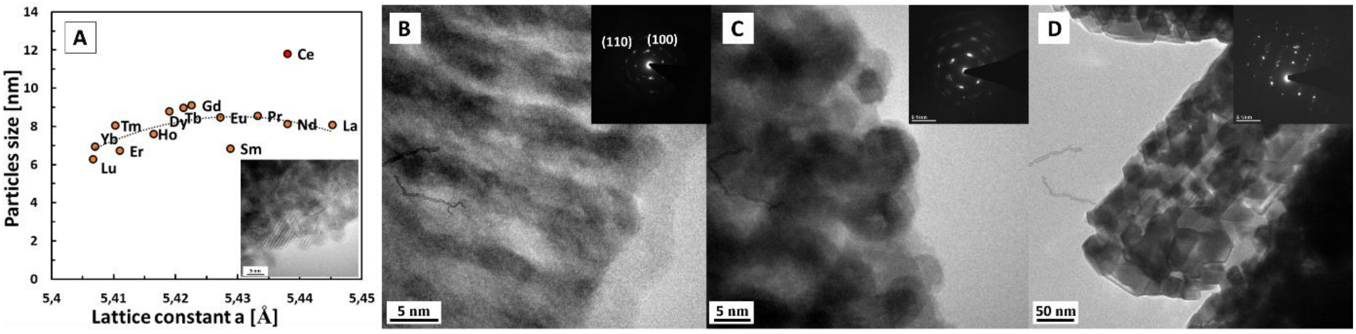

Fig 5.A) Mean size of $Ce_{0.9}Ln_{0.1}O_{1.95}$ nanocrystallites, in calculated for samples prepared by thermolysis at 400ºC, as a function of crystal lattice size (crystal sizes were determined by Scherrer formula; experimental lattice constants were determined by Rietveld refinement) *data for Sc and Y not included on graph. B)-D) HRTEM and TEM images of CeO_2 star-shaped particle heated at 400ºC, C) 550ºC and D) 900ºC.

known to hinder strongly crystallite growth of ceria during heating in an oxidizing atmosphere. This inhibiting effect is explained by additive segregation at the ceria grain boundaries[66]. On the other hand, this observation could be explained by creation of oxygen-ion vacancies through doping that causes contraction of lattice parameter in fluorite-type mixed oxides[67]. Moreover, as Rietveld refinement of PXRD data indicates, systematic lowering of lattice constant with dopant ionic radius decrease is observed (See Figure S3 in Supplementary Information), which reflects Kim's empirical relation[68]. While the calculated and empirical trends are similar in overall shape, the lattice parameter values are systematically larger for ceria materials studied here, which may be attributed to nano-size effect. Lattice expansion has been reported for many metal oxides, and while its origin is debated, it may be ascribed to negative surface stress[69]. The value of lattice expansion of +0,46% for CeO_2 nanoparticles observed here is similar to the literature value of +0.45% reported for particles with sizes 6-25 nm[70]. According to the literature, the influence of surface on pure CeO_2 structure is very strong for very small nanocrystals with mean size ~2 nm (where the ratio Ce^{3+}/Ce^{4+} is ~1), while for visibly larger ceria crystals (>15 nm), with the ratio Ce^{3+}/Ce^{4+} = ~0.01, it is practically negligible[71,72]. As Tsunekawa et al.[71] revealed, this effect is clearly visible in the ceria lattice parameter change, since for large crystals of CeO_2 $a_F = 0.5411$ nm, and a quick raise of this value was observed with nanocrystallites size decrease below 5 nm.

The high resolution TEM image of CeO_2 sample heated at 400ºC is presented in Figure 5.B. Nanocrystallites are arranged regularly, forming longitudinal structures and exposing mainly {100} and {110} crystal planes, which is partially agree with[73,74], as the authors postulated that small CeO_2 particles with the fluorite structure exhibit, most frequently, the truncated octahedral shape defined by eight {111} and six {100} facets. This incompatibility may be related to differences in crystal growth mechanism. Furthermore, {100} and {110} crystal facets are more reactive than {111} terminations due to their less energetic surface stability, hence the prospective boosted catalytic performance of this material is signalized[75]. Size of nanocrystallites that built star-like CeO_2 that was prepared by thermolysis conducted up to 550ºC is nearly the same (9.6 nm) as 400ºC-treated material. Interestingly, higher temperature treatment had induced crystal rearrangement possibly by facilitating the spreading of ceria species, as was previously reported in the case of hierarchically structured ceria multishell hollow spheres growth[76]. This effect is visible here as the change of particles morphology. As shown in Fig. 5C, they are getting more round. Thereinafter, preferential orientation is still observed as indicated by the inlet SAED pattern. However, the growth of nanocrystallites is observed when a material is subjected to temperature of 900ºC. The mean size of crystallites increases to 45.5 nm and ordering is lost, as indicated by SAED pattern that presents more randomly scattered diffraction maxima (Figure 5.B).

Table 1. Concentration of rare earth elements and oxygen vacancies in cerium matrix.

Rare earth element	EDS (% at)[a] formate	EDS (% at)[b] oxide	Oxygen vac. conc.[c]
Sc	2	1	0.08
Y	9	7	0.15
La	11	11	0.16
Ce	-	-	0.07
Pr	11	11	0.46
Nd	9	10	0.17
Sm	9	9	0.15
Eu	9	10	0.16
Gd	11	11	0.15
Tb	12	12	0.35
Dy	11	12	0.18
Ho	9	10	0.18
Er	11	11	0.16
Tm	10	11	0.18
Yb	10	11	0.16
Lu	8	8	0.15

[a]EDX global measurements of the pellet; [b]EDX local measurements of individual star-shaped microparticles. (see Fig. S7 in Supplementary Materials); [c]oxygen vacancy concentration determined from RAMAN spectra.

Introduction of dopants modifies material's oxygen vacancy concentration characteristic[36]. This value can be determined by the RAMAN spectra, on which one intense band at ~460 cm^{-1} and two weak bands at ~546 and 600 cm^{-1}are observed (Figure S4 in Supplementary Information). First of them is attributed to the vibrational mode (F2g) of F-type structure, but the other two can be assigned to oxygen vacancies introduced into the ceria matrix[77,78]. In Table 1, the oxygen vacancy concentrations calculated, as a ratio $I_{Ov(570)}/I_{F2g(460)}$ [77], for all investigated samples has been presented. As defined defect concentration for doped samples is two times higher than for undoped cerium oxide for almost all rear earth admixtures. Increased values for praseodymium and terbium doped ceria may be the method artefact due to radiation absorbtion, since only this samples are coloured (dark samples). Guo et al.[77] revealed that the Pr- or Tb-doped CeO_2 absorbed visible light strongly; thus, by the use of Raman spectroscopy with excitation wavelength applied only the outer surface information of the sample may be determined, what could be a consequence of the surface phase segregation on RE^{3+}-rich and Ce^{4+}-rich phases in the single crystals of the $Ce_{1-x}RE_xO_{2-x/2}$ [66]. Characteristic for fluorite structure F_{2g} mode visible in all Raman spectra undergoes shifts towards higher values with the increase of ionic radii (Figure S5 in Supplementary Information), which is in accordance with literature[79]. FTIR spectra of mixed rare earth cerium formats indicate no difference with industrially produced reference cerium formate material proving that solvothermal synthetic method enable to avoid nitrate deposition as it is a common problem known in the literature[40] (Figure S6 in Supplementary Information).

III.C. Second level of structural hierarchy

The 2nd level of hierarchical organization, designated here as arms of the star-shaped particles, is characterized by diversified microstructure, as determined by TEM and SEM microscopy. Release of CO_2 and H_2O during thermal decomposition of formate precursor is responsible for the formation of voids and channels, which is in accordance with porosity formation by heat treatment control reported in the literature[24]. The most prominent examples of porous structures formed are presented in Figure 6. Macropores are randomly distributed in the star-like $Ce_{0.9}Tb_{0.1}O_{1.95}$ particles with a mean size of 147 ± 90 nm (Figure 6.A), however, the observed dominant mean value of pore size across the RE-doped samples is ~60 nm. Close-up look at the macropore rifts and cavities is visible in $Ce_{0.9}Gd_{0.1}O_{1.95}$ arm in Figure 6.B. Analysis of $Ce_{0.9}Y_{0.1}O_{1.95}$ TEM images indicates that material is characterized by the occurrence of micro- to mesopores with 1.5-2.5 nm in size (Figure 6C). Presented, in this work, images are in agreement with data, which have been shown for pure ceria mesoporous materials[22,46] derived by the thermal decomposition of the $Ce(HCOO)_3$.

For comparative purposes three types of samples treated with two temperature conditions of 550ºC and 900ºC were tested: undoped star-shaped particles (**CeO_2_Star**, heated at 550ºC and 900ºC), gadolinium doped star-shaped particles, (**$Ce_{0.9}Gd_{0.1}O_{1.95}$_Star**, heated at 550ºC) as well as microemulsion-derived nanoparticles (**CeO_2_NPs**, heated at 550ºC and 900ºC). Details of precipitation in microemulsion (water-in-oil, W/O) technique were described in our previous paper[41]. TEM images for corresponding samples (Figure S8 in Supplementary Information) show that microemulsion-derived nanoparticles, with the mean size of 6.4 nm determined from PXRD data, tend to agglomerate into bigger structures comparable to the size of star-shaped particle arms. In our previous papers[36,58], thorough characteristic for the nanocrystalline $Ce_{1-x}Yb_xO_{2-x/2}$ (x = 0 - 1) treated at elevated temperatures and under various atmospheres has been carried out.

S_{BET} surface area determined from N_2 adsorption curves (Table 2) is of the value of 103 m^2/g for CeO_2_Star_550ºC and gives evidence for porosity presumed by TEM and SEM images observation. This value is slightly higher than the one of 79 m^2/g determined for CeO_x_NPs_550ºC. This gives an evidence that ordering of nanocrystallites into second-order porous structure in star-shaped particles is superior over the unstructured organization of nanoparticles in microemulsion-derived sample The values of S_{BET} greatly exceed the one obtained for bulk ceria reported in the literature (8.5 m^2/g)[80]. Nitrogen

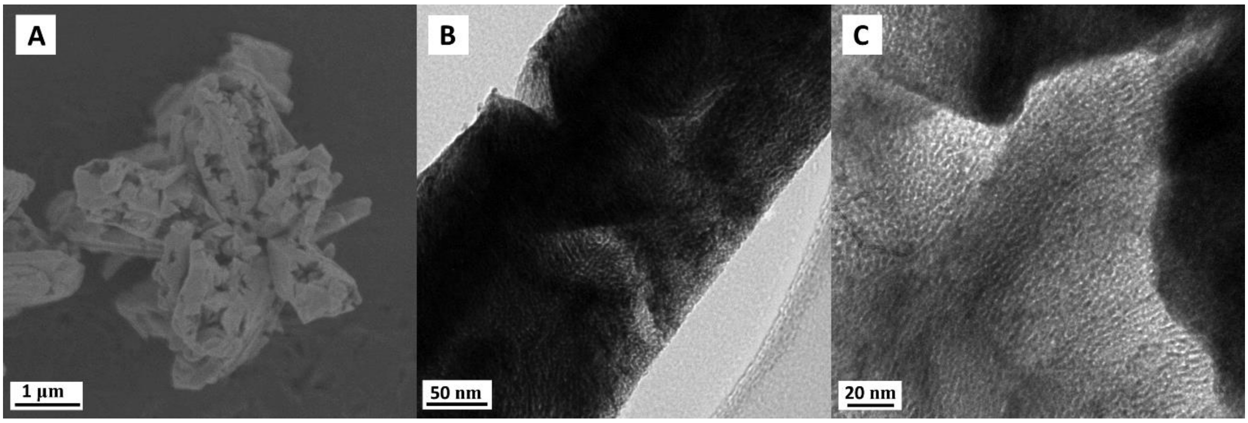

Fig 6. Porous structures unveiled by TEM and SEM imaging: A) macropores randomly distributed in $Ce_{0.9}Tb_{0.1}O_{1.95}$, B) macropores in $Ce_{0.9}Gd_{0.1}O_{1.95}$ arm, C) micro- to mesopores of $Ce_{0.9}Y_{0.1}O_{1.95}$.

adsorption/desorption isotherm of the $Ce_{0.89}Pd_{0.11}O_{2-y}$ sample prepared by microemulsion technique (heated in oxygen flow at 500ºC) was previously presented by Kurnatowska et al.[81]. The value of S_{BET} for above material was 110 m^2/g what is in quite good agreement with our data. The difference is due to the presence of Pd-ions and consequently, smaller than in our case, mean crystallite size (5 nm) calculated for $Ce_{0.89}Pd_{0.11}O_{2-y}$ sample. Data that have been presented here for CeO_2_Star_550ºC are consistent with those obtained for hierarchically structured ceria reported in previous literature works ranging from 57.13 m^2/g for globin-like microspheres[17] to 171.6 m^2/g for spindle-like microparticles[24]. Introduction of 10 mol% Gd^{3+} dopant into the ceria matrix caused an increase of surface area from 103 m^2/g to the value of 146 m^2/g, contrarily to previous report by Xiao et al.[29] in which 10 mol% of La^{3+}, Pr^{3+}, Y^{3+}, Zr^{4+} and Sn^{4+} caused decrease in S_{BET} calculated for the flower-like ceria particles. On the other hand, the RE^{3+} additives (such as La^{3+}, Pr^{3+}, Tb^{3+} and Lu^{3+}) are known to hinder strongly crystallite growth of $Ce_{1-x}REE_xO_{2-x/2}$ oxides during heating in oxidizing atmospheres[40,66,82]. This effect allows to explain the specific surface area increase for $Ce_{0.9}Gd_{0.1}O_{1.95}$_Star_550ºC sample in comparison to CeO_2_Star_550ºC one. The ease of rare-earth ion incorporation along with their good miscibility with cerium formate matrix opens the possibility for testing the influence of dopant on surface availability and engineering materials with increased surface area.

However, the surface area of star-shaped and microemulsion-derived cerium material is lost under temperature treatment at 900 ºC giving the value of one order of magnitude lower than samples heated at 550 ºC, namely 13 m^2/g and 5 m^2/g for CeO_2_Star_900ºC and CeO_2_NPs_900ºC respectively. In spite of surface area decrease, star-shaped particles still possess BET surface area more than two times higher which proves material's endurance and sintering resistance. Probably the basis of this effect is the preferential mutual arrangement of ceria nanocrystals in the star-like particle.

To compare reduction characteristics of five as chosen samples, H_2-TPR measurements were performed. Figure 7 presents H_2 reduction profiles of star-shaped and nanocrystalline particles. Surface reduction at lower temperature range (<625 ºC) and bulk reduction at higher temperatures (> 625 ºC) has been observed, which stays in line with previous literature reports[83,84,85]. Maximum of surface reduction occurs at the temperature of 515ºC for non-doped and gadolinium doped samples, however, the process of H_2 conversion in CeO_2_Star_550ºC sample starts earlier as suggested by additional profile hump at ~400ºC. The presence of two low temperature peaks has been observed

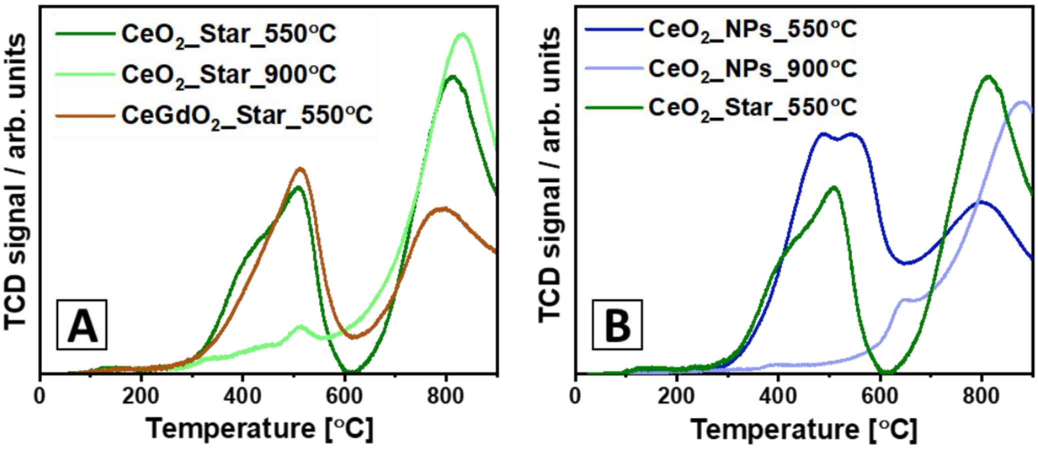

Fig 7. The H_2-TPR profile for the samples with different organization of building units. A) Nanoparticles organized into hierarchically structured star-shaped material (CeO_2_Star, $CeGdO_2$_Star), B) non-organized nanoparticles (CeO2/NPs).

Table 2. BET surface area determined by N_2 adsorption; material's reduction properties determined by H_2-TPR (see description in the text);

Sample	CeO_2_Star	$CeGdO_2$_Star	CeO_2_NPs	CeO_2_Star	CeO_2_NPs
Heating temperature [ºC]	550	550	550	900	900
BET [m^2/g]	103	147	79	13	5
H_2 consumption [mmol/g]	1.09	0.91	1.24	0.94	0.66
Surface H_2 consumption [%]	38.4	49.4	54.8	11.4	5.4
Bulk H_2 consumption [%]	61.6	50.6	45.2	88.6	95,6

by many authors[84,85,86]. This effect, observed also by us for high area pure ceria sample, is most probably due to reduction of surface and sub-surface Ce^{4+} ions, though some contribution from surface carbonates cannot be excluded[86]. On the other hand, Wu et al.[85] postulated that the first surface reduction peak could be assigned to the surface hydroxylation and initial reduction of CeO_2. Also, adsorbed oxygen species may be reduced firstly followed by reduction of oxygen from the surface outermost layer[85]. Moreover, comparison of these two specimens shows the increase of the value of surface to bulk reduction ratio for Gd-doped particles (see Table 2). Surface activation by increasing dynamic oxygen exchange capacity through doping may be responsible for this observation[87]. Concurrently, the maximum amount of oxygen extractable from the sample, indicated by overall H_2 consumption, is lowered for Gd-doped sample, which stays in accordance with Henning's report[87] on bulk reduction suppression in mixed metal $Ce_{1-x}Gd_xO_{2-\delta}$ oxide. This is caused by vacancy stabilization that is connected with, both decrease in Ce^{4+}/Ce^{3+} conversion capability as well as replacement of Ce^{4+} ions by non-reducible Gd^{3+} ions[29,87].

High temperature treatment at 900ºC causes dramatic decrease of hydrogen consumption in the low temperature region of the H_2-TPR profile measured for the star-shaped particles, as suggested by 11.4%/88.6% surface to bulk ratio value. Additionally, in the literature, a linear correlation has been observed between the surface area and the hydrogen consumption at the low temperature region[88,89]. Nevertheless, surface reduction is still more efficient in CeO_2_Star_900ºC than in CeO_2_NPs_900ºC, as indicated by 5.4%/95.6% surface to bulk reduction proportion.

Similar division into the surface and bulk reduction was observed in microemulsion-derived sample, however, after 900ºC temperature treatment the surface reduction and the bulk reduction shift into higher temperatures (Figure 7.B). This indicates lower temperature stability of microemulsion-derived particles, and the lack of such property in star-shaped counterpart samples shows its greater persistence and suggest longer durability. The CeO_2_NPs_550ºC particles showed the highest H_2 consumption value per gram among the tested samples. However, the temperature treatment causes a large change of relative H_2 consumption in microemulsion-derived particles (-47%) as opposed to star-shaped particles (-12%), which also confirms greater stability of pores in hierarchically structured ceria material. Similar result was observed by Terribile et al.[90] for the ceria samples prepared by use of surfactant-assisted route (porous sample) and by conventional precipitation method (powder sample).

All in all, gadolinium-doped star-shaped cerium particles have the lowest H_2 consumption value among the 550ºC heated samples, while at the same time possess the highest BET surface area, as N_2 adsorption study suggest. To explain this discrepancy, namely the large adsorption surface and actually low active surface at once, the doping effect that influences nanocrystallites structure and morphology should be taken into account. While crystallites size depletion and simultaneous retention of secondary porous architecture may be associated with the increase of available surface, the creation of stable oxygen vacancies through doping, on the other hand, may lower the amount of accessible oxygen that is being consumed (by lowering Ce^{4+} ions amount). Simultaneously, however, the rate of oxygen consumption is retained due to more feasible oxygen migration in the material. Our results of H_2 uptake in the H_2-TPR process are presented in Table 2 as the quantity of mmol of hydrogen consumed per 1 g of sample (CeO_2 or $Ce_{0.9}Gd_{0.1}O_{1.95}$). Comparison of H_2 uptake values calculated per 1 mol of the Ce-ions for both samples, the values for CeO_2_star_550ºC and $Ce_{0.9}Gd_{0.1}O_{1.95}$_Star_550ºC becomes almost equal. Thus, $Ce_{0.9}Gd_{0.1}O_{1.95}$_Star_550ºC material microstructural characteristics may improve its catalytic performance due to facilitated redox kinetics, as it is suggested in the literature[87,91,92] (this will be demonstrated in the CO oxidation study presented in the part III.E.1).

III. D. Third level of structural hierarchy

The 3rd level of hierarchical organization constitutes the morphology of micro-particles themselves, and in $Ce_{0.9}REE_{0.1}(HCOO)_3$ specimens, it is determined to be the self-assembly of formate crystallites into star-shaped entities. It is suggested that the water present in synthesis may be the main driving force of crystals assemblage[18] In all of the REE doped samples star-shaped microparticles were formed. However, there is some diverseness in morphology, with the largest differences in micro-particle sizes as well as arm thickness. The thickness of the arms falls into the scope from 50 nm to 1 µm as indicated by TEM and SEM image analysis.

The presence of two types of star-shaped morphology is observed in all of the synthesized samples, namely particles with thick and rank arms, as presented on an insert in Figure 8.A ($Ce_{0.9}Yb_{0.1}(HCOO)_3$ case) as well as star-shaped particles with thinner arms with more space between them, as it is visible on the insert in Figure 8.B ($Ce_{0.9}Dy_{0.1}O_{1.95}$ case). All samples contained mixture of this two morphologies, but nevertheless the dominance of stars with thick arms was observed for Ce, La, Pr, Nd and Yb containing samples. As suggested in the literature, the growth of formate crystals occurs along [001] direction[46]. The comparison of the PXRD, SEM and TEM data with those available in the literature for cerium formate[46] shows a strong agreement between our results and the literature data.

The number of arms in the star-shaped particle across all tested samples is varied from a low number (Figure 2.C.), through moderate amount (Figure 9.A), to arm plentifulness, as presented in Fig 9.B. Regardless of the number of arms and the type of RE dopant, the distribution of pores in most samples is similar (with the mean macropore size of ~60 nm), as illustrated on Figures 9.A and 9.B. All of the RE doped samples have porous texture and are characterized by three-level architecture (see TEM and SEM images in Figure S9 in Supplementary Information). Macropores in the form of cracks on the arms are visible in all of the synthesized materials. Only for Sc-, Lu-doped

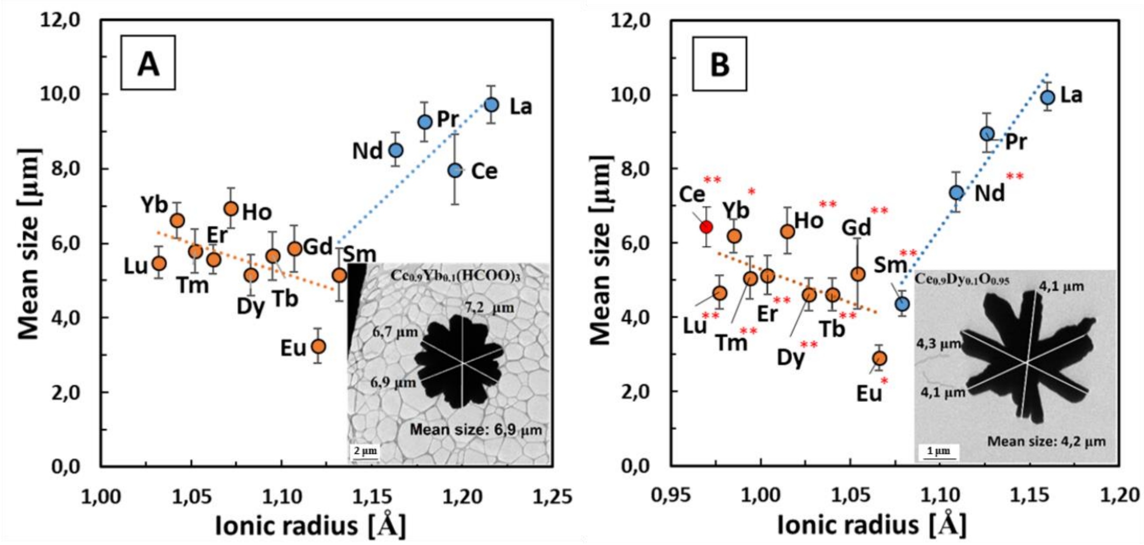

Fig. 8. Mean size of star-like particles as a function of ionic radius of dopant: A) formate samples before calcination; inlet TEM image of $Ce_{0.9}Yb_{0.1}(HCOO)_3$; B) oxides after calcination; inlet TEM image of $Ce_{0.9}Dy_{0.1}O_{1.95}$; Sc. and Y dopants not included on graphs; * $p<0.05$, ** $p<0.001$ (t-student independent samples test)

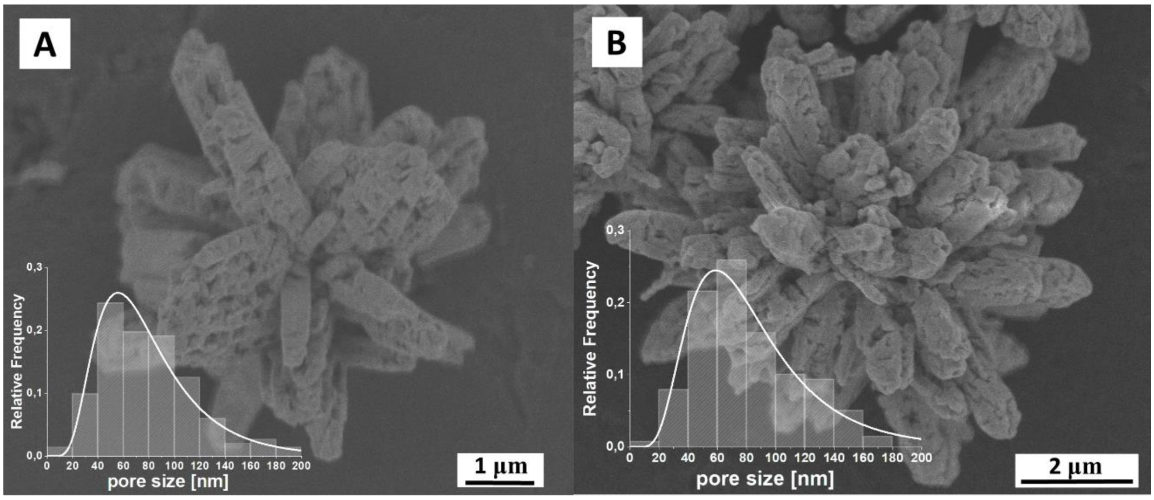

Fig. 9. SEM images with the macropore size distribution (from SEM images analysis) in: A) $Ce_{0.9}Gd_{0.1}O_{1.95}$; B) $Ce_{0.9}Er_{0.1}O_{1.95}$.

specimens star-shaped particles with very thick and short arms similar with their morphology to the ball were observed. Also, Eu-doped sample contained some degree of not fully developed stars with the lowered number of arms (as confirmed by deviation of mean size from the average cluster of size distribution of REE doped formate particles visible in Figure 8.A and 8.B). Ceria-based nanomaterials with 3D architectures may be much more interesting than nanopowders alone. In the literature, many reports about the potential applications of nanomaterials with spatial structures may be found[93,94,95,96,97], which makes our materials very interesting.

The sizes of micro-particles were determined by TEM images analysis followed by statistical averaging of obtained data. Three measurements along the arms of individual particle were performed as indicated on inlets in Figure 8 A. and 8.B, thus star-shaped morphology has been approximated by a sphere model with a length of two arms designating diameter of the sphere. This approach is in line with literature data given by Matyi et al.[65]. Mean sizes of $(Ce_{1-x}Ln_x)$-formate particles range from 3.2 ± 0.5 µm for $Ce_{0.9}Eu_{0.1}(HCOO)_3$ to 9.7 ± 0.5 µm for $Ce_{0.9}La_{0.1}(HCOO)_3$. Two trends in microparticle diameter changes are observed, this is the size decrease with the ionic radius decrease for light lanthanide doped formates (La, Ce, Pr, Nd) and very slight (almost negligible in comparison to light lanthanides) size increase with the ionic radius decrease for heavier lanthanide doped formates (from Sm to Lu; Figure 8.A). The dependence of lanthanide ionic radii ($R_{RE3+}{}^{IX}$) on atomic mass presents a similar relationship. Interestingly, the V-shape trend of micro-particle sizes at the third level of hierarchy is reversed in comparison to U-inverted trend of nanocrystallite sizes at the first mixed oxide's (excluding pure ceria) organizational tier (see Figure 5A). This may be due to difference in crystal structures of $Ce(HCOO)_3$ and CeO_2 [46,98] and the associated differences in the ability to incorporate dopant ions into the crystal lattice.

The same V-shape trend of lanthanide-doped micro-particle size changes are preserved for samples that had underwent oxidative thermolysis, as Figure 8.B indicates, thus confirming the validity of the applied statistical approach and reality of the effect. Independent samples t-student test has demonstrated that there is statistically significant decrease in size for samples after thermal treatment at $p<0.001$. While the mean particle size decrease for doped samples is 0,58 µm, the decrease of undoped cerium oxide is almost tripled (1,53 µm). This could be explained by lattice shrinkage due to conversion of Ce^{3+}(IX) ions ($R_{Ce3+}{}^{IX}$ = 0.1196 nm) in the cerium fromate matrix into Ce^{4+} (VIII) ions ($R_{Ce4+}{}^{VIII}$= 0.0970 nm) in the cerium oxide structure[64]. Moreover, d-block elements that are not presented in the Figure 8, namely Sc-doped (before: 5.1 ± 0.4 µm; after: 4.7 ± 0.5µm) and Y-doped ((before: 4.6 ± 0.5 µm; after: 3.8 ± 0.2µm) samples also undergo size decrease after thermal treatment as observed in lanthanide series.

In the following part, the relevance of the specific ordering of the material at the 2º and the 3º level of material's structural hierarchy in the chemical catalytic performance will be demonstrated in the CO oxidation and soot combustion processes.

III.E.1. Materials functionality: CO oxidation

In order to determine the role of the organization of nanoparticles at the second level of material's structural hierarchy, star-shaped $Ce_{1-x}Gd_xO_{1.95}$ (x=0; 0.1) particles (material with organized building units) and microemulsion-derived CeO_2 nanoparticles (material with non-organized building units) were subjected to catalytic tests for investigation of their activity in the CO oxidation process. For comparative purposes samples were heated at 550ºC and 900ºC. The temperature of 550 ºC is optimal for removal of post-synthetic nitrate residues from microemulsion-derived nanoparticles, as it is known in the literature for being catalytic modifier[40]. However, as suggested by FTIR spectra (Fig S6 in Supplementary Information), formate particles are devoid of nitrate residues, which proves the advantage of such method of synthetic derivation of cerium material. Caria materials derived at 550ºC contain slightly smaller nanocrystallites (9.6 nm for CeO_2) and (8.2 nm for $Ce_{0.9}Gd_{0.1}O_{1.95}$) than 400ºC heated samples (see. Figure 5A), nevertheless the size depletion through doping is still observed in samples heated in higher temperature. Similar nanocrystallite sizes of microemulsion-derived CeO_2 particles (6.4 nm) allowed for making comparisons of the materials used, so that the variable of particle size at the first hierarchy level was controlled.

As presented in Figure 10, the temperature of 10% CO conversion ($T_{10\%}$) for hierarchically organized star-shaped CeO_2 particles (CeO_2_Star_550ºC) reaches 275ºC, and is nearly 100ºC lower than for loosely scattered microemulsion-derived counterparts (CeO_2_NPs_550ºC). Also, the degree of conversion at 400ºC is higher for star shaped particles than for microemulsion-derived ones, reaching the value of 89% and 25%, respectively. This results indicate the superiority of 2º level ordering of nanocrystallites over unstructured organization of particles. It is in good agreement with[99,100], where the key role of the morphology and porosity of the ceria catalysts for activity of CeO_2 materials in the CO oxidation process has been presented.

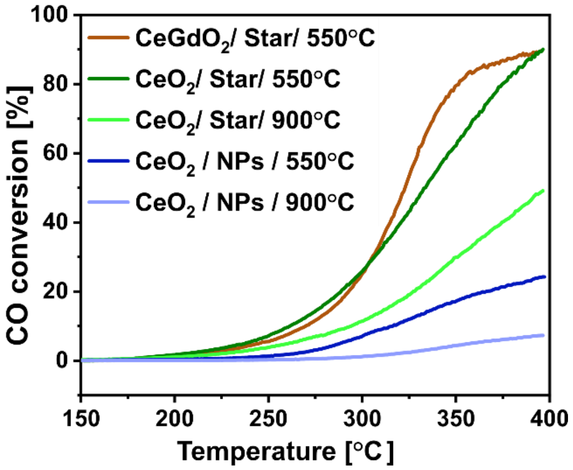

Fig. 10. CO-oxidation activity of samples differed by pre-treatment temperature (550ºC vs 900ºC) and organization of building units: nanoparticles organized into hierarchically structured star-shaped material (CeO_2/Star, $Ce_{0.9}Gd_{0.1}O_{1.95}$/Star) vs non-organized nanoparticles (CeO2/NPs).

Differences in the ordering of building units in tested materials are confirmed by the collected TEM and SAED images (Figure S8), as electron diffraction in the form of slightly scattered but distinct points shows regularity for star-shaped sample (CeO_2_Star_550ºC,) in opposition to randomly distributed concentric diffraction maxima for the microemulsion-derived nanoparticles sample (CeO_2_NPs_550ºC). In our previous papers[101,102,103] the SAED patterns and FFT images indicated almost the same orientation of the $Ce_{1-x}REE_xO_{2-x/2}$ octahedral crystals, agglomerated into larger entities, for individual mixed oxide particles. Additionally, the preferential orientation of crystals in different systems was observed before by many authors[41,73,74,104]. Generally, since the catalytic action takes place at the material's surface, the increased accessibility of active sites due to ordered alignment of nanoparticles enables easier mass exchange. Contrarily, the lack of such ordering may result in the blockage of active sites, thus the potential of nano-dimensionality of particles is not fully utilized[105]. It is worth to mention that the temperature of CO oxidation ($T_{50\%}$= 330ºC) for CeO_2_Star_550ºC sample is lower than for urchin-like (~400ºC) and coral-like (~375ºC) hierarchically structured particles reported in the literature under similar reactant feed conditions[18]. Many previous studies had reported significant reduction of CO oxidation temperature when hierarchically organized material had been compared to bulk or commercial ceria (see table S1 in Support Materials as a brief literature review). Due to different catalytic reaction conditions, $T_{50\%}$ temperatures of the CO oxidation range from 162ºC to 400ºC, which makes them good middle-temperature catalysts[16,17,18,20,21,22,23,24,29,80,19]. However, in this report, detailed structural and morphological characterization of the materials indicates the strong link between nanoparticles organization and their chemical performance. We postulate that the ordering of material at the 2nd organizational tier proves superiority of hierarchical organization over unstructured arrangement of nanoparticles.

Moreover, the presence of gadolinium dopant modifies the CO conversion rate, as the conversion curve take more definite S-shape, while keeping the temperature of conversion similar to undoped star-shaped particles ($T_{50\%}$= 320ºC-330ºC). Intensified redox kinetics at the surface may be responsible for faster CO conversion, as suggested by the H_2-TPR study. Despite the fact that conversion rate above 400ºC is similar for undoped and Gd-doped hierarchically structured ceria, the modified redox kinetics may play significant role in CO oxidation by metallic NPs decorated composite ceria material, since the nature of catalyst active centres is modified by the presence of REE. Mandal et al. revealed improved catalytic activity of Au/Sm-CeO_2 over undoped system, which was attributed to easy surface redox functionality[106]. Moreover, Eu^{3+} doping of cerium oxide prevents sintering and redispersion of Au nanoparticles on the media surface, which in turn play a key-role in low temperature reducibility of Au/$Ce_{1-x}Eu_xO_{2-x/2}$ system, due to active Ce-O-Au sites[107]. In agreement with our results, Polychronopoulou et al.[108] revealed that the $Ce_{0.8}Sm_{0.2}O_{2-x/2}$ catalyst brings the beneficent combination of high activity and thermal stability in comparison to pure ceria. Contrary to previous report of Xiao et al.[29] in which La^{3+} and Y^{3+} ions impaired CO oxidation performance, and catalytic enhancement had been attributed to a mixed valence of dopants like Pr^{3+}/Pr^{4+}, this study shows that the presence of non-mixed valence gadolinium ions in hierarchically structured ceria material retain or even slightly facilitate CO oxidation. Additionally, in[29] as contrasted to our results, the BET surface area had almost the same value while the $T_{50\%}$ of CO oxidation was diversified for rare-earth doped ceria, therefore the differences in BET specific surface seem to be not conclusive in explaining the results. Instead, it is postulated here that exposure of nanocrystallites surface (and the associated number of active sites) due to the arrangement at the second hierarchy level may be responsible for good CO oxidation performance in mixed cerium gadolinium hierarchically structured material. This stays in accordance with microemulsion-derived NPs versus star-shaped particles comparison conclusions.

The temperature of 900ºC is known for being sufficient for ceria sintering, which TEM images in Figure S8 confirm, and CO conversion strongly decreases for microemulsion-derived sample (10% conversion in 400ºC for CeO_2_NPs_900ºC in contrast to 25% conversion at 400ºC for NPs sample treated at 550º). However, star-shaped CeO_2 particles prove to be more resistant for high temperature treatment, since the 25% CO conversion for CeO_2_Star_900ºC occurs at ~340ºC and have increased efficiency at higher temperatures therewithal. As visible in Figure S8, the temperature of 900ºC causes growth of nanoparticles in the CeO_2_Star_900ºC sample into monocrystalline individuals of the mean size of 44.4 nm, as determined from PXRD data, and some loss of regular ordering is observed (see a SAED pattern in Figure S8). Particles in CeO_2_NPs_900ºC sample appear as separated, sometimes conjoined, single crystals (Figure S8.E) with similar mean size of 45.6 nm. Nevertheless, 900ºC temperature treated star-shaped particles still show the presence of residual inner surface, as a BET value of 13 m^2/g indicates (in contrast to 5 m^2/g for powder sample), which may link to its increased catalytic performance. Moreover, Xiao et al.[29] show the effect of hindrance of grain growth in Ln, Pr, Sn, Y and Zr doped flower-like ceria. In higher temperatures of operation sintering resistance may influence the stability of ceria-based material hierarchical structure, which is the promising topic for further investigation.

Hierarchically structured particles presented in this study possess a high surface area, so metal nanoparticles deposition is suggested to further improve the material and explore its utilization in catalytic applications. Our materials may be very interesting, in the discipline of heterogeneous catalysis, as prospective catalysts for environmental applications. The literature provides examples of Cu, Co, Ni, Mn, Fe, Pd, Au deposition of ceria support for CO oxidation[109,110,111] and Rh, Pd, Pt, Ag for soot combustion[112,113].

III.E.2. Materials functionality: soot combustion

CeO_2 star-shaped as well as microemulsion-derived particles were tested as catalysts in the soot combustion process. All of the tested samples were prepared in the same way, as color change into uniform gray tone suggested the well mixing of materials. Star-shaped CeO_2 particle images before mixing with soot and after soot grinding are presented in FigureS10.A. and S10.B-C. respectively. Soot-catalyst contact is one of the most important parameter influencing heterogeneously catalyzed processes[27,114], so increasing its degree improves material's catalytic performance. As visible on Figure S10.C soot particles tend to deposit evenly on arms of star-shaped ceria.

As thermogravimetric curves presented in Figure 11 show, star-shaped CeO_2 particles initiate the soot combustion process at significantly lower temperature, reaching the half-maximum combustion at 443ºC, which is ~100 ºC lower than microemulsion-derived nanoparticles (536ºC). The $T_{50\%}$ temperature of soot combustion catalyzed by nanocrystalline ceria (NPs) is similar to the one previously reported in the literature (507 ºC) for particles prepared by the same method[40]. The small but noticeable difference of ~30ºC in NPs case may be ascribed to surfactants deposited on the material after synthesis (see FT-IR spectra in Fig. S11 in Supplementary

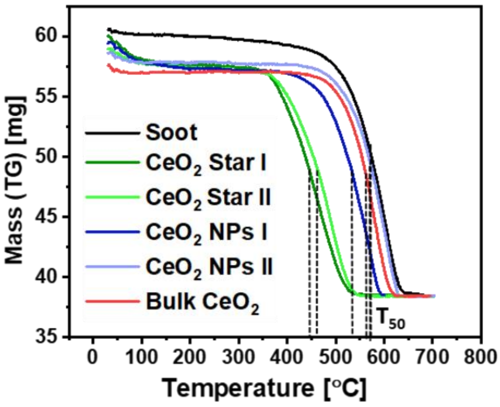

Fig 11. TG curves for soot oxidation by air catalyzed by samples differed by organization of building units: nanoparticles organized into hierarchically structured star-shaped material (CeO_2_Star) vs non-organized nanoparticles (CeO2_NPs). Two cycles of soot combustion – I (first run); II (second run).

Information). Interestingly, T_{50} for CeO_2 star-shaped particles got close to the one for modified ceria $Pt/Ce_{0.6}Zr_{0.4}O$ (T_{50}= ~430ºC) material, that had been tested in reaction conditions facilitated by NO flow[115]. It is worth mentioning that platinum-based catalysts are among the most active in the soot combustion process[116,117].

A second cycle of soot combustion reveals that whereas star-shaped particles change their temperature of half-maximum combustion slightly from 443ºC to 470ºC, there is a large temperature change up to 578ºC for microemulsion-derived sample. This value actually equalizes with the temperature of half-maximum soot combustion of CeO_2 bulk material (577ºC). This proves the superiority of star-shaped material in soot combustion as well as its greater stability. To confirm that, five cycles of soot combustion measurements had been performed (Fig S12 in Supplementary Information). The tests proved the greater stability of hierarchically structured material over microemulsion-derived particles, since the temperature of soot combustion for star-shape particles was always significantly lower than nanopowdered material (see Figure S12). Gradual decline of T_{50} temperature may be attributed to morphological changes of nanoparticles due to ageing, as {100} and {110} planes convert to truncated octahedral nanoparticles exposing {100}, {110} and {111} facets[25]. However, at the 5th cycle of combustion loss of star-shaped particles hierarchical structure was observed (see Figure S13) and the $T_{50\%}$ shifted to 554ºC. Multiple grinding of the material in the “tight contact” mode sample preparation may have caused the disintegration of hierarchical structure which explain the abrupt decline of temperature. The similar effect of difference in reactivity depending on materials morphology was observed by Ying et al.[118] for Au/CeO_2 systems , where the gold catalysts supported on the mesoporous CeO_2 (MCM-48 hard-template synthesis method) exhibited high catalytic activity and stability in benzene oxidation in comparison to the Au decorated nanocrystalline ceria powder.

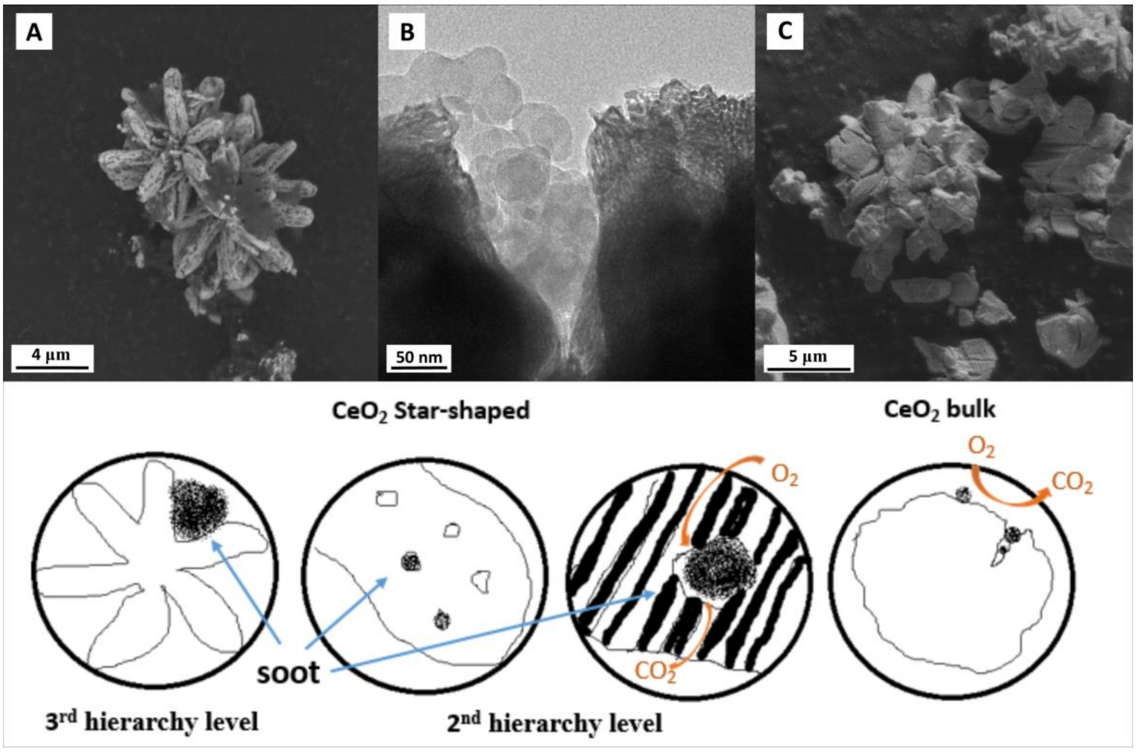

Fig. 12. SEM and TEM images of A) Soot particles deposited on the star-shaped porous CeO_2 star-shaped particles B) Soot particles C) Bulk CeO_2 D) Model of soot combustion.

To explain above results, that are also in accordance to finding of Micelli et al.[26], key-lock catalyst concept was applied[119], taking into account the results of detailed characterization of second and third structural hierarchy levels presented in this report, which extends previous findings. The effuse three-dimensional morphology of star-shaped particles facilitates deposition of large soot particles that are anchoring between the arms (Figure 12.A).Collaterally, the presence of enlarged size macropores in the form of cavities and cracks enable to embed smaller size soot particles into them. Zhang at al.[120] demonstrated that increased soot-ceria contact in 3DOM $Ce_{1-x}Zr_xO_2$ materials facilitated soot combustion, what is in good correlation to our observations. As Figure 12.B presents, large chunks of bulk soot are composed of nanoparticles with sizes of 20-50 nm that may easily fit in into enlarged macropores. As known, the particulate matter that comes from incomplete fuel oxidation in Diesel engines consists of mainly carbonaceous particles with sizes ranging from a few nanometers to hundreds of nanometers[121], which makes our materials interesting for engineering (catalysts in the diesel particulate filters) Figure 12.A shows a porous star-shape CeO_2 particle surrounded by such soot agglomerates, where the soot-ceria media contact is extended

From the other hand, the presence of mesopores, as indicated in N_2 adsorption measurements and electron microscopy studies, facilitates supply of oxygen and diffusion of gaseous products, and thus more efficient combustion of soot particles is observed. On the contrary, whereas CeO_2 bulk material possess cracks-containing coarse surface, as depicted in Figure 12C, and soot anchoring is not excluded, the lack of mesoporosity at the second level of structural hierarchy may be responsible for reduced efficiency of the combustion process by limited oxygen flow. An alternative explanation of the soot combustion enhancement, namely the differences in BET surface areas between star-shaped particles (S_{BET}= 103 m^2/g) and microemulsion-derived ones (S_{BET}= 79 m^2/g) , is challenged by[27], since the variation in soot oxidation reactivity seems to be not relevant for large (> 25 m^2/g) surface ceria catalysts.

Schematic representation of the key-lock catalyst concept adopted to star-shaped ceria catalyst is presented in Figure 12.D. Despite the fact that microemulsion-derived CeO_2 particles have the advantage of being nano-sized, which is known to enhance catalytic activity, the lack of second-level ordering and macropores as anchoring sites reduces the effectiveness of the combustion process in comparison to star-shaped particles. As the diversified boundary contacts are still present in microemulsion-derived nanoparticle agglomerates, the soot combustion efficiency in the first cycle of operation is larger than for bulk material.

Hierarchically structured star-shaped micro-particles have the advantage that thanks to possibility of fitting the shape of soot agglomerates and soot nanoparticles in tandem, they may catalyze soot combustion more efficient. In addition, despite the fact that undoped and rare-earth-doped ceria hierarchical materials described in the literature achieve lower CO oxidation temperatures[16,17,20,22,23,24,29,80], stars have the additional advantage of catalyzing soot afterburning due to the above-mentioned properties. This makes our material very interesting and multifunctional. Increased dynamic oxygen storage capacity is suggested to increase resistance against carbon deposition in the form of nonreactive polymers[122], hence further study with the use of doped samples is necessary to carry out to gain knowledge about the catalytic performance of such materials.

IV. Conclusions

Three research findings were presented in this work. Firstly, it has been demonstrated that oxidative thermolysis of mixed rare-earth cerium formates enable to produce highly porous mixed cerium oxide material. This synthetic procedure allows the fast and reproducible formation of $Ce_{0.9}REE_{0.1}O_{1.95}$ micro-particles (RE: La, Pr, Nd, Sm, Eu, Gd, Tb, Dy, Ho, Er, Tm, Yb, Lu, Sc, Y) with preserved star-shape morphology that could be described by three distinct levels of structural organization, namely, 1º level as $Ce_{0.9}REE_{0.1}O_{1.95}$ nanocrystallites, 2º level as porous rods and 3º level as star-shaped micro-particles.

Secondly, it has been shown that each level of organization has its own functionality and it is vulnerable for modifications. Introduction of rare-earth dopant modifies microstructure of nanocrystallite building blocks, which in turn improves CO oxidation performance as compared to undoped CeO_2 star-shaped porous particles. The presence of varied-sized pores at the second level of the structural hierarchy facilitates mass transfer and thus enhances CO oxidation as well as soot combustion performance as compared to non-organized cerium crystallites and bulk ceria. Controlling thermolysis conditions may enable to design porosity, as the temperature of thermolysis influences the shape and size of cerium crystallites formed, thus potentially influencing porosity. Third level of organization permits easy anchoring of soot particles as compared to unstructured ceria materials, which translates into better soot burning efficiency. Morphology change by synthetic conditions manipulation is a potential area for further research.

Thirdly, key-lock catalysis concept was applied to explain enhanced soot combustion performance in hierarchically structured star-shaped particles. Soot embedding between the star-shaped particles arms followed by macropores penetration extended soot-ceria contact. Anchorage of soot particle in sieve matrix facilitated soot combustion. Thus, specific organization of structural elements at different length scales facilitates materials catalytic activity that outperforms non-hierarchically organized material leading to “one plus one greater than two” behavior.

Conflicts of interest

There are no conflicts to declare.

Acknowledgements

The authors thank Mrs. Zofia Mazurkiewicz for valuable help with preparation of the samples. Special thanks are due to Mrs. Ewa Bukowska, Dr Maciej Ptak and Dr Piotr Kraszkiewicz for XRD, FT-IR and BET measurements, respectively. We acknowledge Degussa S.A. for providing us with Printex-U soot.

Notes and references

1 C. Sun, H. Li and L. Chen, *Energy Environ. Sci.*, 2012, **5**, 8475–8505.

2 A. Trovarelli and P. Fornasiero, *Catalysis by Ceria and Related Materials, 2nd ed.*, Imperical College Press, London, 2013.

3 R. Chockalingam, V. R. W. Amarakoon and H. Giesche, *J. Eur. Ceram. Soc.*, 2008, **28**, 959–963.

4 R. J. Gorte and S. Zhao, *Catal. Today*, 2005, **104**, 18–24.

5 S. Scirè, S. Minicò, C. Crisafulli, C. Satriano and A. Pistone, *Appl. Catal. B Environ.*, 2003, **40**, 43–49.

6 S. Rossignol, F. Gérard, D. Mesnard, C. Kappenstein and D. Duprez, *J. Mater. Chem.*, 2003, **13**, 3017–3020.

7 M. Fernández-García, A. Martínez-Arias, J. C. Hanson and J. A. Rodriguez, *Chem. Rev.*, 2004, **104**, 4063–4104.

8 A. Trovarelli and J. Llorca, *ACS Catal.*, 2017, **7**, 4716–4735.

9 W.-X. Tang and G. Pu-Xian, *MRS Commun.*, 2016, **6**, 311–329.

10 R. Lakes, *Nature*, 1993, **361**, 511–515.

11 P. Yang, T. Deng, D. Zhao, P. Feng, D. Pine, B. F. Chmelka, G. M. Whitesides and G. D. Stucky, *Science (80-.).*, 1998, **282**, 2244–2246.

12 Z. Ren, Y. Guo, C. H. Liu and P. X. Gao, *Front. Chem.*, 2013, **1**, 1–22.

13 W. Schwieger, A. G. Machoke, T. Weissenberger, A. Inayat, T. Selvam, M. Klumpp and A. Inayat, *Chem. Soc. Rev.*, 2016, **45**, 3353–3376.

14 A. Clauset, C. Moore and M. E. J. Newman, *Nature*, 2008, **453**, 98–101.

15 X. Y. Yang, L. H. Chen, Y. Li, J. C. Rooke, C. Sanchez and B. L. Su, *Chem. Soc. Rev.*, 2017, **46**, 481–558.

16 R. Rao, M. Yang, C. Li, H. Dong, S. Fang and A. Zhang, *J. Mater. Chem. A*, 2015, **3**, 782–788.

17 Y. He, X. Liang and B. Chen, *Nano Res.*, 2015, **8**, 1269–1278.

18 J. Wei, Z. Yang and Y. Yang, *CrystEngComm*, 2011, **13**, 2418–2424.

19 W. Shan, X. Dong, N. Ma, S. Yao and Z. Feng, *Catal. Letters*, 2009, **131**, 350–355.

20 J. Li, G. Lu, H. Li, Y. Wang, Y. Guo and Y. Guo, *J. Colloid Interface Sci.*, 2011, **360**, 93–99.

21 R. Yu, L. Yan, P. Zheng, J. Chen and X. Xing, *J. Phys. Chem. C*, 2008, **112**, 19896–19900.

22 J. Wei, Z. Yang, H. Yang, T. Sun and Y. Yang, *CrystEngComm*, 2011, **13**, 4950–4955.

23 W. Liu, L. Feng, C. Zhang, H. Yang, J. Guo, X. Liu, X. Zhang and Y. Yang, *J. Mater. Chem. A*, 2013, **1**, 6942–6948.

24 W. Tang, W. Li, X. Shan, X. Wu and Y. Chen, *Mater. Lett.*, 2015, **140**, 95–98.

25 E. Aneggi, D. Wiater, C. De Leitenburg, J. Llorca and A. Trovarelli, *ACS Catal.*, 2014, **4**, 172–181.

26 P. Miceli, S. Bensaid, N. Russo and D. Fino, *Nanoscale Res. Lett.*, 2014, **9**, 1–10.

27 S. Liu, X. Wu, D. Weng and R. Ran, *J. Rare Earths*, 2015, **33**, 567–590.

28 F. F. Muñoz, L. M. Acuña, C. A. Albornoz, A. G. Leyva, R. T. Baker and R. O. Fuentes, *Nanoscale*, 2015, **7**, 271–281.

29 G. Xiao, S. Li, H. Li and L. Chen, *Microporous Mesoporous Mater.*, 2009, **120**, 426–431.

30 D. Mukherjee and B. M. Reddy, *Catal. Today*, 2018, **309**, 227–235.

31 D. R. Ou, T. Mori, F. Ye, T. Kobayashi, J. Zou, G. Auchterlonie and J. Drennan, *Appl. Phys. Lett.*, , DOI:10.1063/1.2369881.

32 D. R. Ou, T. Mori, F. Ye, J. Zou, G. Auchterlonie and J. Drennan, *Phys. Rev. B - Condens. Matter Mater. Phys.*, 2008, **77**, 1–8.

33 F. Ye, T. Mori, D. R. Ou, A. N. Cormack, R. J. Lewis and J. Drennan, *Solid State Ionics*, 2008, **179**, 1962–1967.

34 F. Ye, T. Mori, D. R. Ou, J. Zou and J. Drennan, *Solid State Ionics*, 2009, **180**, 1414–1420.

35 V. Grover, S. N. Achary and A. K. Tyagi, *J. Appl. Crystallogr.*, 2003, **36**, 1082–1084.

36 M. A. Małecka, J. J. Delgado, L. Kepiński, J. J. Calvino, S. Bernal, G. Blanco and X. Chen, *Catal. Today*, 2012, **187**, 56–64.

37 N. V. Skorodumova, S. I. Simak, B. I. Lundqvist, I. A. Abrikosov and B. Johansson, *Phys. Rev. Lett.*, 2002, **89**, 166601/1-166601/4.

38 S. Bernal, G. Blanco, G. Cifredo, J. A. Pérez-Omil, J. M. Pintado and J. M. Rodríguez-Izquierdo, *J. Alloys Compd.*, 1997, **250**, 449–454.

39 G. Vlaic, P. Fornasiero, S. Geremia, J. Kašpar and M. Graziani, *J. Catal.*, 1997, **168**, 386–392.

40 M. A. Małecka, L. Kepiński and W. Miśta, *Appl. Catal. B Environ.*, 2007, **74**, 290–298.

41 M. A. Małecka and L. Kepiński, *J. Alloys Compd.*, 2007, **430**, 282–291.

42 M. C. Thrun, in *Projection-Based Clustering through Self-Organization and Swarm Intelligence*, Wiesbaden, Springer V., 2018.

43 J. W. Goodby, V. Görtz, S. J. Cowling, G. MacKenzie, P. Martin, D. Plusquellec, T. Benvegnu, P. Boullanger, D. Lafont, Y. Queneau, S. Chambert and J. Fitremann, *Chem. Soc. Rev.*, 2007, **36**, 1971–2032.

44 N. Bao and A. Gupta, *J. Mater. Rsearch*, 2011, **26**, 111–121.

45 A. J. Patil and S. Mann, *J. Mater. Chem.*, 2008, **18**, 4605–4615.

46 B. B. Bokhonov, A. A. Matvienko, K. B. Gerasimov and D. V. Dudina, *Ceram. Int.*, 2019, **45**, 19684–19688.

47 P. Miceli, S. Bensaid, N. Russo and D. Fino, *Chem. Eng. J.*, 2015, **278**, 190–198.

48 M. Hasanpour, M. K. Razavi Aghjeh, M. Mehrabi Mazidi and B. Afsari, *Polym. Bull.*, , DOI:10.1007/s00289-019-02870-4.

49 S. Dikmen, P. Shuk and M. Greenblatt, *Solid State Ionics*,

1999, **126**, 89–95.

50 V. Bellière, G. Joorst, O. Stephan, F. M. F. De Groot and B. M. Weckhuysen, *J. Phys. Chem. B*, 2006, **110**, 9984–9990.

51 H. Nitani, T. Nakagawa, M. Yamanouchi, T. Osuki, M. Yuya and T. A. Yamamoto, *Mater. Lett.*, 2004, **58**, 2076–2081.

52 S. V. Chavan, M. D. Mathews and A. K. Tyagi, *Mater. Res. Bull.*, 2005, **40**, 1558–1568.

53 B. P. Mandal, V. Grover and A. K. Tyagi, *Mater. Sci. Eng. A*, 2006, **430**, 120–124.

54 P. Shuk, M. Greenblatt and M. Croft, 2000, **304**, 465–471.

55 V. Grover and A. K. Tyagi, *Mater. Res. Bull.*, 2004, **39**, 859–866.

56 V. Grover and A. K. Tyagi, *J. Solid State Chem.*, 2004, **177**, 4197–4204.

57 B. P. Mandal, V. Grover, M. Roy and A. K. Tyagi, *J. Am. Ceram. Soc.*, 2007, **90**, 2961–2965.

58 M. A. Małecka, U. Burkhardt, D. Kaczorowski, M. P. Schmidt, D. Goran and L. Kępiński, *J. Nanoparticle Res.*, 2009, **11**, 2113–2124.

59 V. Longo and L. Podda, *J. Mater. Sci. Lett.*, 1981, **16**, 839–841.

60 V. Grover, A. Banerji, P. Sengupta and A. K. Tyagi, *J. Solid State Chem.*, 2008, **181**, 1930–1935.

61 S. V. Chavan and A. K. Tyagi, *Mater. Sci. Eng. A*, 2005, **404**, 57–63.

62 D. Bevan and E. Summerville, in *Handbook on the Physics and Chemistry on Rare Earths, vol.3*, eds. K. Gschneider and L. Eyring, Elsevier, North-Holl., 1979.

63 C. P. Kempter, *Phys. Status Solidi*, 1966, **18**, K117–K118.

64 R. D. Shannon, *Acta Crystallogr.*, 1976, **A32**, 751–767.

65 R. J. Matyi, L. H. Schwartz and J. B. Butt, *Catal. Rev. Sci. Eng.*, 1987, **29**, 41–99.

66 M. F. Luo, Z. L. Yan, L. Y. Jin and M. He, *J. Phys. Chem. B*, 2006, **110**, 13068–13071.

67 V. B. Glushkova, F. Hanic and L. V. Sazonova, *Ceramurg. Int.*, 1978, **4**, 176–178.

68 D.-J. Kim, *J. Am. Ceram. Soc.*, 1989, **72**, 1415–1421.

69 P. M. Diehm, P. Ágoston and K. Albe, *ChemPhysChem*, 2012, **13**, 2443–2454.

70 L. Wu, H. J. Wiesmann, A. R. Moodenbaugh, R. F. Klie, Y. Zhu, D. O. Welch and M. Suenaga, *Phys. Rev. B - Condens. Matter Mater. Phys.*, 2004, **69**, 1–9.

71 S. Tsunekawa, R. Sivamohan, S. Ito, A. Kasuya and T. Fukuda, *Nanostructured Mater.*, 1999, **11**, 141–147.

72 F. Zhang, P. Wang, J. Koberstein, S. Khalid and S. W. Chan, *Surf. Sci.*, 2004, **563**, 74–82.

73 C. Sun and D. Xue, *Phys. Chem. Chem. Phys.*, 2013, **15**, 14414–14419.

74 Z. L. Wang and X. Feng, *J. Phys. Chem. B*, 2003, **107**, 13563–13566.

75 P. W. Tasker, *J. Phys. C Solid State Phys.*, 1979, **12**, 4977–4984.

76 P. Xu, R. Yu, H. Ren, L. Zong, J. Chen and X. Xing, *Chem. Sci.*, 2014, **5**, 4221–4226.

77 M. Guo, J. Lu, Y. Wu, Y. Wang and M. Luo, *Langmuir*, 2011, **27**, 3872–3877.

78 S. A. Acharya, V. M. Gaikwad, V. Sathe and S. K. Kulkarni, *Appl. Phys. Lett.*, , DOI:10.1063/1.4869116.

79 K. Ruschel, L. Nasdala, A. Kronz, J. M. Hanchar, D. M. Többens, R. Škoda, F. Finger and A. Möller, *Mineral. Petrol.*, 2012, **105**, 41–55.

80 J. Zhang, H. Yang, S. Wang, W. Liu, X. Liu, J. Guo and Y. Yang, *CrystEngComm*, 2014, **16**, 8777–8785.

81 M. Kurnatowska, L. Kepinski and W. Mista, *Appl. Catal. B Environ.*, 2012, **117**–**118**, 135–147.

82 H. Borchert, Y. V. Frolova, V. V. Kaichev, I. P. Prosvirin, G. M. Alikina, A. I. Lukashevich, V. I. Zaikovskii, E. M. Moroz, S. N. Trukhan, V. P. Ivanov, E. A. Paukshtis, V. I. Bukhtiyarov and V. A. Sadykov, *J. Phys. Chem. B*, 2005, **109**, 5728–5738.

83 Y. Wei, Z. Zhao, J. Jiao, J. Liu, A. Duan and G. Jiang, *J. Rare Earths*, 2014, **32**, 124–130.

84 G. Ranga Rao, *Bull. Mater. Sci.*, 1999, **22**, 89–94.

85 Z. Wu, Y. Cheng, F. Tao, L. Daemen, G. S. Foo, L. Nguyen, X. Zhang, A. Beste and A. J. Ramirez-Cuesta, *J. Am. Chem. Soc.*, 2017, **139**, 9721–9727.

86 M. A. Małecka, L. Kepiński and W. Miśta, *J. Alloys Compd.*, 2008, **451**, 567–570.

87 U. Hennings and R. Reimert, *Appl. Catal. A Gen.*, 2007, **325**, 41–49.

88 G. R. Rao and B. G. Mishra, *Bull. Catal. Soc. India*, 2003, **2**, 122–134.

89 V. Perrichon, A. Laachir, G. Bergeret, R. Fréty, L. Tournayan and O. Touret, *J. Chem. Soc. Faraday Trans.*, 1994, **90**, 773–781.

90 D. Terribile, A. Trovarelli, C. De Leitenburg, G. Dolcetti and J. Llorca, *Chem. Mater.*, 1997, **9**, 2676–2678.

91 S. Bernai, G. Blanco, M. A. Cauqui, G. A. Cifredo, J. M. Pintado and J. M. Rodriguez-Izquierdo, *Catal. Letters*, 1998, **53**, 51–57.

92 R. Sasikala, S. Varma, N. M. Gupta and S. K. Kulshreshtha, *J. Mater. Sci. Lett.*, 2001, **20**, 1131–1133.

93 J. Zhang, G. Chen, M. Chaker, F. Rosei and D. Ma, *Appl. Catal. B Environ.*, 2013, **132**–**133**, 107–115.

94 C. Y. Cao, Z. M. Cui, C. Q. Chen, W. G. Song and W. Cai, *J. Phys. Chem. C*, 2010, **114**, 9865–9870.

95 J. P. Zhao, Y. Li, Z. Cao and W. H. Xin, *New J. Chem.*, 2008, **32**, 1014–1019.

96 U. M. Graham, R. A. Khatri, A. Dozier, G. Jacobs and B. H. Davis, *Catal. Letters*, 2009, **132**, 335–341.

97 G. Zhang, Z. Zhao, J. Xu, J. Zheng, J. Liu, G. Jiang, A. Duan and H. He, *Appl. Catal. B Environ.*, 2011, **107**, 302–315.

98 C. Hennig, A. Ikeda-Ohno, W. Kraus, S. Weiss, P. Pattison, H. Emerich, P. M. Abdala and A. C. Scheinost, *Inorg. Chem.*, 2013, **52**, 11734–11743.

99 G. Spezzati, A. D. Benavidez, A. T. DeLaRiva, Y. Su, J. P. Hofmann, S. Asahina, E. J. Olivier, J. H. Neethling, J. T. Miller, A. K. Datye and E. J. M. Hensen, *Appl. Catal. B Environ.*, 2019, **243**, 36–46.

100 G. Hua, L. Zhang, G. Fei and M. Fang, *J. Mater. Chem.*, 2012, **22**, 6851–6855.

101 M. A. Małecka, *CrystEngComm*, 2017, **19**, 6199–6207.

102 M. A. Małecka, *ChemistrySelect*, 2019, **4**, 316–320.

103 M. A. Małecka, *ChemistrySelect*, 2018, **3**, 12012– 12016.

104 J. Vecchietti, S. Collins, J. J. Delgado, M. Małecka, E. Del Rio,

X. Chen, S. Bernal and A. Bonivardi, *Top. Catal.*, 2011, **54**, 201–209.
105 Q. X. Chen, Y. H. Liu, X. Z. Qi, J. W. Liu, H. J. Jiang, J. L. Wang, Z. He, X. F. Ren, Z. H. Hou and S. H. Yu, *J. Am. Chem. Soc.*, 2019, **141**, 10729–10735.
106 S. Mandal, K. K. Bando, C. Santra, S. Maity, O. O. James, D. Mehta and B. Chowdhury, *Appl. Catal. A Gen.*, 2013, **452**, 94–104.
107 O. Bezkrovnyi, P. Kraszkiewicz, I. Krivtsov, J. Quesada, S. Ordóñez and L. Kepinski, *Catal. Commun.*, 2019, **131**, 105798.
108 K. Polychronopoulou, A. F. Zedan, M. S. Katsiotis, M. A. Baker, A. A. AlKhoori, S. Y. AlQaradawi, S. J. Hinder and S. AlHassan, *Mol. Catal.*, 2017, **428**, 41–55.
109 L. Zhou, X. Li, Z. Yao, Z. Chen, M. Hong, R. Zhu, Y. Liang and J. Zhao, *Sci. Rep.*, 2016, **6**, 1–7.
110 E. M. Slavinskaya, T. Y. Kardash, O. A. Stonkus, R. V. Gulyaev, I. N. Lapin, V. A. Svetlichnyi and A. I. Boronin, *Catal. Sci. Technol.*, 2016, **6**, 6650–6666.
111 L. Li, Y. Liu, Q. Wang, X. Zhou, J. Li, S. Song and H. Zhang, *CrystEngComm*, 2019, **21**, 7108–7113.
112 Y. Wei, Z. Zhao, X. Yu, B. Jin, J. Liu, C. Xu, A. Duan, G. Jiang and S. Ma, *Catal. Sci. Technol.*, 2013, **3**, 2958–2970.
113 Y. Wei, J. Liu, Z. Zhao, A. Duan and G. Jiang, *J. Catal.*, 2012, **287**, 13–29.
114 A. Bueno-López, K. Krishna, M. Makkee and J. A. Moulijn, *J. Catal.*, 2005, **230**, 237–248.
115 S. Liu, X. Wu, Y. Lin, M. Li and D. Weng, *Chinese J. Catal.*, 2014, **35**, 407–415.
116 D. Fino, S. Bensaid, M. Piumetti and N. Russo, *Appl. Catal. A Gen.*, 2016, **509**, 75–96.
117 A. Bueno-López, *Appl. Catal. B Environ.*, 2014, **146**, 1–11.
118 F. Ying, S. Wang, C. T. Au and S. Y. Lai, *Microporous Mesoporous Mater.*, 2011, **142**, 308–315.
119 D. Sorolla-Rosario, A. Davó-Quiñonero, E. Bailón-García, D. Lozano-Castelló and A. Bueno-López, *ChemCatChem*, 2020, **12**, 1772–1781.
120 G. Zhang, Z. Zhao, J. Liu, G. Jiang, A. Duan, J. Zheng, S. Chen and R. Zhou, *Chem. Commun.*, 2010, **46**, 457–459.
121 S. Liu, X. Wu, D. Weng, M. Li and J. Fan, *Appl. Catal. B Environ.*, 2013, **138**–**139**, 199–211.
122 C. H. Bartholomew, *Appl. Catal. A Gen.*, 2001, **212**, 17–60.

Supplementary materials for

Function of various levels of hierarchical organization of the porous $Ce_{0.9}REE_{0.1}O_{1.95}$ mixed oxides in the catalytic activity.

Piotr Woźniak*, Włodzimierz Miśta, Małgorzata A. Małecka

Institute of Low Temperature and Structure Research, Polish Academy of Sciences,
P.O. Box 1410, 50-950 Wrocław 2, Poland

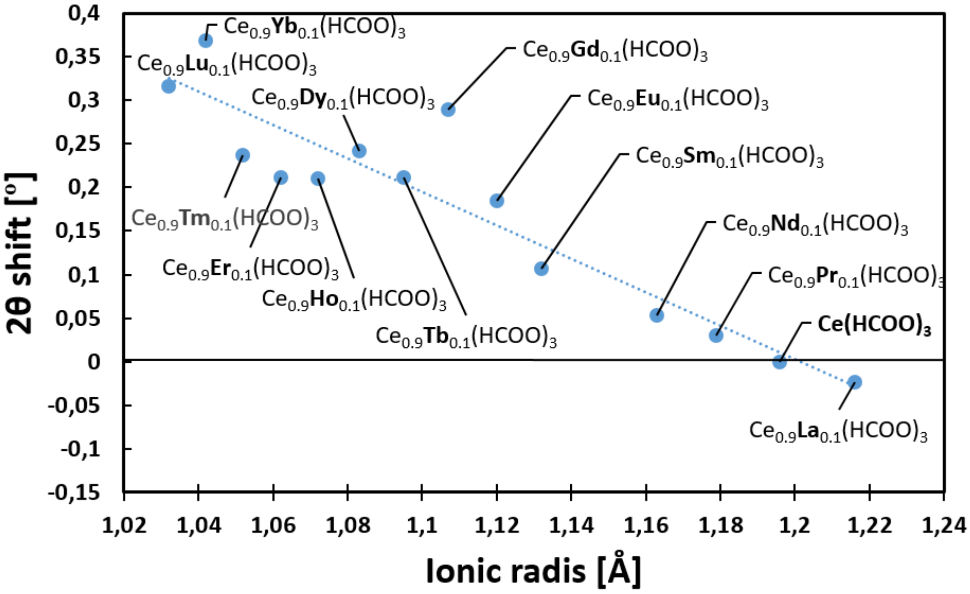

Fig. S1. 2θ angle shift of (411) peak in $Ce_{0.9}Ln_{0.1}(HCOO)_3$ samples (indicator of latticeconstant change) as a function ionic radius (Ln refers to lanthanide ion).

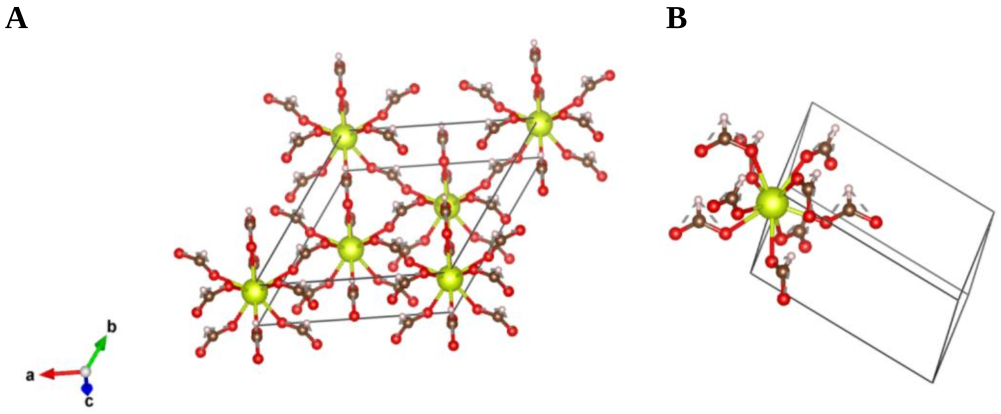

Fig S2. A. Crystal structure of $Ce(HCOO)_3$ (ref. ICSD: 237331); colour codes: cerium (yellow), oxygen (red), carbon (brown), hydrogen (white); B. Ce^{3+}(IX) surrounded by nine $HCOO_3$ molecules.

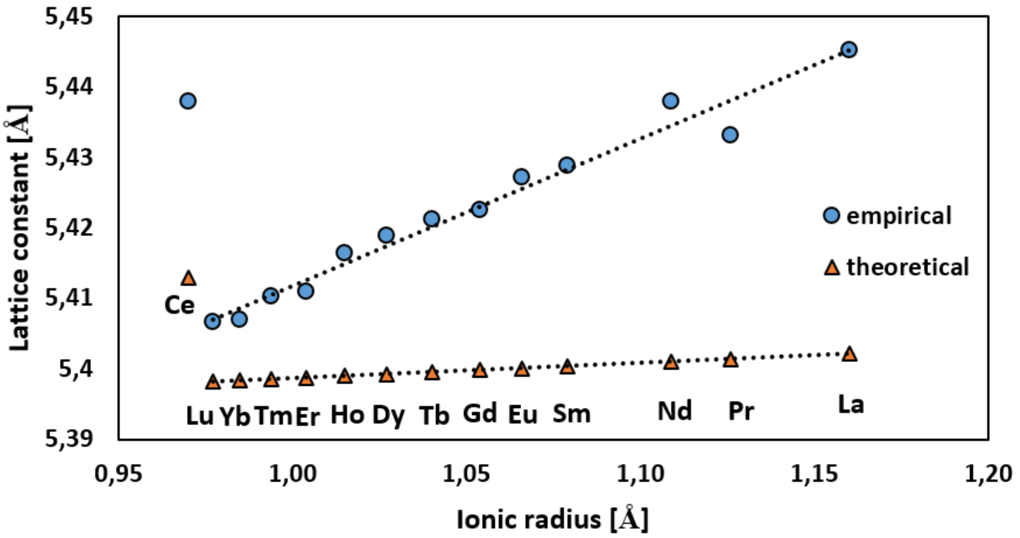

Fig. S3. Lattice constant as a function of ionic radius; Blue circles: Empirical data obtained from Rietveld refinement analysis of PXRD data of star-shaped particles; orange triangles: Lattice constant calculated from Kim's formula for doped cerium oxides [ref. D.-J. Kim, J. Am. Ceram. Soc. 72 (1989) 1415.]

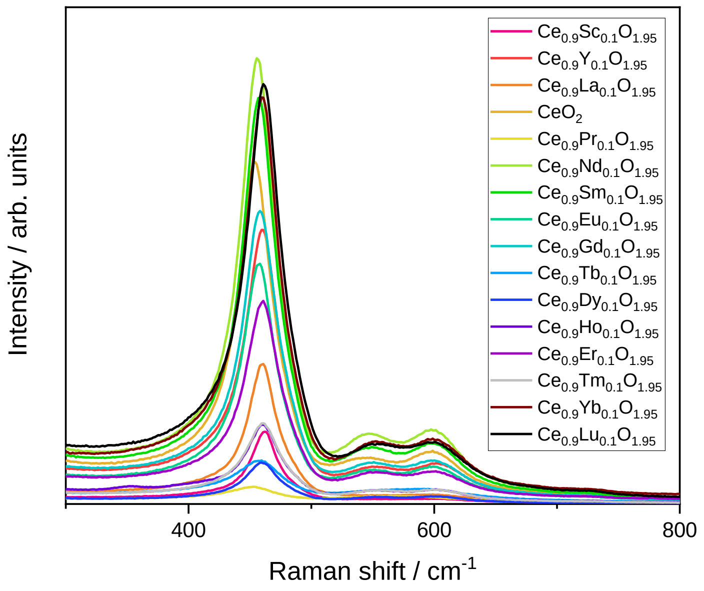

Fig. S4. Raman spectra of star-shaped $Ce_{0.9}RE_{0.1}O_{1.95}$ samples.

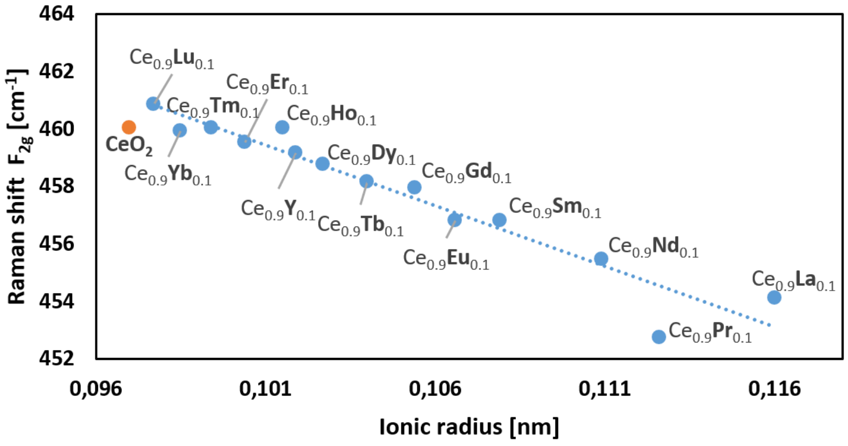

Fig S5. Raman F_{2g} mode shift for lanthanide series

Shift of CeO_2 F_{2g} mode from theoretical value of 465 cm^{-1} to 460 cm^{-1} may be due to crystal size decrease as suggested in [Spanier JE, Robinson RD, Zhang F, Chan SW, Herman IP (2001) Phys Rev B 64:245407].

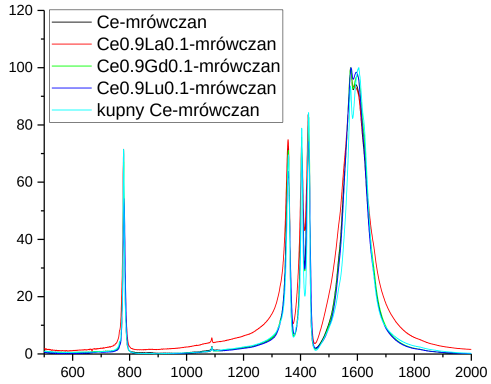

Fig. S6 IR spectra of $Ce_xRE_{1-x}(HCOO)_3$ samples (x= 0; 0.1; RE- La, Gd, Lu)

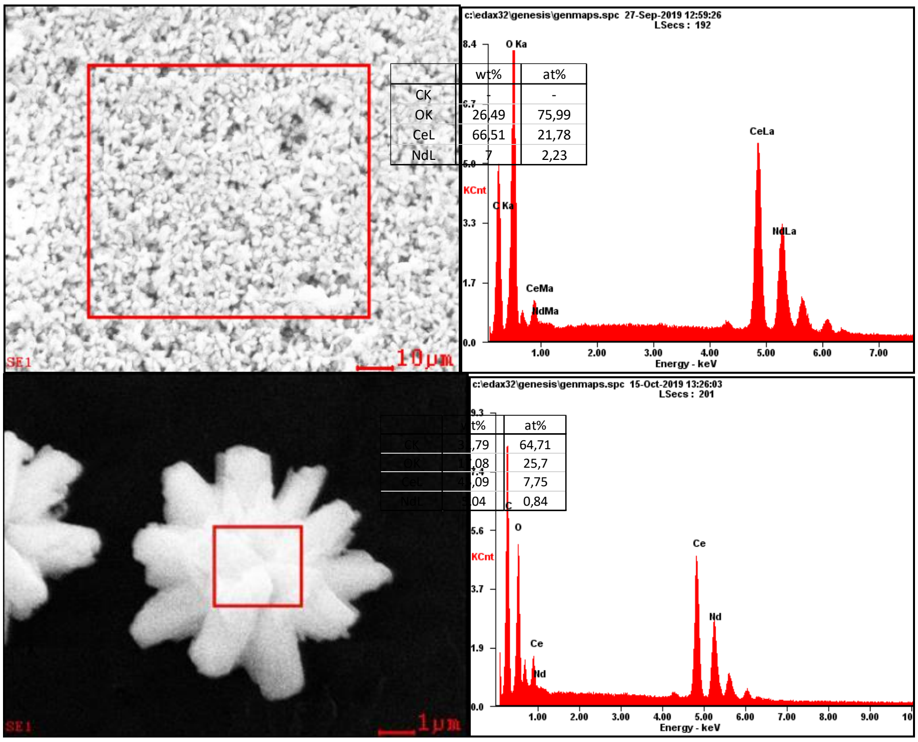

	wt%	at%
CK	-	-
OK	26,49	75,99
CeL	66,51	21,78
NdL	7	2,23

	wt%	at%
CK	3[illegible],79	64,71
OK	1[illegible],08	25,7
CeL	4[illegible],09	7,75
NdL	5,04	0,84

Fig. S7. EDS measurements of $Ce_{0.9}Nd_{0.1}(HCOO)_3$ sample as a presentation of the way of composition determination; A) Global composition; B) local composition.

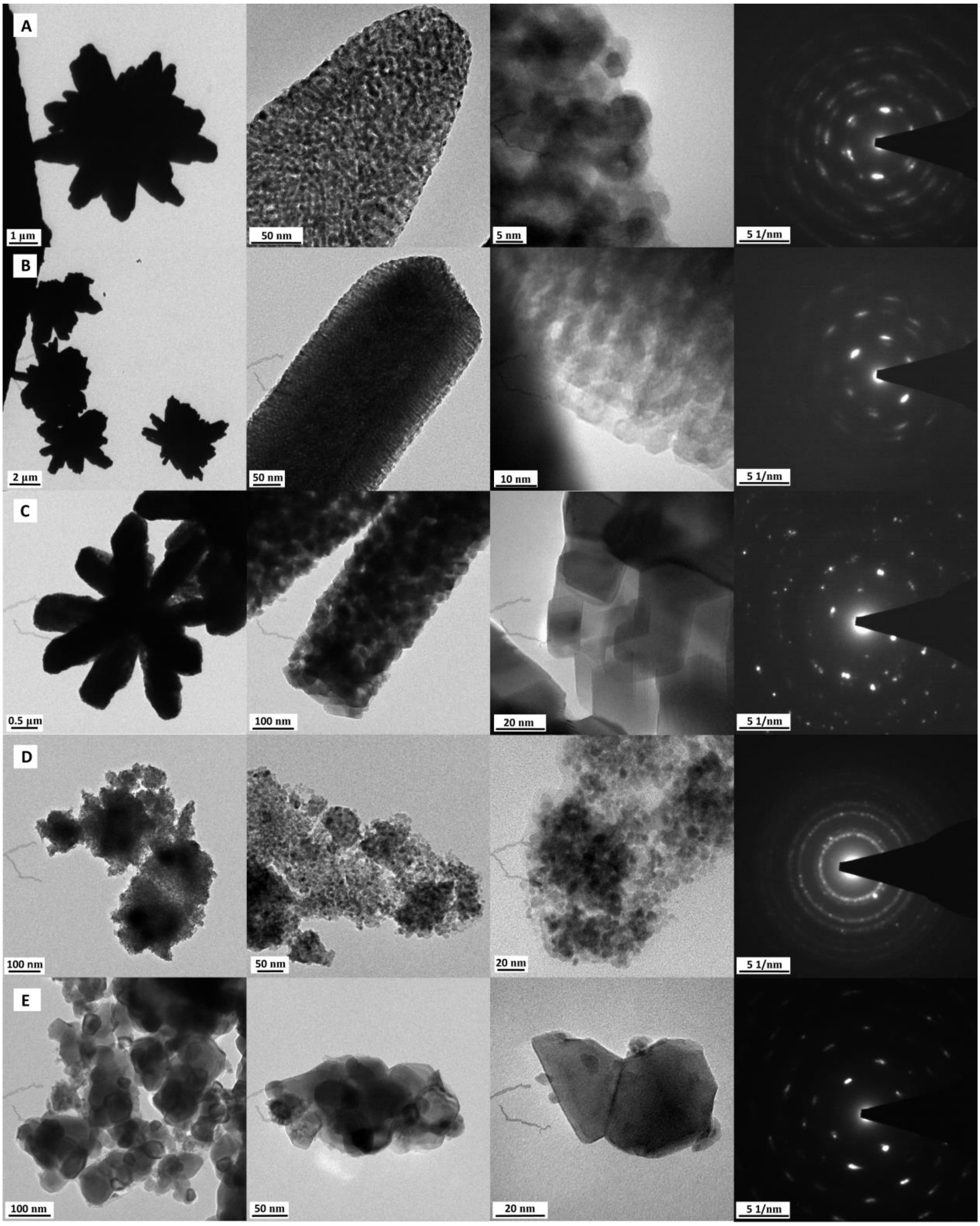

Fig S8. Ceria materials differed by 2nd hierarchy level organization of nanocrystallites; A. Undoped star-shaped particles (**CeO_2_Star**) heated at 550ºC; B. Gadolinium doped star-shaped particles, (**$Ce_{0.9}Gd_{0.1}O_{1.95}$_Star)** heated at 550ºC); C. Undoped star-shaped particles (**CeO_2_Star**) heated at 900ºC; D) Microemulsion-derived nanoparticles (**CeO_2_NPs**) heated at 550ºC; E. Microemulsion-derived nanoparticles (**CeO_2_NPs**) heated at 900ºC.

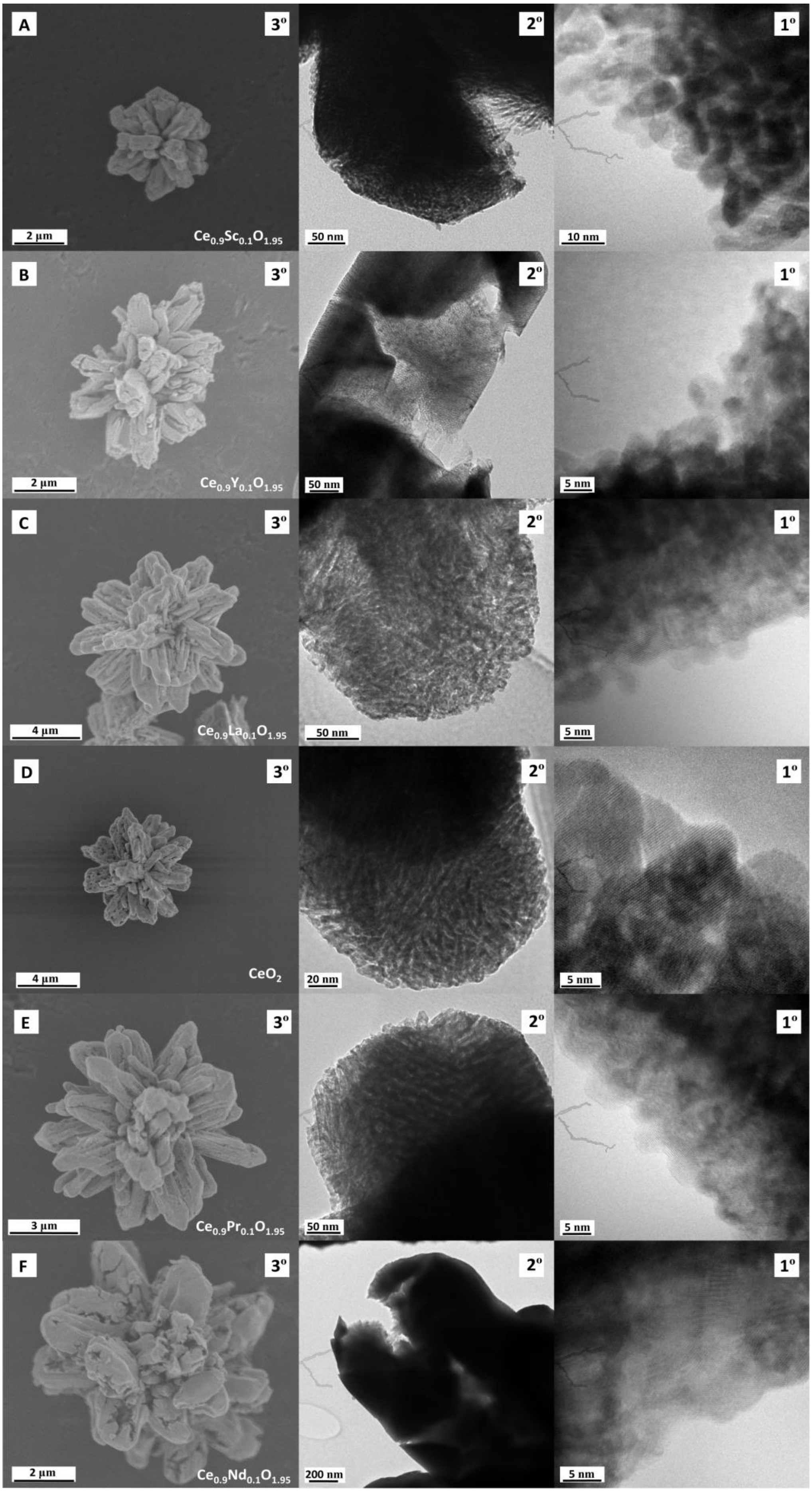
A
3º
2 µm
$Ce_{0.9}Sc_{0.1}O_{1.95}$
2º
50 nm
1º
10 nm
B
3º
2 µm
$Ce_{0.9}Y_{0.1}O_{1.95}$
2º
50 nm
1º
5 nm
C
3º
4 µm
$Ce_{0.9}La_{0.1}O_{1.95}$
2º
50 nm
1º
5 nm
D
3º
4 µm
CeO_2
2º
20 nm
1º
5 nm
E
3º
3 µm
$Ce_{0.9}Pr_{0.1}O_{1.95}$
2º
50 nm
1º
5 nm
F
3º
2 µm
$Ce_{0.9}Nd_{0.1}O_{1.95}$
2º
200 nm
1º
5 nm

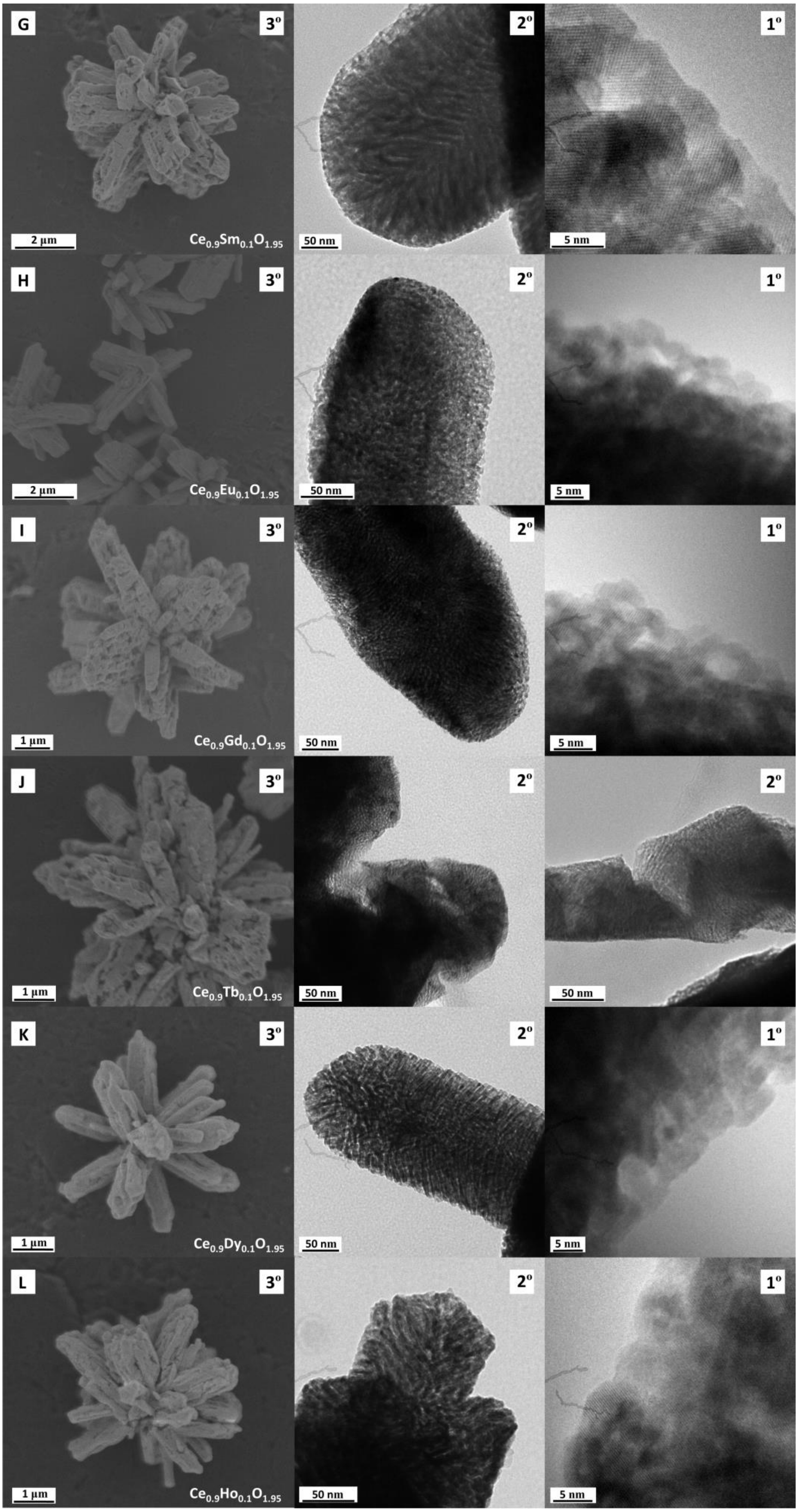
G
3º
2 µm
Ce0.9Sm0.1O1.95
2º
50 nm
1º
5 nm
H
3º
2 µm
Ce0.9Eu0.1O1.95
2º
50 nm
1º
5 nm
I
3º
1 µm
Ce0.9Gd0.1O1.95
2º
50 nm
1º
5 nm
J
3º
1 µm
Ce0.9Tb0.1O1.95
2º
50 nm
2º
50 nm
K
3º
1 µm
Ce0.9Dy0.1O1.95
2º
50 nm
1º
5 nm
L
3º
1 µm
Ce0.9Ho0.1O1.95
2º
50 nm
1º
5 nm

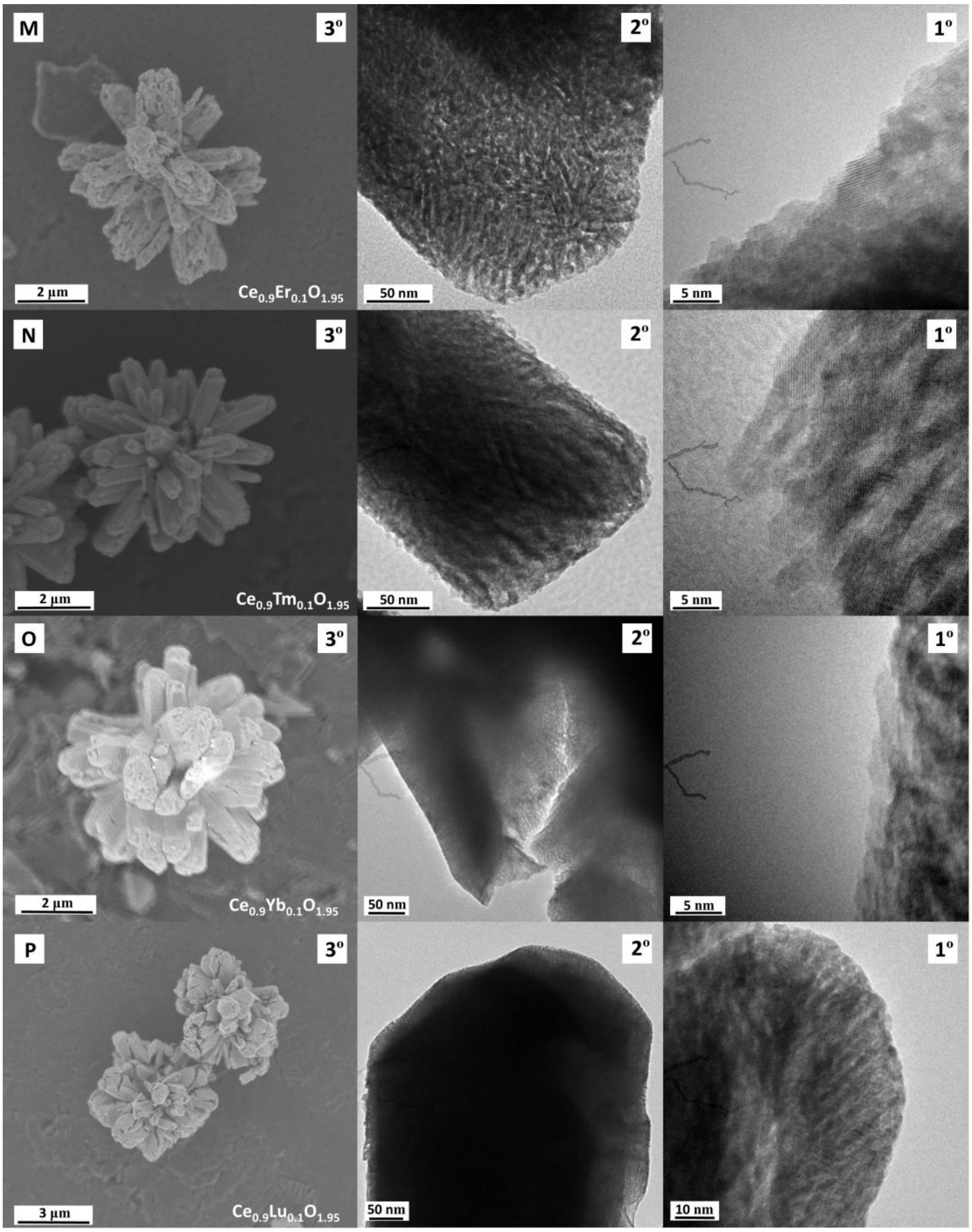

Fig S9. SEM and TEM images showing three-level hierarchical structure of star-like $Ce_{0.9}RE_{0.1}O_{1.95}$ mixed oxides particles; 1º 2º 3º - first, second and third hierarchy levels respectively; A) $Ce_{0.9}Sc_{0.1}O_{1.95}$ B) $Ce_{0.9}Y_{0.1}O_{1.95}$ C) $Ce_{0.9}La_{0.1}O_{1.95}$ D) CeO_2 E) $Ce_{0.9}Pr_{0.1}O_{1.95}$ F) $Ce_{0.9}Nd_{0.1}O_{1.95}$ G) $Ce_{0.9}Sm_{0.1}O_{1.95}$ H) $Ce_{0.9}Eu_{0.1}O_{1.95}$ I) $Ce_{0.9}Gd_{0.1}O_{1.95}$ J) $Ce_{0.9}Tb_{0.1}O_{1.95}$ K) $Ce_{0.9}Dy_{0.1}O_{1.95}$ L) $Ce_{0.9}Ho_{0.1}O_{1.95}$ M) $Ce_{0.9}Er_{0.1}O_{1.95}$ N) $Ce_{0.9}Tm_{0.1}O_{1.95}$ O) $Ce_{0.9}Yb_{0.1}O_{1.95}$ P) $Ce_{0.9}Lu_{0.1}O_{1.95}$.

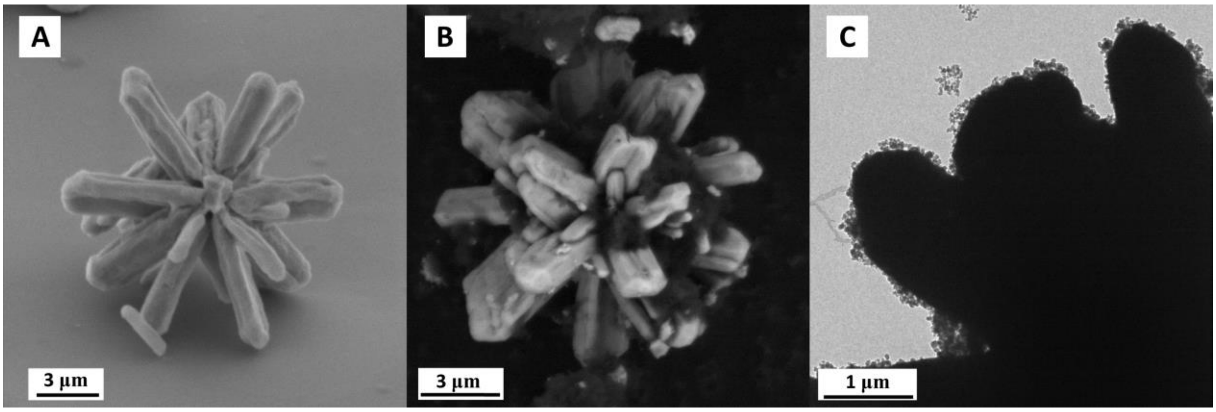

Fig S10. A) SEM image of CeO_2 star-shaped particles before mixing with soot; B) SEM image of CeO_2 star-sahaped particle after mixing with soot; C) TEM image of arms of CeO_2 star-shaped particle after mixing with soot.

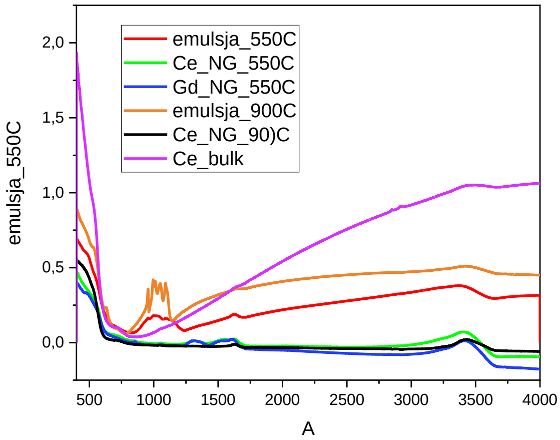

Fig. S11 FT-IR spectra of oxide samples heated at 550 ºC (before catalytic tests).

Fig. S12. Five cycles of soot combustion

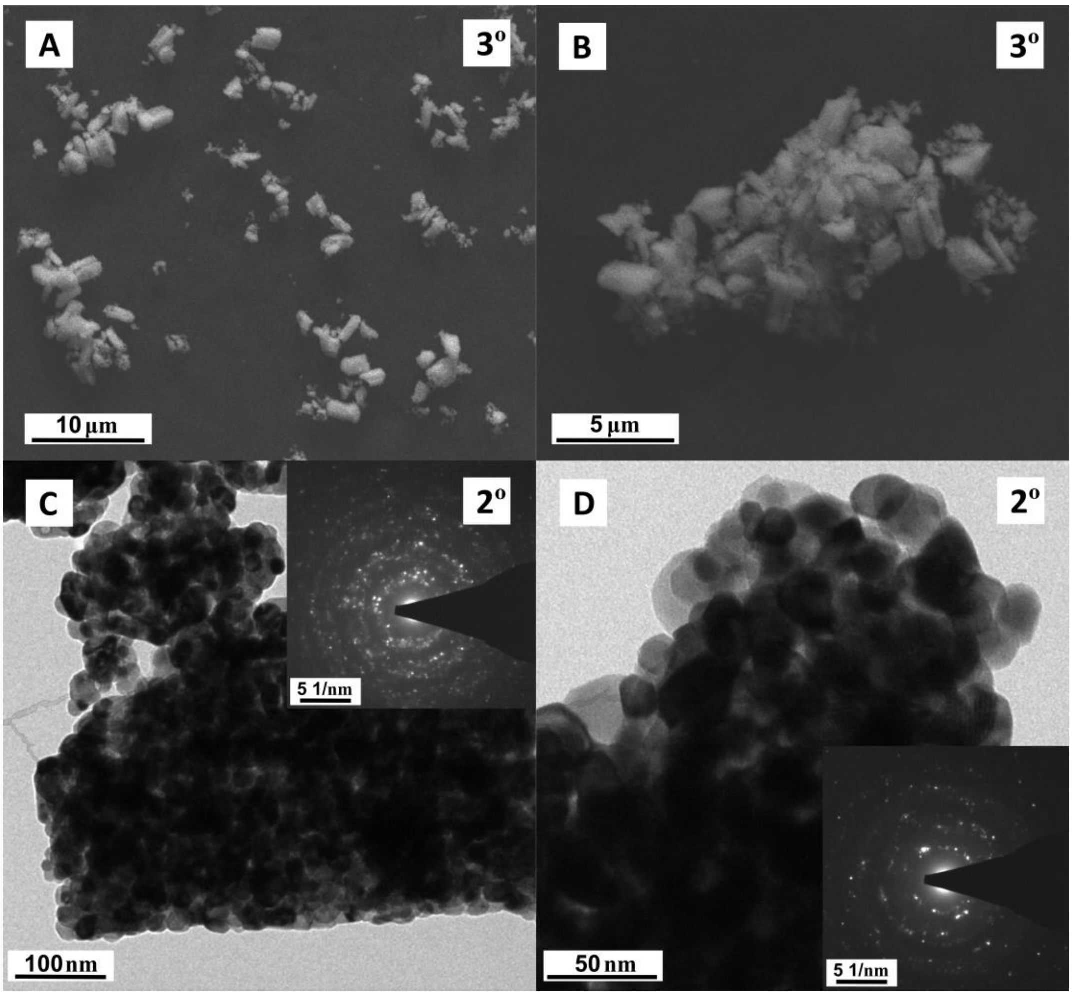

Fig. S13. SEM (A,B) and TEM (C,D) images of $CeO_{2-\delta}$_NG after 5th cycle of soot combustion. Loss of 3° (A, B) and 2° structure (inlet SAED patterns on images C and D) is observed.

Table S1. CeO_2 hierarchical architectures and CO oxidation catalytic performance

Ref.	Hierarchy description		T_{50} (ºC)	T_{50} of compartitive material (ºC)	Reactant feed	Space velocity (mL g^{-1} h^{-1})	BET (m^2/g)
[16]	3rd 2nd 1st	Nanobundles (0,5-1,2μm[b]/2-4μm[a]) Nanorods (<30nm) Nanoparticles(5.4 nm)[d]	213	261 (ceria nanoparticles)	5% CO, CO/O_2=0.15 in N_2	80000	130.4
[17]	3rd 2nd & 1st	Globin-like spheres (2-3 μm) Nano-sized building blocks interconnected by nanoparticles	162	272 (calcined cerium nitrate)	2% CO, 18% O_2, in N_2	18000	57.13
[20]	3rd 2nd 1st	Flowerlike spheres (5-8 μm) Nanowires (~6 nm)[c] Nanoparticles(~6 nm)	227	270 (bulk ceria)	1% CO, 20% O_2 in Ar	60000	64.2
[24]	3rd 2nd 1st	Spindle-like (2-5 μm)/ flower-like (5 μm) Nanoflakes Nanocrystallites (9.4 nm)	239	332 (commercial ceria)	1% CO, 1% O_2 in N_2	120000	171.6
[21]	3rd 2nd 1st	Flower-like (5 μm) Nanorods (20-40 nm[c]/1-2 μm[a]) –[e]	-	-	-	-	-
[18]	3rd 2nd 1st	Urchin-like (2.5-3 μm) Nanorods (50 nm[c]/1 μm[a]) –[e]	~400	~465 (commercial CeO_2)	1% CO, 10% O_2 in N_2	120000	115.2
[18]	3rd 2nd 1st	Coral-like (500-600 nm) Nanorods (50 nm[c]/ 200 nm[a] –[e]	~375	~465 (commercial CeO_2)	1% CO, 10% O2 in N2	120000	139.3
[22]	3rd 2nd 1st	Nanoflowers (250 nm) Nanorods (100 nm[a]/30 nm[c]) Nanocrystals (4.8 nm[d])	~230	-	1% CO, 10% O_2 in N_2	36000	95.7
[80]	3rd 2nd 1st	Nanoparticles (500 nm) Hollow nanocones Nanocrystallites (3-5 nm)	~200	~300 (commercial ceria)	1% CO, 10% O_2 in N_2	72000	147.6
[23]	3rd 2nd 1st	Microflowers (3 μm) Microrods (600nm[c]/2-3 μm[a]) Nanocrystallites (3-5 nm)	~230	~350 (commercial ceria)	1% CO, 10% O2 in N_2	96000	147.6
[19]	3rd 2nd	Sea urchin- like (10-50 μm) Rods (50 μm[a]/1-5	317	-	0.25% CO, 0.50% O_2 in N_2	96000	179 - 234

	1st	μm[c]) Nanocrystallites (10.3-14.7)					
[29]	3rd 2nd 1st	Flowerlike spheres (0,5- 10μm) Wrinkled petals Nanocrystallites (<10 nm)	~255 CeO_2 ~290 CeLa ~225 CePr	T_{20}=~400 (commercial ceria)	2% CO, 3% O_2 in N_2	60000	166 (CeO_2) 155 (CeLa) 140 (CePr)

[a] length, [b] width, [c] diameter, [d] mean grain size calculated by Scherrer equation, [e] no information

3D hierarchically structured $Ce_{1-x}Gd_xO_{2-x/2}$ mixed oxide particles: the role of microstructure, porosity and multi-level architecture stability in soot and propane oxidation.

Piotr Woźniak*[a], Małgorzata A. Małecka[a], Lidia Chinchilla[b], Susana Trasobares[b],

[a]*Institute of Low Temperature and Structure Research, Polish Academy of Sciences,*
P.O. Box 1410, 50-950 Wrocław 2, Poland
[b]*Departamento de Ciencia de los Materiales e Ing. Metalúrgica y Química Inorgánica,*
Universidad de Cádiz, Campus Universitario de Puerto Real, 11510, Cádiz - España

Abstract

In this paper, synoptic description of the hierarchical architecture of mixed ceria particles and its function in catalytic propane and soot oxidation has been presented. The influence of temperature and dopant concentration on the micro- to macroscale structure of the star-shaped particles has been thoroughly investigated by various physicochemical techniques. Two temperature-dependent growth modes of ceria nanoparticles has been observed and their dopant-dependent influence on mesocrystal architecture have been described. It appeared that presence of dopant changes the pattern of nanoparticles intergrowth which ultimately introduces additional porosity into 3D hierarchically structured material (r_{av} =19 nm). Furthermore, emergent phenomenon in catalytic propane oxidation was observed. The substantial increase of propane conversion via low-temperature surface oxidation mechanism was ascribed to nanocrystallites mesoscale organization forming porous hierarchical material. No such conversion was present for a comparative sample of non-organized ceria nanoparticles. Also, increased stability of such architecture was demonstrated in soot combustion tests.

Keywords: oxides , solvothermal, electron microscopy, microstructure, catalytic properties

*corresponding author: Piotr Woźniak, Institute of Low Temperature and Structure Research, Polish Academy of Sciences, P.O. Box, 1410, 50-950 Wrocław, Poland

tel: (48-71) 343 50 21 fax: (48-71) 344 10 29 Email: p.wozniak@intibs.pl

doi.org/10.1016/j.materresbull.2022.111816

1. Introduction

Cerium oxide due to its wide abundance in the earth crust, easy Ce^{4+}-Ce^{3+} reducibility and large potential for lattice defect accumulation leading to high oxygen storage capacity (OSC) have found utilization in broad scope of technologies such as solid oxide fuel cells [1], three-way catalytic converters [2], gas sensors [3]. Owing to the facet-dependent reactivity and the size-dependent vacancy concentration, the oxygen uptake/release of bulk ceria may be enhanced by knowledgeable nanometer level design of shape and size of the particles [4][5]. The 'nanosize effect' next to increasing defect concentration [6][7] comes along with modification of such physicochemical characteristics of the particles as lattice parameter [8], surface area [9], microstrain [10], surface complexation patterns [11] and electronic band structure [12]. The increased active sites availability leads to application of nanosized ceria particles especially in catalysis in such reactions as CO oxidation [13], soot oxidation [14], ethanol reforming [15] and ketones cyanosilylation [16]. However, the agglomeration and sintering of the powdered samples may limit ceria nanoparticles commercial utilization. Also, there are safety concerns related to usage of nano-sized materials that may affect environment and biological organisms in an unpredictable way [11]. One of the possible solutions to this problems is designing hierarchically structured porous materials composed of ceria crystallites that preserve nanosize-arised properties while keeping large size of nanoparticles assemblage unit.

Hierarchical materials are solids that are composed of elements which themselves possess structure [17]. In nature, the architecture of such materials arise from the process of functional adaptation at all levels of hierarchy, which lies behind the exceptional mechanical properties of e.g. wood or bones [18,19]. Despite the far greater architectural sophistication of natural materials, the hierarchy introduced into synthetic inorganic materials gives rise to occurrence of new properties or enhancement of already existing ones such as increased permeability, more efficient light-harvesting, high storage density or fast charge separation, to name a few [20]. Catalytic performance of hierarchical zeolites is facilitated due to synthetically implemented micro-meso-macroporous structure, improved mass transfer and increased active sites availability [21,22]. Due to that, the recent researcher's interests were directed into designing and testing the properties of hierarchical materials and short summary of ceria-based 3D architectures may be found in the literature [23,24]. Many examples of hierarchical materials application in energy storage systems was reviewed by Wu et al. [25] and in catalysis summed up by Parlet et al. [22]. Also, the synthesis of mesocrystals, the solids conceptually related to hierarchical materials (in particular this are superstructures of nanoparticles with mutual order), attracts researcher's attention due to showing collective and emergent properties [26–28]. Testing the catalytic properties arising from such hierarchical structures are not fully examined and may be full of surprises [29].

In addition to designing material on a meso-to-macro scale, dopants may be introduced into nanoparticles which modify their properties at the micro-scale level. Presence of dopant in the cerium oxide structure is inevitably linked to creation of oxygen vacancies by substitution of Ce^{4+} ions by their low-valent counterparts and subsequent removal of oxygen atoms for charge balance [30]. Such defect engineering in ceria has been studied extensively in the past with different rare earth and transition elements [31]. Due to the dependence of oxygen storage capacity on the level of oxygen depletion that changes during the run of the specific catalytic reaction, "the window of catalytic operation" has been postulated to explain and tune catalytic activity [32]. Next to the size and morphology manipulation, dopant concentration may influence oxygen content and diffusion capabilities. Out of all lanthanides Sm and Gd possess the highest conductivity values which is ascribed to optimized ionic radii mismatch and subsequent structural distortions [31]. From the other hand, oxygen storage/release capabilities of ceria is linked to enhanced catalytic activity [33]. Also, it has been evidenced in the literature that increasing Gd dopant concentration within ceria causes gradual microstructure evolution from fluorite to Gd_2O_3 C-type structure, but lowering the size of particles hinders formation of C-type domains on behalf of lattice distortion spreading over full nanoparticle volume [34,35]. Moreover, while OSC is responsive to sample morphology, surface area as well as ageing, the stabilization of mesocrystal architecture would make it possible to maximize the material's utility potential. Therefore, testing the influence of Gd concentration within ceria on catalytic activity while controlling at the same time the material mesoscale architecture is promising research area to pursue.

Automotive exhaust gasses in the form carbon monoxide, hydrocarbons (HCs) and nitrogen oxides (NO_x) as well as particulate matter (PM) constitute the main environmentally harmful pollutants due to ever increasing human mobility [36,37]. Because of undesirable formation of such by-products caused by not complete fuel combustion in Diesel engines, the search for pollutants oxidation techniques is an issue of current research. While utilization of noble metal-free CeO_2-based mixed oxides show potential in low-to-middle temperature oxidation of CO and soot particles [30], its utilization in propane oxidation in nanocrystalline form may be somewhat limited [38]. Engineering 3-dimensionally hierarchically structured porous materials for HCs oxidation may add value to the present automotive exhaust gases treatment.

The objective of this work was to inspect the role of dopant concentration and mesoscale arrangement of nanoparticles in catalytic propane and soot oxidation by mixed gadolinium-cerium hierarchically structured particles. While the majority of recent literature studies focus on designing 0D or 1D nanostructures, this research concentrate on mesocrystal architecture engineering, especially taking into account material facilitated stability and added properties that emerges from collective behavior due to arrangement of nanocrystallites. In particular, dopant-induced changes of mesocrystal hierarchical architecture in terms of microstructure, porosity, morphology and nanoparticles organization and their influence on the catalytic activity were rigorously studied.

2. Method

2.1 Materials and synthesis

Mixed $Ce_{1-x}Gd_x(HCOO)_3$ formate star-shaped particles were obtained by solvothermal method [24]. Proper amounts of $Ce(NO_3)_3$*6 H_2O and $Gd(NO_3)_3$*6 H_2O were dissolved in 15 ml of DMF with the stochiometric ratios corresponding to assumed $Ce_{1-x}Gd_x$ (x=0; 0.1; 0.3; 0.4; 0.5; 0.7; 0.9; 1) mixture concentrations. 0,860 g of $Ce(NO_3)_3$*6 H_2O was used to synthesize $Ce(HCOO)_3$ sample. In the second beaker 0,315 g of benzene-1,3,5-tricarboxylic acid was dissolved in 20 ml of DMF under continuous stirring followed by addition of 15 ml of formic acid. The solution from the two beakers were combined and stirred for 5 minutes followed by thermal treatment in 130°C for 3 h under autogenous pressure in the solvothermal reactor. The product was washed twice in DMF and acetone to remove post-synthetic residues and dried at 65°C throughout the night.

Mixed $Ce_{1-x}Gd_xO_{2-x/2}$ oxide hierarchically structured star-shaped particles (HSPs) were obtained by oxidative thermolysis of formate samples. The formate powders were put into the furnace and heated at 400°C for 3h in static air.

CeO_2 oxide nanoparticles (NPs) were synthesized by microemulsion (water-in-oil) method [39]. The powder sample was dried and then preheated in static air at 550°C for 3 h to get rid of surface nitrate residues [40].

2.2 Characterization methods

The materials were characterized by several physicochemical techniques followed by testing in soot combustion and propane oxidation catalytic reactions. To get insight into the structure and microstructure powder X-ray diffractograms (PXRD) were recorded on a PANalytical X'Pert Pro X-ray diffractometer. Scherrer formula was applied to four main PXRD maxima ((111), (200), (220), (311)) of $Ce_{1-x}Gd_xO_{2-x/2}$ samples to estimate crystallite sizes. Strain and size contributions to PXRD patterns were resolved by Rietveld refinement via the use of FullProf software. Instrumental broadening was included by refinement of standard silicon sample followed by refinement of PXRD profiles with the use of TCH Pseudo-Voigt function.

Materials were subjected to detailed microscopic studies in order to get insight into their architecture in terms of morphology of building units at different levels of hierarchical organization. Transmission Electron Microscope (TEM) images and high resolution (HRTEM) images in bright-filed (BF) and dark-field (DF) modes were collected via the use of Philips CM-20 SuperTwin as well as double aberration corrected FEI Titan^3 Themis 60-300 microscopes at the accelerating voltage of 160 kV and 200 kV, respectively. Selected Area Diffraction (SAED) patterns were collected to get insight into textural characteristics. Scanning electron microscope images were collected on FEI Nova NanoSEM 230 equipped with ETD and TLD detectors. Pole tip protection mode was used to image detailed surface characteristics.

EDS spectrometer (EDAX PegasusXM4) was used for elemental analysis. Global concentration measurements were performed on samples placed in carbon resin and pressed at 180 ^{o}C in 250 bar in order to obtain a flat surface. Signals from three randomly selected areas of ca. 4500 μm^2 were collected to assure satisfactory statistical averaging. For dopant distribution imaging Scanning Transmission Electron Microscope- X-ray Energy Dispersion Spectroscopy (STEM-XEDS) analysis was performed using the high efficient Super-X EDS system, integrated by 4 window-less SDD detectors symmetrically arranged around the sample and the objective lens pole pieces at the FEI Titan^3 Themis 60-300 microscope operated at 200 kV. The acquisition of XEDS maps was carried out using an electron probe less than 0.5 nm, beam current of 200 pA, convergence angle of 19 mrad and 20 keV of range. Each chemical map was collected as a series of frames, where an area of 512 x 512 pixels was scanned 100 times, employing spatially drift-compensation tool, with a dwell time per pixel of 30 µs, taking approximately 15 minutes per spectral image dataset. The XEDS post-treatment data was performed using Velox software, which allows quantification by Cliff-Lorimer (K-factor) method and absorption correction. The elemental maps of cerium and gadolinium were generated using the family of the Ce-Lα and Ga-Lα lines.

Cerium oxidation state analysis was performed by Spectrum Imaging- Electron Energy Loss Spectroscopy (SI-EELS) technique employing a source at 200 kV, the spectrometer was set to 0.25 eV/channel for dispersion, dual-EELS mode, using a convergence angle of 19 mrad and a collection semi-angle of 49 mrad, and operated with relative low beam current (≈ 30 pA). Under those experimental conditions a high energy resolution of 0.9 eV was obtained at the zero-loss peak (ZLP) and that ZLP signal allow us aligned all EELS spectra. Additionally, PCA-ICA routine was used to separate signals of different oxidation states employing Hyperspy [41].

Raman spectra in the 50-1500 cm^{-1} range were collected on Renishaw InVia Raman microscope equipped with confocal DM 2500 Leica optical microscope, a thermoelectrically cooled CCD as a detector and an argon laser operating at 488 nm. Oxygen vacancy concentration was determined from Raman profiles data as intensity ratio of I_{570}/I_{460} peaks [42].

N_2 physisorption study was performed on ASAP 2020 Micromertics in order to get insight into materials porosity and stability. Temperature programmed reduction tests (H_2-TPR) were performed on Autochem II 2920 (Micromeritics, USA) equipped with TCD detector. 50 mg of sample was placed in quartz reactor and flushed with helium for 15 minutes followed by reduction measurements in the 30 cm^3/min flow of 5% H_2/Ar_2 in the temperature range of 25 – 900°C and 10°C/min temperature increase.

3.3 Catalytic tests

The catalytic activity of the samples was tested in propane oxidation reaction. Typically, 50 mg of sample was placed in fixed-bed flow reactor (quartz U-shaped tube, 10 mm inner diameter) followed by installation in programmable furnace. The step-wise propane conversion measurements were performed in the temperature range of 180-540°C in the gas flow (mixture 2500 vppm propane in the air, 50 cm^3/min) followed by gas chromatography analysis (Perkin-Elmer ARNEL Clarus 500 equipped with Elite Plot-Q chromatographic column and a flame ionization detector). Conversion at each temperature point was recorded when steady-state conversion was reached in terms of peak area differences less than 1% between consecutive readings. The propane conversion was calculated using the following formula:

$$K = \frac{A_{RT} - A_T}{A_{RT}} * 100\%$$

when K- conversion [%], A_{RT} – area of the peak at room temperature, A_T- area of the peak at selected temperature.

Soot oxidation measurements were performed in “tight contact” mode by placing the grinded mixture of 40 mg of ceria and 20 mg of soot (carbon black Printex-U, Degussa S.A.) in corundum crucible into TG analyzer Derivatograph MOM Q- 1500D with a programed temperature increase of 5 °C/min in range 25 – 550 °C/700 °C under static air.

3. Results and discussion

3.1 Architecture of hierarchically structured star-shaped particles (HSPs)

The applied solvothermal approach has led to formation of $Ce(HCOO)_3$ particles possessing emergent star-shaped morphology (Fig. 1.A). From the practical chemistry point of view, the morphology of cerium formate and mixed cerium formate crystals depends on two factors recognized in the literature, the type of ceria precursor and the temperature, leading to formation of needle-shaped or rod-shaped cerium formate crystals [43]. In addition to the recognized factors, the composition of the solvothermal reaction mixture also influences the particles morphology, as tested in this study by synthetic protocol modification. Carrying out the synthesis under strongly acidic conditions and without the use of dimethylformamide has led to formation of sphere-like $Ce(HCOO)_3$ particles (Fig. 1.B), while neutralization of the reaction mixture by NH_3 has led to formation of clumped rod-shaped $Ce(HCOO)_3$ crystals (Fig. 1.C; see PXRD patterns and synthetic details on Fig. S1 in Supporting Information). The presence of DMF and acidic conditions impose formation of star-shaped particles. As literature reports, DMF may not only serve as the inert polar aprotic solvent for the reaction but it may also take active role in the crystallization as a stabilizer [44] that may modify growing process.

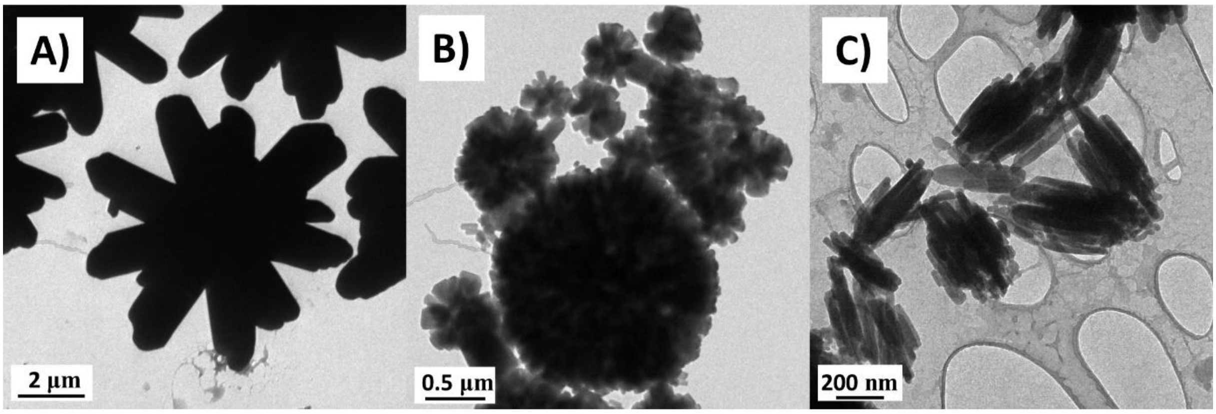

Fig. 1. TEM images of $Ce(HCOO)_3$ particles synthesized in different conditions: A) star-shaped morphology (DMF and formic acid), B) Sphere-shaped morphology (formic acid), C) Clumped rod-shaped morphology (DMF and formic acid neutralized by ammonia).

Despite the fact that complex morphologies formation can be explained by classical crystallization mechanisms, i.e. spherulitic growth in the high supersaturation conditions leading to formation of polycrystalline spheres or dumbbell particles [45], the formation of $Ce(HCOO)_3$ star-shaped particles seems to be multistep and involve non-classical growth mode by e.g. oriented attachment. Such oriented attachment may take place at the early stage of crystallization as the self-limited nanoclusters/nanoparticles agglomeration followed by classical crystal elongation or at the late stage of the process in the form of self-limited agglomeration of fully developed formate crystals. DMF may act as stabilizing agent for cerium formate nanoclusters formation at the early stage. This type of stabilizing effect by DMF was observed for several Au, Cu metal and Fe_2O_3 metal oxide nanoparticles (>2 nm) as well as for Ir, Pd nanoclusters (< 2nm) [44]. On another note, acidic conditions trigger hydrolysis of DMF, as has been described in the process of formation of Pd nanoparticles [46]. It is not excluded that solvent decomposition may serve as driving force for nanoparticles agglomeration. Such self-limiting process of aggregation of formate particles at the early stage of crystallization is followed by multidirectional growth into the star-shaped morphology.

Alternatively, site-selective adsorption at the specific primary crystal sites may be responsible for multidirectional crystallization. Cölfen et al. presented detail description of the multistep process of 10-petal flowerlike $BaSO_4$ particles, in which site-selective adsorption of polymer additives triggered preferential growth [47]. Hence, the self-limiting adsorption of reaction mixture moieties (e.g protonated DMF) on the particular crystal planes may be the factor that modulates the hindrance and growth of cerium formate crystals. Since there is no available data in the literature on the early stages of cerium formate crystal formation further research is needed to determine the complex morphology formate crystallization by the use of such techniques as in situ fluid cell HRTEM imaging or cryo-TEM shock-frozen samples monitoring.

The applied solvothermal synthesis has led to the formation of mixed $Ce_{1-x}Gd_x(HCOO)_3$ formate particles in the whole tested dopant range (x=0; 0.1; 0.3; 0.4; 0.5; 0.7; 0.9; 1). All the samples are phase pure and match well the cerium formate reference data in terms of 2θ positions and intensity ratios (Fig. 2.A). Shift of diffraction maxima into higher angles with the increase of dopant (Fig. 2.B) is in line with the Vegard's empirical law, since incorporation of Gd^{3+} ions ($r\ {}^{IX}Gd^{3+} = 0.1107$ nm) [48] bring contraction to the cerium formate lattice ($r\ {}^{IX}Ce^{3+} = 0.1196$ nm) [48]. This proves the wide range miscibility of Gd^{3+} ions within the cerium formate matrix. Good dopant mixing at the microstructural level is accompanied by the formation of the particles with well-defined star-shaped morphology up to 70% of the dopant concentration level (Fig. 2.C) and homogeneity of sizes (Fig. 2.D). Also, EDS spectroscopy confirmed the well miscibility of Gd^{3+} ions within cerium formate for all the samples, as empirical concentration does not deviate significantly from the nominal values (Fig. 2.D). In the literature, synthesis of undoped $Ce(HCOO)_3$ star-shaped particles [49], $Ce_{0.9}REE_{0.1}(HCOO)_3$ (REE- rare earth element) [24] and $Ce_{0.9}Gd_{0.1}(HCOO)_3$ rods [43] has been presented. Solvothermal synthesis applied in this study proves to be an effective method in producing the whole range Gd-doped particles with well-defined morphology.

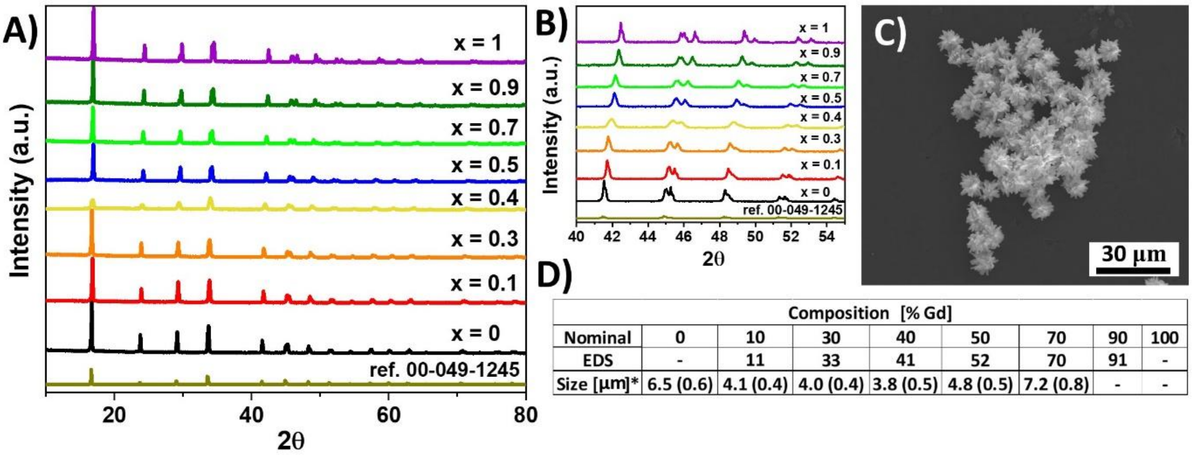

Composition [% Gd]								
Nominal	0	10	30	40	50	70	90	100
EDS	-	11	33	41	52	70	91	-
Size [μm]*	6.5 (0.6)	4.1 (0.4)	4.0 (0.4)	3.8 (0.5)	4.8 (0.5)	7.2 (0.8)	-	-

Fig. 2. A)-B) PXRD patterns of $Ce_{1-x}Gd_x(HCOO)_3$ (x=0 – 1) particles before oxidative thermolysis; C) SEM image of $Ce_{0.3}Gd_{0.7}(HCOO)_3$ particles; D) data summary for composition and average size of star-shaped mixed cerium formate particles; *size calculation of star-shaped particles according to ref. 24.

Oxidative thermolysis induced the chemical change of $Ce_{1-x}Gd_x(HCOO)_3$ formate particles into $Ce_{1-x}Gd_xO_{2-x/2}$ mixed oxide materials characterized by hierarchically ordered architecture. The morphological constitution of the particles may be described by three distinctive levels of structural organization. At the first level particles are composed of nanocrystallites that form porous rods at the second level of hierarchy. The third level is constituted of effuse star-shaped particles that preserve the morphology after thermolysis. The detailed description of structural hierarchy and its functionality is presented in our previous paper [24]. In this contribution the influence of the dopant-induced architectural changes in terms of microstructure, porosity and morphology on catalytic activity were studied.

The evolution of particles morphology for the whole mixed oxide $Ce_{1-x}Gd_xO_{2-x/2}$ series is presented in Fig.3. The well-defined star-shaped morphology is preserved for up to 70% of dopant concentration. Above this concentration level, formation of fragmented arms and plain rods is observed. This morphological alternation is accompanied by loss of mesoscale nanocrystallites organization which is confirmed by selected area electron diffraction (SAED) patterns collected at low magnification from the zones of the arms shown in Fig. 3. Discrete SAED patterns that are observed for particles with a dopant level below 70% indicate preferential orientation of nanocrystallites within the material volume. As indicated in the literature, such effect was previously observed by us for star-like ceria [24] and by many authors for other systems [39,50]. However, the change of SAED patterns into complete diffraction circles for $Ce_{0.1}Gd_{0.9}O_{1.55}$ and Gd_2O_3 samples suggest the loss of ordering of nanocrystallites in highly doped Gd-based mixed oxides (see Fig. 3). As described in section 3.1.3, this results in a loss of material varied porosity as well as a uniform crystal facets exposition of catalytically active CeO_2 along the channels. Also, since the 3rd level morphology of particles in the form of effuse-armed stars enhances ceria-soot contact and surface oxygen availability [51,52], particles for up to 70% of dopant were studied in catalytic oxidation tests.

In many nature's hierarchical materials the architecture arises as a functional adaptation to specific constraints through adaptable growth during which the material's form and microstructure are created in the same process [18]. In the case of formate-derived ceria particles this type of directed adaptation occurs through optimized escape of post-reaction gases from the material's bulk interior during thermolysis process that ultimately creates porosity. Following that, due to such fine-tuned architecture for facilitated mass transfer, as synthesized star-shaped particles are interesting for catalytic applications.

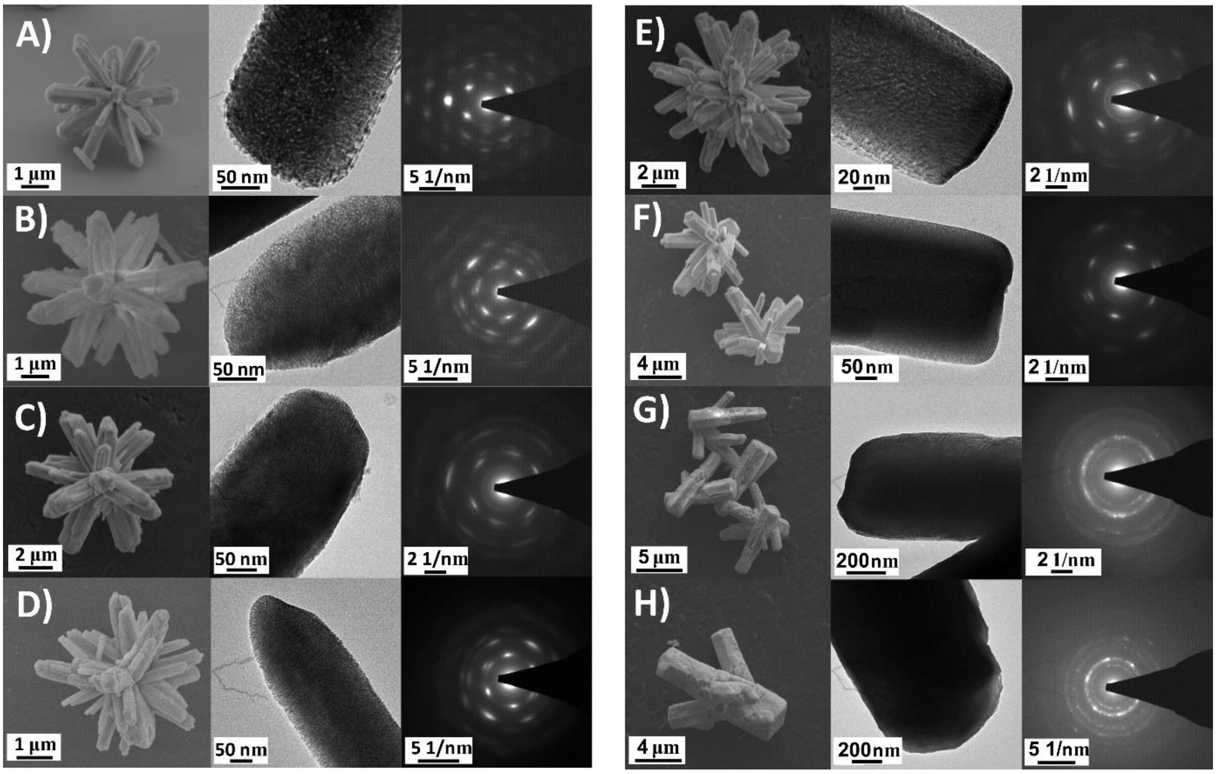

Fig. 3. SEM image (first column), TEM image (second column), SAED pattern of corresponding TEM image (third column) of hierarchically structured star-shaped particles: A) CeO_2 ; B) $Ce_{0.9}Gd_{0.1}O_{1.95}$; C) $Ce_{0.7}Gd_{0.3}O_{1.85}$; D) $Ce_{0.6}Gd_{0.4}O_{1.8}$; E) $Ce_{0.5}Gd_{0.5}O_{1.75}$; F) $Ce_{0.3}Gd_{0.7}O_{1.65}$; G) $Ce_{0.1}Gd_{0.9}O_{1.55}$; H) Gd_2O_3.

3.1.1 Morphology and structure

To assess the temperature-triggered changes of materials microstructure and architecture, particles were annealed step-wise at 400°C, 450°C, 500°C, 550°C, 600°C, 700°C, 800°C, 900°C, 1000°C for 3h each followed by collection of powder diffraction patterns (PXRD) at as selected temperatures (Fig. 4.A). The heating rate of 5°C/min was applied to bring the samples to the selected isothermal temperature exposure. Since CeO_2 nanocrystallites are prone to grow and coarsen at the elevated temperatures [53], this investigation allows to assess the stability of hierarchical material architecture at the temperatures of diesel engines exhaust gas catalyst real operating conditions. Soot particles spontaneously burn in air at about 600–625°C. As known, this temperature range is not regularly achieved in the typical diesel engine operations for enough periods of time to enable selfregeneration [54]. For this reason, it is necessary to use catalysts that effectively lower the soot combustion temperature.

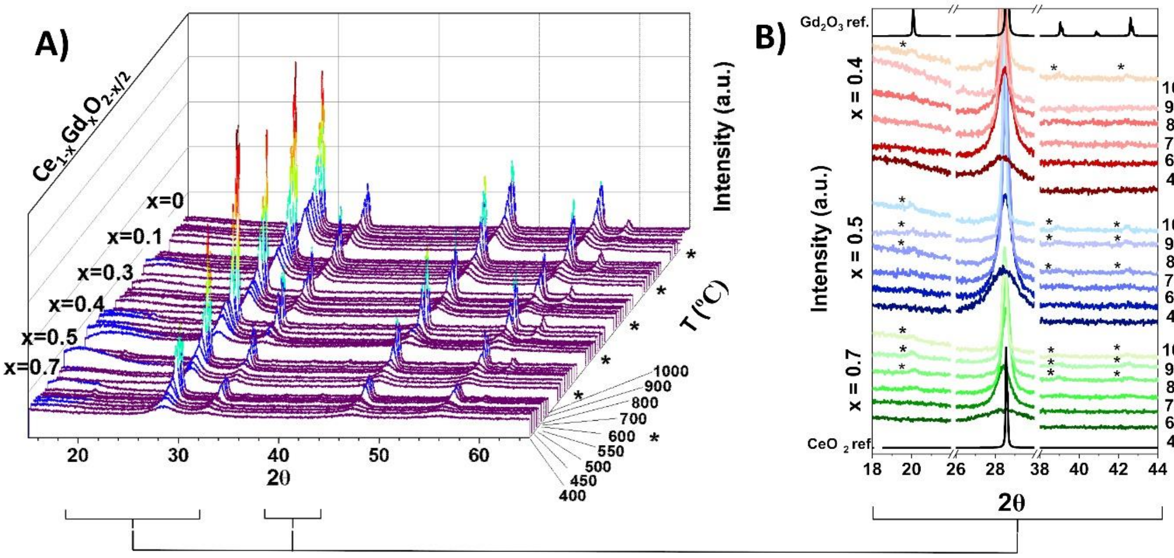

Fig. 4. A) PXRD patterns of $Ce_{1-x}Gd_xO_{2-x/2}$ (x= 0; 0.1; 0.3; 0.4; 0.5; 0.7) hierarchically structured star-shaped particles organized according to dopant concentration (left axis) and heating temperature (right axis); B) Magnification of low 2θ range of PXRD patterns presenting maxima arising from C-phase formation (marked by asterisk).

All of the tested mixed oxide samples (Fig. 4.A) have the 2θ peak positions that correspond well to CeO_2 fluorite structure ((111)= 28,5491°; (200)= 33,0766°; (220)= 47,4886°; (311)=56,3265°, ref. 00-004-0593). No signs of phase segregation or the presence of additional phases were observed for samples at the starting temperature of 400°C, but heating the samples triggered the structural change. Closer inspection of powder diffractograms presented in Fig. 4.B reveals the overall limit of fluorite F structure stability in mixed gadolinium–cerium oxides, within the capabilities of X-ray diffraction technique. The first occurrence of C-type phase that is characteristic for sesquioxide Gd_2O_3 was observed for $Ce_{0.6}Gd_{0.4}O_{1.8}$ at 1000°C as well as for $Ce_{0.5}Gd_{0.5}O_{1.75}$ and $Ce_{0.3}Gd_{0.7}O_{1.65}$ at 800°C (see Fig. S2 in Supplementary Materials for SAED pattern that confirm superstructure formation in $Ce_{0.3}Gd_{0.7}O_{1.65}$ heated at 900°C). Since PXRD data average over all unit cells in the crystal volume, the local fluorite symmetry distortions or C-phase aggregates are invisible as far as the particular threshold of the defect size is exceeded, so the presence of sesquioxide-type microdomains is not excluded in the low temperature-treated samples [55]. EXAFS spectroscopy [56], Monte Carlo modelling [57] and μ-RAMAN spectroscopy [58] reveal local fluorite symmetry distortions in low concentration Gd-, Sm- and Y-doped ceria. Additionally, HRTEM study of $Ce_{1-x}Gd_xO_{2-x/2}$ (x=0.1-0.8) systems heated at 800°C show progressive evolution of C-type domains [34]. For that matter, TEM study of Gd-doped ceria sintered at 1400°C in air [59] reveals already the presence of C-domains at 10 at% Gd doping level. As reported in the literature [55,60], oxygen ion migration via the hopping mechanism occurs within fluorite F-type structure, while C-type domains hinder the ionic conductivity. Thereout, the assessment of the boundary of F-C structure transition is of particular importance from the catalytic point of view. The existence of hybrid H structure in between those of F-type and C-type instead of F-C microdomain segregation is proposed in the literature as well [61]. So, the presence of local deviations from fluorite symmetry that introduces microstrain and thus the new chemo-mechanical characteristics makes mixed ceria interesting in catalytic study [62].

Due to the oxygen vacancies, the oxygen ion (O^{2-}) travels through the lattice by hopping mechanism enabling the ionic conduction [63]. The results of studies on structure evolution of nanocrystalline ceria-based $Ce_{1-x}Yb_xO_{2-y}$ mixed oxides with increasing Yb content (distributed randomly in the ceria lattice) were presented by Małecka at al. [64]. OSC tests had shown that the highest reducibility of Ce ions and the highest oxygen extraction were observed for $Ce_{0.5}Yb_{0.5}O_{1.75}$, which has a hybrid H structure with the highest number of defects and the highest average maximum strain. On the other hand, too large structural distortions in ceria based mixed oxides could be responsible for the lowering of oxygen ions conductivity [31].

The shape of PXRD maxima is strongly affected by the temperature as well as the dopant concentration level. While there is the overall increase of peak broadening with the dopant concentration increase, the peaks are getting narrower when heating at higher temperatures. The qualitative interpretation of the PXRD data suggest that the increase of Gd^{3+} ions hinders the growth of nanocrystallites. In order to asses this effect quantitively, crystallite sizes were estimated by application of Scherrer formula (eq. 1) to four (111), (200), (220), (311) peaks of PXRD data followed by averaging of as obtained D sizes:

$$D \approx \frac{K\lambda}{\beta cos\theta} \qquad \text{(eq. 1)}$$

where, D- particle size, K- dimensionless shape factor (0,9), λ- X-ray wavelength (1,54056 Å) β- line broadening at half the maximum intensity (FWHM), θ- Bragg angle.

Then, Arrhenius-type plots were created (Fig. 5.A) followed by calculation of the nanoparticles overall growth activation energies by the use of the equation (eq. 2):

$$lnD = Ae^{-\frac{E_a}{RT}} \qquad \text{(eq. 2)}$$

where, D- particle size, A- pre-exponential factor, E_a- activation energy, R- gas constant, T- temperature.

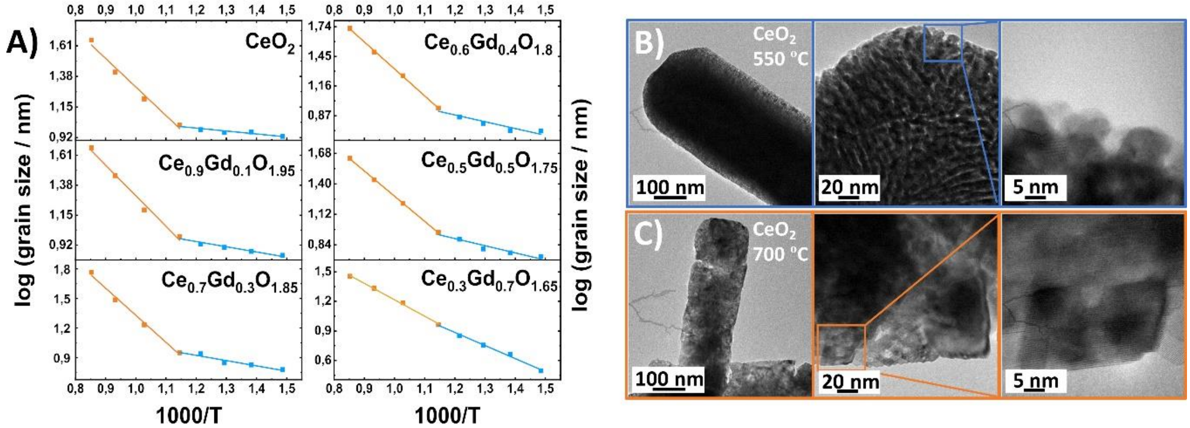

Fig. 5. A) Arrhenius-type plots for $Ce_{1-x}Gd_x O_{2-x/2}$ HSPs; B) TEM images showing architecture of CeO_2 star-shaped particle arm heated in 550°C (blue frame); C) TEM images showing architecture of CeO_2 star-shaped particle arm heated in 700°C (orange frame; see description in text).

Various mechanisms of CeO_2 nanoparticles growth have been proposed in the literature. As shown on Fig. 5.A, pronounced division into two growing modes is visible in the constructed Arrhenius-type plots with one and the same demarcating temperature of 600°C occurring in all the differently Gd-doped samples. For temperatures below 600°C (blue lines in Fig. 5.A) the growth of nanoparticles is rather slow, since the particles size changes from 3-8 nm at 400°C to 9-10 nm at 600°C (see details in Table S1 in Supporting Information). At the same time, in this temperature regime the calculated activation energy of overall growth is low (4-25 kJ/mol, see Fig. 6). Ivanov at al. have shown, that in case of hydrolysis-derived CeO_2 nanoparticles the threshold crystallite intergrowth mechanism occurs at temperatures of 200-700°C [53]. In this temperature regime, isothermal treatment of the ceria powder for 2-8 h show the lack of nanoparticle size change within the measurement error that is explained by limitation in particle movement as well as hindrance of surface (grain) boundary mass transfer due to various types of stoppers such as surface defects and contacts with other particles, which explains rather slow growing rate of nanocrystallites observed in this study [53]. On the other hand, the low values of as obtained activation energies may be attributed mainly to strain relaxation within the nanoparticles rather than growth triggered by mass transfer (see section 3.1.2). TEM images of the CeO_2 sample heated in 550°C (Fig 5.B) confirm the presence of homogeneously sized small nanoparticles (<10 nm) arranged into the well preserved second-order architecture of porous rods.

On the contrary, in temperatures above 600°C (orange lines in Fig. 5.A) the growth is more rapid which may be linked to the change of growth mechanism into coarsening through Ostwald ripening [65]. In this case complete redissolving of smaller crystallites behalf of growth of bigger ones occurs, which is triggered by the particles surface energy reduction. Because this process demands more broad mass transfer, the activation energy is larger (32-53 kJ/mol, see. Fig. 6). Han et al. have shown that ceria growth at 800°C is time-dependent, as the particles grew in size from ~30 nm to ~55 nm in 8 h time period [66]. This is in accordance with the rapid size change observed in this study (from 15-16 nm at 700°C up to 65-80 nm at 1000°C; see details in Table 1 in Supporting Information). Also, TEM images presented in Fig. 5.C show polydisperse distribution of particle sizes in the sample heated at 700°C for 3 h. In addition to small-sized particles (below 10 nm), there are crystallites many times larger (up to 40 nm), which indicates the crystallite coarsening. The as observed change in growing mechanism may yield the more rapid porosity decline of HSPs above 600°C. Simultaneously, stability of architecture may be extended through doping, since Gd^{3+} ions lowers the capability of nanocrystallites growth and thus the possible inhomogeneous volume expansion.

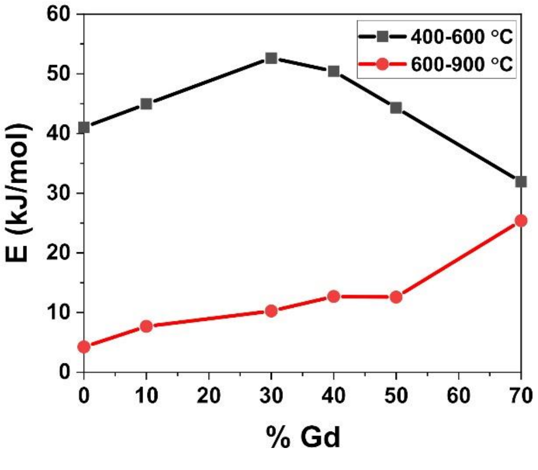

Fig. 6. Activation energy of overall growth of nanoparticles as a function of dopant concentration for $Ce_{1-x}Gd_xO_{2-x/2}$ HSPs for two temperature regimes: 400-600°C (red line) and 600-900°C (black line).

Introduction of dopant systematically increase the activation energy of nanocrystallites overall growth in the lower temperature range (400-600°C) from 4,2 kJ/mol (CeO_2) up to 25,4 kJ/mol ($Ce_{0.3}Gd_{0.7}O_{1.65}$) which indicates the enhanced resistance for temperature-triggered growth (see. Fig. 6). In the higher temperature regimes (600-900°C) the profile of activation energy has a maximum for $Ce_{0.7}Gd_{0.3}O_{1.85}$ particles indicating that this is the most growth-resistant sample. Comparison to the literature data for microemulsion derived NPs show that the values of nanoparticles overall growth activation energy for HSPs, tested in this study, are significantly lower. The activation energy of CeO_2 NPs growth treated up to 500°C equals 20 kJ/mol and above 600°C is as high as 105 kJ/mol [65]. The differences may result from the mutual orientation and thus the greater contact of noncrystallites in formate-derived star-shaped particles, which determine coarsening dynamics by facilitation of ion transfer [53]. Regardlessly, the material treated in 550°C preserves the high surface area and porosity, so it is a good candidate as a catalyst support.

3.1.2 Microstructure

In order to evaluate the influence of Gd^{3+} doping on the microstructural-level characteristics of the materials, PXRD profiles were subjected to Rietveld refinement. The main advantage of this approach is that it takes into account the whole profile and due to the different angle dependence of Lorentzian and Gaussian contributions to peak shape it is possible to discern micro-strain and size contributions to the pattern [67]. This approach enabled to evaluate microstructural characteristics of the samples for which fluorite structure is retained ($Ce_{1-x}Gd_xO_{2-x/2}$, $0<x<3$) [61]. Instrumental broadening was included by refinement of the standard silicon sample followed by refinement of 18 PXRD profiles with the use of TCH Pseudo-Voigt function [68,69]. The applied procedure gave reasonable results in terms of cell parameters (Fig. S3 in Supplementary Materials) as well as nanoparticle size and strain values (Fig. 7.B and C, respectively).

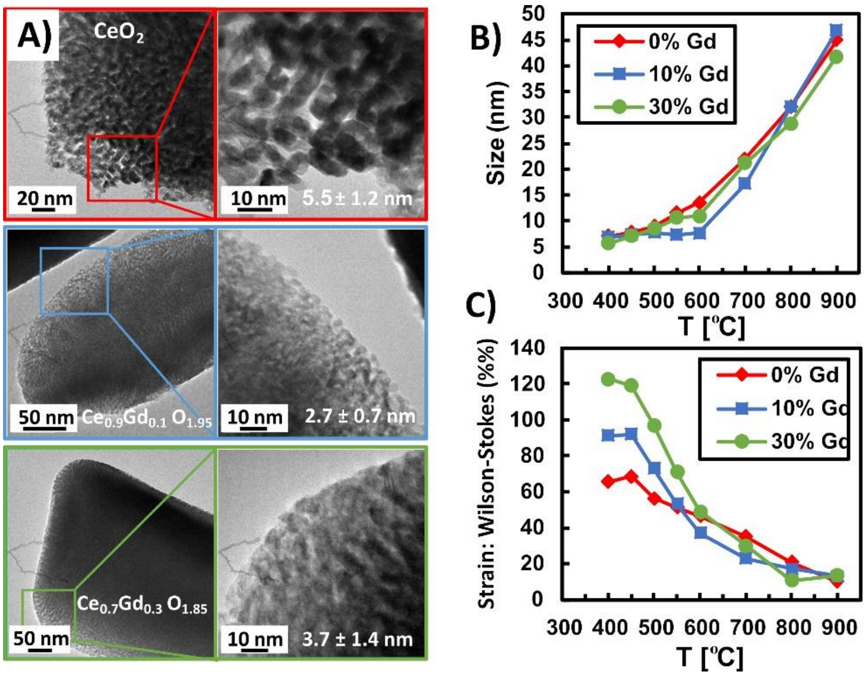

Fig. 7. A) TEM images of HSP arm (left) and magnification of the selected area (right) showing nanoparticles of: CeO_2 (red frame), $Ce_{0.9}Gd_{0.1}O_{1.95}$ (blue frame), $Ce_{0.7}Gd_{0.3}O_{1.85}$ (green frame); size

averaged over 150 nanoparticles; B) Nanocrystallite size as a function of temperature derived from PXRD data (Rietveld refinement); C) Nanocrystallite microstrain as a function of temperature derived from PXRD data (Rietveld refinement).

As visible in Fig. 7.C, the introduction of dopant induces considerable value of strain in the crystallites heated at 400°C and the differences between variously doped samples are clearly distinguishable, whereby the more dopant concentration, the larger the strain. This result is consistent with studies on phase evolution of nanocrystalline $Ce_{1-x}Lu_xO_{2-y}$ and $Ce_{1-x}Yb_xO_{2-y}$ mixed oxides (nanopowders) [70]. While the heating temperature increases, the strain relaxes, and the differences of microstrain for samples heated above 600°C became less discernible. This two trends correspond well to the two growth modes described in section 3.1.1 with strain contribution becoming less significant in the higher temperature growth mode. Also, since the overall nanoparticle growth energy is divided into two contributions, to relax strain and to increase the size, Gd-doped samples show slower nanocrystallites size enhancement when heated. This affects the mesoscale architecture of the materials that manifest in the formation of additional porosity (Fig.10; description in section 3.1.3). The nanoparticle size values obtained from Rietveld refinement for samples heated in 400°C (Fig. 7.B) are close to the ones calculated from TEM images by averaging the size of nearly 150 nanocrystalites (Fig. 7.A). Also, the morphology of geometrical CeO_2 nanoparticles that expose clearly defined planes changes into round particles when Gd-dopant is introduced.

To elucidate the global Gd distribution, a set of STEM-XEDS analysis were taken at different angles in a chosen arm of the star shaped-particle. STEM-HAADF images along with Ce versus Gd maps reveal the spatial distribution of both elements indicating their well mixing along the arm (Fig. S4 in Supplementary Materials). This is in accordance with our previous study, but the result gives additional 3D-resolved insight into the elemental architecture of the arm. To get even more insight of the elemental distribution, a line profile analysis of Ce and Gd in atomic percent was performed (Fig. S4. Supplementary Materials). No significant inhomogeneity in Gd distribution has been observed and dopant level was detected between 9-12 at% Gd –balanced Ce for $Ce_{0.9}Gd_{0.1}O_{1.95}$ sample. Analysis taken at higher magnification (Fig. 8.A) confirm the good homogeneity of Gd distribution within ceria matrix.

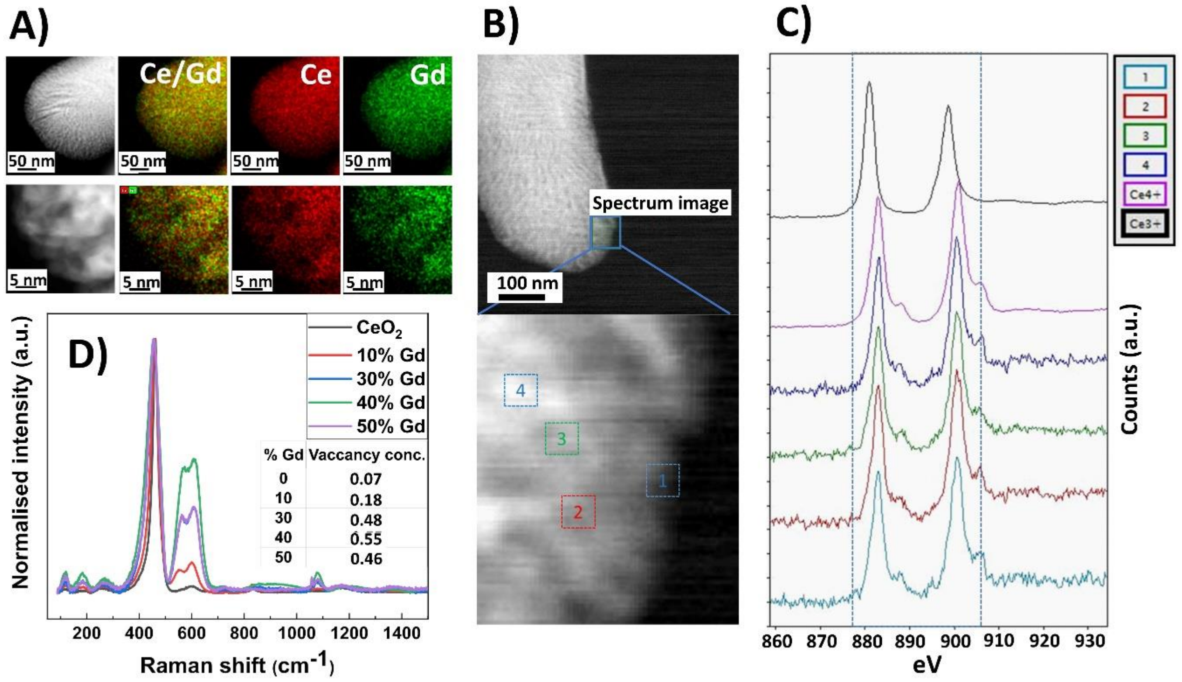

Fig. 8. A) HAADF-STEM (left) and EDS elemental mapping (Ce: red, Gd: green) images of the $Ce_{0.9}Gd_{0.1}O_{1.95}$ star-shaped particle arm (top) and high magnification area of the arm (bottom); B) DF image of the $Ce_{0.9}Gd_{0.1}O_{1.95}$ star-shaped particle arm (top) and individual areas used in EELS analysis (bottom); C) EELS spectra collected from individual regions of the $Ce_{0.9}Gd_{0.1}O_{1.95}$ star-shaped particle arm; D) Raman spectra of the $Ce_{1-x}Gd_xO_{2-x/2}$ (x= 0; 0.1; 0.3; 0.4; 0.5) star-shaped particles; oxygen vacancy concentration presented in insert.

Additionally, some knowledge about the microstructural-level dopant distribution was obtained from the comparison of SI-EELS spectroscopy (Fig. 8.B and C) and Raman spectroscopy (8.D) findings. The SI-EELS profiles collected from the various particle arm edge areas that cover different depths of the material clearly show that there is no Ce^{3+} ions present in the $Ce_{0.9}Gd_{0.1}O_{1.95}$ sample. Analytical post-treatment of the SI-EELS profiles by PCA-ICA method confirmed no Ce^{3+} ion contribution to the spectra (see Fig. S5 in Supplementary Materials). Apparently, this result suggests no presence of oxygen vacancies in $Ce_{1-x}Gd_xO_{2-x/2}$ nanocrystallites, since overall charge balance demands the presence of Ce^{3+} ion near the vacancy or single Gd^{3+} ion.

From the other hand, RAMAN spectroscopy data provide information about the large oxygen vacancy concentration within the materials volume (see insert table in Fig. 8.D), as 1 µm-resolution depth limit of this technique covers the full volume of the HSPs arm [62]. Strong F_{2g} mode around Δ_{465} cm^{-1} is visible for samples with Gd concentration up to 50%. Presence of lower symmetry defect-induced D modes around $\Delta_{\sim570}$ and $\Delta_{\sim600}$ cm^{-1} Raman modes are clearly visible up to 50% of Gd doping concentration with the highest intensity for $Ce_{0.6}Gd_{0.4}O_{0.8}$ sample. In the literature, these bands appear due to oxygen vacancies and Δ_{550} peak (in our case $\Delta_{\sim570}$) is treated as their fingerprint [71].

RAMAN study results stands in a seeming contradiction to SI-EELS spectroscopy findings and may be explained by the dopant cluster formation. If at least two Gd^{3+} ions are neighboring each other in the fluorite F structure, as this holds true for $Ce_{0.9}Gd_{0.1}O_{1.95}$ sample, there is charge balance without cerium reduction. This suggests the non-random Gd distribution at the microstructural level.

To conclude, the synthesis method by mixed gadolinium-cerium formate decomposition creates a material that is characterized by atomic non-random ordering of Gd^{3+} dopant at the microscale level. If such Gd^{3+} ions are neighboring in a systematic way, e.g. through linear chain formation, there are the channels within the material that facilitates oxygen migration due to neighboring easily reducible seven oxygen-coordinated ceria species. Extensive research conducted on the microstructure of $Ce_{1-x}Ln_xO_{2-y}$ mixed oxides indicates that the oxygen vacancies present in clusters tend to form the chain structures or very stable isolate triangle structures (the dumbbell model) [72,73]. At the same time, the adjacent oxygen vacancies (regardless of the short range structure) prefer to locate along 1/2 <110> lattice vector, what is in agreement, again, with earlier work by Wallenberg et. al. [74]. Further study, by e.g. IDPC method, is demanded to confirm proposed postulate.

As Fig. S6 in Supplementary Information shows, doping level above 70% introduces distortion to Ce^{4+} coordination environment. Change of local structure is indicated by the reversed intensity ratios of Δ_{465} and Δ_{600} bands for $Ce_{0.3}Gd_{0.7}O_{1.65}$ sample and the presence of Δ_{370} band in $Ce_{0.1}Gd_{0.9}O_{1.55}$ sample. As Banerji et al. have shown, 80% Gd concentration in ceria matrix causes a change of structure into disordered C-type phase [75]. In the literature, Δ_{370} peak is ascribed to fluorite double-fluorite phase transition [76]. Interestingly, this band is visible in $Ce_{0.5}Gd_{0.5}O_{1.75}$ sample heated in 800°C which is in accordance with PXRD results (Fig. 4.B) indicating the change of structure. However, $Ce_{0.5}Gd_{0.5}O_{1.75}$ sample heated at 400°C show no presence of Δ_{370} band that may indicate that nanocrystallites preserve the fluorite structure up to 50% Gd dopant level.

3.1.3 Porosity

As known in the literature, cerium formate decomposition creates a material that is characterized by well-developed porosity [49]. Introduction of different amounts of Gd dopant into star-shaped HSPs leads to formation of materials characterized by diversified porosity that, however, changes in a systematic way with the increase of dopant concentration, as visible in Fig. 9.A. Since the isotherms of samples $Ce_{1-x}Gd_xO_{2-x/2}$ (x=0 to x=0.7) shown in Fig. 9.A (upper and middle part) have the shape between type II and type IV , the presence of meso- and macroporosity may be inferred, respectively. Sharp rise of adsorption-desorption curves in large p/p_0 regime may be ascribed to condensation in inter-particle voids [77].

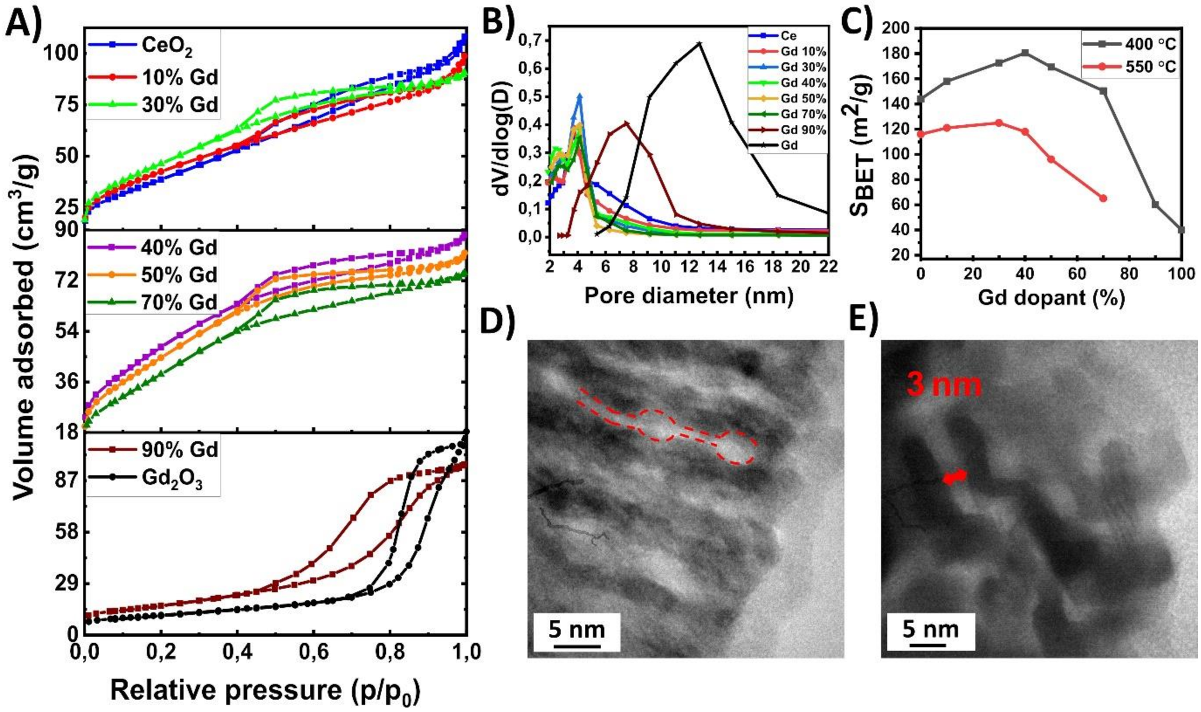

Fig. 9. A) Adsorption-desorption isotherms of $Ce_{1-x}Gd_xO_{2-x/2}$ (x=0 to 1) hierarchically structured star-shaped particles (HSPs); B) Pore size distribution of $Ce_{1-x}Gd_xO_{2-x/2}$ (x=0 to 1) HSPs; C) S_{BET} surface area of $Ce_{1-x}Gd_xO_{2-x/2}$ HSPs determined for samples heated in 400°C (black) and 550°C (red); D) TEM image of CeO_2 HSPs heated in 400°C showing pore shapes and E) pore size.

The shape of hysteresis loops of $Ce_{1-x}Gd_xO_{2-x/2}$ (x=0 to x=0.7) samples show the intermediate state between H2 and H3 type according to IUPAC classification [78]. The steep desorption branch and the low closure point, the features that are characteristic for the H2 type, suggest the occurrence of larger cavities enclosed by small necks [79]. Though, the type II-resembling form of adsorption isotherm and no plateau at very high p/p_0 range, that is characteristic for H3-type hysteresis loop, suggest the main occurrence of thin slits [79]. TEM image in Fig. 9.D present such slit-like pores conjoined with cavities. Due to the mutual displacement of nanocrystallites that form a zig-zag pattern (Fig. 9.E) such cavities are formed which introduces pore diversity. Interestingly, for $Ce_{0.1}Gd_{0.9}O_{1.55}$ and Gd_2O_3 samples (Fig.9.A, bottom part) the shape of hysteresis loops resembles the H1 type, which indicates the cylindrical channels formation. Intriguingly, the SAED patterns collected for these samples (see Fig. 2) do not confirm regular arrangement of crystallites that may suggest the occurrence of sparse and differently oriented ceria nanocrystallites among elongated regularly-arranged gadolinium oxide crystals.

The desorption isotherm was used to calculate pore size distribution according to BJH model [80]. As visible in Fig. 9.B, introduction of dopant changes the proportion of pores with a certain size occurrence in the overall pore size distribution. The most diagnostic region that lies between 5-12 nm indicates that dopants up to 50% concentration level systematically lower the participation of pores in this size range. Since the introduction of dopant reduce the nanocrystallite size, this effect translates into the reduction in the size of the pores. The maximum around 4 nm may be ascribed to tensile strength effect that is a method artifact [81]. Keeping in mind that the desorption branch-calculated pore size distribution is slightly shifted to lower values of pore sizes due to the effect of delayed pore evaporation [81], as calculated pore sizes are in quite good agreement with the pore size values assessed by TEM image analysis (Fig. 9.D and 9.E). However, since 90-100% Gd doped samples possess H1 type hysteresis loop, the desorption branch is more reliable for pore size assessment giving the peak values of 8 nm and 13 nm for $Ce_{0.1}Gd_{0.9}O_{1.55}$ and Gd_2O_3 samples, respectively.

All the samples possess a large surface area extending from 140 m^2/g for CeO_2 up to 180 m^2/g for $Ce_{0.4}Gd_{0.6}O_{1.7}$ (Fig. 9.C). The Gd dopant increases the overall surface area up to 40% of concentration level. This value is very large for cerium oxide family compounds and makes up a good premise for using them as high-surface area active catalyst supports. The repeated measurement of surface area for the same samples heated in 550°C provides information about the stability of the particles architecture. As visible in Fig. 9.C, the heat treatment causes the loss of the surface area to the values of nearly 120 m^2/g for samples up to 40% of Gd. Since the temperature of 550°C belongs to low-temperature nanoparticles growing mode (see section 3.1.1), this may transfer to smaller rate of nanoparticles intergrowth [53].

The SEM-based experiment that consisted of imaging the selected individual star-shaped particles heated both, in 400°C and 900°C, allowed to assess the temperature-triggered changes of architecture. The particles with modest number of macropores were chosen for this study for better visualization. As visible in Fig. 10.A, the morphology of CeO_2 star-shaped HSP is preserved when heated to 900°C. Almost no change of the arm texture is observed which indicate strict coalescence of crystallites (see also Fig. 5.B.). Oppositely, additional pore formation (r_{av}= 19 nm) was observed for 10% Gd-doped HSPs heated up to 900°C for 3h in 5°C/min rate (Fig. 10.B). Due to the lower susceptibility of the doped particles to coalesce into larger crystals, the particles collapse inwardly, forming clusters of nanoparticles (see also Fig. 15.C) that creates the intricate architecture that preserves some porosity at high temperatures [24].

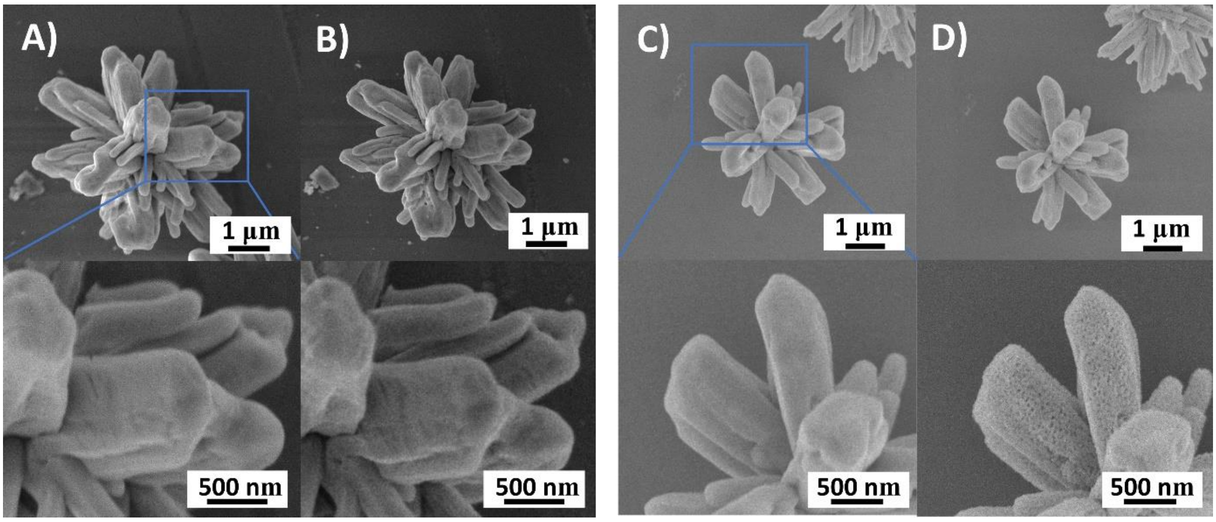

Fig. 10. SEM images of star-shaped particles: A) CeO_2 heated in 400°C; B) CeO_2 heated in 900°C; C) $Ce_{0.9}Gd_{0.1}O_{1.95}$ heated in 400°C; D) $Ce_{0.9}Gd_{0.1}O_{1.95}$ heated in 900°C.

3.2 Catalytic activity

3.2.1 H_2-TPR

In order to evaluate the reduction capabilities of materials, $Ce_{1-x}Gd_xO_{2-x/2}$ (x = 0-1) HSPs were subjected to H_2-TPR measurements. The influence of NPs organization degree within CeO_2 mesocrystal on reducibility was presented in our previous paper [24]. This study reveals that low-doped samples up to 40% of Gd concentration possess high surface reduction capabilities as indicated by maximum around 510°C (Fig. 11.A), which in literature is ascribed to surface-capping oxygen in ceria [33]. The highest value of the relative surface reduction (55%) is observed for 30-40% Gd^{3+}-doped samples (Fig. 11.B). This was calculated as the ratio between surface H_2 consumption to the overall H_2 consumption and may be treated as an indicator of HSPs stability in the middle-to-high temperatures of catalyst operation, due to retention of nanoparticles surface exposition. However, the highest surface H_2 consumption, that is an indicator of low temperature catalytic capabilities, has been observed in 10% Gd^{3+}-doped sample.

Bulk H_2 consumption above 620°C is systematically lowered when Gd concentration increases, which indicates the inhibitory effect of dopant amount on oxygen vacancy migration for high doping levels (>40% Gd^{3+}). Due to that, HSPs up to only this dopant concentration level where subjected to further propane oxidation tests. Additionally, there is additional hump visible in undoped cerium oxide HSPs sample which may indicate facilitated oxygen consumption of both, surface and subsurface oxygen layers in ceria [82].

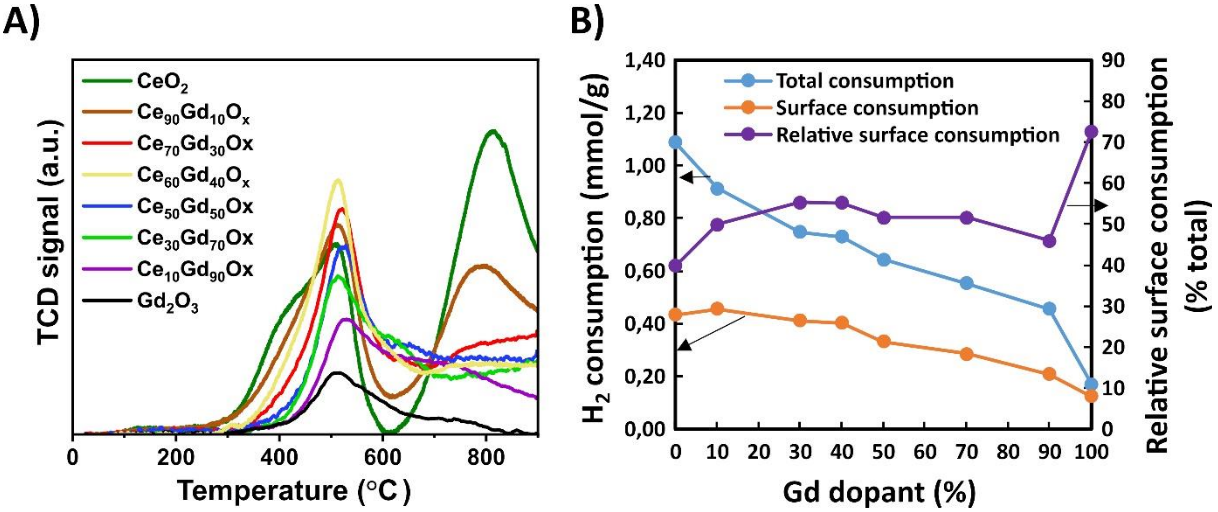

Fig. 11. A) H_2-TPR profiles of $Ce_{1-x}Gd_xO_{2-x/2}$ (x = 0-1) HSPs; B) Total H_2 consumption, surface H_2 consumption and relative surface H_2 consumption as a function dopant concentration.

3.2.2 Soot combustion

To evaluate catalytic performance, T_{50}, which corresponds to the temperature when conversion reaches 50%, was determined for each sample. All of the tested mixed oxide HSPs lowered the T_{50} when compared to bulk ceria (Fig. 12.A) that is in agreement with literature data on nanocrystalline mixed ceria NPs [36,40]. Undoped CeO_2 HSPs reached T_{50}= 478°C as compared to T_{50}= 577°C for bulk ceria sample. The introduction of 10% of Gd^{3+} dopant slightly lowered the soot oxidation temperature to T_{50}= 469°C. This may be explained by elevated surface reduction that was determined in H_2-TPR study (Fig. 11B). However, the greater amount of dopant causes the reaction to shift towards higher temperatures. This may be linked to decrease in degree of surface reduction as TPR study had shown. It is known from our previous work that hierarchical organization at the meso- and macro-scale enhances soot combustion due to facilitated transfer of reagents as well as intensification of the ceria-soot contact, respectively [24]. Since the well porosity and high surface area in doped HSPs is preserved, the result of gradual decrease of soot oxidation performance may be linked to progressive decrease of the number of available surface oxygen species [83,84].

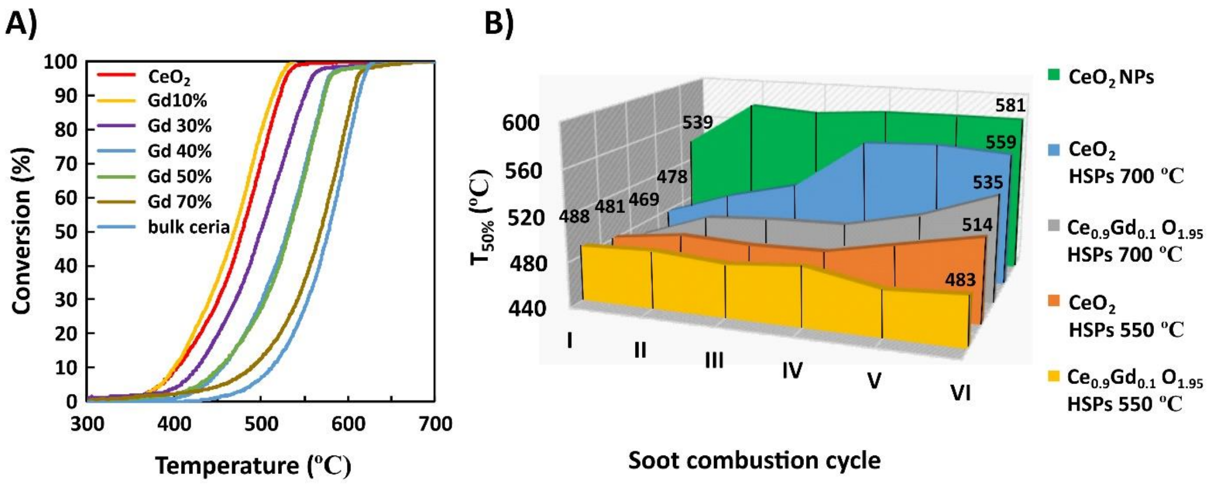

Fig. 12. A) Soot oxidation conversion profiles of hierarchically structured star-shaped particles (tested in tight contact mode under static air); B) Six cycles of soot combustion of $Ce_{1-x}Gd_xO_{2-x/2}$ (x= 0; 0.1) hierarchically structured star-shaped particles (HSPs) at two temperature conditions of 550°C and 700°C compared with soot combustion by non-hierarchically organized CeO_2 NPs (green).

The stability of particles in the soot oxidation was assessed by measuring six cycles of soot combustion (Fig. 12.B). Due to two distinct temperature-dependent growing modes of nanocrystallites (see section 3.1.1) the soot combustion of CeO_2 and $Ce_{0.9}Gd_{0.1}O_{1.95}$ was performed in two temperature conditions, namely the TG experiment was executed up to 550°C or up to 700°C for all six oxidation cycles. Also, to compare the materials performance with non-hierarchically organized ceria nanoparticles (NPs), microemulsion-derived sample was prepared and tested (S_{BET} = 79 m^2/g, average size = 6,4 nm; see TEM images in Fig. S7 in Supporting Information).

As visible in Fig. 12.B, microemulsion-derived NPs lost stability after first cycle of combustion shifting T_{50} from 539°C to 580°C, the temperature that is comparable to bulk ceria soot oxidation performance. CeO_2 HSPs, in 700°C temperature condition, lost stability after 4th soot combustion cycle. At the same time, $Ce_{0.9}Gd_{0.1}O_{1.95}$ HSPs in 700°C temperature condition, shows slower T_{50} increase for successive cycles indicating it greater stability. Comparison of 550°C- treated samples show that whereas undoped CeO_2 HSPs slowly lose soot oxidation performance, there is no such loss for $Ce_{0.9}Gd_{0.1}O_{1.95}$ HSPs. The particles preserve average T_{50}= ~485°C in all trials that proves the well stability of this material. The shapes of TG profiles for all tested cycles may be found in Supplementary Information (Fig. S8).

In order to assess the stability of particles architecture after rather violent soot oxidation reaction, the samples were inspected by TEM after 6th combustion cycle (Fig. 13). Loss of the 3rd level hierarchy structure is observed for materials treated up to both temperature conditions of 550°C and 700°C, but for 550 °C- treated samples the preserved morphology of the whole star particles still can be detected (Fig. 13.C and 13.D). As visible in Fig. 13.A, CeO_2 HSPs heated up to 700 °C lost 2nd level nanocrytsallites ordering, since diffraction maxima visible on SAED patterns collected from the broader area of the arms are dispersed and form circles instead of clearly defined points. CeO_2 HSPs treated in 550°C show some degree of conservation of crystallites organization but still SAED patterns in the form of blurred circles may be detected which indicates loss of arrangement followed by porosity decline (Fig. 13.B). As distinct from undoped samples, $Ce_{0.9}Gd_{0.1}O_{1.95}$ HSPs show greater stability which is confirmed by SAED patterns (Fig. 13.C and 13.D). Both in 550°C and 700°C soot oxidation conditions there is still ordering of crystallites, therefore porous interior of material is still present which explains low temperature of soot combustion.

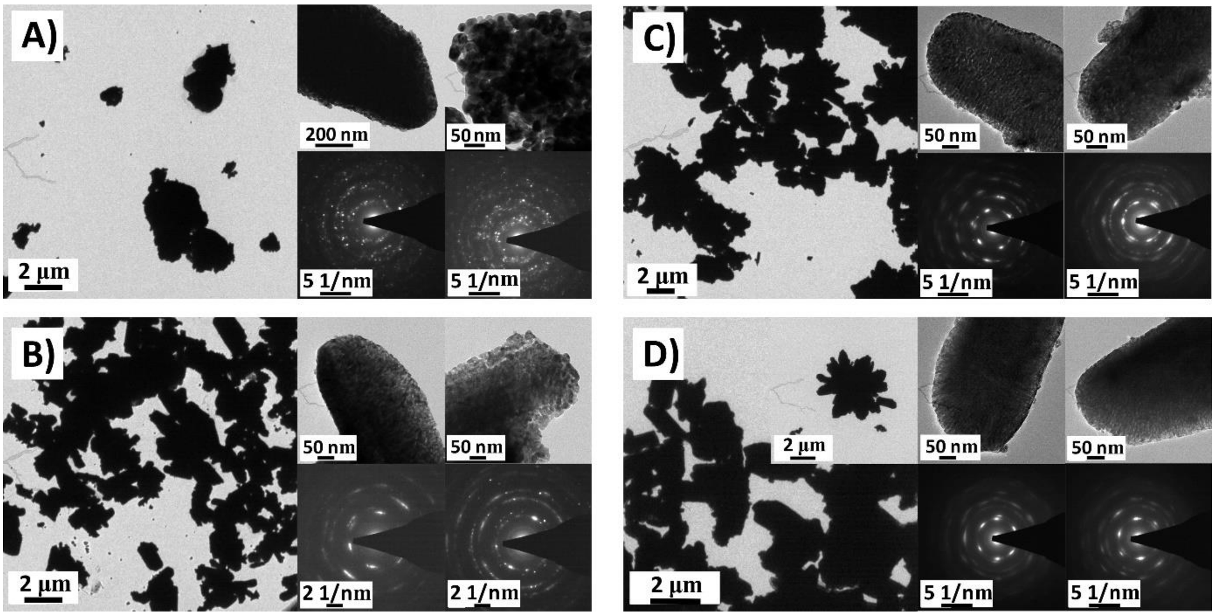

Fig. 13. TEM images of 3rd level (left) and 2nd level of hierarchical architecture (upper right) with corresponding SAED patterns (bottom right) of $Ce_{1-x}Gd_xO_{2-x/2}$ (x = 0 or 0.1) HSPs after 6th soot combustion cycle: A) CeO_2 treated up to 700°C; B) $Ce_{0.9}Gd_{0.1}O_{1.95}$ treated up to 700°C; C) CeO_2 treated up to 550°C; D) $Ce_{0.9}Gd_{0.1}O_{1.95}$ treated up to 550°C.

It is worth to notice that the nanoaprticles arrangement within the mesocrystal seem to facilitate soot oxidation for highly Gd-doped HSPs despite the fact that the high Gd content decreases material oxidation capabilities per se. For samples up to 50% Gd concentration T_{50} is less than 532°C, the value that is lower to microemulsion-derived NPs performance (T_{50} = 539°C). This proves that interdependence of dopant effect and nanoaprticles organization effect allows to design materials with increased stability and facilitated catalytic activity.

However, in this study tight contact mode in soot combustion was used, so there is a room for testing the lose contact and therefore the influence of 3rd order morphology loss on combustion efficiency. In real conditions soot is in the form of particles dispersed in air and effuse star arms will potentially increase the process of catching particles thus increasing the probability of soot-catalyst contact.

3.2.3 Propane oxidation

Taking into account the occurrence of two temperature-dependent nanocrystallites growing modes (see section 3.1.1) and thus, temperature-dependent architecture stability (as this has been demonstrated in section 3.2.2 on soot combustion reaction), propane oxidation measurements were performed up to 540°C. In this temperature regime the low-temperature growth mode of crystallites prevails and thus the hierarchical architecture of the materials is preserved.

Propane oxidation tests (Fig. 14.A) show that undoped CeO_2 as well as $Ce_{1-x}Gd_xO_{2.-x/2}$ (x=0.1;0.3;0.4) HSPs outperform greatly the commercial bulk ceria for which there was almost no propane conversion in the tested temperature range. Since HSPs are composed of $Ce_{1-x}Gd_xO_{2.-x/2}$ nanocrystallites, this phenomenon may be explained by the nanosize effect. Additionally, to differentiate the effect of nanoparticles organization at the second hierarchy level (porous arms) from unorganized nanoparticles performance, microemulsion-derived nanoparticles (NPs) propane oxidation measurement result was used as comparative data.

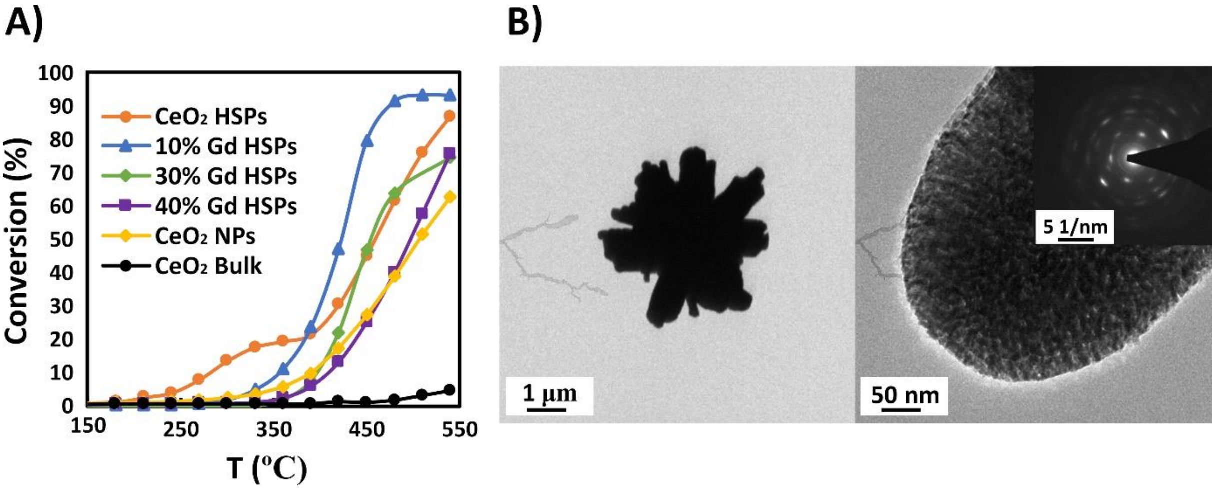

Fig. 14.A) Propane oxidation profiles for $Ce_{1-x}Gd_xO_{2-x/2}$ (x= 0; 0.1; 0.3; 0.4) HSPs, powdered NPs and bulk ceria; B) TEM images of CeO_2 HSP after propane oxidation test showing preserved star-shaped morphology (left) and mesoscale nanocrystal arrangement (right) confirmed by SAED pattern (insert).

As Fig. 14.A shows, $Ce_{1-x}Gd_xO_{2.-x/2}$ (x=0; 0.1; 0.3) HSPs outperform propane oxidation capability of non-organized powdered ceria NPs, confirming the effect of nanoparticles ordering on oxidation performance. Mutual arrangement of nanocrystallites in the volume of star-shaped particle arm introduces porosity, which facilitates transfer of reactants. However, 40% Gd-doped particles show similar catalytic performance as non-organized NPs, despite having the fine hierarchical architecture and a large surface area. This may indicate that $Ce_{0.6}Gd_{0.4}O_{1.8}$ HSPs have decreased number of surface active sites, that is also visible in lowered surface H_2 consumption probed by TPR studies. But taking into consideration the increased stability of Gd-doped material, the synergic effect of dopant and mesoscale NPs arrangement in $Ce_{0.6}Gd_{0.4}O_{1.8}$ HSPs evinces its superiority over non-organized NPs. Comparison of turnover frequencies (TOF) calculated at 450°C with literature data for V_2O_5/CeO_2 nanorods and nanoparticles show superiority of HSPs [85] (see Table S2 in Supplementary Materials).

Interestingly, for undoped CeO_2 HSPs, the additional propane conversion process was observed at the considerable maximum conversion degree of 20% in the temperature range of 180 – 400°C. This process reaches saturation at 360-400°C and emerges only for CeO_2 HSPs. No such conversion was present for comparative sample of non-organized ceria NPs (Fig. 14.A). Also, loosely arranged agglomerates of ceria rods, cubes and nanoparticles do not show such conversion [86]. Based on literature considerations, this reaction may be ascribed to surface heterogeneous pathway of propane oxidation in which the active sites are oxygenated sites O(s) on the materials surface [87]. Highly-developed surface area and porous structure of hierarchical organized stars-like ceria based oxides play a key role in a catalytic activity of the materials. As known, the CeO_2 is not a good candidate for propane oxidation catalyst, because at 400°C the conversion of propane achieved ~10 % [88] or even 0 % [38] for materials with a specific surface of about 60 m^2/g. You et al. have shown that C_3H_8 oxidation by ceria-based catalysts at temperatures below 400°C proceeds by Mars-van-Krevelen (MvK) mechanism [89]. Since the main controlled difference between CeO_2 HSPs and microemulsion-derived NPs, for which there is no such low-temperature propane conversion, is the presence of well-developed porosity, it is postulated here that ordering of CeO_2 nanocrystallites at the second level of the materials hierarchical organization favors the surface propane oxidation. The surface exposition of CeO_2 nanocrystallites in HSPs may facilitate mass transfer, thus amend low-temperature propane oxidation. Also, the material hierarchical porosity that consists of confined slits and cavities may contribute to facilitation of the low-temperature surface heterogenous propane oxidation by CeO_2 HSPs.

Above 400°C mixed hetero-homogeneous mechanism prevails in propane oxidation by CeO_2 HSPs. As compared to literature data the conversion at 500°C is only 20% whereas in this study it reaches 50%, which may suggest that the mesocrystalline arrangement strongly facilitate this process.

However, the introduction of 10% Gd dopant into ceria HSPs kills the occurrence of as observed low-temperature mechanism of propane oxidation while shifting the T_{50} conversion into lower temperatures when compared to undoped CeO_2 HSPs. Lowering of T_{50} may be linked to facilitated oxygen migration due to increased microstrain. Due to non-random distribution of Gd-dopant in nanocrystallites, the segregation of dopant is not excluded and may be linked to modification of mechanism of propane oxidation. $Ce_{0.7}Gd_{0.3}O_{1.85}$ HSPs are as effective as undoped CeO_2 ones, so the best doped sample are below 30% concentration of Gd. The higher dopant concentration hinders migration of ions in the material probably due to formation of stable oxygen vacancies, thus reducing propane oxidation capabilities.

At temperatures above 400°C the gas chromatography results show the occurrence of trace amount of conversion by-product for all the samples (Fig. S9. A and B). Due to its 200 times smaller quantity as compared to propane this product was treated as minor impurity in the conversion process. Its occurrence may be link to the shift from surface heterogeneous pathway of propane oxidation (<400°C) into mixed hetero-homogeneous mechanism (>400°C) for which gas phase reactions start to dominate [87]. Also, it's amount is inversely proportional to the cerium oxide content except the $Ce_{0.9}Gd_{0.1}O_{1.95}$ sample indicating that this sample has the highest catalytic conversion performance (Fig. S9. C).

3.3 Summary: the role of mesocrystal architecture in catalytic activity

The illustrative graphic that presents dopant-dependent changes of mesocrystal architecture triggered by temperature is shown on Fig. 15.A. It has been conceived based on collected experimental data concerning: (1) temperature-dependent two growth modes of ceria nanocrystallites (presented in section 3.1), (2) dopant-dependent porosity formation triggered by temperature (section 3.1.3), (3) the particles mesocrystal structure preservation characteristics after 6th cycle of soot combustion (section 3.2.2), (4) TEM inspection of samples heated at 700°C (Fig. 15.B and C). As visible on Fig. 15.A, the well-ordered CeO_2 nanocrystallites undergo rapid growth at temperatures above 600°C resulting in formation of system of grown-together cubo-octahedral particles of different sizes. The whole structure preserves some porosity and overall morphology. Conversely, Gd-doped ceria nanoparticles evolve into fused small crystallite agglomerates forming the porous arm with well-preserved mesoscale organization. This may be linked to lower growth rate of nanoparticles that is connected with higher growth activation energy. In this case the arm collapses inwardly creating additional porosity. This is also linked to greater stability of such architecture as soot oxidation tests had shown.

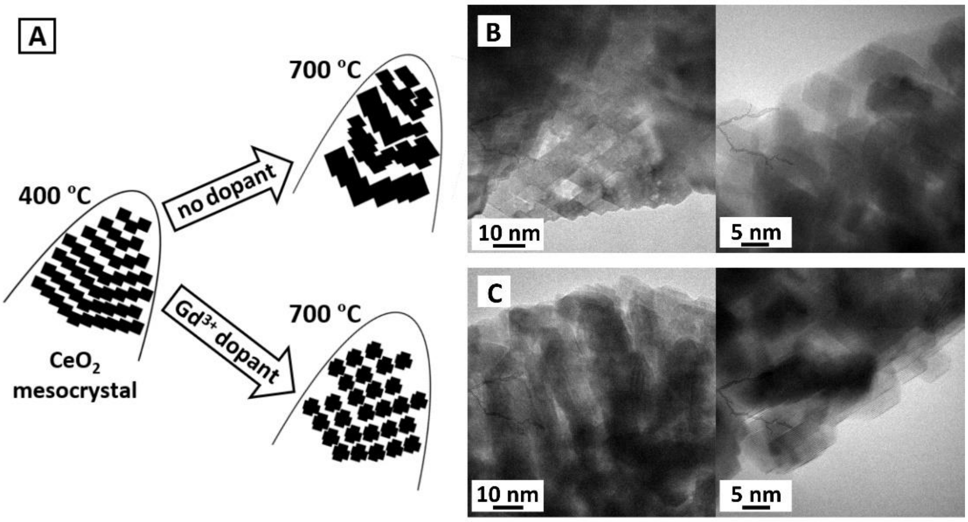

Fig. 15 A) Graphic showing dopant-dependent changes of mesocrystal architecture induced by temperature; B) TEM images of CeO_2 HSP heated in 700°C; C) TEM images of $Ce_{0.9}Gd_{0.1}O_{1.95}$ HSP heated in 700°C.

Comparison of catalytic activity of star-shaped particles with loosely arranged microemulsion-derived NPs in both, soot and propane oxidation, show the superiority of NPs arrangement in the reactivity. Concerning catalytic propane oxidation by CeO_2 star-shaped particles, emergent phenomenon of low-temperature oxidation mechanism with considerable conversion (~20%) has been observed. This phenomenon was not observed for microemulsion-derived NPs, and its occurrence in mesocrystal material may be linked to enhanced contact between catalyst surface and reactant molecules due to diversified mesoscale-confined pores in star-shaped particles. Also, soot combustion temperature was significantly lowered (478°C) as compared to microemulsion-derived NPs (539°C) and commercial ceria (578°C). However, due to reduced stability of architecture owing to tendency of ceria crystallites to coalesce, especially in temperatures above 600°C, gradual decline of soot combustion activity has been observed. This may be linked to loss of 2nd level of hierarchical organization due to activation of interparticle growth mode due to local soot combustion temperature rise. Nevertheless, star-shaped particles show considerable propane oxidation performance (80% conversion at 500°C) at temperatures below the ones that induce architectural changes, which implicate their potential stability in low-to-middle temperature gas purification processes.

10% Gd-doped cerium oxide star-shaped particles show enhanced oxidation activity, both in propane and soot catalytic combustion, as compared to undoped CeO_2 star-shaped particles, which evinces in lower T_{50} temperatures, 410 °C and 460 °C respectively. This proves that intersection of dopant effect and mesoscale crystallite arrangement results in an enhanced catalytic activity of hierarchical material. The nanoparticles have larger microstrain values which may be linked to facilitated oxygen migration and hence oxygen supply into surface where active centers are present. In fact, 10% Gd-doped sample have the highest absolute H_2 surface consumption value that may indicate that the surface processes play the main role in catalytic oxidation. Despite that 30% and 40% doped samples possess greater relative surface to bulk H_2 consumption, this samples show higher T_{50} propane conversion values. For this samples, the presence of dopant may block the effective supply of oxygen into surface where active centers are present, that is in accordance with ionic conductivity studies. Interestingly, the low-temperature mechanism of propane oxidation is impeded. The important conclusion is that Gd dopant stabilizes the architecture of the material, since at six soot combustion cycles the oxidation temperature is stable (480°C-490°C).

The obtained results may inspire for further studies on the influence of dopant on mesocrystal architecture evolution and stability as well as its subsequent catalytic performance. Varying the dopant nature and amount is potential research area to pursue.

4. Conclusions

In this contribution, the role of dopant-induced changes of mesocrystal hierarchical architecture in terms of microstructure, porosity, morphology and crystallites mesoscale organization in the catalytic oxidation of soot and propane was studied with the use of $Ce_{1-x}Gd_xO_{2-x/2}$ (x= 0, 0.1, 0.3, 0.4, 0.5, 0.7, 0.9, 1) hierarchically structured star-shaped particles (HSPs). Several dependencies has been found that are listed below:

1. Hydrothermal synthesis allows to obtain mixed $Ce_{1-x}Gd_x(COOH)_3$ formate particles in the whole dopant concentration range (x=0-1) with strictly defined star-shaped morphology (for dopant level up to 70%) and rod-shape-like particles (for dopant amount higher than 70%).

2. Oxidative thermolysis of mixed cerium formates has led to formation of hierarchically structured materials composed of three levels of hierarchy: 1st level: mixed cerium oxide nanoparticles (average size < 10 nm), 2nd level: porous arms with well-developed surface area (S_{BET} = 140-180 m^2/g for samples of up to 70% of Gd concentration), 3rd level: star-shaped morphology (4-7 μm in average size). Thermal decomposition of formates forms nanocrystallites with non-random distribution of dopant, as was confirmed by EELS and RAMAN study. Increasing dopant concentration causes decrease of size and increase of NPs microstrain. The porosity is characterized by occurrence of slits and cavities creating confined spaces and overall S_{BET} area may be increased by changing dopant concentration (the highest BET observed for 40% doped sample). The samples preserve high surface area (> 115 m^2/g) at 550°C.

3. Two temperature-dependent growing modes of nanocrystallites was observed. For temperatures below 600°C, growth on NPs was rather slow on behalf of fast reduction of NPs microstrain. This contributes to maintaining the stability of particle architecture, which is especially important in low-temperature catalytic oxidation. The second mode above 600°C is linked to fast growth of nanoparticles but the architecture changes are dopant-dependent. While undoped CeO_2 HSPs form system of grown-together cubo-octahedral particles of different sizes in which well-defined architecture is preserved to lesser extent, Gd-doped ceria evolve into fused small crystallite agglomerates forming the porous arm with well-preserved mesoscale organization. Such collective intergrowth of NPs in mesocrystal creates additional porosity, as was inspected by SEM imaging. This thermally-induced functional adaptation of the material is linked to greater stability of such architecture in violent soot combustion reaction.

4. Emergent phenomenon in catalytic propane oxidation was observed. Due to arrangement of ceria crystallites into porous hierarchical structure, the substantial increase of conversion via low-temperature propane oxidation mechanism (up to ~20% below 400°C) was observed. No such conversion was present for comparative sample of non-organized ceria NPs. Interestingly, the presence of Gd-dopant killed the occurrence of as observed low-temperature mechanism of propane oxidation while shifting the T_{50} conversion into lower temperatures as compared to CeO_2 HSPs.

5. Presence of Gd-dopant stabilizes architecture in soot oxidation, since six cycles of combustion did not change the average T_{50} = 485°C, which was not the case in undoped CeO_2 HSPs

Also, propane oxidation reaction goes with high conversion (>80% for CeO_2 and >90% for $Ce_{0.9}Gd_{0.1}O_{1.95}$ HSPs) at temperatures up to 500ºC that is far below the one in which architectural changes appear.

Acknowledgments

The research leading to these results has received funding from the European Union Horizon 2020 research and innovation programme under grant agreement No. 823717-ESTEEM3. The authors thank Mrs. Ewa Bukowska and Dr Maciej Ptak for XRD and FT-IR measurements, respectively. We acknowledge Degussa S.A. for providing us with Printex-U soot

References

[1] R. Chockalingam, V.R.W. Amarakoon, H. Giesche, Alumina/cerium oxide nano-composite electrolyte for solid oxide fuel cell applications, Journal of the European Ceramic Society. 28 (2008) 959–963. https://doi.org/10.1016/j.jeurceramsoc.2007.09.031.

[2] A. Trovarelli, P. Fornasiero, Catalysis by Ceria and Related Materials, 2nd ed., Imperical College Press, London, 2013.

[3] T.S. Stefanik, H.L. Tuller, Ceria-based gas sensors, Journal of the European Ceramic Society. 21 (2001) 1967–1970. https://doi.org/10.1016/S0955-2219(01)00152-2.

[4] A. Trovarelli, J. Llorca, Ceria Catalysts at Nanoscale: How Do Crystal Shapes Shape Catalysis?, ACS Catalysis. 7 (2017) 4716–4735. https://doi.org/10.1021/acscatal.7b01246.

[5] Y. Xu, S.S. Mofarah, R. Mehmood, C. Cazorla, P. Koshy, C.C. Sorrell, Design strategies for ceria nanomaterials: Untangling key mechanistic concepts, Materials Horizons. 8 (2021) 102–123. https://doi.org/10.1039/d0mh00654h.

[6] A. Filtschew, K. Hofmann, C. Hess, Ceria and Its Defect Structure: New Insights from a Combined Spectroscopic Approach, Journal of Physical Chemistry C. 120 (2016) 6694–6703. https://doi.org/10.1021/acs.jpcc.6b00959.

[7] C. Sun, D. Xue, Size-dependent oxygen storage ability of nano-sized ceria, Physical Chemistry Chemical Physics. 15 (2013) 14414–14419. https://doi.org/10.1039/c3cp51959g.

[8] S. Deshpande, S. Patil, S.V. Kuchibhatla, S. Seal, Size dependency variation in lattice parameter and valency states in nanocrystalline cerium oxide, Applied Physics Letters. 87 (2005) 1–3. https://doi.org/10.1063/1.2061873.

[9] S. Kurajica, I. Minga, M. Guliš, V. Mandić, I. Simčić, High Surface Area Ceria Nanoparticles via Hydrothermal Synthesis Experiment Design, Journal of Nanomaterials. 2016 (2016). https://doi.org/10.1155/2016/7274949.

[10] V.F. Solovyov, M. Gibert, T. Puig, X. Obradors, Size-dependent strain in epitaxial (001) gadolinium-doped ceria nanoislands, Applied Physics Letters. 97 (2010) 20–23. https://doi.org/10.1063/1.3527079.

[11] D. Andreescu, G. Bulbul, R.E. Özel, A. Hayat, N. Sardesai, S. Andreescu, Applications and implications of nanoceria reactivity: Measurement tools and environmental impact, Environmental Science: Nano. 1 (2014) 445–458. https://doi.org/10.1039/c4en00075g.

[12] J.D. Cafun, K.O. Kvashnina, E. Casals, V.F. Puntes, P. Glatzel, Absence of Ce3+ sites in chemically active colloidal ceria nanoparticles, ACS Nano. 7 (2013) 10726–10732. https://doi.org/10.1021/nn403542p.

[13] S.T. Lakshmi, R. V., Bera, Parthasarathi, Pal, Kamalesh, Alwera, Vijay, Gayen, Arup, Mandal, Tapas Kumar, Aruna, Effect of Cerium Oxide Nanostructures on CO Oxidation, Journal of Nanoscience and Nanotechnology. 21 (2021) 1641-1652(12). https://doi.org/10.1166/jnn.2021.18988.

[14] W. Zhang, X. Niu, L. Chen, F. Yuan, Y. Zhu, Soot Combustion over Nanostructured Ceria with Different Morphologies, Scientific Reports. 6 (2016) 1–10. https://doi.org/10.1038/srep29062.

[15] W.I. Hsiao, Y.S. Lin, Y.C. Chen, C.S. Lee, The effect of the morphology of nanocrystalline CeO2 on ethanol reforming, Chemical Physics Letters. 441 (2007) 294–299. https://doi.org/10.1016/j.cplett.2007.05.024.

[16] F. Garnes-Portolés, M.Á. Rivero-Crespo, A. Leyva-Pérez, Nanoceria as a recyclable catalyst/support for the cyanosilylation of ketones and alcohol oxidation in cascade, Journal of Catalysis. 392 (2020) 21–28. https://doi.org/10.1016/j.jcat.2020.09.032.

[17] R. Lakes, Materials with structural hierarchy, Nature. 361 (1993) 511–515.

[18] P. Fratzl, R. Weinkamer, Nature’s hierarchical materials, Progress in Materials Science. 52 (2007) 1263–1334. https://doi.org/10.1016/j.pmatsci.2007.06.001.

[19] D. Sen, M.J. Buehler, Structural hierarchies define toughness and defect-tolerance despite simple and mechanically inferior brittle building blocks, Scientific Reports. 1 (2011) 1–9. https://doi.org/10.1038/srep00035.

[20] X.Y. Yang, L.H. Chen, Y. Li, J.C. Rooke, C. Sanchez, B.L. Su, Hierarchically porous materials: Synthesis strategies and structure design, Chemical Society Reviews. 46 (2017) 481–558. https://doi.org/10.1039/c6cs00829a.

[21] Y. Wang, F.F. Ren, D.H. Pan, J.H. Ma, A hierarchically micro-meso-macroporous zeolite caa for methanol conversion to dimethyl ether, Crystals. 6 (2016) 1–10. https://doi.org/10.3390/cryst6110155.

[22] C.M.A. Parlett, K. Wilson, A.F. Lee, Hierarchical porous materials: Catalytic applications, Chemical Society Reviews. 42 (2013) 3876–3893. https://doi.org/10.1039/c2cs35378d.

[23] C. Sun, H. Li, L. Chen, Nanostructured ceria-based materials: Synthesis, properties, and applications, Energy and Environmental Science. 5 (2012) 8475–8505. https://doi.org/10.1039/c2ee22310d.

[24] P. Woźniak, W. Miśta, M.A. Małecka, Function of various levels of hierarchical organization of porous Ce0.9REE0.1O1.95mixed oxides in catalytic activity, CrystEngComm. 22 (2020) 5914–5930. https://doi.org/10.1039/d0ce00883d.

[25] L. Wu, Y. Li, Z. Fu, B.L. Su, Hierarchically structured porous materials: Synthesis strategies and applications in energy storage, National Science Review. 7 (2020) 1667–1701. https://doi.org/10.1093/nsr/nwaa183.

[26] M.G. Ma, H. Cölfen, Mesocrystals - Applications and potential, Current Opinion in Colloid and Interface Science. 19 (2014) 56–65. https://doi.org/10.1016/j.cocis.2014.03.001.

[27] E. V. Sturm, H. Cölfen, Mesocrystals: Past, presence, future, Crystals. 7 (2017). https://doi.org/10.3390/cryst7070207.

[28] L. Zhou, Mesocrystals Properties and Applications, (2012).

[29] W. Deng, X. Wang, F. Jiao, K. Zhu, A platelet-like CeO2 mesocrystal enclosed by {100} facets: Synthesis and catalytic properties, Journal of Nanoparticle Research. 15 (2013). https://doi.org/10.1007/s11051-013-1944-3.

[30] D. Mukherjee, B.M. Reddy, Noble metal-free CeO2-based mixed oxides for CO and soot oxidation, Catalysis Today. 309 (2018) 227–235. https://doi.org/10.1016/j.cattod.2017.06.017.

[31] M. Coduri, S. Checchia, M. Longhi, D. Ceresoli, M. Scavini, Rare earth doped ceria: The complex connection between structure and properties, Frontiers in Chemistry. 6 (2018) 1–23. https://doi.org/10.3389/fchem.2018.00526.

[32] T.X.T. Sayle, F. Caddeo, X. Zhang, T. Sakthivel, S. Das, S. Seal, S. Ptasinska, D.C. Sayle, Structure-Activity Map of Ceria Nanoparticles, Nanocubes, and Mesoporous Architectures, Chemistry of Materials. 28 (2016) 7287–7295. https://doi.org/10.1021/acs.chemmater.6b02536.

[33] P. Li, X. Chen, Y. Li, J.W. Schwank, A review on oxygen storage capacity of CeO 2 -based materials: Influence factors, measurement techniques, and applications in reactions related to catalytic automotive emissions control, Catalysis Today. (2019) 90–115. https://doi.org/10.1016/j.cattod.2018.05.059.

[34] F. Ye, D.R. Ou, T. Mori, Microstructural evolution in a CeO 2-Gd 2O 3 system, Microscopy and Microanalysis. 18 (2012) 162–170. https://doi.org/10.1017/S1431927611012396.

[35] M. Coduri, M. Scavini, M. Pani, M.M. Carnasciali, H. Klein, C. Artini, From nano to microcrystals: Effects of different synthetic pathways on the defect architecture in heavily Gd-doped ceria, Physical Chemistry Chemical Physics. 19 (2017) 11612–11630. https://doi.org/10.1039/c6cp08173h.

[36] A. Bueno-López, K. Krishna, M. Makkee, J.A. Moulijn, Enhanced soot oxidation by lattice oxygen via La3+-doped CeO2, Journal of Catalysis. 230 (2005) 237–248. https://doi.org/10.1016/j.jcat.2004.11.027.

[37] J. Liu, Z. Zhao, J. Xu, C. Xu, A. Duan, G. Jiang, H. He, The highly active catalysts of nanocomposite K-Co-CeO2 for soot combustion, Chemical Communications. 47 (2011) 11119–11121. https://doi.org/10.1039/c1cc14338g.

[38] Q. Song, R. Ran, J. Ding, X. Wu, Z. Si, D. Weng, The controlled preparation and performance of Fe, Co-modified porous ceria nanorods for the total oxidation of propane, Molecular Catalysis. 480 (2020) 110663. https://doi.org/10.1016/j.mcat.2019.110663.

[39] M.A. Małecka, L. Kepiński, Solid state reactions in highly dispersed praseodymium oxide-SiO2 system, Journal of Alloys and Compounds. 430 (2007) 282–291. https://doi.org/10.1016/j.jallcom.2006.05.011.

[40] M.A. Małecka, L. Kepiński, W. Miśta, Structure evolution of nanocrystalline CeO2 and CeLnOx mixed oxides (Ln = Pr, Tb, Lu) in O2 and H2 atmosphere and their catalytic activity in soot combustion, Applied Catalysis B: Environmental. 74 (2007) 290–298. https://doi.org/10.1016/j.apcatb.2007.02.021.

[41] F. Peña, T. Ostasevicius, V.T. Fauske, P. Burdet, E. Prestat, P. Jokubauskas, M. Nord, M. Sarahan, K.E. MacArthur, J. Taillon, J. Caron, V. Migunov, T. Furnival, A. Eljarrat, S. Mazzucco, T. Aarholt, M. Walls, T. Slater, F. Winkler, B. Martineau, G. Donval, R. McLeod, E.R. Hoglund, I. Alxneit, I. Hjorth, T. Henninen, L.F. Zagonel, A. Garmannslund, No Title, (2018) 5ht2. https://doi.org/doi.org/10.5281/ZENODO.1221347.

[42] M. Guo, J. Lu, Y. Wu, Y. Wang, M. Luo, UV and visible Raman studies of oxygen vacancies in rare-earth-doped ceria, Langmuir. 27 (2011) 3872–3877. https://doi.org/10.1021/la200292f.

[43] Y.B. Go, A.J. Jacobson, Solid solution precursors to gadolinia-doped ceria prepared via a low-temperature solution route, Chemistry of Materials. 19 (2007) 4702–4709. https://doi.org/10.1021/cm071310k.

[44] M.M. Heravi, M. Ghavidel, L. Mohammadkhani, Beyond a solvent: Triple roles of dimethylformamide in organic chemistry, RSC Advances. 8 (2018) 27832–27862. https://doi.org/10.1039/c8ra04985h.

[45] L. Gránásy, T. Pusztai, G. Tegze, J.A. Warren, J.F. Douglas, Growth and form of spherulites, Physical Review E - Statistical, Nonlinear, and Soft Matter Physics. 72 (2005). https://doi.org/10.1103/PhysRevE.72.011605.

[46] N.I. Skripov, T.P. Stepanova, L.B. Belykh, F.K. Schmidt, The nature of nanoparticles formed in the system PdCl2-elemental phosphorus, Russian Journal of General Chemistry. 83 (2013) 1021–1028. https://doi.org/10.1134/S1070363213060029.

[47] H. Cölfen, L. Qi, Y. Mastai, L. Börger, Formation of Unusual 10-Petal BaSO4 Structures in the Presence of a Polymeric Additive, Crystal Growth and Design. 2 (2002) 191–196. https://doi.org/10.1021/cg025507v.

[48] R.D. Shannon, Revised effective ionic radii and systematic studies of interatomic distances in halides and chalcogenides, Acta Crystallographica. A32 (1976) 751–767.

[49] B.B. Bokhonov, A.A. Matvienko, K.B. Gerasimov, D. v. Dudina, Formation of ordered nanocrystalline CeO2 structures during thermal decomposition of cerium formate Ce(HCOO)3, Ceramics International. 45 (2019) 19684–19688. https://doi.org/10.1016/j.ceramint.2019.06.219.

[50] Z.L. Wang, X. Feng, Polyhedral shapes of CeO2 nanoparticles, Journal of Physical Chemistry B. 107 (2003) 13563–13566. https://doi.org/10.1021/jp036815m.

[51] D. Sorolla-Rosario, A. Davó-Quiñonero, E. Bailón-García, D. Lozano-Castelló, A. Bueno-López, Key-lock Ceria Catalysts for the Control of Diesel Engine Soot Particulate Emissions, ChemCatChem. 12 (2020) 1772–1781. https://doi.org/10.1002/cctc.201902177.

[52] P. Miceli, S. Bensaid, N. Russo, D. Fino, Effect of the morphological and surface properties of CeO2-based catalysts on the soot oxidation activity, Chemical Engineering Journal. 278 (2015) 190–198. https://doi.org/10.1016/j.cej.2014.10.055.

[53] V.K. Ivanov, O.S. Polezhaeva, G.P. Kopitsa, P.P. Fedorov, K. Pranzas, V. V. Runov, Specifics of high-temperature coarsening of ceria nanoparticles, Russian Journal of Inorganic Chemistry. 54 (2009) 1689–1696. https://doi.org/10.1134/S0036023609110023.

[54] D. Fino, Diesel emission control: Catalytic filters for particulate removal, Science and Technology of Advanced Materials. 8 (2007) 93–100. https://doi.org/10.1016/j.stam.2006.11.012.

[55] C. Artini, S. Massardo, M.M. Carnasciali, B. Joseph, M. Pani, Evaluation of the Defect Cluster Content in Singly and Doubly Doped Ceria through In Situ High-Pressure X-ray Diffraction, Inorganic Chemistry. 60 (2021) 7306–7314. https://doi.org/10.1021/acs.inorgchem.1c00433.

[56] A. Kossoy, A.I. Frenkel, Q. Wang, E. Wachtel, I. Lubomirsky, Local structure and strain-induced distortion in Ce0.8Gd 0.2O1.9, Advanced Materials. 22 (2010) 1659–1662. https://doi.org/10.1002/adma.200902041.

[57] O. Kraynis, J. Timoshenko, J. Huang, H. Singh, E. Wachtel, A.I. Frenkel, I. Lubomirsky, Modeling Strain Distribution at the Atomic Level in Doped Ceria Films with Extended X-ray Absorption Fine Structure Spectroscopy, Inorganic Chemistry. 58 (2019) 7527–7536. https://doi.org/10.1021/acs.inorgchem.9b00730.

[58] C. Artini, M. Pani, M.M. Carnasciali, M.T. Buscaglia, J.R. Plaisier, G.A. Costa, Structural features of Sm- and Gd-doped ceria studied by synchrotron X-ray diffraction and -raman spectroscopy, Inorganic Chemistry. 54 (2015) 4126–4137. https://doi.org/10.1021/acs.inorgchem.5b00395.

[59] F. Ye, T. Mori, D.R. Ou, J. Zou, G. Auchterlonie, J. Drennan, Compositional and structural characteristics of nano-sized domains in gadolinium-doped ceria, Solid State Ionics. 179 (2008) 827–831. https://doi.org/10.1016/j.ssi.2008.02.034.

[60] C. Artini, S. Massardo, M.M. Carnasciali, B. Joseph, M. Pani, In situ high pressure structural investigation of sm-doped ceria, Energies. 13 (2020). https://doi.org/10.3390/en13071558.

[61] C. Artini, G.A. Costa, M. Pani, A. Lausi, J. Plaisier, Structural characterization of the CeO 2/Gd 2O 3 mixed system by synchrotron X-ray diffraction, Journal of Solid State Chemistry. 190 (2012) 24–28. https://doi.org/10.1016/j.jssc.2012.01.056.

[62] R. Schmitt, A. Nenning, O. Kraynis, R. Korobko, A.I. Frenkel, I. Lubomirsky, S.M. Haile, J.L.M. Rupp, A review of defect structure and chemistry in ceria and its solid solutions, Chemical Society Reviews. 49 (2020) 554–592. https://doi.org/10.1039/c9cs00588a.

[63] P. Arunkumar, M. Meena, K.S. Babu, A review on cerium oxide-based electrolytes for ITSOFC, Nanomaterials and Energy. 1 (2012) 288–305. https://doi.org/10.1680/nme.12.00015.

[64] M.A. Małecka, J.J. Delgado, L. Kepiński, J.J. Calvino, S. Bernal, G. Blanco, X. Chen, Structure transformations and reducibility of nanocrystalline Ce 1-xYb xO 2-(x/2) mixed oxides, Catalysis Today. 187 (2012) 56–64. https://doi.org/10.1016/j.cattod.2012.01.004.

[65] H.F. Lopez, H. Mendoza, Temperature Effects on the Crystallization and Coarsening of Nano-CeO 2 Powders , ISRN Nanomaterials. 2013 (2013) 1–7. https://doi.org/10.1155/2013/208614.

[66] B. Han, H. Li, L. Li, Y. Wang, Y. Zhang, G. Li, Kinetic control of CeO2 nanoparticles for catalytic CO oxidation, Journal of Materials Research. 34 (2019) 2201–2208. https://doi.org/10.1557/jmr.2018.456.

[67] D. Balzar, N. Audebrand, M.R. Daymond, A. Fitch, A. Hewat, J.I. Langford, A. Le Bail, D. Louër, O. Masson, C.N. McCowan, N.C. Popa, P.W. Stephens, B.H. Toby, Size-strain line-broadening analysis of the ceria round-robin sample, Journal of Applied Crystallography. 37 (2004) 911–924. https://doi.org/10.1107/S0021889804022551.

[68] R.A. Young, D.B. Wiles, Profile shape functions in Rietveld refinements, Journal of Applied Crystallography. 15 (1982) 430–438. https://doi.org/10.1107/s002188988201231x.

[69] L.B. Mccusker, R.B. Von Dreele, D.E. Cox, D. Louër, P. Scardi, Rietveld refinement guidelines, Journal of Applied Crystallography. 32 (1999) 36–50. https://doi.org/10.1107/S0021889898009856.

[70] M.A. Małecka, U. Burkhardt, D. Kaczorowski, M.P. Schmidt, D. Goran, L. Kępiński, Structure and phase stability of nanocrystalline Ce 1-x Ln x O 2-x/2-δ (Ln = Yb, Lu) in oxidizing and reducing atmosphere, Journal of Nanoparticle Research. 11 (2009) 2113–2124. https://doi.org/10.1007/s11051-008-9577-7.

[71] A. Nakajima, A. Yoshihara, M. Ishigame, Defect-induced Raman spectra in doped CeO2, Physical Review B. 50 (1994) 13297–13307. https://doi.org/10.1103/PhysRevB.50.13297.

[72] F. Ye, T. Mori, D.R. Ou, A.N. Cormack, R.J. Lewis, J. Drennan, Simulation of ordering in large defect clusters in gadolinium-doped ceria, Solid State Ionics. 179 (2008) 1962–1967. https://doi.org/10.1016/j.ssi.2008.06.025.

[73] Z.P. Li, T. Mori, F. Ye, D. Ou, J. Zou, J. Drennan, Ordered structures of defect clusters in gadolinium-doped ceria, Journal of Chemical Physics. 134 (2011). https://doi.org/10.1063/1.3599089.

[74] R. Wallenberg, R. Withers, D.J.M. Bevan, J.G. Thompson, P. Barlow, B.G. Hyde, The fluorite-related “solid solutions” of CeO2Y2O3 I: A re-examination by electron microscopy and diffraction, Journal of The Less-Common Metals. 156 (1989) 1–16. https://doi.org/10.1016/0022-5088(89)90402-5.

[75] A. Banerji, V. Grover, V. Sathe, S.K. Deb, A.K. Tyagi, CeO2 - Gd2 O3 system: Unraveling of microscopic features by Raman spectroscopy, Solid State Communications. 149 (2009) 1689–1692. https://doi.org/10.1016/j.ssc.2009.06.045.

[76] R. Schmitt, J. Spring, R. Korobko, J.L.M. Rupp, Design of Oxygen Vacancy Configuration for Memristive Systems, ACS Nano. 11 (2017) 8881–8891. https://doi.org/10.1021/acsnano.7b03116.

[77] F.J. Sotomayor, K.A. Cychosz, M. Thommes, Characterization of Micro/Mesoporous Materials by Physisorption: Concepts and Case Studies, Acc. Mater. Surf. Res. 3 (2018) 34–50.

[78] J. Sing, K. S. W., Everett, D. H., Haul R. A. W., Moscou, L., Pierotti, R. A., Rouquerol, T. Siemieniewska, REPORTING PHYSISORPTION DATA FOR GAS/SOLID SYSTEMS with Special Reference to the Determination of Surface Area and Porosity, Pure & App!. Chem. 57 (1985) 603–619.

[79] M. Thommes, K. Kaneko, A. V. Neimark, J.P. Olivier, F. Rodriguez-Reinoso, J. Rouquerol, K.S.W. Sing, Physisorption of gases, with special reference to the evaluation of surface area and pore size distribution (IUPAC Technical Report), Pure and Applied Chemistry. 87 (2015) 1051–1069. https://doi.org/10.1515/pac-2014-1117.

[80] J.C. Groen, J. Pérez-Ramírez, Critical appraisal of mesopore characterization by adsorption analysis, Applied Catalysis A: General. 268 (2004) 121–125. https://doi.org/10.1016/j.apcata.2004.03.031.

[81] J.C. Groen, L.A.A. Peffer, J. Pérez-Ramírez, Pore size determination in modified micro- and mesoporous materials. Pitfalls and limitations in gas adsorption data analysis, Microporous and Mesoporous Materials. 60 (2003) 1–17. https://doi.org/10.1016/S1387-1811(03)00339-1.

[82] Z. Wu, M. Li, S.H. Overbury, On the structure dependence of CO oxidation over CeO 2 nanocrystals with well-defined surface planes, Journal of Catalysis. 285 (2012) 61–73. https://doi.org/10.1016/j.jcat.2011.09.011.

[83] A. Bueno-López, Diesel soot combustion ceria catalysts, Applied Catalysis B: Environmental. 146 (2014) 1–11. https://doi.org/10.1016/j.apcatb.2013.02.033.

[84] E. Aneggi, C. De Leitenburg, A. Trovarelli, On the role of lattice/surface oxygen in ceria-zirconia catalysts for diesel soot combustion, Catalysis Today. 181 (2012) 108–115. https://doi.org/10.1016/j.cattod.2011.05.034.

[85] X. Gao, C. Chen, S. Ren, J. Zhang, D. Su, Structural effects of cerium oxides on their thermal stability and catalytic performance in propane oxidation dehydrogenation, Cuihua Xuebao/Chinese Journal of Catalysis. 33 (2012) 1069–1074. https://doi.org/10.1016/S1872-2067(11)60404-X.

[86] X. Zhang, R. You, D. Li, T. Cao, W. Huang, Reaction Sensitivity of Ceria Morphology Effect on Ni/CeO2 Catalysis in Propane Oxidation Reactions, ACS Applied Materials and Interfaces. 9 (2017) 35897–35907. https://doi.org/10.1021/acsami.7b11536.

[87] C. Hognon, Y. Simon, P.M. Marquaire, C. Courson, A. Kiennemann, Hydrogen production by catalytic partial oxidation of propane over CeO2, Chemical Engineering Science. 181 (2018) 46–57. https://doi.org/10.1016/j.ces.2018.01.038.

[88] X. Zhang, S., Liu, S., Zhu, X., Yang, Y., Hu, W., Zhao, H., Qu, R., Zheng, C., Gao, Low temperature catalytic oxidation of propane over cobalt-cerium spinel oxides catalyst, Applied Surface Science. 479 (2019) 1132–1140.

[89] R. You, X. Zhang, L. Luo, Y. Pan, H. Pan, J. Yang, L. Wu, X. Zheng, Y. Jin, W. Huang, NbOx/CeO2-rods catalysts for oxidative dehydrogenation of propane: Nb–CeO2 interaction and reaction mechanism, Journal of Catalysis. 348 (2017) 189–199. https://doi.org/10.1016/j.jcat.2016.12.012.

Supplementary materials for

3D hierarchically structured $Ce_{1-x}Gd_xO_{1-x/2}$ mixed oxide particles: the role of microstructure, porosity and multi-level architecture stability in soot and propane oxidation.

Piotr Woźniak*[a], Małgorzata A. Małecka[a], Lidia Chinchilla[b], Susana Trasobares[b]

[a]Institute of Low Temperature and Structure Research, Polish Academy of Sciences,
P.O. Box 1410, 50-950 Wrocław 2, Poland

[b]Departamento de Ciencia de los Materiales e Ing. Metalúrgica y Química Inorgánica, Universidad de Cádiz, Campus Universitario de Puerto Real, 11510, Cádiz - España

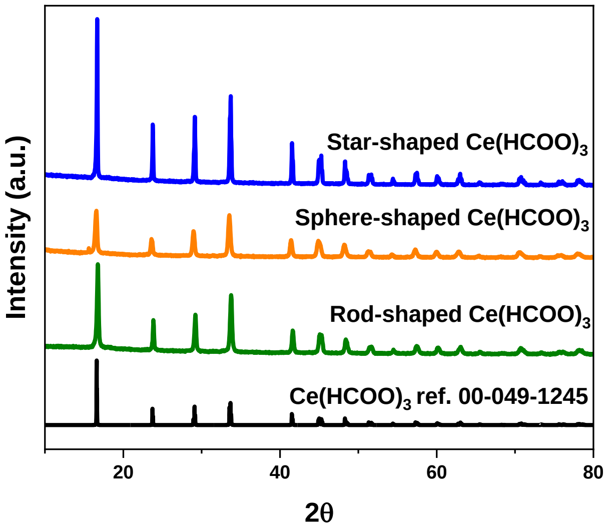

Fig. S1. PXRD patterns of $Ce(HCOO)_3$ particles synthesized in different conditions: star-shaped morphology (DMF and formic acid), sphere-shaped morphology (formic acid), clumped rod-shaped morphology (DMF and formic acid neutralized by ammonia).

Sphere-like $Ce(HCOO)_3$ particles were obtained by mixing $Ce(NO_3)_3$*6 H_2O (1,0855g) in 50 ml of formic acid followed by similar solvothermal treatment as star-shaped particles. Before running the solvothermal synthesis the reaction mixture was stirred for 5 min and change of color into blue and then milky white was observed. Rod-shaped $Ce(HCOO)_3$ particles were obtained by applying the same synthetic protocol as in the case of star-shaped particles with one exception, the reaction mixture was neutralized by 25% NH_3.

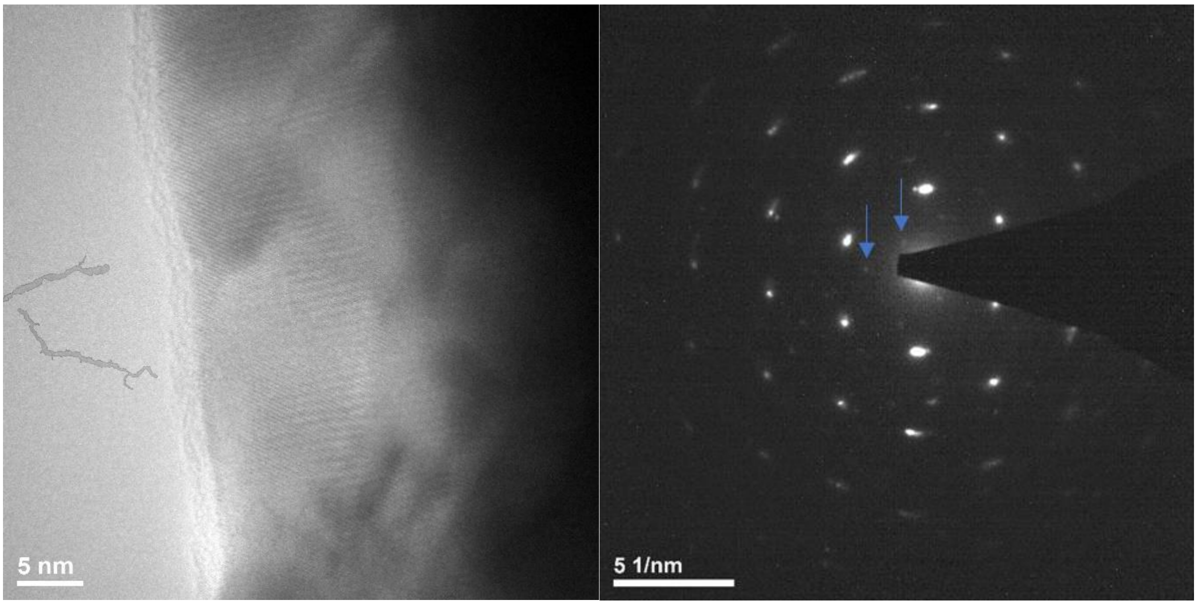

Fig. S2. A) HRTEM image of $Ce_{0.3}Gd_{0.7}O_{1.65}$ heated at 900 °C; B) corresponding SAED pattern showing additional diffraction maxima that arises from double-fluorite superstructure formation (marked by arrow).

T [ºC]	Gd dopant concentration [%]					
	0	10	30	40	50	70
400	8,5	6,9	6,0	5,3	5,4	3,1
450	9,2	7,4	6,7	5,3	5,8	4,6
500	9,1	8,0	7,0	6,2	6,3	5,7
550	9,5	8,4	8,7	7,2	7,8	7,1
600	10,4	9,7	8,9	8,8	9,0	9,2
700	16,2	15,4	17,1	18,2	16,6	15,3
800	25,8	28,4	30,5	31,0	27,3	21,4
900	45,0	46,5	58,2	53,0	43,1	28,5
1000	79,6	71,5	84,8	54,4	61,8	64,1

Table S1. Average size of crystallites in HSPs (hierarchically structured particles) as a function of dopant concentration and temperature determined from PXRD data by Scherrer formula.

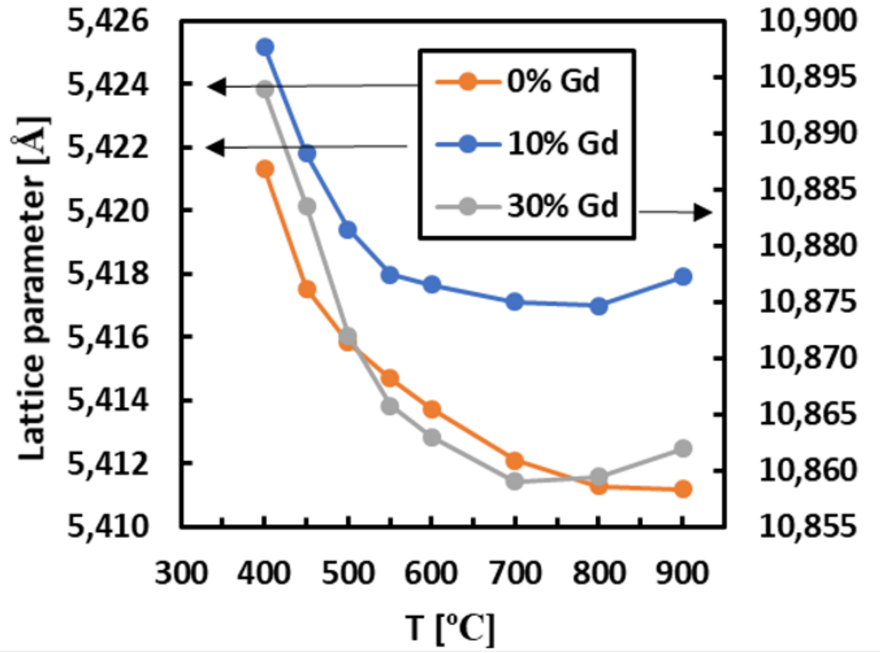

Fig. S3. Lattice parameters determined from Rietveld refinement of PXRD data.

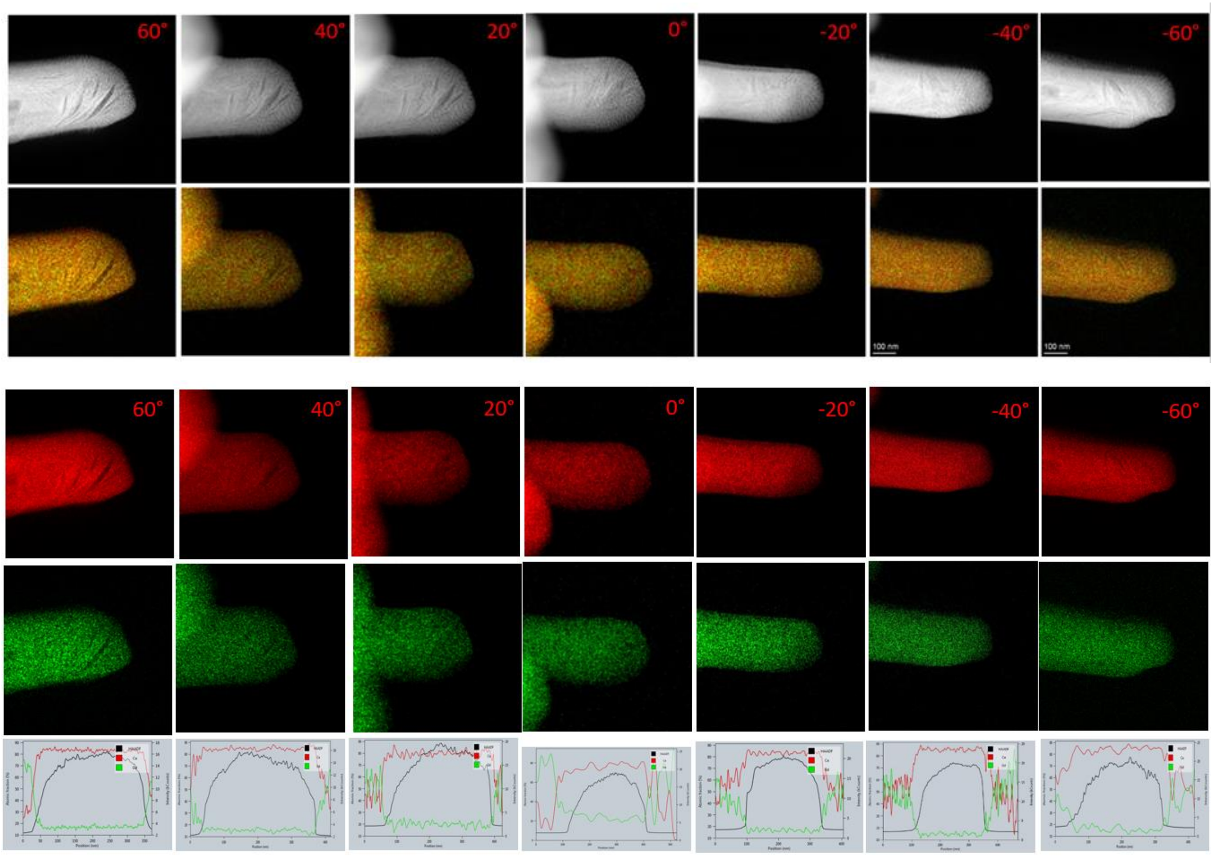

Fig. S4. STEM-XEDS images at different angles in an arm of $Ce_{0.9}Gd_{0.1}O_{1.95}$ star-shaped HSP with the visualization of elemental distribution of Ce (assigned red), Gd (assigned green) and corresponding line profile analysis of elemental distribution showing no significant inhomogeneity in Gd distribution

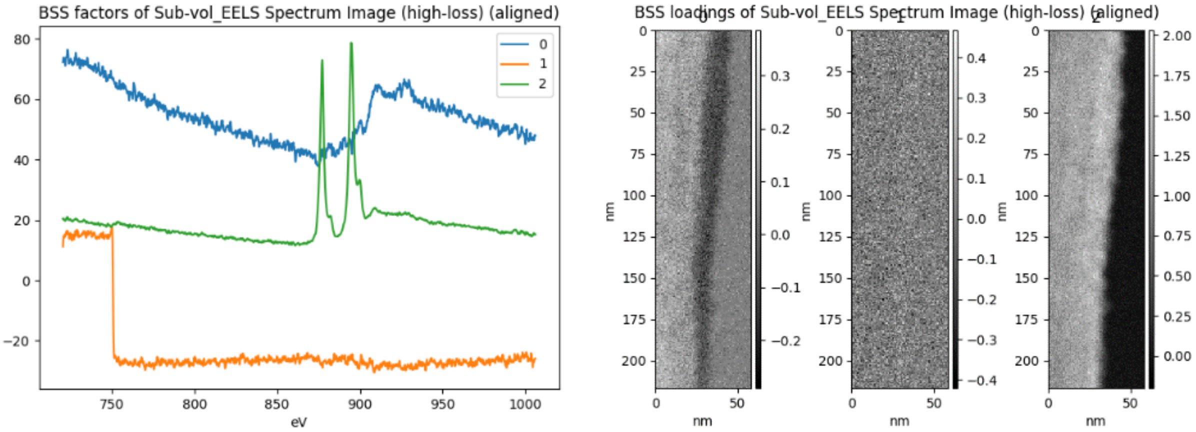

Fig S5. PCA-ICA routine post-treatment on SI-EELS data for separation of signals of different oxidation state. Results of of blind source separation shows exclusively one component for cerium (1) and other signals related to background and noise. As can be seen, the features of the obtained spectrum based on the intensities of the Ce-$M_{4,5}$ peaks can be only related to (IV) oxidation state.

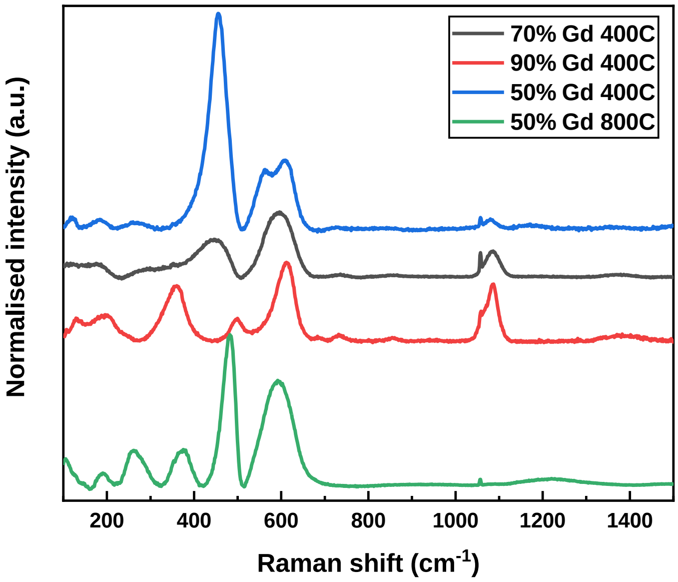

Fig. S6. RAMAN profiles of $Ce_{1-x}Gd_xO_{2-x/2}$ (x= 0.5; 0.7; 0.9)

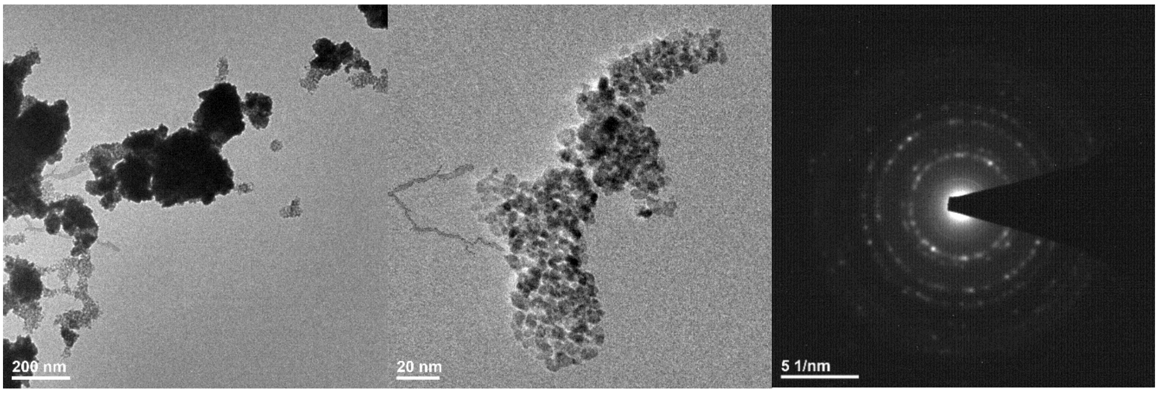

Fig. S7. TEM images and SAED of microemulsion-derived non-hierarchically organized NPs.

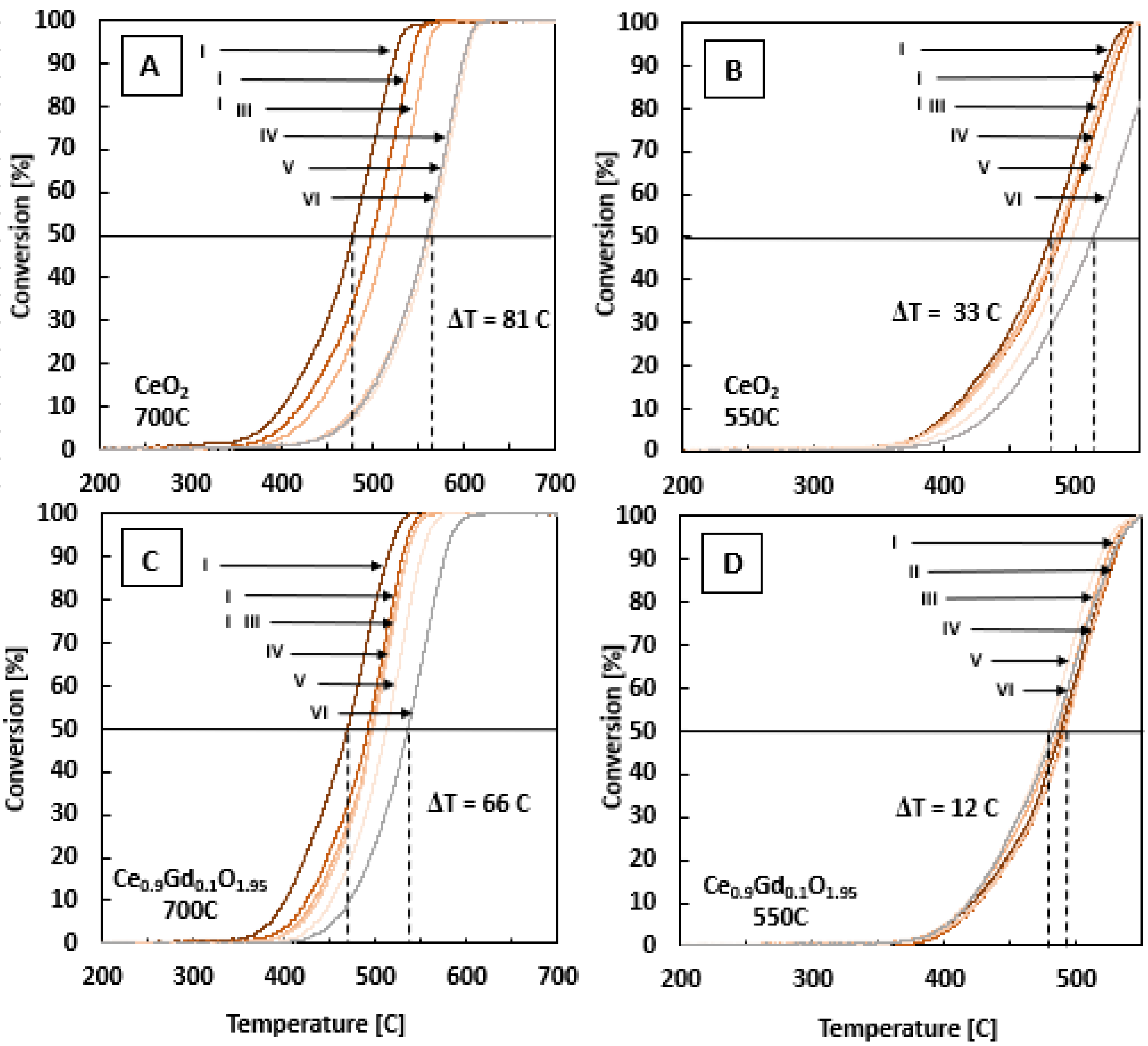

Fig. S8. TG profiles of soot oxidation for CeO_2 and $Ce_{0.9}Gd_{0.1}O_{1.95}$ HSPs heated in two temperature conditions of 550°C and 700°C.

Sample	TOF (h^{-1})
CeO_2 HSPs	12,8
$Ce_{0.9}Gd_{0.1}O_{1.95}$	21,6
$Ce_{0.7}Gd_{0.3}O_{1.85}$	14,0
$Ce_{0.6}Gd_{0.4}O_{1.80}$	7,6

Table S2. Propane oxidation performance of $Ce_{1-x}Gd_xO_{2-x/2}$ (x= 0; 0.1; 0.3; 0.4) HSPs. For comparative purposes (ref. 84) conversion of propane obtained at 450℃ was used for turnover frequency (TOF) calculation.

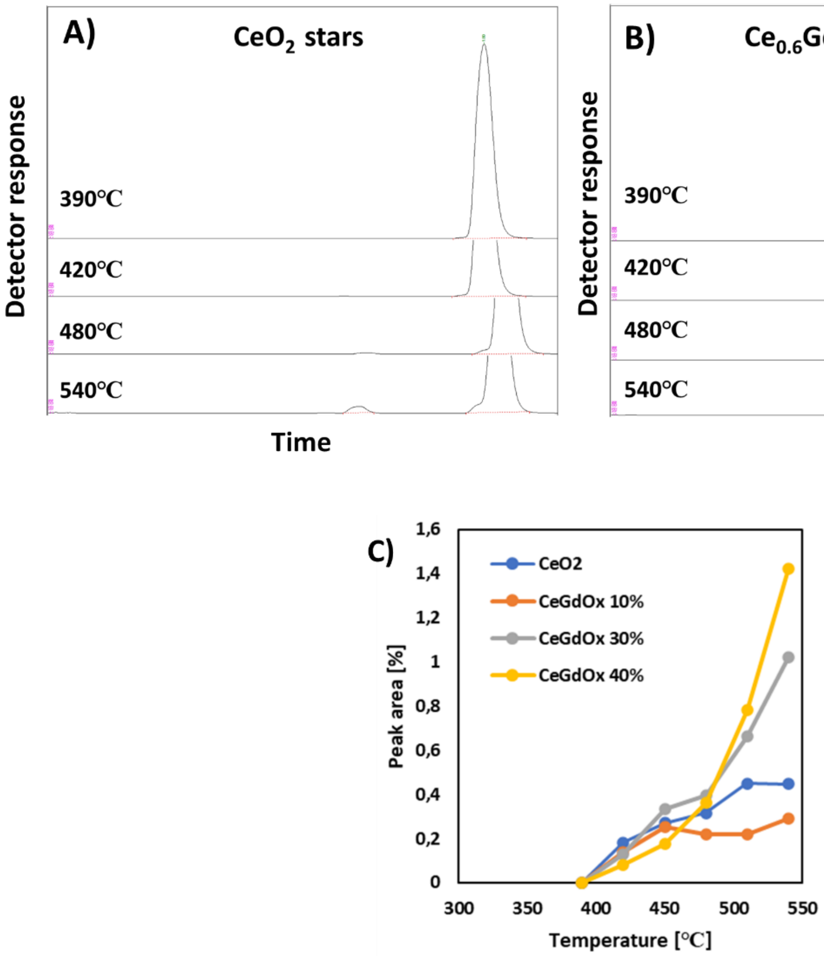

Fig. S9. Gas chromatograms of CeO_2 sample (A) and $Ce_{0.6}Gd_{0.4}O_{1.8}$ (B) at selected temperatures showing formation of trace by-product of propane conversion above 400°C ; C) Plot of the peak area of the detected propane conversion by-product as a function of temperature.

Hierarchical macroparticles of ceria with tube-like shape – synthesis and properties.

Małgorzata A. Małecka*, Piotr Woźniak
Institute of Low Temperature and Structure Research, Polish Academy of Sciences,
P.O. Box 1410, 50-950 Wrocław 2, Poland

ABSTRACT

This work presents results of a multitechnique (HRTEM – high resolution transmission electron microscopy, EDX – energy-dispersive X-ray spectroscopy, XRD – X-ray diffraction and H_2-TPR - temperature programmed reduction by H_2) studies on the hierarchical organized Yb-doped ceria nanocrystals ($Ce_{1-x}Yb_xO_{2-x/2}$) into the tube-like macro-particles. Hierarchical organized ceria based mixed oxides (macroparticles) were prepared by wet chemical method. It was observed that the predetermined shape of the investigated macroparticles was kept up to x = ~0.2. Above this value, the additional forms (like large, un-shapely aggregates of the nanoparticles) were created. A very important feature of these materials is very high shape stability, even at high temperatures. The overall shape of the macroparticle remained unchanged even at up to 900 ^oC. Moreover, the effect of the hierarchical arrangement of nanocrystallites into the tube-like macroparticles on activity in the propane oxidation and soot combustion reactions has been investigated. The CeO_2 nanopowder (prepared by the microemulsion technique) was used as an example of an unorganized structure. It was concluded that the presence of the 3D structure composed of CeO_2 nanocrystals significantly improves the catalytic activity of the tube-like material in comparison to the ceria nanopowder. The investigated oxides are good candidates for catalysts of soot oxidation. For the tube-like ceria the temperature of half oxidation ($T_{50\%}$ = 468 ^oC) was 62 ^oC lower than that for nanopowder ($T_{50\%}$ = 538 ^oC) and 103 ^oC lower than that for non-catalysed oxidation ($T_{50\%}$ = 592 ^oC). Moreover, introduction of the Yb^{3+} ions into the ceria matrix led to further improvement of the propane oxidation performance. For the tube-like $Ce_{0.9}Yb_{0.1}O_{1.95}$ the temperature of half oxidation ($T_{50\%}$ = 455 ^oC) was 40 ^oC lower than that for undoped tube-like CeO_2 ($T_{50\%}$ = 495 ^oC) and 95 ^oC lower than that for catalysed by the ceria nanopowder ($T_{50\%}$ = 550 ^oC).

Key words: catalysis; ceria; mixed oxides; hierarchical structure; TEM

*corresponding author:
Małgorzata Alicja Małecka

P.O. Box 1410, 50-950 Wrocław, Poland,
Tel: (4871) 3954150, Fax (4871) 441029, e-mail: M.Malecka@intibs.pl

doi.org/10.1039/D1CE00755F

INTRODUCTION

Nowadays, hierarchical materials are starting to play more and more important role in the catalysis [1;2], biomedicine [3] or environmental protection (sorbents) [4]. Researchers around the world are studying a variety of materials that can be defined as hierarchical materials. According to the one of the definitions, the hierarchical materials contain structural elements which themselves have structure. The hierarchical order of a structure or a material may be defined as the number n of levels of scale with recognized structure [5]. There are various materials in this group that show a certain hierarchy in their structure. Examples of such materials are meso-microporous materials with an ordered pore structure (pore hierarchy) [6], as well as 3D macrostructures built of nanoparticles in an ordered manner (structure hierarchy) [7]. In the literature, a whole range of methods for synthesizing hierarchical materials such as: template methods [8], self-organization [9], post-synthetic processing [7] or 3D printing can be found [2]. In heterogeneous catalysis, the size and shape of the developed surface of the catalyst which comes into contact with the reactants during the catalytic act is of key importance. Designing the macro-structure of catalysts, based on the knowledge of the basic structure-function relations, may lead to the creation of a new generation catalyst with interesting properties and significant catalytic activity. Literature reports indicate that hierarchical materials are used in various catalytic processes such as: Fischer-Tropsch synthesis [10], cracking [11], oxidation [12], epoxidation [13] and reduction [14].

One of the most important environmental problems are the atmospheric pollution and climate change [15;16]. Ceria-based $Ce_{1-x}Ln_xO_{2-y}$ (Ln = lanthanide ion) mixed oxides are important materials in significant environmental applications such as the three-way catalysts (TWC) [17] as well as the others significant technological applications e.g. the electrolyte and anode materials for solid oxide fuel cell (SOFC) technology [18;19]. Pure ceria has strong ability to reversible change of cerium oxidation state $Ce^{4+} \leftrightarrow Ce^{3+}$ ($Ce^{IV}O_2 \leftrightarrow Ce^{IV}{}_{1-x}Ce^{III}{}_xO_{2-(x/2)}$) [20;21]. This process can be modified by partial substitution of Ce^{+4} with Ln^{+3}, what facilitates a bulk reduction of ceria [22;23]. The improved reducibility is due to the creation of extrinsic oxygen vacancies in the lattice, which enhances the oxygen anion mobility [22;23]. The reduction-oxidation reaction of ceria is fully reversible and may be performed cyclically. In contrast to well-defined structure of pure cerium oxide, defective structures of mixed oxides ($Ce_{1-x}Ln_xO_{2-y}$) are less known. In the literature, some ideas about a model of the structure of the mixed oxides were presented [24-27]. The knowledge about the microstructure and properties of the nanocrystalline $Ce_{1-x}Ln_xO_{2-y}$ can significantly contribute to a better understanding of the operation of doped ceria catalysts and can be extremely useful for the design of new, active catalysts.

For catalysis of the most important parameters are the size and shape of the catalyst particles. Research carried out by many groups shows that nanoparticles have significantly different properties than bulk materials. Importantly, they strongly depend on the size of the investigated objects. A good example is the melting point of gold [28], which noticeably decreases in particles size less than 3 nm. Research shows that the redox characteristics and catalytic activity of $Ce_{1-x}Ln_xO_{2-y}$ materials strongly depend on the size of nanoparticles [29]. This effect is largely due to a very high proportion of surface atoms compared to volumetric atoms in particles with a size of single nanometers [28]. Unfortunately, the aggregation of nanoparticles into larger groups is a very important problem [30]. To prevent the aggregation, nanoparticles are often deposited on the supports, which provides greater size stability of the $Ce_{1-x}Ln_xO_{2-y}$ nanoparticles [31;32]. On the other hand, the nanoparticles of Ln-doped CeO_2 can interact with the support at elevated temperatures to form unwanted by-products (silicates, aluminates), which leads to catalyst deactivation [33;34]. The solution of the stability problem (due to aggregation effect) may be the construction of a hierarchical structure composed of mixed oxide nanoparticles.

In the literature, some information about the properties of hierarchically organized macro-structures composed of ceria nanoparticles are available. Such materials are synthesized using three basic methods: hard-templating, soft-templating, and self-templating methods [35] (and their combinations). Most of the available information applies to ceria materials based on ordered mesoporous materials (OMMs), where the role of the hard template is played by mesoporous, ordered materials [36;37] or spherical colloidal crystals [38]. The second route is the soft-template method [39-44] using such a template as surfactants, ionic liquids or organic macromolecules. The self-templating methods use the oxide precursor as a template. A good example is the thermal decomposition of Ce-MOF [45] or $Ce(HCOO)_3$ [7]. By using various organic-inorganic precursors, materials with different properties can be obtained.

Ceria based hierarchical materials are beginning to increasingly focus the attention of scientists from around the world. The combination of the unique properties of nanoparticles (CeO_2 or $Ce_{1-x}Ln_xO_{2-y}$) with a high specific surface area and a structural hierarchy is a very interesting topic for catalysis and environmental protection. Modifications of the hierarchy may result in significant changes to the properties of the material. It is a wide field of research and exploration of materials with desired properties. In this paper, the synthesis, thermal stability and redox properties of the tube-like Yb-doped ceria build by the hierarchically organized nanocrystalline $Ce_{1-x}Yb_xO_{2-y}$ have been investigated.

EXPERIMENTAL

The tube-like, hierarchical $Ce_{1-x}Yb_xO_{2-y}$ macro-particles build by the nano-sized mixed oxide crystallites were prepared by wet chemical synthesis involving several steps. First, nanocrystalline $Ce_{1-x}Yb_xO_{2-y}$ oxides (where x = 0; 0.1; 0.2; 0.3; 0.4; 0.5) were prepared by precipitation in microemulsion (water-in-oil, W/O) method. Details of this technique were described in our previous paper [46]. Briefly, Triton X-100 was used as a non-ionic surfactant and cyclohexane and 1-pentanol as an organic phase. Aqueous solutions of lanthanides (as nitrates-mixed in appropriate molar ratios) and ammonia were used as a water phase. Syntheses were performed at room temperature. In the next step, the powder samples obtained by centrifugation were treated with formic acid for 5 days to obtain mixed Ce-Yb formates. Then, formates were dried in atmospheric air. Subsequently, the tube-like macroparticles were prepared by the precipitation method in the presence of CTAB as an auxiliary agent. Details of this technique was inspired by [47]. Briefly, to the surfactant solution ($CTAB/H_2O/NH_4OH$ in the appropriate amounts), the water-ethanol suspension of cerium (or mixed Ce-Yb) formate was added dropwise. After stirring for 1 h the precipitate was centrifuged and washed with deionized water. Finally, after drying at 60 ^oC in atmospheric air, the samples were heated at 400 ^oC for 3 h (heating rate:1 ^oC/min).

The phase composition and structural parameters of the crystalline phases present in the samples were determined by XRD (X'Pert PRO PANalytical powder diffractometer, Cu Kα radiation) with a FullProf program [48] used for the display and analysis of the diffractograms. The Scherrer formula was used to estimate crystallite mean sizes. The morphology and microstructure were investigated by TEM (Philips CM-20 SuperTwin operating at 160 kV). HRTEM images and SAED patterns were analysed with a DigitalMicrograph program. The uniformity, chemical composition and topography of the samples were checked with a FE-SEM microscope (FEI NovaNanoSEM 230) equipped with an EDS analyser (EDAX Genesis XM4). The EDX analyses were performed from the large area (250 μm × 200 μm) of the samples. The powder samples were included in the carbon resin and then pressed at 180 ^oC and 250 bar to obtain a large, flat area. Nitrogen adsorption-desorption isotherms were carried out at 77 K on a Micromeritics ASAP 2020 instrument. Before measurements, the samples were degassed in vacuum at 200 ^oC for 4 h. The BET method was utilized to calculate the specific surface areas. The pore size distribution was derived from the desorption branch using the BJH method. The reducibility of the selected samples was tested by H_2-TPR (temperature programmed reduction in hydrogen). Typically, 50 mg of sample was placed in a quartz-glass microreactor (Autochem II 2920, Micromeritics) and heated with a temperature ramp of 10 ^oC/min up to 900 ^oC in a stream of 5% H_2 in Ar. The hydrogen consumption was monitored by a thermal conductivity detector

(TCD), calibrated with CuO (99.99%) as the reference material. The catalytic activity of the samples was tested in propane oxidation process. 50 mg of catalyst was heated up to 180 °C and stabilized at this temperature for 0.5 h in the gas flow (mixture 2500 ppm of propane in the synthetic air (10% O_2/N_2); 100 cm^3/min). The measurements were performed using Perkin-Elmer ARNEL Clarus 500 gas chromatograph equipped with a flame ionization detector and Elite Plot-Q chromatographic column. Measurements were performed at each step until the steady-state activity was obtained. The soot oxidation reaction was performed by heating a soot–catalyst mixture in air in a TG analyser Derivatograph MOM Q-1500D. The model soot used in this work was a carbon black Printex-U from Degussa S.A. Samples were prepared in "tight contact" mode by grinding a mixture of the catalyst (ca. 40 mg) and soot (2 : 1 by weight) in an agate mortar.

RESULTS AND DISCUSSION

Macroparticles characteristic

A series of works on hierarchical CeO_2 materials can be found in the literature [49-51]. One of the macroparticle morphologies are tubes made of interconnected cerium oxide nanocrystallites [52]. In this work, the series of the hierarchical, tube-like $Ce_{1-x}Yb_xO_{2-y}$ (where $0 < x < 0.5$) syntheses were performed. The details of the synthesis method used in this work were shown in the Supplementary Materials (Fig S1; Table S1). The samples are marked as CeYbx_T_t, where x – nominal Yb^{3+}-ions concentration, t – temperature of treatment [°C]. In the first step all samples were investigated by SEM-EDS. The measured compositions of the oxides were collected in Table 1. As noted, the amount of incorporated Yb-ions into the CeO_2 structure is visibly lower than nominal one. It could be due to with the synthesis route of the investigated in this work materials. The synthesis procedure, which was used here, is multi-step and time-consuming. In the first step, $Ce_{1-x}Yb_xO_{2-y}$ mixed oxide nanopowder was synthesized using the precipitation in microemulsion technique. At this stage, as shown in earlier works [27;53], the chemical composition of the mixed oxides was analogous to the nominal one in the full concentration range ($0 < x < 1$). The next stage of the synthesis was the preparation of the mixed Ce-Yb formate by treating the mixed oxide with formic acid. At this point, as indicated by the EDX research, the concentration of ytterbium ions in the half-substrate ($Ce_{1-x`}Yb_{x`}(HCOO)_3$) decreased. The mixed formate obtained in this way was then used for the synthesis of tube-like ceria based hierarchical materials.

Table 1. Concentration of Yb^{3+} in the ceria matrix (from SEM-EDX measurement - (% at) calculated as

(Yb ∗ 100) / (Yb + Ce).)

sample	CeYb0_T	CeYb10_T	CeYb20_T	CeYb30_T	CeYb40_T	CeYb50_T
nominal Yb^{3+}-ions concentration	0	10	20	30	40	50
measured Yb^{3+}-ions concentration	0	9	17	22	30	40

The hierarchical, tube-like (hollow inside and closed on one side) CeO_2 materials can be described as shaped macroparticles being composed of the cerium oxide nanocrystallites (Fig.1.A,C and Fig S2). The average size of crystallites for as-prepared materials was determined as 8 nm (from XRD data). The annealing process at the 400 ^{o}C under oxidizing atmosphere leads to a small increase in the size of the oxide crystallites to about 12 nm (Fig.2.A). The heating of the CeYb0_T materials at high temperatures up to 900 ^{o}C leads to a strong sintering of ceria crystallites (~72 nm), but the overall shape of tube-like macroparticles is preserved even in such extreme conditions (Fig.1.B and Fig.2.B). Similar results for the shape stability of the ceria macroparticles at high temperatures was previously observed in the analogous star-like material [54]. This is an undoubted advantage of the hierarchical materials. To investigate the effect of cerium oxide nanoparticles organization degree on material catalytic performance, the CeO_2 nanopowder (CeYb0_NP) prepared by the microemulsion technique [27;46] was used as an example of an unorganized structure for comparison purposes. Due to the synthesis procedure (using cerium nitrate as starting material) the product is not pre-heated at 400 ^{o}C but at the 550 ^{o}C to remove the nitrate groups from the surface [55]. For CeYb0_NP samples heated at 550 and 900 ^{o}C, the similar increase in crystalline size was observed as for CeYb0_T material (Fig.2). As presented in the literature, nanoparticles obtained by the precipitation in microemulsion method have the same size and are separated from each other during synthesis [56]. However, as have been shown in our other works [27;55], annealing of powder samples (both pure CeO_2 and doped oxides) at elevated temperatures leads to the formation of large, quite compact, shapeless agglomerates. In the literature [57;58], many attempts to reduce the sintering and agglomeration processes of cerium oxide nanoparticles can be found. Mainly, such methods are based on the use of inert carriers and modification of the nanoparticles surface. In our case, it was not possible to inhibit the process of crystallite growth (due to the direct crystallite-crystallite contact), but we managed to keep the overall shape of the microparticles. As noticed, the overall shape of the macroparticle was maintained even after annealing at 900 ^{o}C, which is very important from the catalytic point of view [54].

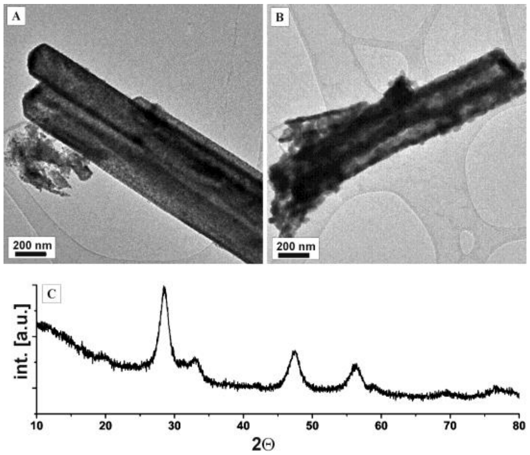

Fig.1. TEM images of the (A) CeYb0_T_400 and (B) CeYb0_T_900 and (C) XRD pattern of CeYb0_T (as-prepared sample).

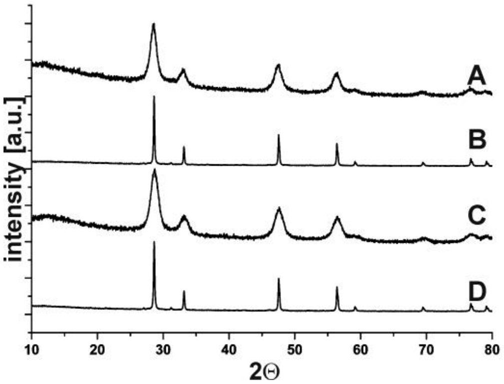

Fig.2. XRD patterns of the (A) CeYb0_T_400, (B) CeYb0_T_900, (C) CeYb0_NP_550 and (D) CeYb0_NP_900.

The analysis of the shape of the N_2 adsorption-desorption isotherm can be very helpful in characterizing the porous material. IUPAC [59] classified the adsorption isotherms into six types (Type I to VI), along with four hysteresis pattern types (H1 to H4). The characteristics of pores (microporous, mesoporous and microporous/nonporous) in the tested material can be determined [60;61] thanks to examining the course of the N_2 isotherm shapes exhibited by the material. Usually, meso- to macroporous materials (exhibiting the IV-type isotherm), with pore diameter in the range 2–100 nm will have a characteristic hysteresis loop, which is associated with capillary condensation and evaporation in the mesopores [60]. The shape of the isotherm hysteresis pattern (H1 to H4) reflects the material porosity characteristics and hence may be used to predict the types of pores present in the tested sample [60;62-64]. In the case of the CeYb0_T_400 sample, we are dealing with the isotherm assigned to a meso-macroporous material with a characteristic H3-type hysteresis loop [60]. Figure 3 shows the N_2 adsorption-desorption isotherms obtained for CeYb0_T_400 (red) and CeYb0_T_900 (grey). Careful analysis of the data indicated that the course of the hysteresis loop for the CeYb0_T_400 sample is best described by as mentioned the H3 loop model. This indicates the presence of the slit-like pores between non-rigidly aggregated particles [64-66] or presence of the pore network consists of macropores which are not completely filled with pore condensate [65]. The pore characteristics obtained from the N_2 adsorption study are consistent with the TEM results. In the case of CeYb0_T_400 sample, the CeO_2 nanocrystallites building tube-like macroparticles do not adhere closely to each other and create small pores/slits (slit-like pores) between them. In other words, the walls of such tubes are not solid but porous. Increasing the annealing temperature to 900 ^{o}C causes the sintering of the crystallites and thus an intense reduction of pores/slits and creation of a "more solid" surface of the tube walls. However, such analyzes should be performed very carefully, because the authors interpret isotherms with a very similar course very differently and the model curves do not always match the experimental data perfectly [64;66].

Table 2. BET surface area for investigated samples.

sample	CeYb0_T_400	CeYb10_T_400	CeYb20_T_400	CeYb0_T_900	CeYb0_NP_550	CeYb0_NP_900
BET surface area [m^2/g]	65	94	94	6	79	5

The similar shape of N_2 isotherm was also obtained by Guo et al [67] for mixed Mn_3O_4/CeO_2 hybrid nanotubes. On the other hand, as shown in [68], globin-like ceria macroparticles (GLM CeO_2) exhibits the type IV isotherm with an apparent H4-type hysteresis loop. Such run of adsorption-desorption isotherm made us believe that surfactant-assisted wet chemical synthesis method followed by thermal treatment allows to obtain macroporous hierarchically structured tube-like particles built of ceria nanocrystals non-rigidly arranged in the particle walls. Interestingly, the porous structure observed for CeYb0_T_400 was preserved to some extent for the sample annealed at a high temperature of 900 ^{o}C (Fig.3). Despite the strong decrease in the specific surface area from 64 to 6 m^2/g (for CeYb0_T_400 and CeYb0_T_900, respectively), the isotherm hysteresis loop is still visible. The strong decrease in specific surface area after thermal treatment at 900 ^{o}C, which was observed for CeYb0_T_900 sample, is related to the tube-like structure of macroparticles. In the case of CeYb0_T_400 sample, the CeO_2 nanocrystallites building tube-like macroparticles do not adhere closely to each other and create small pores/slits (slit-like pores) between them. In other words, the walls of such tubes are not solid but porous. Increasing the annealing temperature to 900 ^{o}C causes the sintering of the crystallites and thus an intense reduction of pores/slits and creation of a "more solid" surface of the tube walls. This approach is also confirmed by the analogous tests of the specific surface area for CeYb0_NP samples. For the CeYb0_NP_550 sample, the specific surface area was large due to the greater availability of the surface for N_2, while the sintering process at 900 oC resulted in its drastic reduction (table 2). It must be mentioned here that the so-called nanopowder cannot be regarded as entirely individual crystallites but rather loose agglomerates of nanocrystallites. Fig. S3 shows the pore size distributions for CeYb0_T_400, CeYb10_T_400, CeYb20_T_400 and CeYb0_T_900 samples. They are very difficult to interpret because there are no clear maxima. It is associated with very different values $Ce_{1-x}Yb_xO_{2-x/2}$ tubes (diameter and length). Such wide differences mean that the average meso-macro pore size cannot be determined. From the analysis of TEM images, it can be concluded that the tube diameters are around 200 nm, but this value is an estimate and in fact varies from 50 to 500 nm. Contrary to the definition of pore hierarchy (classical hierarchical materials) [69], our materials that show the hierarchy of structure (architecture) [54] do not have to show good pore distribution, especially in the meso-macro part. It is worth mentioning that acute maxima at ~3 nm (marked with a yellow line) cannot be associated with the sample characteristics because they are an artefact associated with the limit of the mechanical stability of liquids in pores [70-72].

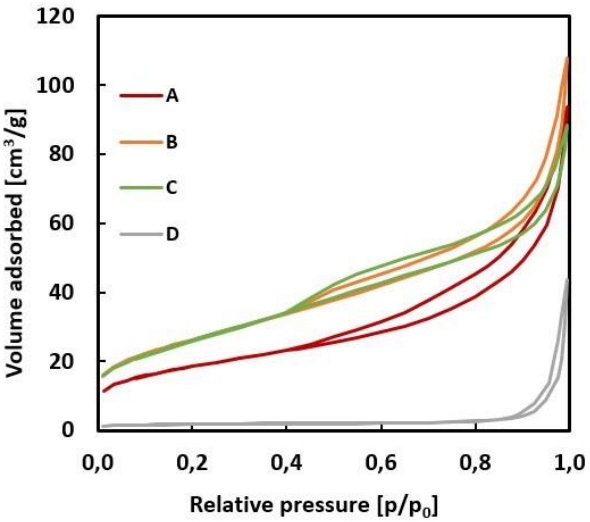

Fig.3. Nitrogen adsorption−desorption isotherm of the (A) CeYb0_T_400, (B) CeYb10_T_400 (C) CeYb20_T_400 and (D) CeYb0_T_900.

According to the same recipe, a series of samples doped with ytterbium ions were prepared. As expected, in the synthesis process a series of $Ce_{1-x}Yb_xO_{2-y}$ mixed oxides (0<x<0.5) was obtained, which is confirmed by XRD tests (see Fig.4A). The Figure 4B shows the X-ray diffraction patterns for the CeYbx_T_400 samples, which indicate the presence of the F or F# structure in the tested compounds [27]. It is known that the doping of CeO$_2$ with Yb^{3+} ions or other trivalent ions leads to changes in the oxide structure [24-27;73-75]. According to our previous experience, for low concentrations of Ln^{3+} in the CeO$_2$ structure, deformation of the F-type structure is observed, and in the case of the high concentration of Ln^{3+} ions, there is a structural transformation to the C-type (deformed) structure [27]. The limit of stability of the F-type structure in the case of Ce$_{1-x}$Yb$_x$O$_{2-y}$ oxides is the dopant concentration at the level of 50% (Yb*100/(Ce+Yb)) [27]. However, in our case, for sample CeYb50_T_400, the peak 1 1 2 (~ 20 °2Θ), characteristic for the C-type structure, was not observed. It is related to the lower actual concentration of Yb^{3+} ions in the doped samples than assumed (Table 1) and the low annealing temperature (400 °C). The annealing temperature is a key parameter because, as we know, the solubility limits of the trivalent lanthanide ions in the CeO$_2$ matrix change with increasing temperature [76].

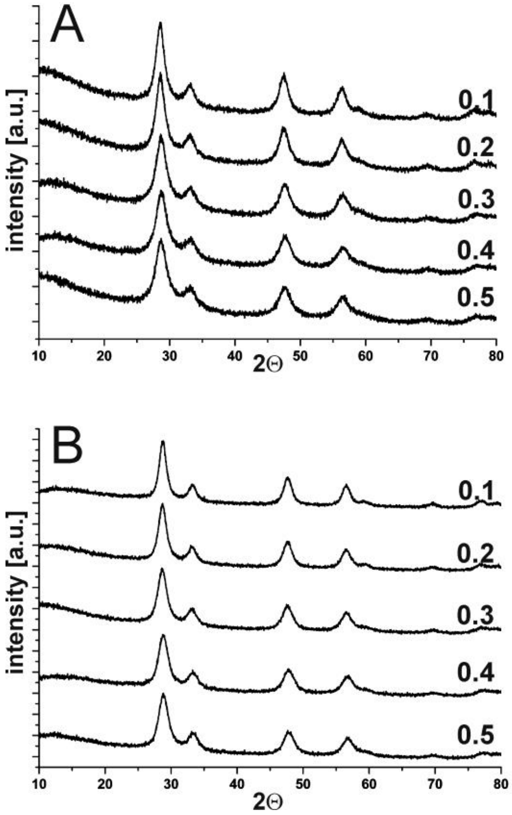

Fig.4. XRD patterns of the series of the (A) as-prepared tube-like Ce$_{1-x}$Yb$_x$O$_{2-y}$ samples and (B) after heat treatment at 400 °C in static air fir 3 h.

Table 3. Lattice parameter [nm] / mean size [nm] of Ce$_{1-x}$Yb$_x$O$_{2-y}$ nanocrystals calculated from XRD

data.

Treatment	CeYb0_T	CeYb10_T	CeYb20_T	CeYb30_T	CeYb40_T	CeYb50_T
As-prepared	0.5423 / 12	0.5422 / 10	0.5417 / 12	0.5418 / 12	0.5417 / 8	0.5413 / 8
400 °C/3 h air	0.5415 / 12	0.5413 / 12	0.5408 / 12	0.5402 / 12	0.5400 / 8	0.5400 / 9

As shown in Table 3, the average crystal size of the mixed oxides varies around 10 nm. This value does not change significantly during annealing of samples at 400 °C. This is a slightly different behaviour than in the case of powder samples (nanocrystalline), where a decrease in the size of mixed oxide crystallites was observed with an increase in the amount of ytterbium ions in the CeO_2 matrix [53]. This discrepancy is probably related to the different sources of Yb^{3+} ions used in the synthesis process and hence the different mechanism of formation of nanocrystalline $Ce_{1-x}Yb_xO_{2-y}$ mixed oxides. A mixture of cerium and ytterbium nitrates was used in the precipitation process in the microemulsion [53], while in this case the source of lanthanide ions was mixed Ce-Yb formate ($(Ce_{1-x}Yb_x)(HCOO)_3$). Both after and before pre-heating it can be seen that the mixed oxide lattice parameter decreases with increasing dopant concentration (Fig.S4). This effect is related to the doping of the CeO_2 matrix by a slightly smaller Yb^{3+} ion ((Ce^{4+} = 0.0870 nm, Yb^{3+} = 0.0868 nm, — for coordination VI [77]), and thus the formation of oxygen vacancies with the smaller estimated oxygen vacancy radius in the structure than the radius of O^{2-} ion [53] (Ov = 0.1164 nm [78], O^{2-} = 0.1400 nm [77]). A detailed description of this phenomenon was described in our earlier work [53] on nanocrystalline mixed Ce-Yb oxides obtained by microemulsion precipitation.

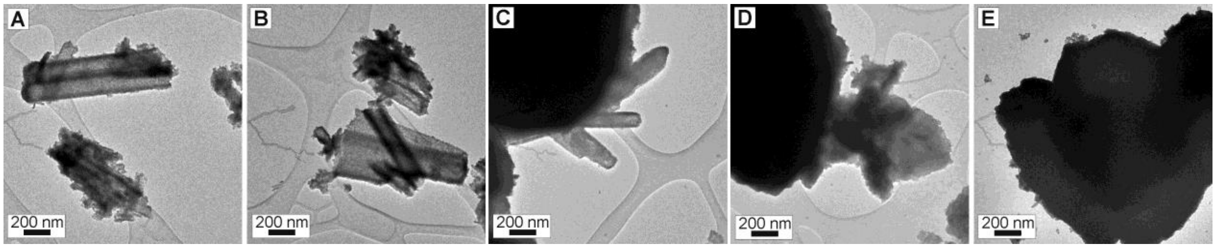

Fig.5. TEM images of the tube-like $Ce_{1-x}Yb_xO_{2-y}$ macroparticles ((A) x = 0.1, (B) x = 0.2, (C) x = 0.3, (D) x = 0.4, (E) x = 0.5,) after heat treatment at 400 °C in static air for 3 h.

Unfortunately, the assumed shape of macroparticles was achieved only for low-doped materials (up to about 20%). Figure 5 shows the series of TEM images obtained for the CeYbx_T_400 samples.

As can be seen in Fig.5AB, the macroparticles of the CeYb10_T_400 and CeYb20_T_400 follow the tube-like shape very well. In the TEM images of samples where the concentration of dopant exceeds 20% (Fig.5CDE) was observed more and more shapeless forms with increasing of Yb^{3+} ions content (large agglomerates of the nanoparticles mixed oxide). Finally, in the case of the highest doped sample CeYb50_T_400, no tube-like objects were found during the imaging. The addition of another ion to the ceria structure is often associated with the loss of shape of the mixed oxide particles relative to pure CeO_2. This effect was observed in the case of shape-selective synthesis of mixed Ce-Yb mixed oxides with the morphology of octahedrons and cubes [79]. In our opinion, problems with the formation of shaped, hierarchical, tube-like mixed oxide macroparticles for higher concentrations of Yb^{3+} ions in the CeO_2 matrix ($x > 0.2$) may be related to: a) phase separation into a Ce-rich and Yb-poor phase ($Ce_{1-a}Yb_aO_{2-a/2}$) and a Yb-rich and Ce-poor phase ($Yb_{2-b}Ce_bO_{3+b}$) [80] and b) change of the mixed oxide structure from a defective F-type (F#) structure to a defective C-type (C#) structure [27]. Both phenomena are possible. Taking into account the above results, samples CeYb10_T_400 and CeYb20_T_400 which kept their shapes best were selected for further research. BET tests performed for the doped samples showed visible changes in the porosity characteristics of CeYb10_T_400 and CeYb20_T_400 materials in relation to CeYb0_T_400 (Fig.3). It was noticed that the specific surface area of both doped samples increased significantly and amounted to 144% of the initial value measured for CeYb0_T_400. The results collected in the table 2 are in good agreement with those published by Guo et al [67]. As shown in [67], the specific surface area of the tube-like Mn_3O_4/CeO_2 (98 m^2/g) was very similar to that measured for the CeYb10_T_400 and CeYb20_T_400 samples. An in-depth analysis of the adsorption-desorption isotherms suggests that the type of pores present in the material slightly changes as a result of doping. It seems that the curves obtained for the samples doped with ytterbium ions can be described by the model being the intermediate state between H3 and H4 loop types, unlike the CeYb0_T_400 sample for which the H3 hysteresis loop type was the best fit. According to literature [66], in the CeYb10_T_400 and CeYb20_T_400 samples, more narrow slit pores should appear. H4 loops are often found for micro-mesoporous materials [65;81]. The presence of micropores in the macroparticle of the hierarchical catalyst (with increasing OSC for $Ce_{1-x}Ln_xO_{2-y}$ mixed oxides in comparison to pure ceria [82]) can play a key role in the catalytic act.

Reducibility and catalytic tests

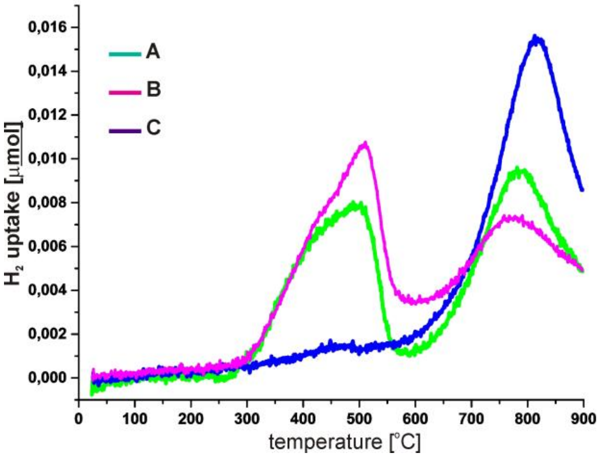

Fig.6. H_2-TPR curves obtained for the (A) CeYb0_T_400, (B) CeYb10_T_400 and (C) CeYb0_T_900.

Before the reducibility and catalytic tests, all the tested samples were subjected to a thermal treatment to remove any synthesis residues from their surfaces and to test the dependence of the redox properties on the annealing temperature. In this part, two-track considerations on the dependence of catalytic activity on the porosity characteristics of the material and the presence of the trivalent dopant in the CeO_2 matrix will be presented. The following materials were selected for research: CeYb0_T_400, CeYb0_T_900 (big difference in porosity characteristics) and CeYb10_T_400 as a representative mixed sample. The CeYb10_T_400 sample was chosen because of the best shape stability (a little better than for CeYb20_T_400) and the promising BET results as well as good compatibility the nominal and measured chemical composition. In our previous paper [54], a thorough analysis of the H_2-TPR results obtained for hierarchical star-like organized $Ce_{1-x}Gd_xO_{2-y}$ (x = 0 or 0.1) nanocrystals was carried out. As in the case of the tube-like materials described in this work, star-like ones were made of oxide nanoparticles with an average crystallite size of about 12 nm. Contrary to tube-like particles characteristics presented here, the star-like oxides had a well-defined porosity due to ceria nanocrystal mesoscale arrangement and thus the specific surface area 1.5 times larger than CeYb0_T_400 or CeYb10_T_400 samples. It is an opportunity to compare the redox and catalytic properties not only because of the degree of organization of nanoparticles into a macroparticle (nanopowder vs tube-like) but also in terms of the type of organization of the oxide nanoparticles into the macrostructure (tube-like vs star-like).

In Fig. 6, the H_2-TPR curves obtained for CeYb0_T_400, CeYb10_T_400 and CeYb0_T_900 are presented. According to the previous literature reports [83-85], the surface reduction in the lower temperature range (<600 ^{o}C) and the bulk reduction at higher temperatures (in range 600-900 ^{o}C) have been observed. In the Table 4, the data of H_2-TPR for investigated samples have been collected. The numbers correspond to the hydrogen uptake in μmol consumed by the 50 mg of sample. The shape of surface reduction curve is strongly related to the exposed facets by the crystallites. Studies of reducibility depending on the morphology of the cerium oxide crystals have been carried out by many groups [79;86;87]. These studies indicate that for each type of exposed walls, a separate maximum of hydrogen uptake can be assigned [79;88;89], and the scale of surface CeO_2 reduction is directly related to the size of the crystallites [90]. The results presented in this work agree well with the above literature considerations. As shown in Fig. 6, the low-temperature reduction peak, both for the CeYb0_T_400 and CeYb10_T_400 samples, is doubled. It is related to the shape of CeO_2 nanoparticles, which are the building blocks for the tube-like macroparticles. As known, small CeO_2 particles exhibit, most frequent, the truncated octahedral shape defined by eight {1 1 1} and six {1 0 0} facets. As indicated in the literature [91;92], the surface energy for low-index facets of CeO_2 follows: $\gamma\{1\ 1\ 1\} < \gamma\{1\ 0\ 0\}$. In consequence of that the formation of an anionic vacancies in {1 0 0} facets is significantly easier and the redox activity of these facets is higher than of {1 1 1} ones. Taking into account the above data, we can assign the acts of reduction on walls {1 1 1} and {1 0 0} to the maxima of H_2 uptake at temperatures 510 ^{o}C and 440 ^{o}C, respectively (Fig.6 and Fig.S5). As expected, the addition of Yb-ions into the ceria matrix ($x = 0.1$) caused the increase of the total hydrogen uptake. As can be seen in Table 4, the contribution of the low temperature part (in the temperature range 100-600 ^{o}C) of the hydrogen uptake visibly increased from 44.9% to 52.5% for samples CeYb0_T_400 and CeYb10_T_400, respectively. It is associated with the better diffusion of oxygen in the mixed oxide structure due to the presence of oxygen vacancies (Ov) formed by the trivalent Yb-ions doping in to the ceria matrix [27;93]. Also, Table 4 shows a comparison of H_2 uptake of cerium oxide nanoparticles organized into hierarchical tube-like macroparticles and the corresponding nanopowder. Interestingly, the total reduction for sample CeYb0_NP_550 is much greater than for CeYb0_T_400, but for the same samples treated at high temperature (900 ^{o}C), sample CeYb0_T_900 has a higher hydrogen uptake than CeYb0_NP_900. As can be seen, the organization of nanocrystalline CeO_2 into hierarchical macroparticles, slightly reduces the access of H_2 to the crystallite surface, but on the other hand, it increases the stability of gas access to the ceria surface for sintered samples (thanks to shape stability - see Fig. 1). A similar relationship was observed for hierarchical ceria based materials with porous star morphology [54]. This observation can be very important in determining the stability of the catalyst operation under the process conditions.

Table 4. H_2 uptake during H_2-TPR for investigated oxides

Sample	Low temperature H_2 uptake [μmol H_2] (100-600 °C)	High temperature H_2 uptake [μmol H_2] (600-900 °C)	Total H_2 uptake [μmol H_2] (100-900 °C)
CeYb0_T_400	19.9 (44.9%)	24.4 (55.1%)	44.3
CeYb0_T_900	7.2 (16.0%)	37.7 (84.0%)	44.9
CeYb10_T_400	26.5 (52.5%)	24.0 (47.5%)	50.5
CeYb0_NP_550	32.5 (52.9%)	28.9 (47.1%)	61.4
CeYb0_NP_900	2.6 (7.9%)	30.2 (92.1%)	32.8

In the literature [94-101], many reports on the catalytic activity of CeO_2 or ceria based mixed oxides could be found. Most of the found publications concern the relationship between the size and shape of the oxide crystallites [102-104] or the content of the Ln-dopant ions in the ceria matrix [105;106]. One of the most important catalytic processes from an environmental point of view is the combustion of soot, which is formed during the operation of diesel engines. What is worth noting, there are many mechanisms describing the catalytic oxidation act associated with the presence of oxygen vacancies in pure and doped CeO_2 [107]. The differences are based on a different approach to "active oxygen" directly taking part in the oxidation reaction. This is an important point for describing the active sites in the catalyst. The first of them and the simplest mechanism is based on the excellent red-ox properties of cerium oxide. In the oxidation of, eg. soot, the network oxygen is involved, released due to the partial reduction of cerium ions. Then, oxygen from the atmosphere is adsorbed on the catalyst surface and oxidizes Ce^{+3} to Ce^{+4}. An alternative to the simple red-ox mechanism described above is the carbonate mechanism, which consists in the simultaneous reaction of gaseous and network oxygen with particles, e.g. soot (or particles of other carbon compounds). As a result, CO_2 (s) bound to the catalyst surface is formed in the form of surface carbonates (intermediate carbon compounds). The decomposition of the previously formed surface carbonates is then stimulated by gaseous oxygen from the air, which also provides re-oxidation of the cerium oxide and regeneration of the catalyst [107;108]. In the Fig.7, the results of the soot (PRINTEX U) combustion tests for the series of ceria samples with varying degrees of nanoparticle organization were shown. In our case, the $T_{50\%}$ for the non-catalysed soot combustion was 592 °C [55]. As shown, use the nanocrystalline ceria particles, as a catalyst of the soot combustion process, lowers the half combustion temperature ($T_{50\%}$) from 592 °C to 538 °C. In our previous work [55], the soot combustion process catalysed by the nanocrystalline ceria and doped ceria nanopowders (Pr, Tb, Lu) was meticulously tested. Contrary to the present work, in this work the temperature of the pre-annealing of nanopowders was lower (400 °C) and thus the surface of nanoparticles was not cleaned of nitrates. This resulted in a further reduction of $T_{50\%}$ by another 30 degrees [55]. But in this work we deal with the dependence of the degree of organization of nanoparticles into hierarchical macrostructures, therefore the powder samples were subjected to annealing at 550 ^{o}C to clean their surface. Bueno-López et al [106], revelated that CeO_2 decreases this temperature to 575 ^{o}C but the synthesis procedure by thermal decomposition of cerium nitrate at high temperature lead to formation of rather large ceria crystals. High dispersion of the oxides is important for achieving high activity in combustion since the activity of polycrystalline commercial oxides (bottle) generally appeared to be negligible (581 ^{o}C) [55]. In [54], the catalytic activity of the porous, star-like ceria macroparticles was compared with CeO_2 nanopowder (obtained by precipitation in W-in-O microemulsion). As shown, the star-shaped ceria particles initiate the soot combustion process at significantly lower temperature that for microemulsion-derived nanoparticles. Fig.7 shows that the half combustion temperature observed for the star-like particles (463 ^{o}C – pink curve) is very close to that designated for the CeYb0_T_400 sample (468 ^{o}C – green curve). This coincidence could be due to the same mechanism of the catalytic act on porous ceria based materials. Woźniak et al [54] postulated that the key–lock catalysis concept could be used to explain the enhanced soot combustion performance in hierarchically structured star-shaped particles. The same mechanism could be assigned to the process catalyzed by the CeYb0_T_400, where the large pores (related to the shape of the tube) were observed by the electron microscopy technique (Fig.1). Those observations are in good agreement with data presented in [109;110] where macroporous 3DOM CeO_2 and $Ce_{1-x}Zr_xO_2$ materials were more active than ceria powder in the soot combustion process.

Additionally, the second cycle of soot combustion was performed for CeYb0_T_400 and CeYb0_NP_550 to check the stability of these materials. As expected, the $T_{50\%}$ temperatures for both samples were higher than in the first cycle and they were 512 ^{o}C and 570 ^{o}C for CeYb0_T_400 and CeYb0_NP_550, respectively. As shown in Fig.7, CeYb0_T_400 material in the second run of catalytic process (CeYb0_T_400_II) is still more active than nanopowder in the first cycle. This is evidence of the dependence of the ceria activity on the degree of organization of nanoparticles into the 3D macrostructures. The above observation is also confirmed by the catalytic tests shown in our previous work [54].

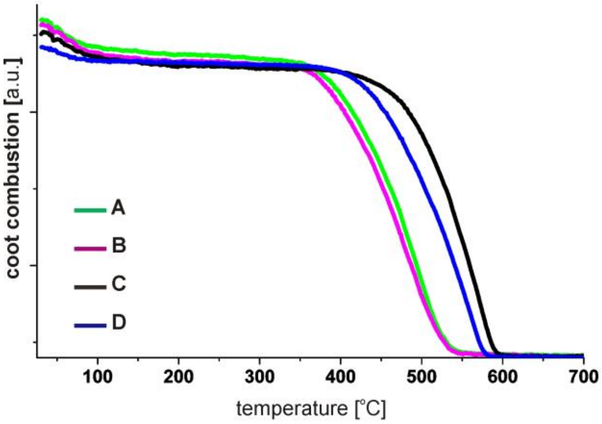

Fig.7. TG curves for soot oxidation by air catalysed by the (A) CeYb0_T_400, (B) star-like CeO_2 (heated at 400 °C) [54], (C) CeYb0_NP_550 and (D) CeYb0_T_400_II (second soot oxidation cycle).

As in the case of soot particles, the emission of volatile organic compounds (VOCs) poses a harmful risk to the environment and human health [111-113]. VOCs include such compounds as methane, benzene, xylene, propane and butane. Additionally, for better characterization, the second catalytic test was carried out. In Fig. 8, the results of the propane oxidation tests for all investigated samples are presented. As indicated in the literature [114;115], CeO_2 is not a good catalyst for this process. According to literature, at 400 °C the conversion of propane was ~10 % [115] or even 0 % [114] for materials where surface area (S_{BET}) was 54 and 66 m^2/g, respectively. In the case of research conducted on our samples (CeO_2), at 400 °C the propane conversion is also around 10%. A comparison of the propane conversion curves for samples CeYb0_T_400, CeYb0_NP_550 and CeYb0_NP_400 shows that at 400 °C the conversion was 8, 5 and 15%, respectively. The visible difference for CeYb0_NP_550 and CeYb0_NP_400 samples is probably related to the presence of nitrate groups on the surface of CeO_2 nanocrystallites and consequently, their increased (one-time) catalytic activity [55]. In the case of sample CeYb0_T_400, the conversion was similar to that for [115], and at the same time, compared to the purified nanopowder (CeYb0_NP_550), it was noticeably higher. A difference was also noticed in the dynamics of propane oxidation process on the ceria catalyst with a hierarchical structure and nanopowder. The estimated $T_{50\%}$ value for process catalysed by the CeYb0_T_400 sample (495 °C) was 55 °C lower than one for CeYb0_NP_550 (see Table 5). The strong influence of the hierarchical structure of CeO_2 macroparticles on catalytic activity is also confirmed by studies presented in the literature. A comparison of the course of the propane oxidation reaction on CeO_2 materials with rod-like morphology (10x300 nm) [114] and hierarchical tubes (CeYb0_T_400) showed that the conversion at 550 °C was 22 % and 70 %, respectively. Interestingly, the BET specific surface area calculated for both samples were similar and amounted to about 65 m^2/g, which indicates the key importance of the hierarchical arrangement of cerium oxide particles for catalytic activity. As shown in Table 5, the high temperature treatment leads to the deactivation of the catalyst. It is probably related to the lowering of the specific surface of the material and the loss of micropores. Such observation is in good agreement with literature data [116] where the relationship between specific surface area of ceria catalysts and activity in CO oxidation and dry reforming of methane process was discussed.

Table 5. Performances of the investigated materials: C_3H_8 oxidation reaction.

sample	$T_{50\%}$ [°C]	max conversion at 550 °C [%]
CeYb0_T_400	495	70
CeYb10_T_400	455	90
CeYb0_NP_400	510	62
CeYb0_NP_550	550	50
CeYb0_T_900	-	5
commercial (bulk) CeO2	-	5

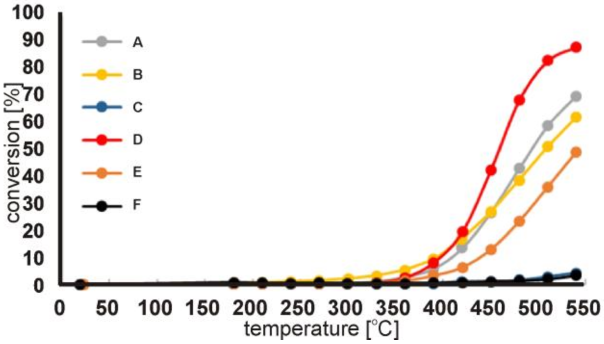

Fig.8. C_3H_8 oxidation activity of the (A) CeYb0_T_400, (B) CeYb0_NP_400, (C) commercial (bulk) CeO_2, (D) CeYb10_T_400; (E) CeYb0_NP_550 and (F) CeYb0_T_900.

An even greater decrease in $T_{50\%}$ was noted for the process catalysed by the sample doped with ytterbium ions (CeYb10_T_400). As can be seen in Table 5, the $T_{50\%}$ for CeYb10_T_400 decreased by another 50 °C in relation to CeYb0_T_400, and the maximum propane conversion at the 550 °C reached 90%. It is a significant improvement of the catalytic properties in the C_3H_8 oxidation process by doping the ceria structure with other ions, which was also confirmed in the literature [114;115]. As indicated in the literature [114;115], the presence of the dopant ions in the ceria structure improves the reducibility and the oxygen mobility which were found to be necessary for the promotion of propane oxidation.

CONCLUSIONS

Summarizing, hierarchical, tube-like $Ce_{1-x}Yb_xO_{2-y}$ where x = 0, 0.1 and 0.2 were synthesized using a simple wet chemical method. It was noticed that, the shape of the mixed oxide macroparticles for the Yb-ions doping level above x = 0.2, has been changed into rather shapeless agglomerates of nanoparticles. As noticed, the overall shape of the macroparticle was maintained even after annealing at 900 ^{o}C, despite the strong growth of crystallites. It could be very important from the catalytic point of view.

The reducibility and catalytic activity of the pure and Yb-doped ceria were also investigated depending on the arrangement level of nanocrystallites in to the macroparticles. Due to the hierarchical arrangement of CeO_2 nanoparticles, the degree of reducibility of cerium ions is constant even after annealing the material at high temperature. The presence of ytterbium ions in the CeO_2 matrix visibly increases the surface reducibility of the hierarchical $Ce_{1-x}Yb_xO_{2-y}$ mixed oxide. As shown in the soot combustion and propane oxidation reaction as an example, the organization of nanoparticles into hierarchical macroparticles and the presence of the trivalent dopant ions causing the formation of oxygen vacancies in the cerium oxide structure effectively increases the catalytic activity of these materials.

ACKNOWLEDGMENTS

The author thanks Prof. Leszek Kępiński for inestimable help with discussion of experimental results and unshakable belief in author’s capacity, Mrs. Zofia Mazurkiewicz for valuable help with preparation of the samples and Mrs. Ewa Bukowska for XRD measurements.

REFERENCES

[1] R.P. Ye, J. Ding, W. Gong, M.D. Argyle, Q. Zhong, Y. Wang, C.K. Russell, Z. Xu, A.G. Russell, Q. Li, M. Fan and Y.-G. Yao, Nat. Commun., 2019, 10, 5698.

[2] C. Zhu, Z. Qi, V.A. Beck, M. Luneau, J. Lattimer, W. Chen, M.A. Worsley, J. Ye, E.B. Duoss, C.M. Spadaccini, C.M. Friend and J. Biener, Sci. Adv., 2018, 4, 9459.

[3] Q. Chen, N.M. Pugno and J. Mech. Beh. Bio. Mater., 2013, 19, 3.

[4] Y. Liu, Z. Wu, X. Chen, Z. Shao, H. Wang and D. Zhao, J. Mater. Chem., 2012, 22, 11908.

[5] R. Lakes, Nature, 1993, 36, 511.

[6] F. Kurosaki, H. Koyanaka, M. Tsujimoto and Y. Imamura, Carbon, 2008, 46, 850.

[7] J. Wei, Z. Yang, H. Yang, T. Sun and Y. Yang, CrystEngComm., 2011, 13, 4950.

[8] I.Y. Kaplin, E.S. Lokteva, E.V. Golubina and V.V. Lunin, Molecules, 2020, 25, 4242.

[9] L.S. Zhong, J.S. Hu, H.P. Liang, A.M. Cao, W.G. Song and L.J. Wan, Adv. Mater., 2006, 18, 2426.

[10] C.M.A. Parlett, K. Wilson and A.F. Lee, Chem. Soc. Rev., 2013, 42, 3876.

[11] J. Liu, G. Jiang, Y. Liu, J. Di, Y. Wang, Z. Zhao, Q. Sun, C. Xu, J. Gao, A. Duan, J. Liu, Y. Wei, Y. Zhao and L. Jiang, Sci. Rep., 2014, 4, 7276.

[12] N.V. Zaletova, A.O. Turakulova and V.V. Lunin, Stud. Surf. Sci. Catal., 2010, 175, 305.

[13] K. Lin, O.I. Lebedev, G. Van Tendeloo, P.A. Jacobs and P.P. Pescarmona, Chem. Eur. J., 2010, 16, 13509.

[14] C. Hiragond, S. Ali, S. Sorcar and S.-I. In, Catalysts, 2019, 9, 370.

[15] B.J. Finlayson-Pitts and J.N. Pitts Jr., Science 1997, 276, 1045.

[16] C.M. Somers, B.E. McCarry, F. Malek and J.S. Quinn, Science, 2004, 304, 1008.

[17] S. Bernal, G. Blanco, M.A. Cauqui, M.P. Corchado, C. Larese, J.M. Pintado and J.M. Rodriguez-Izquierdo, Catal. Tod., 1999, 53, 607.

[18] K.C. Wincewicz and J.S. Cooper, J. Power Sources, 2005, 140, 280.

[19] T. Mori, R. Buchanan, D.R. Ou, F. Ye, T. Kobayashi, J. Kim, J. Zou and J. Drennan, J. Solid State Electrochem., 2008, 12, 841.

[20] E. Aneggi, C. de Leitenburg, G. Dolcetti and A. Trovarelli, Catal. Tod., 2006, 114, 40.

[21] S. Rossignol, F. Gerard, D. Mesnard, C. Kappenstein and D. Duprez, J. Mater. Chem., 2003, 13, 3017.

[22] S. Bernal, G. Blanco, G. Cifredo, J.A. Perez-Omil, J.M. Pintado and J.M. Rodrıguez-Izquierdo, J. Alloys Compd., 1997, 250, 449.

[23] G. Vlaic, P. Fornasiero, S. Geremia, J. Kaspar and M. Graziani, J. Catal., 1997, 168, 386.

[24] D.R. Ou, T. Mori, F. Ye, J. Zou, G. Auchterlonie and J. Drennan, Phys. Rev. B, 2008, 77, 024108.

[25] F. Ye, T. Mori, D.R. Ou, A.N. Cormack, R.J. Lewis and J. Drennan, Solid State Ionics, 2008, 179, 1962.

[26] F. Ye, T. Mori, D.R. Ou, J. Zou and J. Drennan, Solid State Ionics, 2009, 180, 1414.

[27] M.A. Małecka, J.J. Delgado, L. Kępiński, J.J. Calvino, S. Bernal, G. Blanco and X. Chen, Catal. Tod., 2012, 187, 56.

[28] S. Tjong and H. Chen, Mater. Sci. Eng. R, 2004, 45, 1.

[29] A.G. Thomé, S. Peters and F. Roessner, Catal. Commun., 2017, 97, 10.

[30] B. Faure, G. Salazar-Alvarez, A. Ahniyaz, I. Villaluenga, G. Berriozabal, Y.R De Miguel and L.

Bergström, Sci. Technol. Adv. Mater., 2013, 14, 023001.

[31] S. Phanichphant, A. Nakaruk and D. Channei, Appl. Surf. Sci., 2016, 387, 214.

[32] Y. Shen, S. Zhu, T. Qiu and S. Shen, Catal. Comm., 2009, 11, 20.

[33] M.A. Małecka, Ceram. Inter., 2016, 42, 14826.

[34] M.A. Małecka and L. Kępiński, Mater. Res. Bull., 2013, 48, 2571.

[35] L. Zhang, L. Jin, B. Liu and J. He, Front. Chem., 2019, 7, 22.

[36] Q. Wang, Y. Zhang, Y. Zhou, Z. Zhang, J. Xue, Y. Xu, C. Zhang, X. Sheng and N. Kui, RSC Adv., 2016, 6, 730.

[37] F. Sakina, J.M. Muñoz-Ocaña, A. Bouziane, M. Lopez-Haro and R.T. Baker, Nanoscale Adv., 2019, 1, 4772.

[38] V. Alcalde-Santiago, E. Bailón-García, A. Davó-Quiñonero, D. Lozano-Castelló and A. Bueno-López, Appl. Catal. B, 2019, 248, 567.

[39] T. Wang and L. Dai, Coll. Surf. A, 2002, 209, 65.

[40] L. Xu, H. Song and L. Chou, Inter. J. Hydrogen Energy, 2012, 37, 18001.

[41] A.S. Araujo, J.M.F.B. Aquino, M.J.B. Souza and A.O.S. Silva, J. Solid State Chem., 2003, 171, 371.

[42] A.S. Araujo and M. Jaroniec, J. Coll. Inter. Sci., 1999, 218, 462.

[43] D. Kumar, S. Varma, G.K. Dey and N.M. Gupta, Micro. Meso. Mater., 2004, 73, 181.

[44] H.R. Li, J. Lin, L.S. Fu, J.F. Guo, Q.G. Meng, F.Y. Liu and H.J. Zhang, Micro. Meso. Mater., 2002, 55, 103.

[45] J. Zheng, Z. Wang, Z. Chen and S. Zuo, J. Rare Earths, in press https://doi.org/10.1016/j.jre.2020.08.009.

[46] M.A. Małecka and L. Kępiński, J. Alloys Compd., 2007, 430, 282.

[47] M. Grun, K. Unger, A. Matsumoto and K. Tsutsumi, Micropor. Mesopor. Mater., 27 (1999) 207.

[48] J. Rodríguez-Carvajal, Phys. B, 1993, 192, 55.

[49] K. Pugazhendhi, V. Bharathi Lenin, D. J. Sharmila, J. Kethzy Agnes, B. Praveen, and J. Merline Shyla, AIP Conference Proceedings, 2019, 2115, 030606.

[50] G. Shen, M. Liu, Z. Wang and Q. Wang, Nanomaterials 2018, 8, 773.

[51] J. Wei, Z. Yang and Y. Yang, CrystEngComm, 2011,13, 2418.

[52] Z. Wang, J. Qi, K. Zhao, L. Zong, Z. Tang, L. Wang and R. Yu, Mater. Chem. Front., 2017,1, 1629.

[53] M.A. Małecka, U. Burkhardt, D. Kaczorowski, M.P. Schmidt, D. Goran and L. Kępiński, J. Nanopart. Res. 2009, 11, 2113.

[54] P. Woźniak, W. Miśta and M.A. Małecka, CrystEngComm, 2020, 22, 5914.

[55] M.A. Małecka, L. Kępiński and W. Miśta, Appl. Catal. B, 2007, 74, 290.

[56] B.J. Palla, D.O. Shah, P. Garcia-Casillas and J. Matutes-Aquino, J. Nanoparticle Res., 1999, 1, 215.

[57] K.A. Ledwa, L. Kępiński, M. Pawlyta, ChemNanoMat, 2020, 6, 1260.

[58] M.A. Małecka and L. Kępiński, Catal. Tod., 2012, 180, 117.

[59] K. Sing, D. Everett, R. Haul, L. Moscou, R. Pierotti, J. Rouquérol and T. Siemieniewska, Pure Appl. Chem., 1985, 57, 603.

[60] L.M. Anovitz, D.R. Cole, Rev. Mineralogy Geochem., 2015, 80, 61.

[61] M. Naderi, Progress in Filtration and Separation, 2015, 585. https://doi.org/10.1016/C2009-0-64471-8

[62] S. Yang, G. Chen, C. Lv, C. Li, N. Yin, F. Yang and L. Xue, Energy Expl. Expl., 2018, 36, 265.

[63] M. Abunowara, M.A. Bustam, S. Sufian, M. Babar, U. Eldemerdash, H. Suleman, R. Bencini, and S. Ullah, J. Environ. Eng., 2020, 146, 04020087.

[64] Z. Wang, X. Jiang, M. Pan and Y. Shi, Minerals 2020, 10, 377.

[65] M. Thommes, K. Kaneko, A.V. Neimark, J.P. Olivier, F. Rodriguez-Reinoso, J. Rouquerol and K.S.W. Sing, Pure Appl. Chem., 2015, 87, 1051.

[66] D.S. Ivanova,J.K.Angarska and E.D.Manev, Bulgarian Chem. Commun., 2016, 48, 101.

[67] S. Guo, W. Sun, W. Yang, Z. Xu, Q. Li, and J.K. Shang, ACS Appl. Mater. Interfaces, 2015, 7, 26291.

[68] Y. He, X. Liang and B. Chen, Nano Res., 2015, 8, 1269.

[69] G.S. Chai, I.S. Shin, J-S. Yu, Adv. Mater., 2004, 16, 2057.

[70] W. Lai, S. Yang, Y. Jiang, F. Zhao, Z. Li, B. Zaman, M. Fayaz, X. Li, Y. Chen, Adsorption, 2020, 26, 633.

[71] J.C. Groen, L.A.A. Peffer, J. Perez-Ramirez, Micro. Meso. Mater., 2003, 60 1.

[72] J.C. Groen, J. Perez-Ramirez, Appl. Catal. A, 2004, 268, 121.

[73] D.R. Ou, T. Mori, F. Ye, T. Kobayashi, J. Zou, G. Auchterlonie and J. Drennan, Appl. Phys. Lett., 2006, 89, 171911.

[74] M.A. Małecka and L. Kępiński, J. Microscopy, 2010, 237, 391.

[75] O. Bezkrovnyi, M.A. Małecka, R. Lisiecki, V. Ostroushko, A.G. Thomas, S. Gorantla and L. Kepinski, CrystEngComm, 2018, 20, 1698.

[76] V. Longo and L. Podda, J. Mater. Sci., 1981, 16, 839.

[77] R. D. Shannon, Acta Cryst., 1976, A32, 751.

[78] S.J. Hong and A.V. Virkar, J Am. Ceram. Soc., 1995, 78, 433.

[79] M.A. Małecka, P. Kraszkiewicz, O. Bezkrovnyi, Mater. Charact. 2019, 155, 109796.

[80] B. Mandal, V. Grover, M. Roy, A. Tyagi, J. Am. Ceram. Soc. 2007, 90, 2961.

[81] S. Fu, Q. Fang, A. Li, Z. Li, J. Han, X. Dang and W. Han, Energy Sci Eng., 2021, 9, 80.

[82] D. Devaiah, L.H. Reddy, S.-E. Park and B.M. Reddy, Catal. Rev., 2018, 60, 177.

[83] Y. Wei, Z. Zhao, J. Jiao, J. Liu, A. Duan and G. Jiang, J. Rare Earths, 2014, 32, 124.

[84] G.R. Rao, Bull. Mater. Sci., 1999, 22, 89.

[85] J. Ramirez-Cuesta, J. Am. Chem. Soc., 2017, 139, 9721.

[86] E.W. Zhao, Y. Xin, H.E. Hagelin-Weaver and C.R. Bowers, ChemCatChem, 2016, 8, 2197.

[87] E. Aneggi, D. Wiater, C. de Leitenburg, J. Llorca, and A. Trovarelli, ACS Catal., 2014, 4, 172.

[88] X. Tong, T. Luo, X. Meng, H. Wu, J. Li, X. Liu, X. Ji, J. Wang, C. Chen and Z. Zhan, Small, 2015, 11, 5581.

[89] M. Kovacevic, B.L. Mojet, J.G. van Ommen and L. Lefferts, Catal. Lett., 2016, 146, 770.

[90] F. Giordano, A. Trovarelli, C. Leitenburg and M. Giona, J. Catal., 2000, 193, 273.

[91] C. Sun and D. Xue, Phys. Chem. Chem. Phys., 2013, 15, 14414.

[92] Z. Wang and X. Feng, J. Phys. Chem. B, 2003, 107, 13563.

[93] H.A. Lara-García, D.G. Araiza, M. Méndez-Galván, S. Tehuacanero-Cuapa, A. Gómez-Cortés and G. Díaz, RSC Adv., 2020, 10, 33059.

[94] S. Sato, K. Koizumi and F. Nozaki, Appl. Catal. A ,1995, 133, L7.

[95] W. Liu, C. Wadia and M. Flytzani-Stephanopoulos, Catal. Tod., 1996, 28, 391.

[96] S. Imamura, J. Tadani, Y. Saito, Y. Okamoto, H. Jindai and C. Kaito, Appl. Catal. A, 2000, 201, 121.

[97] M. Abid, V. Paul-Boncour and R. Touroude, Appl. Catal. A, 2006, 297, 48.

[98] S.-Y. Lai, Y. Qiu and S. Wang, J. Catal., 2006, 237, 303.

[99] U.R Pillai and S. Deevi, Appl. Catal. A, 2006, 299, 266.

[100] H. Sakurai, T. Akita, S. Tsubota, M. Kiuchi and M. Haruta, Appl. Catal. A, 2005, 291, 179.

[101] Q. Fu, A. Weber and M. Flytzani-Stephanopoulos, Catal. Lett., 2001, 77, 87.

[102] K. Zhou, X. Wang, X. Sun, Q. Peng and Y. Li, J. Catal., 2005, 229, 206.

[103] M. Lykaki, E. Pachatouridou, S.A.C. Carabineiro, E. Iliopoulou, C. Andriopoulou, N. Kallithrakas-Kontos, S. Boghosian and M. Konsolakis, Appl. Catal. B, 2018, 230, 18.

[104] G. Wang, L. Wang, X. Fei, Y. Zhou, R.F. Sabirianov, W.N. Meia and C.L. Cheung, Catal. Sci. Technol., 2013, 3, 2602.

[105] F. Yang, J. Wei, W. Liu, J. Guo and Y. Yang, J. Mater. Chem. A, 2014, 2, 5662.

[106] A. Bueno-López, K. Krishna, M. Makkee and J.A. Moulijn, J. Catal., 2005, 230, 237.

[107] E. Aneggi, M. Boaro, C. de Leitenburg, G. Dolcetti, A. Trovarelli, J. Alloys Compd., 2006, 408-412, 1096.

[108] L. Zhu, J. Yu, X. Wang, J. Hazardous Mater ., 2007, 140, 205.

[109] V. Alcalde-Santiago, A. Davó-Quiñonero, D. Lozano-Castelló and A. Bueno-López, Appl. Catal. B, 2018, 234, 187.

[110] G. Zhang, Z. Zhao, J. Liu, G. Jiang, A. Duan, J. Zheng, S. Chena and R. Zhou, Chem. Commun., 2010, 46, 457.

[111] X. Zhang, R. You, D. Li, T. Cao, and W. Huang, ACS Appl. Mater. Interfaces, 2017, 9, 35897.

[112] O. Demoulin, B. Le Clef, M. Navez and P. Ruiz, Appl. Catal. A, 2008, 344, 1.

[113] C. He, X. Liu, J. Shi, C. Ma, H. Pan and G. Li, J. Coll. Interface. Sci., 2015, 454, 216.

[114] Q. Song, R. Ran, J. Ding, X. Wu, Z. Si and D. Weng, Molecular Catal., 2020, 480, 110663.

[115] S. Zhang, S. Liu, X. Zhu, Y. Yang, W. Hu, H. Zhao, R. Qu, C. Zheng and X. Gao, Appl. Surf. Sci., 2019, 479, 1132.

[116] S.C. Rood, H.B. Ahmet, A. Gomez-Ramon, L. Torrente-Murciano, T.R. Reina and S. Eslava, Appl. Catal. B, 2019, 242, 358.

Supplementary materials for

Hierarchical macroparticles of ceria with tube-like shape – synthesis and properties.

Małgorzata A. Małecka*, Piotr Woźniak
Institute of Low Temperature and Structure Research, Polish Academy of Sciences,
P.O. Box 1410, 50-950 Wrocław 2, Poland

The details of the synthesis method.

In order to produce the material, the method of synthesis inspired by [M. Grun, K. Unger, A. Matsumoto, K. Tsutsumi, Micropor. Mesopor. Mater., 1999, 27, 207.] were used (Synthesis I in Table S1). It was noted that, a big part of cerium formate was not transformed into the CeO_2 during the synthesis process. The presence of $Ce(HCOO)_3$ was clearly visible in the XRD pattern collected from as-prepared sample (Fig.S1). In order to avoid biphasic sample, the amount of the base (NH_4OH) in the reaction mixture was doubled (Synthesis II in Table S1). In this case, only one phase (CeO_2) was visible on the XRD pattern of the as-prepared sample. It was one more attempt modifying the synthesis method (Synthesis III). In this case, the presence of CTAB was missing from the reaction mixture. As shown in Fig.S1, the presence of hexadecyltrimethylammonium bromide is necessary for the correct run of the synthesis. On the XRD pattern of sample prepared without CTAB, the strong peaks characteristic for the cerium formate near to CeO_2 ones were visible (despite the increased amount of base). In conclusion, only the synthesis procedure II was efficient and it was chosen for further syntheses of the hierarchical, tube-like $Ce_{1-x}Yb_xO_{2-y}$ (where $0 < x < 0.5$) materials which were studied in this work.

Table S1. Synthesis parameters.

		Synthesis I	Synthesis II	Synthesis III
Mixture I	$Ce(HCOO)_3$	0.25 g	0.25 g	0.25 g
	H2O	1 ml	1 ml	1 ml
	C2H5OH	0.5 ml	0.5 ml	0.5 ml
Mixture II	CTAB	0.125 g	0.125 g	-
	H2O	6 ml	4 ml	4 ml
	NH4OH	0.5 ml	2.5 ml	2.5 ml

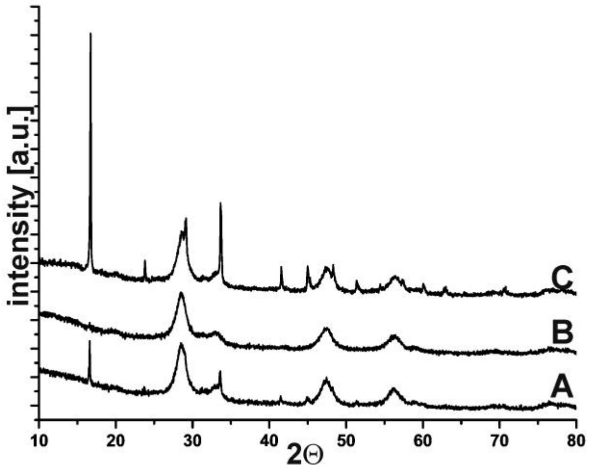

Fig.S1. XRD patterns of the CeO_2 samples prepared by the method (A) inspired by [M. Grun, K. Unger, A. Matsumoto, K. Tsutsumi, Micropor. Mesopor. Mater., 1999, 27, 207.] (synthesis I), (B) with double amount of base (synthesis II) and (C) without CTAB in the reaction mixture (synthesis III).

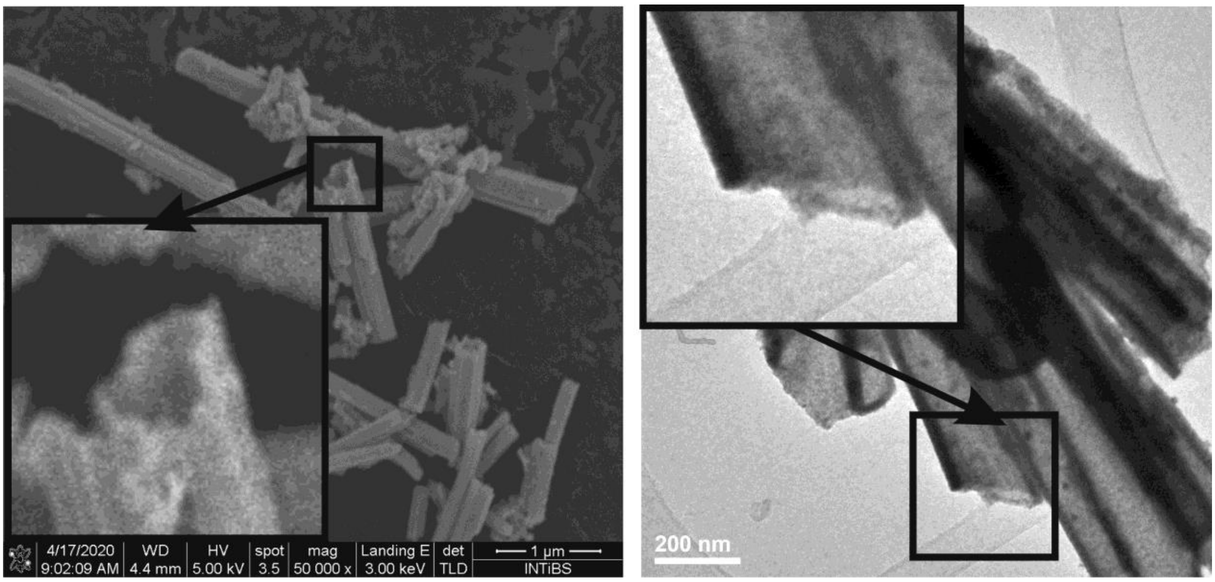

Fig.S2. SEM and TEM images of CeYb0_T_400 sample.

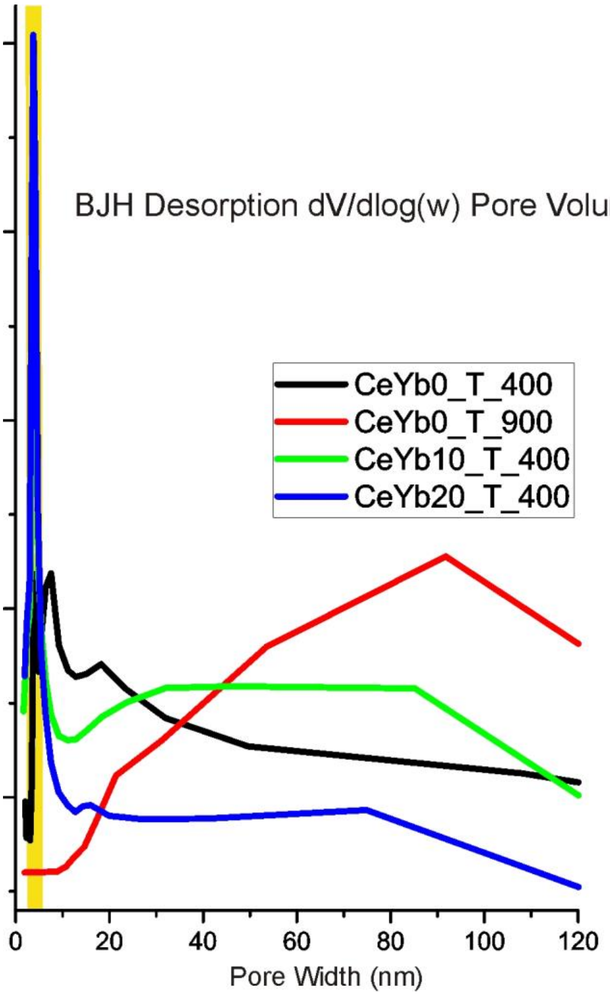

Fig.S3. The pore size distribution of the investigated samples.

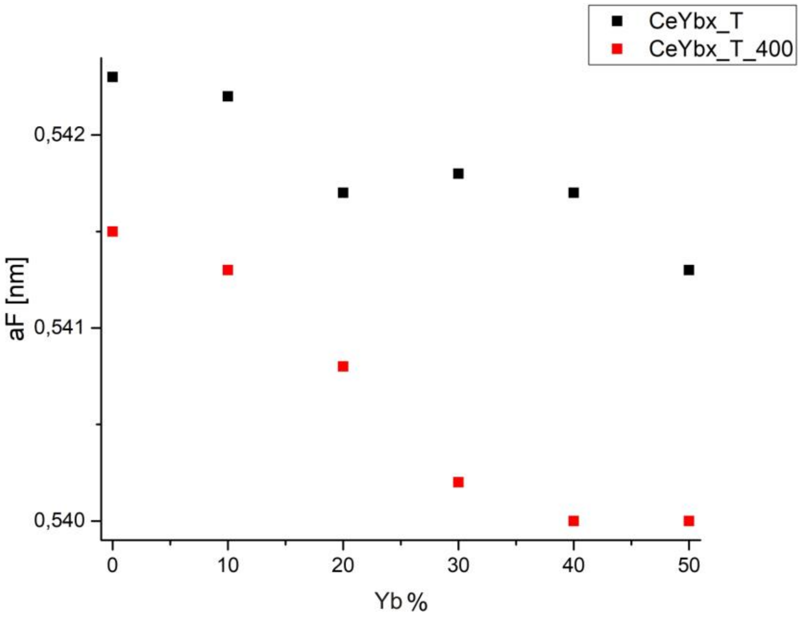

Fig.S4. Lattice parameters for CeYbx_T and CeYbx_T_400.

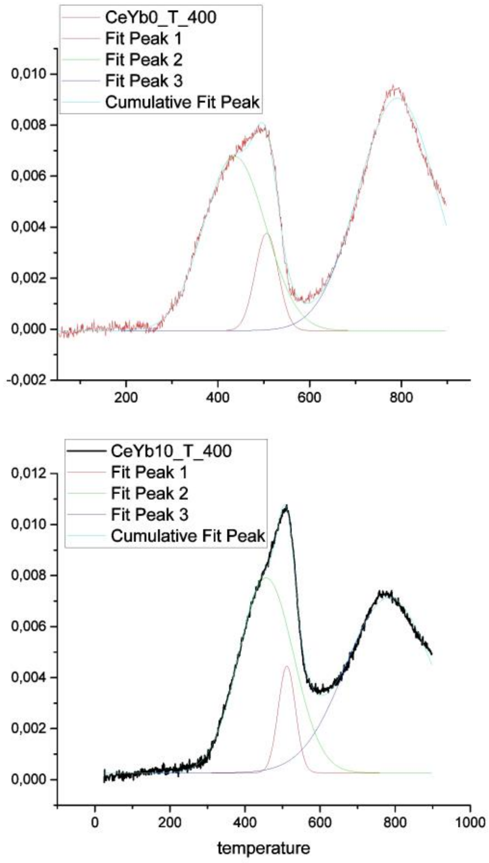

Fig.S5. H2-TPR profiles with peaks shown.